Seismic imaging of the structure of the central Ecuador convergent margin : relationship with the inter-seismic coupling variations

Eddy Sanclemente Ordoñez Sanclemente Ordoñez

UNIVERSITE DE NICE-SOPHIA ANTIPOLIS - UFR Sciences
École Doctorale de Sciences Fondamentales et Appliquées

T H E S E

pour obtenir le titre de :

Docteur en Sciences

de l'UNIVERSITÉ de Nice-Sophia Antipolis

Discipline : **Sciences de la Planète et de l'Univers**

présentée et soutenue par

Eddy SANCLEMENTE

IMAGERIE SISMIQUE DE LA STRUCTURE DE LA MARGE CONVERGENTE D'EQUATEUR CENTRAL : RELATIONS AVEC LES VARIATIONS DE COUPLAGE INTERSISMIQUE

SEISMIC IMAGING OF THE STRUCTURE OF THE CENTRAL ECUADOR CONVERGENT MARGIN: RELATIONSHIP WITH THE INTER-SEISMIC COUPLING VARIATIONS

Thèse dirigée par : ***Jean-Yves COLLOT*** et ***Alessandra RIBODETTI***

soutenue le 28 Mai 2014

Jury :

M. Bertrand Delouis,	Professeur,	Examinateur
M. Jacques Deverchère,	Professeur,	Rapporteur
M. Serge Lallemand,	Directeur de Recherche CNRS,	Rapporteur
M. Valenti Sallares,	Chargé de Recherche,	Examinateur
M. David Graindorge,	Maitre de conference,	Examinateur
Mme. Alessandra Ribodetti,	Chargé de Recherche IRD,	Co-Directrice de Thèse
M. Jean-Yves Collot,	Directeur de Recherche émérite IRD,	Co-Directeur de Thèse

Résumé

L'interprétation structurale de sections de Sismique Réflexion Multitrace-2D acquises pendant la campagne SISTEUR sur la marge convergente de l'Equateur Central et migrées en profondeur avant sommation (PSDM) a été combinée avec la bathymétrie multifaisceaux, des modèles tomographiques de sismique grand-angle OBS, un modèle d'inversion GPS, et 13 années de sismicité relocalisée, afin de déchiffrer les causes de la variabilité de la sismicité et du Couplage Inter Sismique (CIS) le long de la subduction. Cette partie de la marge, dont le socle est formé de roches océanique crétacé, est étroite (50-80 km) et érosive. Elle chevauche vers l'Ouest, à 4.7 cm/an, la Ride de Carnégie épaisse de ~15 km avec une surface irrégulière. Ce segment de subduction est découplé, à l'exception d'un patch bloqué de 50 X50 km et centré sur la région de l'Ile La Plata. Notre étude montre que la marge de l'Equateur Central comprend deux segments caractérisés par des propriétés physiques long termes différentes qui peuvent rendre compte de leur CIS et de leur sismicité. Le segment nord « Manta-Ile La Plata » de la marge, qui est bloqué, est caractérisé par une pente lisse entaillée par un réentrant de 50 km de large à morphologie douce. Aucun chenal de subduction n'est identifié le long de ce segment qui révèle la présence d'un important (50 X 40+ km) massif océanique (MO) subduit, haut de ~2.5 km, et dont le flanc arrière irrégulier plonge vers le continent de 2-4°, et coïncide avec la zone de CIS bloquée. Cette concordance suggère que le MO, qui est en contact avec le socle océanique résistant (Vp= 5 km/s) de la marge, concentre suffisamment d'énergie élastique pour créer une barrière sismique, et peut-être rompre comme une aspérité sismique. Le flanc avant du MO déduit de notre étude coïncide avec une zone de CIS partiel et des essaims de séismes chevauchant déformant le socle de la marge. Sous l'Ile de La Plata, la sismicité associé à un séisme lent (SSE) de 2010 se corrèle avec une zone de faible vitesse sismique et des réflecteurs sismique de forte amplitude (DR) à l'intérieur du MO subduit, traduisant un cisaillement intra plaque plongeante sous l'effet de fortes contraintes. A l'inverse, le segment sud « Puerto-Lopez-Salinas » de la marge, qui est découplé, affiche une pente sous-marine très perturbée avec des escarpements abrupts, de profond réentrants et d'importants dépôts en masse. Le contact inter plaque plonge de 6-7° sous le continent et porte des monts sous-marins isolés séparés par un chenal de subduction de ~1km d'épaisseur qui agit comme lubrifiant, facilitant le découplage inter-plaques. Les monts sous-marins sont en contact avec une marge à faible vitesse (Vp = 3.5 km/s) interprétée comme un complexe tectonique écaillé se déformant le long de failles normales listriques et incapable d'accumuler suffisamment d'énergie élastique pour permettre la propagation de la rupture. Un scénario en 3 étapes est proposé pour la subduction d'un MO de forme émoussée sous la marge résistante de l'Ile La Plata. 1) La subduction de OM est partiellement accommodée par fluage contre sa proue, alors que sa poupe reste bloquée. 2) Les contraintes accumulées dans le MO et dans le prisme interne de la marge sont partiellement libérées lors de SSE et d'essaims sismiques (Mw ~6.0), tandis que la déformation élastique s'accumule dans le prisme externe. 3) La zone bloquée se rompt de façon exceptionnelle lors un séisme de Mw 6.9-7.1 provoquant un éventuel tsunami. Un modèle cinématique est proposé pour rendre compte du soulèvement de l'île de La Plata en réponse à la subduction du MO au cours des derniers 1.3-1.4 Ma.

Abstract

The structural interpretation of 2D-Pre-stack Depth Migrated Multichannel Seismic Reflection sections collected during the SISTEUR cruise across the Central Ecuadorian convergent margin was combined with multibeam bathymetry, OBS wide-angle tomographic models, a GPS inversion model, and 13 years of relocated seismicity to decipher the causes of the along-trench variability of the seismicity and Inter-Seismic Coupling (ISC). The margin submarine part, which basement consists of Cretaceous Oceanic terranes, is narrow (50-80 km) and dominated by subduction erosion. It is underthrust eastward at 4.7 cm/yr by the ~15 km-thick, rugged Carnegie Ridge, and figures a decoupled subduction segment with the notable exception of a 50 X 50 km locked patch centered over La Plata Island region. Our study shows that the Central Ecuador margin divides in two contrasting segments with dissimilar long-lived physical properties that may account for their specific ISC and seismicity patterns. The locked northern "Manta-La Plata Island" segment shows a smooth outer-wedge slope scalloped by a gentle, 50 km-wide morphologic re-entrant. No subduction channel is detected across this segment that reveals a broad 50 X 40+ km, ~2.5-km-high subducted Oceanic Massif (OM), which bumpy trailing flank dips landward 2-4° and coincides with the ISC locked zone. This connection suggests that the OM, which is in contact with the strong (Vp= 5 km/s) oceanic margin basement, concentrates sufficient elastic strain energy to form a barrier to seismic slip propagation, and eventually break as a seismic asperity. The inferred OM leading flank concurs with partial ISC and thrust earthquakes swarms deforming the margin basement. Beneath La Plata Island, the seismicity associated with a 2010 Slow Slip Event correlates with a Low Velocity Zone and high-amplitude reflectors DR identified within the subducted OM, thus reflecting OM internal thrusting under high shear stress. In contrast, the decoupled southern Puerto Lopez-Salinas margin segment shows a highly disrupted outer-wedge seafloor with steep scarps, deep re-entrants and large Mass Transport Deposits. The plate interface dips landward ~6-7°, and is spotted by isolated seamounts separated by a ~1 km-thick subduction channel that may act as a lubricant favoring inter-plate decoupling. The seamounts impact against a low velocity (Vp=3.5 km/s) margin interpreted as a thrust sheet complex prone to deform along listric normal faults and incapable of accumulating sufficient elastic strain energy to support rupture propagation. A 3-step scenario is put forward for the subduction of a low-drag shaped OM beneath the resistant margin wedge of La Plata Island. 1) The OM subduction is partly accommodated by creeping along its leading flank, whereas its trailing flank remains locked; 2) Stress accumulated within the OM and inner margin wedge is partially released during slow slip events and earthquakes swarms (Mw ~6.0), whereas elastic strain keeps building up within the outer margin wedge; 3) Infrequent Mw 6.9-7.1 earthquakes may break the locked zone resulting in a possible tsunami. Moreover, a kinematic model accounting for the uplift history of La Plata Island is proposed as a result of the OM subduction over the last 1.3-1.4 Myr.

Remerciements

Je tiens tout d'abord consacrer ce travail à ma mère Celeste et à toute ma famillie, ainsi, je la remercie de son soutien, son courage et son éternel appui, grâce aux quels j'ai pu réussir ce qu'un jour on avait rêvé, et qui ont vécu cette longue aventure avec moi.

Je remercie et exprime mes sentiments de respect et admiration à mes directeurs de these: Jean-Yves COLLOT et Alessandra RIBODETTI, son appui personnel et professionnel, pour son énorme intérêt a ma formation, pour avoir partagé avec moi ses connaissances et pour les avoir mis dans ce manuscrit, et pour avoir suivi de très près toutes les étapes de ma thèse.

Je tiens a remercier a l'organisme qui a financé cette thèse, l'Institut de Recherche pour le Développement (IRD), et Geosciences Azur. Aussi a Escuela Superior Politécnica del Litoral (ESPOL), sans laquelle j'aurai pas pu contacter à l'IRD.

Je remercie également à Mansour Ioualalen, François Dumont, et Edison Navarrete qui étaient à l'époque et au bon endroit pour me conseiller et partager ses intérêts scientifiques avec moi, pour son enseignement et pour son ouverture.

Je remercie à toutes les personnes du laboratoire, particulièrement à Martine M., Laure S, Yvonne F., Marc R., partie d'une liste très grande, merci pour leur soutien, qui montre pendant ma period en France. Et aussi merci à l'Institut Geofísico de la Escuela Superior Politécnica Nacional, qui m'a permit faire partie de mon stage à Quito, Ep-Petroecuador, et au BCSI à Barcelona.

Enfin mais pas en dernier, aux membres du jury de thèse pour avoir lu, discuté et amélioré ce travail de thèse.

Eddy Sanclemente Ordóñez

28-05-2014

Contents

Figures

Chapter 1

Chapter 2

Chapter 3

Chapter 4

Chapter 5

Chapter 6

Chapter 7

Tables

Résumé Extensif

L'interprétation structurale de sections de Sismique Réflexion Multitrace-2D acquises pendant la campagne SISTEUR sur la marge convergente de l'Equateur Central et migrées en profondeur avant sommation (PSDM) a été combinée avec la bathymétrie multifaisceaux, des modèles tomographiques de sismique grand-angle OBS, un modèle d'inversion GPS, et 13 années de sismicité relocalisée, afin de déchiffrer les causes de la variabilité de la sismicité et du Couplage Inter Sismique (CIS) le long de la subduction.

Cette thèse a été decoupée en 7 chapitres suivis d'une conclusion, de persvectives, d'un manuscrit d'article à soumettre, et 3 profils supplémentaires de SISTEUR. Les chapitres de la thèse sont présentés ci-dessous :

Chapitre 1

Le chapitre 1 donne des generalites sur les zones de subduction et presente la problématique générale. Les structures dans une marge convergente, la zone sismogène, le couplage sismique, et le cicle sismique sont aussi abordés dans ce chapitre de manière general afin d'avoir de notions qui vont être utilisées plus tard dans le manuscrit. Une section est consacrée aux grands seismes de Tohoku 2011, Maule 2010, et Sumatra 2004 car ils nous ont montré que notre connaisance sur le comportant du segment supérieur de la marge est encore très pauvre. L'impact des monts sous-marins sur une marge est aussi presenté dans ce chapitre. On parle du décollement, et on donne des exemples afin de trouver la relation avec l'inversion de polarité dans notre zone d'étude.

Chapitre 2

Ce chapitre 2 presente le contexte géologique, morphologique, et geodynamique de la Marge Équatorienne. On aborde les seismes de 1906, 1942, 1958, et 1979, aussi que la microsismicité. Les principaux characteristiques de la plaque plongeante et les regions de l'Équateur sont presentées de manière résumé. Une description de l'île de la Plata avec ses terrasses est realisée à la fin de ce chapitre, cela va nous permettre utiliser l'information sur les mouvements verticaux, et la nature des terrasses afin qu'on pourrait l'utiliser dans la discussion.

Chapitre 3

Le Chapitre 3 montre la zone d'étude, qui se trouve entre Manta et Salinas dans la Marge Centrale

Équatorienne. Les terrases marines qui affleurent sur l'île de La Plata sont analisées pour comprendre l'origen de l'île. La sismicité est presentée pour les deux segments de la zone d'étude. Le segment nord est characterisé par une concentration de seismes entre l'île de la Plata et la côte. Par contre, dans le segment sud, la sismicité est abscente pour la period de 13 années qu'on a utilisé. Le Slow Slip Event du 2010 qui eu lieu sous l'île de la Plata est aussi décrit dans ce chapitre. On presente les modèles de vitesse (Vp) des profils SIS12 et SIS64 de STM traités par Sage *et al*., (2006), et de Sismique de Grand Angle (SGA) des profils SIS01, SIS02, et SIS04 obtenus par Graindorge et al. (2004) et Gailler (2005).

Chapitre 4

Ce chapitre décrit la methodologie utilisée pour migrer les données en temps et profondeur. On detaille également les méthodes de sismique de réflexion et réffration. Dans le chapitre 4, on montre la chaine de traitement qui nous a permit d'améliorer les profils traités à bord du Nadir, SISTEUR 2000. Les nouvelles images sont montrées dans la partie finalle du chapitre.

Chapitre 5

Dans le chapitre 5, on a realisé la migration pré-stack en profondeur et la correction des modèles de vitesse. Pour les profils SMT qui ont des données de SGA, on a construit des modèles mixtes afin d'améliorer les résultats à profondeurs de plus de 5 km.

Chapitre 6

Le chapitre 6 décrit les résultats de l'analyse d'imagerie sismique, et fournit l'interpretation des profils. Ils ont été divisés dans 3 ensembles : 1) les profils du segment nord, où la partie marine de la marge est characterisée par une pente lisse entaillée par un réentrant d'environ 50 km de large avec une morphologie douce ; 2) un segment sud qui a une pente sous-marine très pertubée avec des escarpéments abrupts, de profond réentrants, et d'importants dépôts en masse ; et une zone de transition characterisée par les lentilles de sediments. La dernière partie de ce chapitre est consagrée aux inversions de polarités, où on a essayé de corroborer l'association entre le décollement et les inversions de vitesse.

Chapitre 7

Le chapitre 7 se présente sous forme de discussion qui permet de récapituler les résultats de la thèse. Pour cette discussion on a combiné l'interprétation structurale de sections de Sismique Réflexion Multitrace-2D migrées en profondeur avant sommation (PSDM) avec la bathymétrie multifaisceaux, des modèles tomographiques de sismique grand-angle OBS, un modèle d'inversion

GPS, et 13 années de sismicité relocalisée, afin de déchiffrer les causes de la variabilité de la sismicité et du Couplage Inter Sismique (CIS) le long de la subduction.

Dans ce chapitre on discute sur : 1) la distribution 2D et 3D des monts sous-marins ; 2) la relation entre les monts sous-marins en subduction, la morphologie du fond de la mer, et les structures moins profondes ; 3) le soulèvement de l'île de la Plata qui resulte de la subduction de l'un massif oceanique identifié au segment nord ; 4) l'interaction tectonique entre les monts sous-marins et les segments de la zone d'étude ; 5) les variations de réflectivité le long de la base du socle ; 6) la correlation entre la distribution spatielle du couplage intersismique et la microsismicité, et l'éppaiseur et la rugosité du contact interplaque.

Dans ce chapitre un scénario en 3 étapes est proposé pour la subduction du massif oceanique de forme émoussée sous la marge résistante de l'Ile La Plata, les étapes sont : 1) la subduction de MO est partiellement accommodée par fluage contre sa proue, alors que sa poupe reste bloquée ; 2) les contraintes accumulées dans le MO et dans le prisme interne de la marge sont partiellement libérées lors de SSE et d'essaims sismiques (Mw ~6.0), tandis que la déformation élastique s'accumule dans le prisme externe ; 3) la zone bloquée se rompt de façon exceptionnelle lors un séisme de Mw 6.9-7.1 provoquant un éventuel tsunami. Additionellement, on propose un modèle cinématique pour rendre compte de la surrection de l'île de La Plata en réponse à la subduction du MO au cours des derniers 1.3-1.4 Ma.

Dans ce chapitre on montre que la marge de l'Equateur Central comprend deux segments caractérisés par des propriétés physiques long termes différentes qui peuvent rendre compte de leur CIS et de leur sismicité.

Introduction

Les grands séismes de subduction (Mw >8) posent une menace sismique et de tsunami le long des côtes densément peuplées. Ces séismes ne se produisent cependant pas le long de tous les segments de zone de subduction de la planète. Certains segments de fosse de subduction ont été frappés de façon récurrente par de très grands séismes et des tsunamis dévastateurs tel que à Sumatra (2004, Mw 9.2, Subarya *et al.,* 2006), au Japon (2011, Mw 9.0, Ide *et al*., 2011), au sud Pérou (2011, Mw 8.5, Pritchard *et al*., 2007), et au Chili (Maule 2010, Mw 8.8, Vigny *et al.,* 2011) indiquant qu'un haut niveau de contrainte et un fort couplage mécanique contrôle la méga-faille de subduction. En revanche, d'autres segments de fosse de subduction ne sont pas l'objet de si grands séismes instrumentaux ou historiques tel que sur la côte pacifique NO de la Colombie (Carena *et al*., 2011) et dans le sud de l'Equateur et le Nord du Perou (Carena *et al*., 2011; Pritchard *et al*., 2007), suggérant que soit la méga-faille de subduction est faiblement couplée et ne produit que des séismes de faible magnitude soit que cette méga-faille est bloquée depuis longtemps produisant de grands séismes avec un temps de retour très long (plus de 500 ans au Nord Pérou et sud de l'Equateur). Nocquet *et al*., (2014) ont récemment montré que la zone de subduction du Nord Pérou au sud de l'Equateur est découplée. Il est donc important de mieux comprendre quelles propriétés physiques de la méga-faille de subduction et des roches environnantes contrôlent le couplage inter-sismique (ISC) ainsi que ses transitions latérales et transversales vers le glissement asismique.

Les modèles mécaniques classiques de subduction stipulent qu'un grand séisme de subduction ne peut pas s'initier sous la front de la marge, i.e. le long du segment supérieur de la méga-faille de subduction, à cause des propriétés de glissement stable des sédiments non- ou semi-consolidés à la base d'un prisme d'accrétion (Byrne *et al.,* 1988; Hyndman *et al.,* 1997). En conséquence, le couplage ISC est supposé être très faible au front de la marge. A l'inverse, sous la marge interne, dans la zone sismogène fortement couplée, le type de glissement est instable (stick-slip) car les sédiments subduits sont plus compactés et leurs propriétés minéralogiques se transforment (Byrne *et al*., 1988; Scholz, 1998; Moore *et al.,* 2007).

Cependant, lors du séisme de Mw 9.0 de Tohoku-Oki en 2011 (Ide *et al.,* 2011) la rupture sismique s'est propagée jusqu'à la fosse avec un important glissement co-sismique horizontal qui

a atteint 50 m voir 80 m (Tsuji *et al*., 2011; Lay *et al*., 2011; Ide *et al*., 2011, Ito *et al*., 2011), alors que les modèles GPS avaient prédit un couplage inter-sismique (ISC) relativement faible près de la fosse (Loveless *and* Meade, 2010; Ozawa *et al*., 2011). De la même manière, le glissement co-sismique a atteint de faibles profondeurs et vraisemblablement la fosse lors du séisme de Maule, Chili de Mw 8.8 en 2010 (Vigny *et al*., 2011).

Du fait que les modèles ISC au voisinage de la fosse étaient peu contraints car établis à partir de mesures GPS faites à terre loin de la fosse, les menaces sismiques et tsunamis de ces 2 séismes ont été sous-estimées. D'autre part, nos connaissances des paramètres contrôlant le couplage ISC sous la pente externe de la marge se révèlent insuffisants pour rendre compte de la propagation de la rupture jusqu'à la fosse. Parmi les causes potentielles de cette propagation, un fort degré de couplage ISC le long du segment supérieur de la faille interplaque est possible comme cela a été montré en face de Lima au Pérou à partir de mesures de géodésie sous-marines (Gagnon *et al*., 2005). Les raisons de ce fort couplage restent néanmoins inconnues. Bien que sujet à controverse, la subduction de monts sous-marins a souvent été évoquée comme cause potentielle du blocage de la faille inter-plaque.

L'Equateur est un excellent exemple pour l'étude de la segmentation sismo-tectonique d'une marge convergente et de ses relations avec les grands séismes de subuduction le long de la moitié nord de cette marge et l'absence de tels séismes le long de sa moitié sud, par exemple au large du Golf de Guayaquil (Collot *et al.*, 2004; Calahorrano *et al.* 2008). Le long de l'Equateur central, entre Manta et Salinas /Santa Elena, la marge convergente est érosive et si étroite que des mesures GPS ont pu être acquises le long de la côte a ~70 km de la fosse et sur l'ïle de La Plata a seulement ~ 35 km de la fosse, permettant ainsi de contraindre le couplage ISC sous le front de la marge. Les modèles d'inversion GPS (Nocquet *et al*., 2014; Chlieh *et al*., submitted) ont montré que la marge centrale d'Equateur est très faiblement couplée entre Manta et Salinas, à l'exception d'un segment fortement couplé sous le front de marge jusqu'à la fosse, à proximité de l'ile de La Plata. Le modèle classique de segmentation transversale du couplage ISC de Byrne *et al.,* (1988) ne s'applique donc pas pleinement sur ce segment. Au sud de la zone bloquée de La Plata et jusqu'à Salinas, le modèle GPS de Chlieh *et al*., (submitted) indique un très faible couplage sur toute la largeur de la marge. Ce remarquable contraste de couplage entre deux segments voisins l'un bloqué, l'autre en glissement libre se produit dans une zone ou les enregistrements de sismicité n'indiquent pas de séisme de Mw > 6.5 (Font *et al*., 2013; *Vallée et al*., 2013). Elle est donc considérée comme un segment de subduction asismique

L'objectif de cette thèse est d'explorer les causes des variations transversales et longitudinales de couplage ISC et de la sismicité dans le secteur de marge étroit de notre zone d'étude entre Manta et Salinas. Nous avons utilisé une grille de données de Sismique réflexion multi-trace acquise pendant la campagne SISTEUR (2000) ainsi que des modèles de vitesse Vp obtenus par sismique grand angle OBS (Gailler, 2005) pour migrer en profondeur et en 2D des sections sismiques. Pour la migration PSDM, nous avons utilisé une approche en deux étapes s'appuyant sur une migration/inversion ray + Born des formes d'onde (Thierry *et al.,* 1999) complètes par des corrections itératives du macro-modele de vitesse Vp (Al-Yahya, 1985). Cette procédure permet d'imager correctement la géométrie des structures de la marge, d'évaluer les variations de réflectivité le long du contact inter-plaque, et d'identifier des monts sous-marins en subduction sous la pente externe de la marge.

Les nouvelles données de sismique réflexion migrées en profondeur sont combinées avec des données de bathymétrie haute résolution, des modèles de vitesse Vp à échelle crustale, un modèle de couplage ISC obtenu par GPS et la distribution de la sismicité pour comprendre pourquoi le segment de l'Ile de Plata est bloquée alors que celui situé immédiatement au Sud est en glissement libre.

En fonction des résultats de l'imagerie sismique et afin de comprendre les causes de ces variations de couplage ISC, nous analysons l'hypothèse de l'interaction entre des monts sous-marins subduits, la nature de la marge et du contact inter-plaque, considérant deux modèles extrêmes : (1) un mont sous-marin produit un fort coupage ISC qui peut engendrer de grands séismes (Scholtz *and* Small, 1997) et (2) un mont sous-marin fracture la marge et ne peut être la cause d'un grand séisme (Wang *and* Bilek, 2011). Finalement, en s'appuyant sur les variations spatiales du couplage ISC, la distribution spatiale et temporelle de la sismicité, l'existence d'un séisme lent (SSE) et nos interprétations structurales, nous proposons un modèle de subduction de mont sous-marin qui considère comme d'importance significative la rugosité de la topographie du mont sous-marin, la présence ou l'absence d'un chenal de subduction ainsi que les variations spatiales de la nature et donc de la résistance du socle de la marge.

Introduction

Large subduction earthquakes (Mw > 8) pose a seismic and tsunami threat to densely populated coasts. However, these earthquakes (EQ) have not occurred along all segments of the worldwide subduction zones. Some trench segments have been repeatedly hit by very large EQ and local devastating tsunamis such as Sumatra (2004, 9.2 Mw, Subarya *et al.,* 2006), Japan (2011, 9.0 Mw; Ide *et al*., 2011), Southern Peru (2001, 8.5 Mw; Pritchard et al., 2007) and Chile (8.8 Mw Maule 2010; Vigny *et al*., 2011) indicating that high stress and strong mechanical coupling control their interplate megathrust. In contrast, other trench segments do not have instrumental or even historical records of such very large EQ like in Northwestern Colombia (Carena *et al*., 2011), and southern Ecuador and northern Peru (Carena *et al.,* 2011; Pritchard *et al.,* 2007), suggesting that either their plate interface is dominated by free sliding and produce only smaller size events, or that the interplate contact has been long locked producing great earthquakes with a very large recurrence time (over 500 years in northern Peru southern Ecuador). Nocquet *et al*., (2014) have shown recently that the northern Peru southern Ecuador is free sliding. Therefore, it is important to better understand which physical properties of the subduction fault and adjacent rocks control the inter-seismic coupling (ISC) as well as the cross and dip transitions to aseismic slip.

Classical mechanical models of Subduction state that a large subduction EQ could not generate beneath the outer margin wedge i.e. along the updip interplate fault segment because of the stable slip properties of unconsolidated to semi-consolidated sediments at the base of an accretionary wedge (Byrne *et al.,* 1988; Hyndman *et al*., 1997). Consequently the inter-seismic coupling (ISC) is supposed to be weak along the up-dip fault segment. Conversely within the highly coupled seismogenic zone beneath the inner-margin wedge, the slip behavior changes to unstable stick-slip sliding because the subducting sediments are more consolidated and their mineralogic properties have changed (Byrne *et al*., 1988; Scholz, 1998,).

However, during the 2011 Mw 9.0 Tohoku-Oki earthquake (Ide *et al*., 2011), the earthquake rupture propagated up to the trench with a large horizontal coseismic slip that had reached ~50 m and up to 80 m (Tsuji *et al* 2011; Lay *et al.,* 2011; Ide *et al*., 2011, Ito *et al*., 2011), even though the

GPS models had predicted a low ISC near the trench (Loveless *and* Meade, 2010; Ozawa *et al*., 2011). Similarly, the coseismic slip reached shallow depths and likely the trench during the 2010 Mw 8.8 Maule (Vigny *et al*., 2011).

Likely, due to the fact the ISC models were poorly constrained near the trench because they derived from onshore GPS data taken too far from the trench, the seismic and tsunami threats of these two large earthquakes had been underestimated. Moreover, our knowledge of the parameters controlling the ISC beneath the outer-margin wedge revealed insufficient to account for the rupture propagation up to the trench. Among the potential causes is a high degree of ISC along the updip segment of the subduction fault as demonstrated offshore Lima in Peru on the basis of submarine geodetic measurements (Gagnon *et al.,* 2005). Nevertheless, the cause for such high coupling has remained unknown. Although controversial, seamount subduction has often been invoked as a potential cause for locking the plate interface. Ecuador has shown to be an excellent example to study the seismo-tectonic segmentation of a convergent margin and its relationship to large subduction earthquakes (up to Mw 8.8) along the north half of the margin and the absence of such large earthquakes in the southern segment of that margin, for example off the Gulf of Guayaquil (Collot *et al*., 2004; Calahorrano *et al*. 2008). In central Ecuador, between Manta and Salinas/Santa Elena, the convergent margin is erosive and so narrow that GPS measurements were acquired along the coastline some ~70 km from the trench, and on La Plata Island only ~35 from the trench to constrain confidently the ISC beneath the outer-margin wedge. GPS inversion models (Nocquet *et al*., 2014; Chlieh *et al*., submitted) revealed that the central Ecuador margin is weakly coupled between Manta and Salinas with the exception of a strong ISC patch beneath the outer margin wedge near La Plata Island. Thus, the classic model of down dip segmentation of the interplate fault coupling of Byrne *et al.,* (1988) does not fully apply across the La Plata Island margin segment. South of La Plata Island patch until Salinas, the GPS inversion model of Chlieh *et al*., (submitted) indicates a weak ISC across the entire margin segment. This remarkable contrast of ISC between two margins segments one being locked and the other one free sliding occurs within a small zone where the seismic records do not show Mw>6.5 earthquakes (Font *et al*., 2013; Vallée *et al.,* 2013), and therefore is considered an aseismic subduction.

The objective of this thesis is to investigate the causes of the variations of Inter-Seismic Coupling (ISC) and seismicity across and along the narrow margin wedge of our study area between Manta and Salinas.

We used a grid of Multichannel Seismic (MCS) data collected during the SISTEUR cruise (2000) and OBS wide-angle Vp velocity models (Graindorge et al., 2006; Gailler, 2005) to obtain 2D-depth-migrated seismic sections. To perform PSDM, we use a two-step approach base on ray + Born waveform migration/inversion (Thierry *et al*., 1999) and an iterative correction of the Vp macromodel (Al-Yahya, 1985). This procedure permitted to properly image structural geometry of the margin wedge, evaluate reflectivity variations along the plate interface, and identify subducting seamounts beneath the outer-margin wedge.

The new Pre-Stack Depth Migration MCS data are combined with high-resolution bathymetry, Vp velocity crustal models, GPS derived ISC models, and seismicity distribution to understand why the La Plata Island patch is locked whereas the margin segment located immediately to the south of it is freely sliding. As a result of MCS imaging, and in order to understand the causes of these ISC variations, we analyze the hypothesis of the interaction between subducted oceanic seamounts and the margin wedge and megathrust fault nature considering two extreme models: (1) Seamount produce strong coupling and can generate large earthquakes (Scholtz and Small, 1997) and (2) seamount heavily fracture the margin and cannot produce large earthquakes (Wang and Bilek, 2011). Finally, based on ISC spatial variations, microseismicity temporal and spatial distribution, the occurrence of a Slow Slip Event, and our structural interpretations, we propose a model for seamount subduction that considers significant the roughness of the seamount topography, the absence or presence of a subduction channel and the spatial variation of the nature and strength of the margin basement.

CHAPTER 1

GENERALITIES, SUBDUCTION ZONE

1.1 Subduction Zone

A subduction zone is a convergent lithospheric plate boundary where a tectonic plate underthrusts another plate. In the case of an oceanic subduction zone (Figure 1.1), an oceanic lithospheric plate underthrusts a continental margin (oceanic-continental convergence) or a volcanic island arc (intra-oceanic convergence), giving place to tectonic deformations, earthquakes and in many cases important volcanism (Clift *et al.,* 2009). The two plates are separated by a lithospheric discontinuity, which includes the inter-plate fault or mega-thrust fault.

Subduction occurs because of thermal convection in the earth mantle, and differences in plate density. Continental rocks are on average lighter (d= 2.69 and 2.74 g/cm3) than oceanic rocks (d= 3.0 and 3.25 g/cm3), so that an oceanic plate is generally subducted beneath a continent. In an oceanic plate, the difference in densities occurs because the lithosphere becomes thicker and denser as it ages.

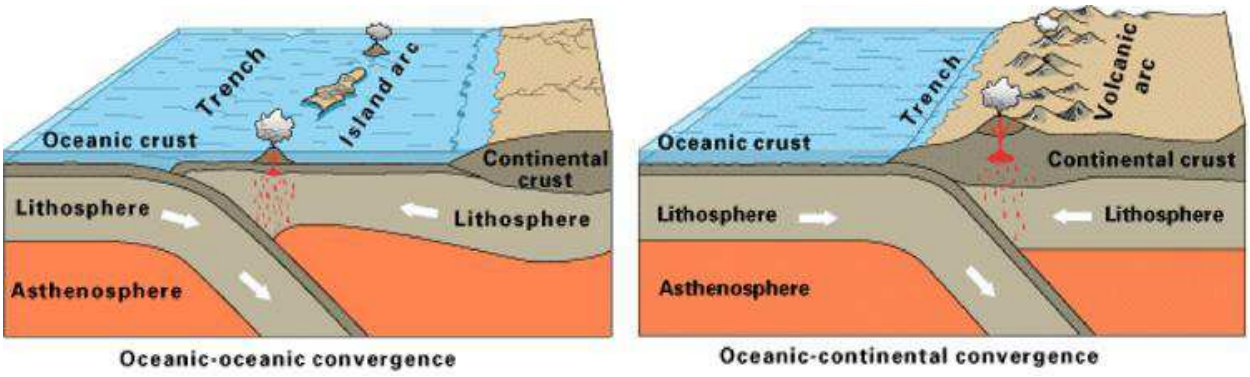

Figure 1.1 Example of a Subduction zone; left: intra-oceanic subduction and formation of an island arc; right: underthrusting of an oceanic plate beneath continental tectonic plate and formation of a volcanic arc (USGS).

1.1.1 Oblique convergence

At subduction zones, the relative motion between two plates generally includes an oblique component of motion (Figure 1.2), as described Fitch *et al*. (1972); DeMet *et al*. (1994). According

to Soofi *and* King, (2002), oblique convergence produces strain partitioning with both compressional and shear components, giving place to a variety of structures, depending on the ratio of compressional to shearing motion. Subduction zones with oblique plate motion show transcurrent faults (Fitch fault), which are faults involving motion parallel to the strike of the margin and delineating a fore-arc tectonic sliver (e.g., Atacama Fault in Chile (Cembrano *et al*., 2005); Alpine fault extremities in New Zealand (Schofield, 1960) ; The Queen Charlotte/Fairweather fault system in Alaska (Doser *and* Lomas, 2000).

According to Chemenda *et al*. (2000), strain partitioning is caused by basal high friction and can only exists in compressional subduction zones where the overriding plate contains a zone of mechanical weakness; they further suggest that other factors such as the length of the margin segment along which the subduction is oblique, and the boundary conditions at the limits of the forearc sliver also control the strain partitioning.

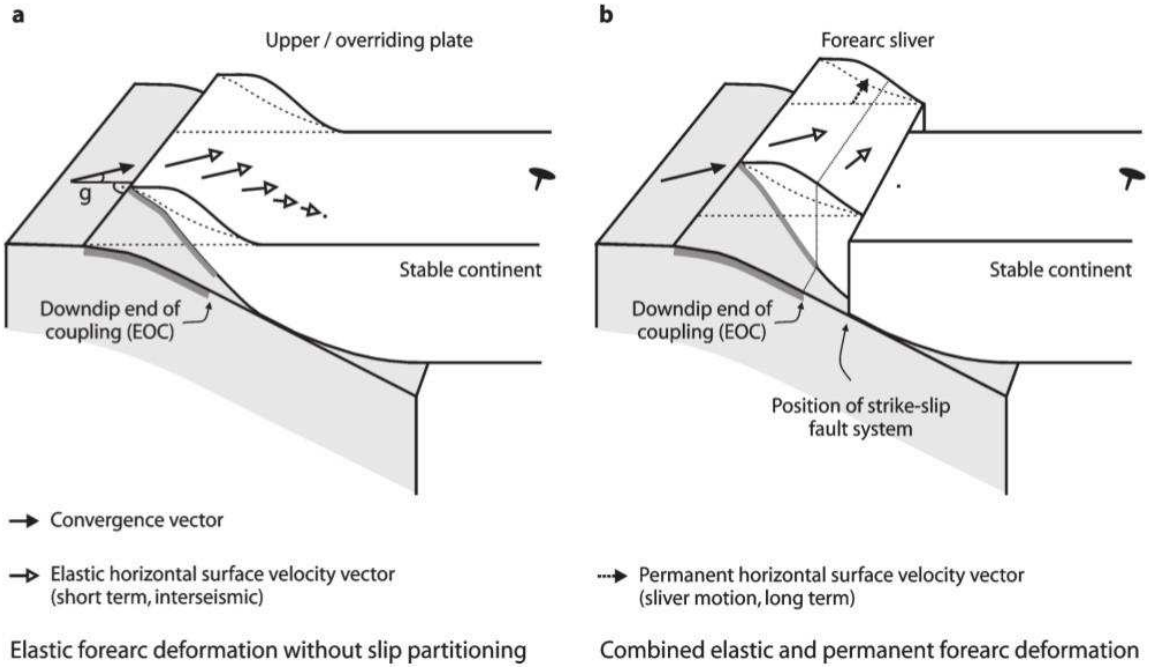

Figure 1.2 Oblique Convergent Subduction; a) pure elastic strained fore-arc; b) the fore-arc accommodates part of the trench-parallel component along a strike-slip fault (Hoffmann-Rothe, 2006).

1.1.2 Types of convergent margins

Convergent margins can be divided into two end-members types: the **accretionary margin** showed in Figure 1.3a, and, **the erosive margin** showed in Figure 1.3b (von Huene *and* Scholl, 1991; Clift *and* Vanucchi, 2004).

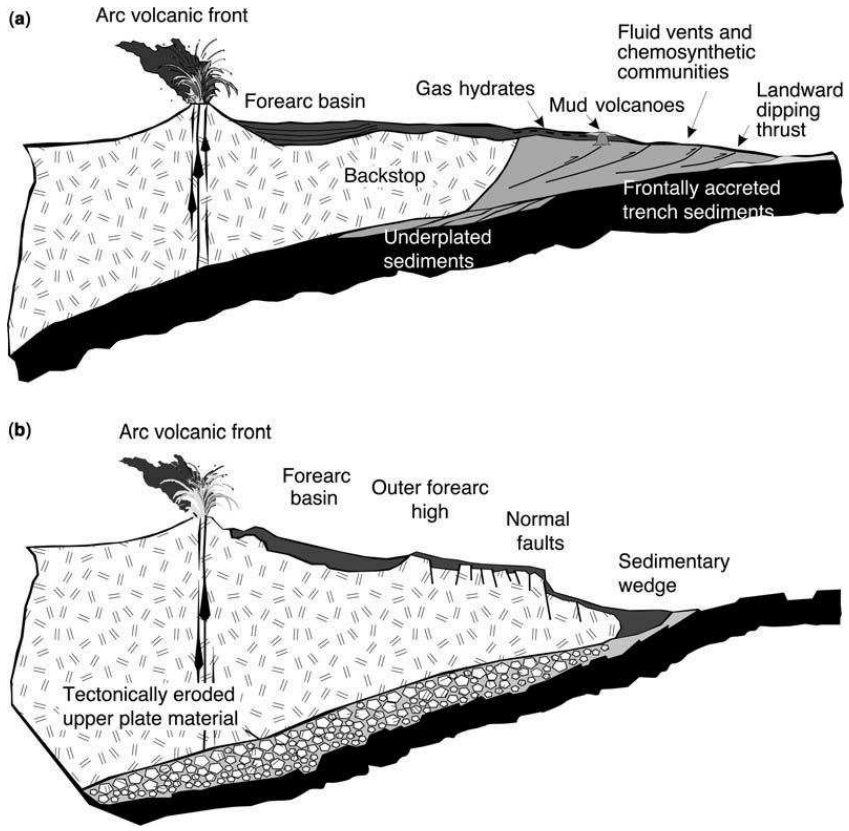

Figure 1.3 The two basic types of convergence margin: (a) accretionary active margin, with underplating and frontal accretion; landward dipping thrust fault are observed in the sedimentary prism; (b) erosional active margin, characterized by normal faulting and subduction of tectonically eroded material (Clift and Vannucchi, 2004).

1.1.2.1 Accretionary Margins

Accretionary margins are characterized by forearc regions fronted by an accretionary wedge that is composed of thrust and deformed slices of trench and oceanic sediment (Clift *et al.,* 2009; Moore G. *et al.*, 2007). Accretionary wedges have (Figure 1.4), a seaward part (outer wedge) and a landward part (inner wedge). Some examples of accretionary wedges are: the Calabrian Accretionary wedge in the Central Mediterranean (Minelly *and* Faccenna, 2010); The Neogene

accretionary wedge off Kenai Peninsula in Alaska (Fruehn *et al.,* 1999); The Barbados accretionary wedge (Westbrook *et al.,* 1998) and the Nankai accretionary wedge (Obana *et al.,* 2006).

An accretionary wedge (*e.g.*, Makran accretionary prism) is composed of initially water-saturated sediments transferred from the subducting plate to the overriding plate (von Huene *et al.*, 2004; Moore *and* Vrolijk, 1992). The subducting sediments loose fluid by tectonically induced consolidation and thermally induced dehydration processes (Moore *and* Vrolijk, 1992).

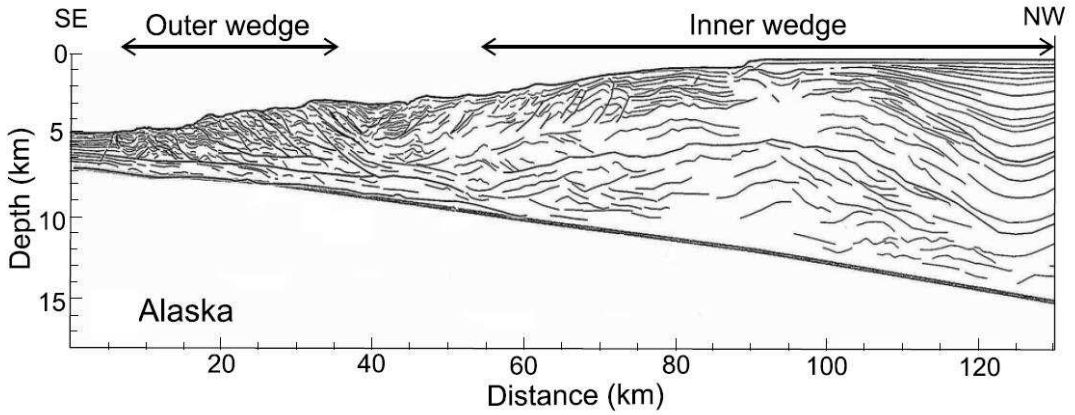

Figure 1.4 Example of an accretionary wedge from Alaska, showing the outer and inner segments (Wang and Hu, 2006).

There are two types of accretion acting onto convergent margins (Figure 1.5):

1) Frontal accretion that gives birth to an accretionary wedge takes place by incorporation of trench sediments and/or upper crustal material of the down going plate into the wedge (Selzer *et al.,* 2008).

2) **Basal accretion or under-plating** corresponds to the process where subducting sediment is accreted below the accretionary prism, increasing prism thickness. As results of the basal accretion, orogens grow by underplating of nappes that are off-snaped from the subducting upper crust (Gutscher *et al.,* 1999; Selzer *et al.,* 2008; Collot *et al.,* 2011). Basal accretion or underplating occurs by a process known as duplex accretion. A duplex is an imbricate package of isolated thrust slices bounded on top by a thrust and below by a low-angle detachment fault (Sample *and* Ficher, 1986). Evidence for active duplex emplacement has been shown at the Pacific Colombia convergent margin (Collot *et al*., 2008).

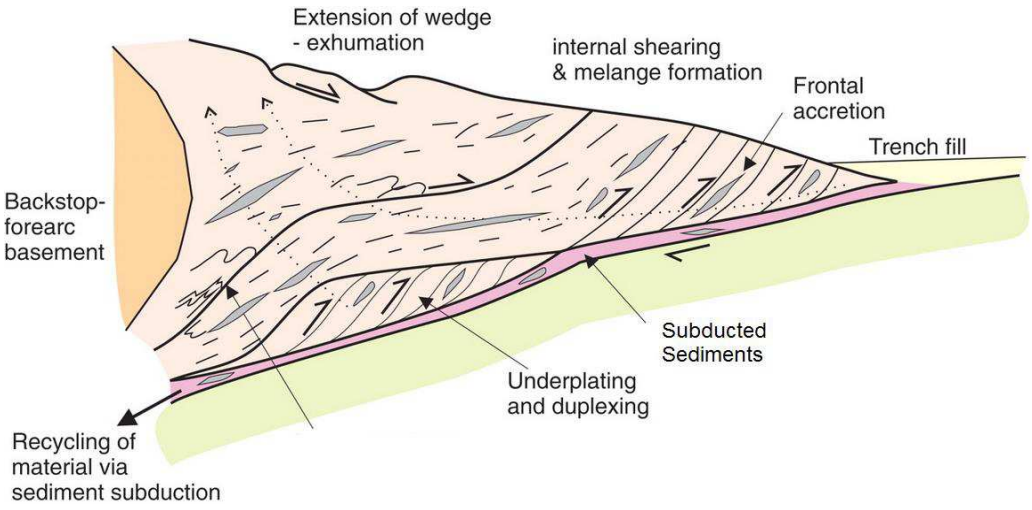

Figure 1.5 Schematic section of accretionary prism. Thrust faulting is observed in the outer part of the wedge and above the subduction channel (in dark pink). Both frontal accretion, basal accretion are present in this section. Here, the basement thickens specially by duplexing (Cawood et al., 2013).

The Coulomb wedge theory (Davis *et al*. 1983, Dahlen *et al.* 1990, Lallemand *et al.,* 1994) models the mechanics of accretionary wedges along compressive plate boundaries for non-cohesive materials. This theory states that a wedge will develop as material deforms internally and piles up in front of the backstop until the surface slope reaches a critical taper (*i.e*., shape for which the wedge is on the verge of failure under horizontal compression everywhere). Before reaching this critical angle, the wedge is unstable (sub-critical wedge). In the theory, once, the wedge has reached its critical shape it will start sliding along a basal detachment without continuing internal deformation. After reaching this stage, the wedge becomes stable. Additional material will get accreted at the toe, but the wedge will maintain its critical slope. When the wedge has reached the critical angle, deformation is occurring internally via thrust faulting and basal shear along the décollement.

Wang *and* Hu (2006) expanded the classical theory to the dynamic Coulomb wedge theory. According to them, during large thrust earthquakes, the outer wedge is pushed into a compressional critical state with a decrease in basal and internal stress and pore fluid pressure. In this state sediment accretion, basal erosion, and activation of splay faults take place. After the earthquake, the outer wedge returns to a stable state. During consecutives earthquakes, the inner wedge will remain mostly in a stable state, acting as backstop that permits formation of fore-arc basins.

1.1.2.2 Erosive Margins

In contrast with accretionary margins, erosive margins are progressively destroyed by the subduction process, thus resulting in margin seafloor subsidence and landward migration of the trench axis and volcanic arc (von Huene *and* Scholl, 1991; Clift *and* Vannucchi, 2004; Wang *et al.,* 2010). Erosive margins (Figure 1.3b) are common in the circum-Pacific region where they are marked by steep trench slopes underlain by volcanic, plutonic and mantle rocks and a quasi-absence of an accretionary wedge (Clift *et al.,* 2009).

Along erosional convergent margins (*e.g.,* Tonga margin), most fluid-rich sediment accumulated in the trench is dragged down the subduction together with the under riding plate (Clift *et al.,* 2009). The subduction erosion process includes frontal and basal erosion, and can take place at all convergent plate boundaries, including accretionary margins. The **frontal erosion** results from a combination of erosion and structural collapse of the forearc wedge into the trench; whereas the **basal erosion** is produced by the abrasion and hydrofracturing of the base of the overriding plate above the subduction channel. This process results in mass transfer from the bottom of the forearc wedge to the lower plate, as dislodged fragments of the margin basement are subducted (von Huene *et al.*, 2004).

A small frontal prism occurs along most margins undergoing subduction erosion. It is structured like an accretionary prism with landward-dipping reflection (von Huene *et al.*, 2004) but it is composed of slump debris derived from the outer-wedge slope. According to von Huene e*t al.* (2000), the subducting high-relief features destroy the frontal prism; however, it can grow rapidly until it reaches its specific width (e.g., 140 ky for a 7-km-wide prism with a 1.5-km-high landward boundary, von Huene *et al.* (2004).

1.2 Inter-plate structures in a convergent margin

1.2.1 The Décollement

The décollement, also known as basal detachment fault, is a fault that develops along sediment beds, parallel to the stratification, or when sedimentary beds slid over or under more compacted or basement rocks (Sikder *and* Alam, 2003). In subduction zones, the décollement represents the shallow segment of the megathrust fault or plate interface, which separates fluid-rich incoming sediment from the overriding margin wedge. Basically, the décollement is a thin, highly fractured

layer where the shear localizes (Figure 1.6). In the décollement zone, the pore pressure is relatively high compared to surrounding material, as a result of channelized flow of deep fluid (Raimbourg *et al*., 2011; Saffer *and* Berking, 1998). Its propagation into incoming material is favored in horizons where the shear strength is reduced (Raimbourg *et al*., 2011). The décollement is often imaged on MCS profiles by a strong and continuous reflector with a reverse seismic polarity, which reflects a velocity inversion related to weak, low-velocity, fluid-rich sediment underthrusting a higher-velocity basement, or more compacted sediment (Figure 1.6).

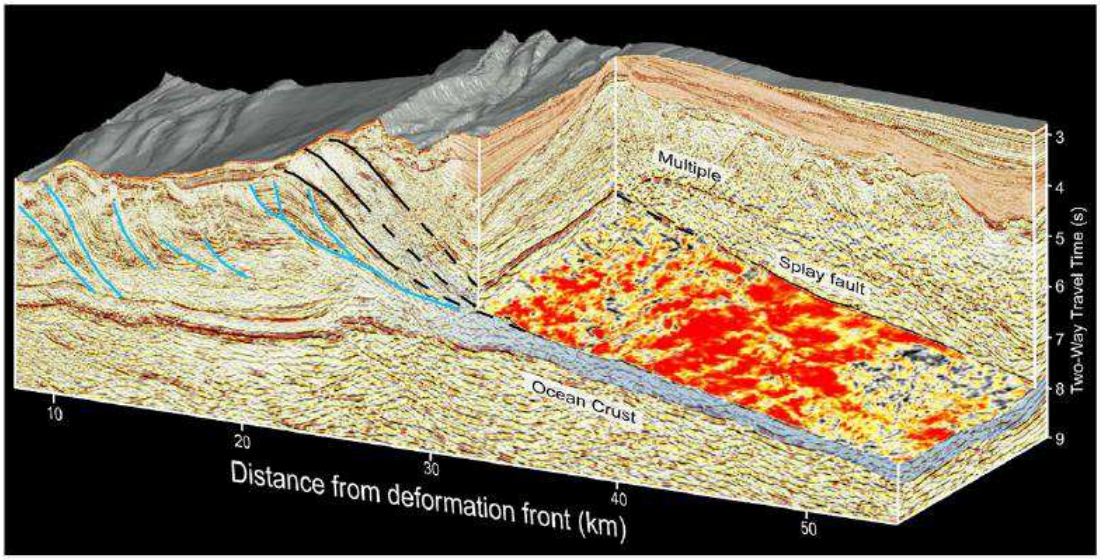

Figure 1.6 Example of 3D seismic reflection survey of the décollement fault through the accretionary wedge into the Kumano fore-arc basin; reversed-polarity seismic reflection from the deep décollement (red areas); blue shaded area is 1–2 km thick underthrust layer between décollement and top of the subducting ocean crust *(Bang et al., 2009).*

Two main growth mechanisms act simultaneously in different parts of a multiple-décollement wedge (Malavielle, 2010):

i) frontal accretion above the décollement located within the incoming material; and

ii) deep underplating of thrust slices (basal accretion) beneath the margin wedge due to duplex formation above a lower detachment (Gutscher *et al.,* 1998; Collot *et al.,* 2011).

The resulting low-angle slope of the frontal part of the wedge reflects the low-friction, whereas higher slope angles are a consequence of the higher basal friction that controls domains of underplating (Lallemand *et al.,* 1994).

1.2.2 The décollement indicated by the Reverse Polarity of seismic reflections

High-amplitude reflections along the inter-plate fault have been recognized and analyzed at several convergent margins (Bang *et al.,* 1996; Collot *et al*., 2008). According to Bang *et al*. (1996), fault plane reflections result from an impedance contrast at the fault zone, which occurs by: thrust sedimentary sequences that place materials with contrasting physical properties on either side of the fault, or by alteration of the shear zone properties. They consider that the polarity of the reflections is determined by the largest lobe of the waveform considered to be the dominant component of the reflection.

The water bottom can be identified by a large positive followed by a lower negative lobe. Negative-polarity reflections are produced by a layer of low-velocity and low density material (Bangs *and* Westbrook, 1991). The change in the impedance (product of the velocity and density) that produces the reversed polarity, results from changes in sediment porosity in the décollement zone rather than changes in the lithology (Bangs *et al.,* 1996). The décollement produces a layer of low-acoustic impedance (Bangs *et al.,* 1996) and its seismic wave is a low-amplitude positive lobe followed by a stronger negative lobe followed by a similar amplitude positive lobe as shown in Figure 1.7 (Moore and Shipley, 1993). By reproducing the scenario of low seismic velocity, it is possible to estimate the thickness of the décollement (Figure 1.8) (Bang *et al.,* 1996). The décollement can reach 12 m in thickness as in the case of Barbados (Bang et al., 1996), or 19 m thick in the Nankai Trough (Moore *and* Shipley, 1993). Vannucchi *and* Tobin (2000) suggest than the décollement in Costa Rica is highly heterogeneous with respect to the distribution of brittle and ductile deformation. From drilling at ODP Sites 1040 and 1043, they measured décollement thicknesses of 9 m and 38.6 m in thick, and they consider that it is possible to subdivide the décollement into two domains: a brittle and a ductile lower domain. Figure 1.9 shows conjugate shear bands and breccias in the décollement zone from the Nankai Thrust.

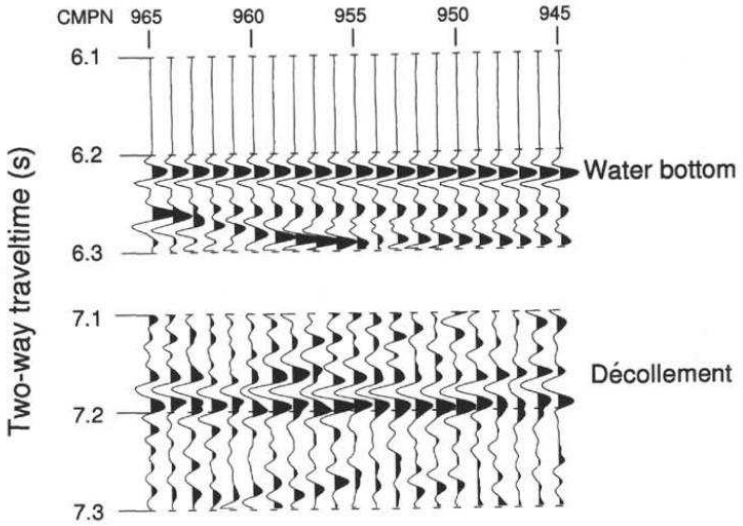

Figure 1.7 Section from Nankai in Japan, showing positive water bottom reflection and reversed-polarity décollement reflection (positive amplitude side of waveform, in black) (Moore and Shipley, 1993).

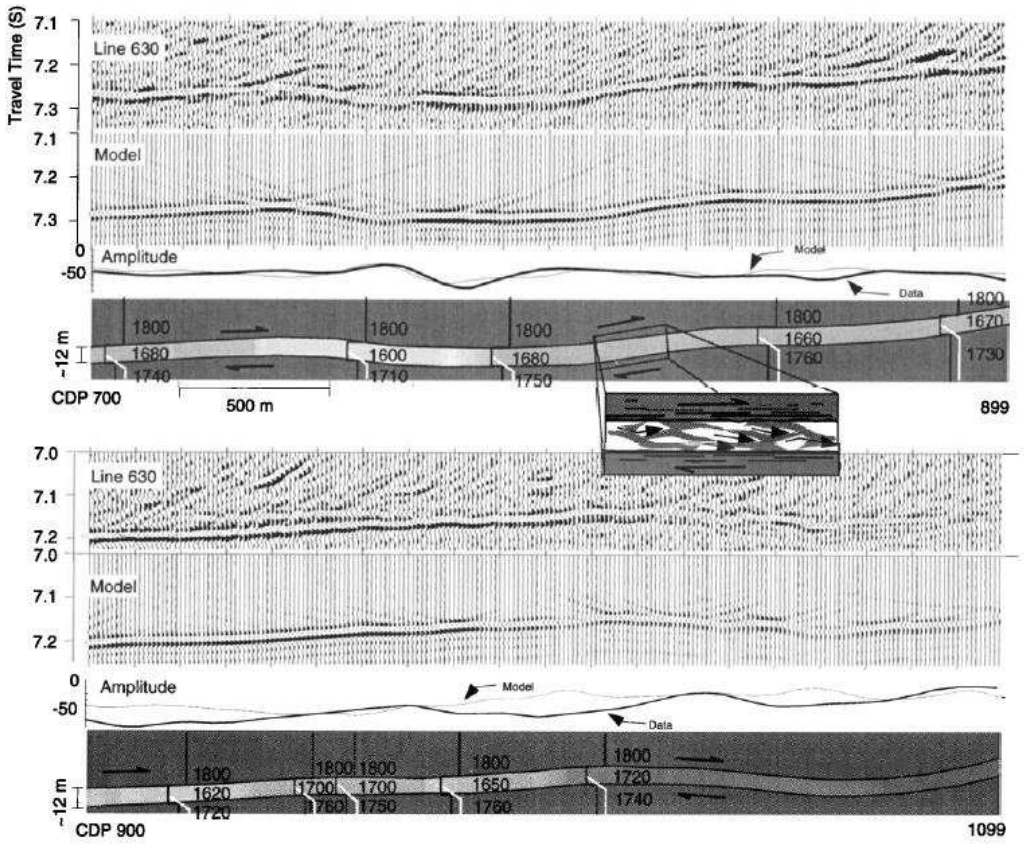

Figure 1.8 Two-dimensional models of the décollement reflection based on results of one-dimensional model (bottom); top panels show the décollement reflections. The amplitude of the negative lobe of the décollement is displayed for the data (heavy line) and for the model (thin line) (Bang *et al., 1996).*

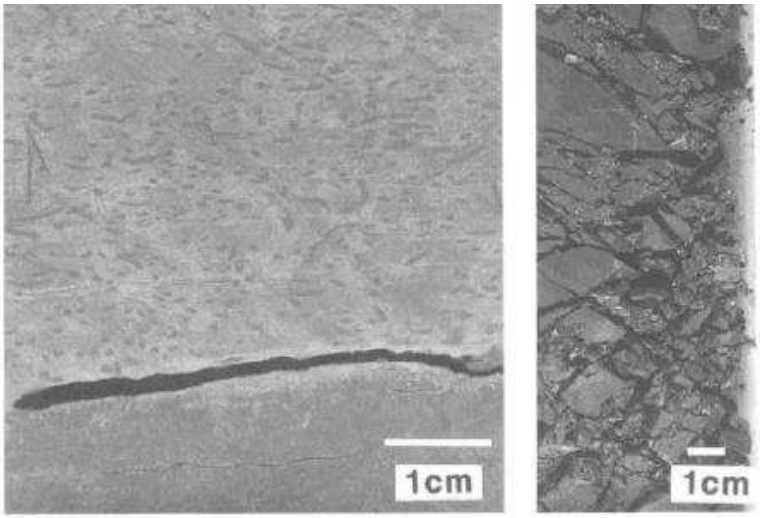

Figure 1.9 Example of rocks from Nankai Trough subduction zone; left: Conjugate shear bands; right, breccias in the décollement zone (Taira *et al*., *1992)*

Taira *et al.* (1992) suggest that between the frontal thrust and the décollement (Figure 1.10) the material can be over-consolidated and the porosity can reach values close to 30%. They further consider that below the décollement the stress is mainly vertical, the material is under-consolidated, and the porosity is higher (40%) than above of the décollement.

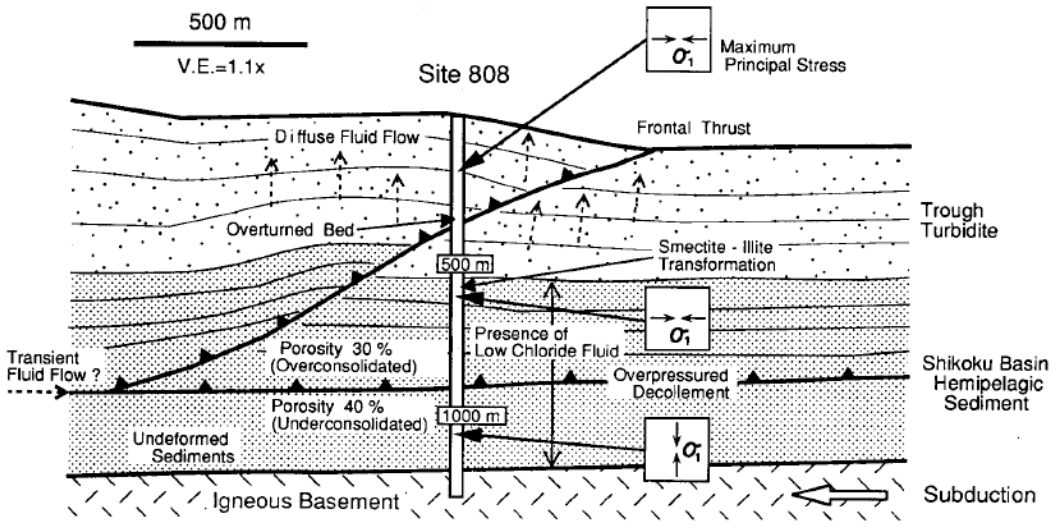

Figure 1.10 Results from drilling site 808 in Nankai Trough; the figure shows the relative shallow décollement (1000 mbsf) and the differing properties and principal stress orientation above and below it (Taira *et al*., *1992).*

1.2.3 The Subduction Channel

Tectonic mass transfer in subduction zones is achieved through the subduction channel (Lohrmann *et al.*, 2006), which is a narrow zone between the upper and lower plate containing material (Figure 1.11) that exhibits a tectonic velocity gradient with respect to both plates on a long term basis (Cloos *and* Shreve 1988a; Beaumont *et al*. 1999; Ellis *et al.,* 1999). Sediments "flowing" within the subduction channel (SC) come from trench deposits, the top of subducting oceanic crust and basal erosion (Lohrmann *et al*., 2006). Models such as that of Shreve *and* Cloos (1986) consider that deformation within the SC is by viscous shear as material flows downward under various driving forces (Poiseuille flow and Couette flow, England *and* Holland (1979)). However, observations of exhumed SC and accretionary wedges that were buried at depths <7 km (Moore *et al.,* 2007; Vannucchi *et al*., 2008) reveal, that their rocks mainly deformed in the brittle field, under 50°–150°C temperatures. Moreover, the interpretation by Collot *et al.,* (2011) of the remarkable SC in the Gulf of Guayaquil strongly supports brittle and slip behavior within a mega-shear zone (figure 1.11).

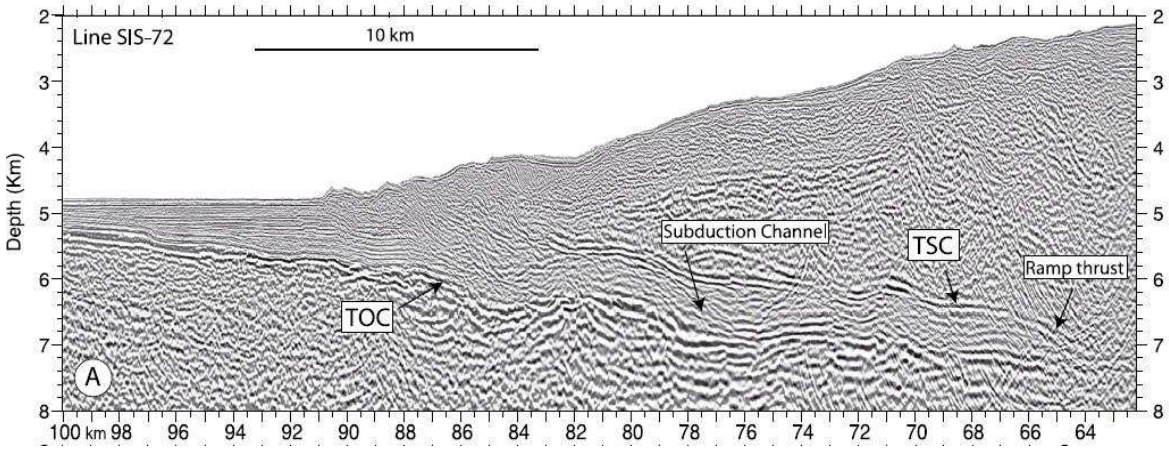

Figure 1.11 PSDM Seismic reflexion image of the Ecuadorian margin, showing the subduction channel reflectors (Calahorano *et al.,* 2008; Collot *et al.,* 2011); TOC= top of the oceanic crust. TSC= top of the subduction channel.

This shear zone may typically be up to a few kilometers thick, and probably extends to a depth of more than 100 km (Gerya *and* Stöckhert, 2002) where it deforms as a viscous fluid. At the shallow interplate (<15 km) MCS data (Sage *et al*., 2006; Calahorrano *et al.,* 2008; Collot *et al*., 2011) show that the uppermost and basal reflectors of the subduction channel (Figure 1.11) are associated with low-velocity perturbations layers, which are fluid rich and mechanically weak

(Collot *et al.*, 2011). The physical and mechanics properties of the SC are not completely understood, but they control the transition from fluid-rich sediments poorly consolidated to a strongly coupled zone (Davis *et al.,* 1983, Lallemand *et al.,* 1994). As pore fluid is lost from the sediments in the subduction channel, the interplate rigidity raises (Bilek *and* Lay, 1999) and the strength of coupling between the two plates increases (Stern, 2011) so that earthquake rupture becomes possible.

It is necessary to better understand the behavior of the under-riding material, because it seems to control the mechanical processes such as: interplate friction, hydro-fracturing, location of the décollement, heat transfer and the down-dip physical, and chemical transformations of the subducted material, location of seismic zone and the amount of co-seismic slip propagation (Collot *et al.,* 2011; Calahorrano *et al.,* 2008).

1.2.4 The Splay Fault

Accretionary wedges are constructed by adding new tectonic sediment thrusts at the front of the wedge along in-sequence thrust faults that splay away from the décollement. However, old thrust faults can be re-activated within or at the rear of an accretioanry wedge, thus forming an out-of-sequence splay fault. Splay faults (SF) are faults at the extremities of a major fault (Bates and Jackson, 1987) that may be a pathway for updip seismic rupture propagation (Gulick *et al.,* 2010; Park *et al*., 2002). Fukao (1979) pointed out the importance of this type of SF, which can provide a mechanism for earthquakes to generate tsunamis. The geometry of the SF has been imaged at several convergent margins using seismic images (Figure 1.12) (Moore et al., 2007; Park *et al.,* 2002; Collot *et al.,* 2008).

1.3 The Seismogenic Zone

The seismogenic zone (Figure 1.13) is the portion of the plate interface or megathrust fault where earthquakes are nucleated via stick-slip sliding (Brace *and* Byerlee, 1966), giving place to the largest tsunamis and greatest earthquakes M>8 (Brace *and* Byerlee, 1966; Scholz, 1998). The depth interval of the seismogenic zone is best identified by aftershock zones of large earthquakes (Moore *et al.,* 2007), inversion of tsunami (Satake *and* Kanamori, 1991) and earthquake waves (Abercrombie *et al.,* 2001), and GPS data inversion (Satake, 1993). A better understanding of the processes and properties that control and the limits the seismogenic zone will help to better estimate

the seismic hazard.

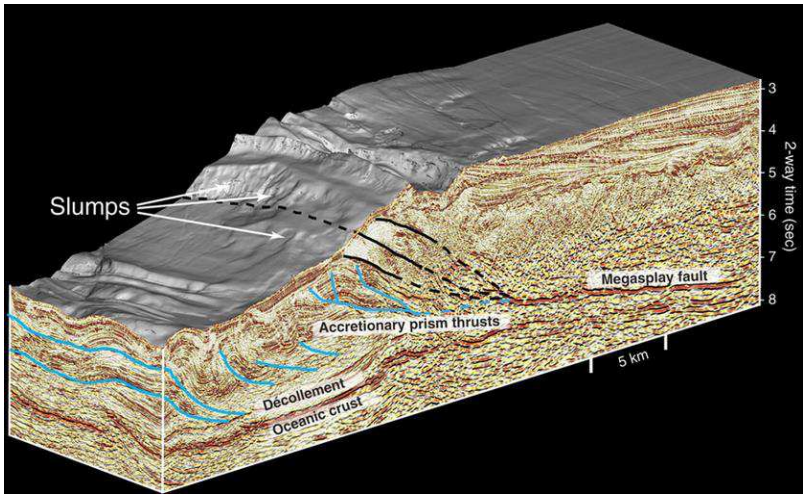

Figure 1.12 Example of a 3D representation of the convergent margin, showing the location of the megasplay fault and the older in-sequence thrusts; the décollement and some slumps can be also identified (Moore *et al.,* 2007).

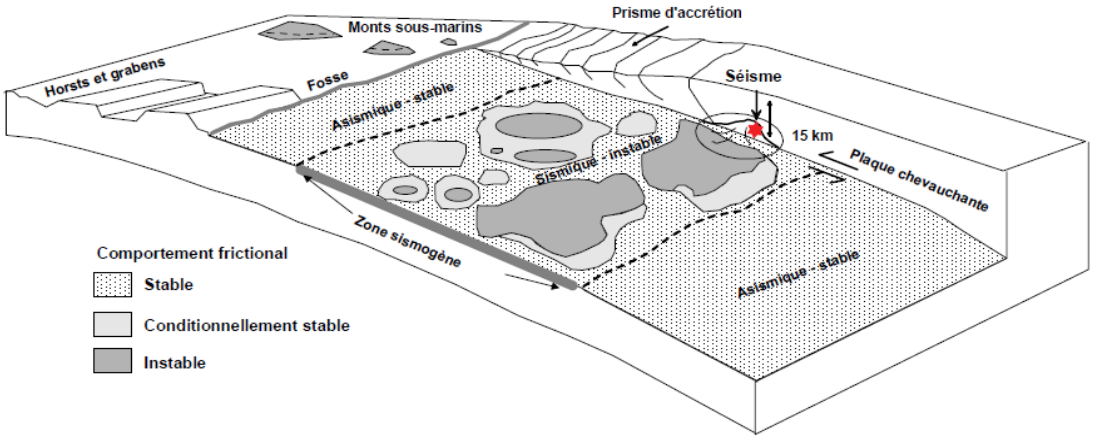

Figure1.13 Frictional properties from a seismogenic zone, showing the stable and unstable zones; the seismogenic zone would correspond to the unstable seismic segment (Moore, 2007; Bilek, 2007).

1.3.1 The Boundaries of the Seismogenic zone

The seismogenic zone is bounded by the Updip (UdL) and a Downdip (DdL) limits (Tichelaar *and* Ruff, 1991). The updip limit of the seismogenic zone has frequently been identified by the shallowest occurrence of microearthquakes (Obana *et al*., 2003), and compared to other geophysical indicators of the onset of seismogenesis, such as the shallowest extent of large earthquake rupture and geodetically locked regions (Schwartz *and* DeShon, 2009). The UdL is attributed to a transition in the physical properties of subducting sediments, both unconsolidated or semi-consolidated (Byrne *et al.,* 1988; Vrolijk, 1990). The updip limit of strain accumulation reflects the aseismic to seismic transition and the updip extent of potential rupture during large underthrusting earthquakes; the transition is most likely thermally controlled (Schwartz *and* DeShon, 2009).

On the other hand, the DdL is likely caused by the increasing ductile behavior of the deformed material due to an increased temperature (Nedimovic *et al.,* 2003) or the serpentinization of the forearc mantle leading to a talc rich layer along the contact of both plates, which lubricated the plate interface (Hyndman *et al*, 1997; Peacock *and* Hyndman, 1999). The downdip limit is defined by the Downdip rupture limit of great earthquakes, and the downdip extension of their aftershocks (Peacock *and* Hyndman, 1999), by the small thrust earthquakes occurring between great events and by modeling onshore geodetic data.

The temperature at the seismic zone boundaries can be calculated once the limits of the seismogenic zone are inferred (Hyundman *et al*., 1997). The temperature may vary between 60° and 150°C for the Updip limit (e.g., Nankai, Marcaillou *et al.,* 2012), and between 350 and 450 °C for the Downdip limit. The 350°C corresponds to the change in the Vp velocity, and 450°C to the brittle-ductile zone (Hyndman *et al.,* 1997).

1.4 Seismic Coupling

The term “Seismic coupling” was introduced by Kanamori (1971) and is used as a qualitative measure of the "mechanical interaction" between two converging tectonic plates between two large earthquakes and is better known as the Inter-Seismic Coupling (ISC). This term refers to the fraction of the plate convergence rate that quantifies the slip or moment deficit that is increasing during the inter-seismic period and that will released through large megathrust earthquake (Ruff

and Kanamori, 1983). Variation of inter-plate seismic coupling at subduction zones is a major factor controlling the size of the largest under-thrusting events (Figure 1.14), and it has a profound effect on the regional intra-plate stresses around the subduction zone (Christensen *and* Ruff, 2012). In a kinematic description, a locked or fully coupled fault has no or very low slip between great earthquakes (Dixon *and* Moore, 2013).

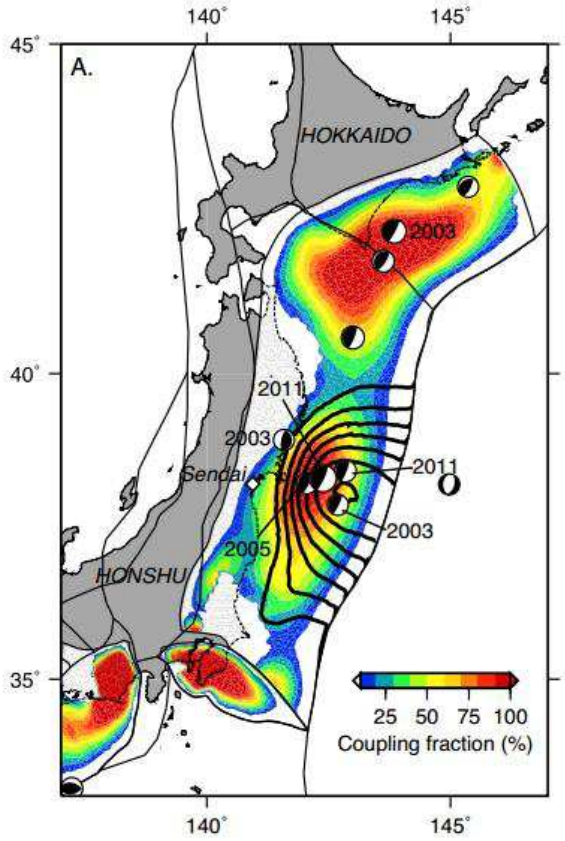

Figure 1.14 Pre-seismic coupling, seismicity, and coseismic slip of the March 11, 2011 Tohoku-Oki earthquake (modified from Loveless *and* Meade, 2011); coupling, expressed as the fraction of longterm slip represented by coseismic slip deficit ("backslip"), is based on a blockmodel of nominally inter-seismic horizontal GPS velocities from the GEONET network, 1996–2000 (Loveless *and* Meade,2010). Focal mechanisms show earthquakes from the Global CMT catalog with MW ≥ 7.0 and depth shallower than100 km from 1994 up to and including the Tohoku-oki mainshock; year labeled for events mentioned in the text. Coseismic slip, shown as 2.5-m contours, is based on an inversion of GEONET coseismic horizontal displacements from JPL/Caltech (Simons *et al.,* 2011).

Earthquakes result from a stick-slip frictional instability (Brace *and* Byerlee, 1966) that can be explained with frictional mechanics models. According to Scholz (1998), during the time between

two earthquakes (inter-seismic period) the stress and strain accumulate along the locked or stick fault, and then when the stress reaches the limit of the rock resistance, the fault fails producing an earthquake (co-seismic period, slip). This model represents a simple "stick-slip" frictional model, and the frictional behavior is referred to as velocity weakening (Schwartz *and* Rokosky, 2007). In the standard model of stick-slip friction, the slip is produced when the ratio of shear to normal stress on the surface reaches a value Us (the static friction coefficient); once sliding has initiated, the frictional resistance falls to a low dynamic friction coefficient (Ud), and this weakening of sliding resistance may result in a dynamic instability, which depends on the system rigidity (Scholz, 1998). The frictional behavior of stable sliding is known as velocity weakening (Schwartz *and* Rokosky, 2007). Schwartz *and* Rokosky (2007) suggest that the termination of earthquakes and accommodation of plate motion through stable sliding probably result of the transition from velocity weakening to velocity strengthening frictional behavior, as temperature increases with depth.

According to Scholz (1998), the frictional stability depends on two parameters *(L, (a-b)),* defined as the velocity dependence of steady-state friction. *L* corresponds to the critical slip distance, and (*a-b*) is the parameter of stability, where *"a*" and *"b"* are material properties. When (*a-b*) ≥ 0, the material is stable; for (*a-b)* > 0, no earthquake can nucleate and any earthquake propagation will be stopped. If (*a-b*) < 0, there is a bifurcation between an unstable regime and a conditionally stable regime, which depends of the critical value of effective normal stress (Figure 1.15). For (*a-b*) < 0 an earthquake can nucleate in the unstable region, and the rupture can propagate in both the unstable and conditionally stage regions.

1.5 The Seismic Cycle

A section of a fault or of the plate interface limited by strong barriers is defined as a fault segment (Jackson *and* Kagan, 2011). Sometimes, a segment ruptures in a single great earthquake (characteristic earthquake) (Rudolf *and* Szirtes, 1911), but at other times, it breaks in a series of smaller earthquakes (Figure 1.16) abutting to each other (Mitsui *and* Hirahara, 2004; Kanamori *and* McNally, 1982). According to Jackson *and* Kagan (2011), a seismic cycle is defined by a sequence of events on a fault segment starting with a large earthquake, followed by aftershocks, subsequent strain release, and then by steady stress accumulation, and culminating with another large earthquake. The term "cycle" does not imply that the size of the earthquakes or the duration of the inter-seismic interval between two events remains constant.

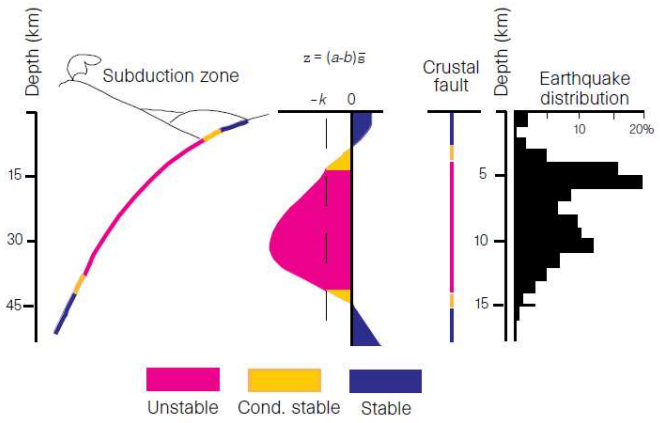

Figure 1.15 Model of Stability as a function of the depth for crustal faults and subduction zone. Image from left to right: 1) Subduction zone showing the unstable, conditional stable and stable regions on the interplate contact; 2) negative and possible values of (a-b) factor according to the depth; k: spring rigidity constant 3) crustal fault with the zones of stability and instability; 4) earthquake distribution (Scholz, 1998).

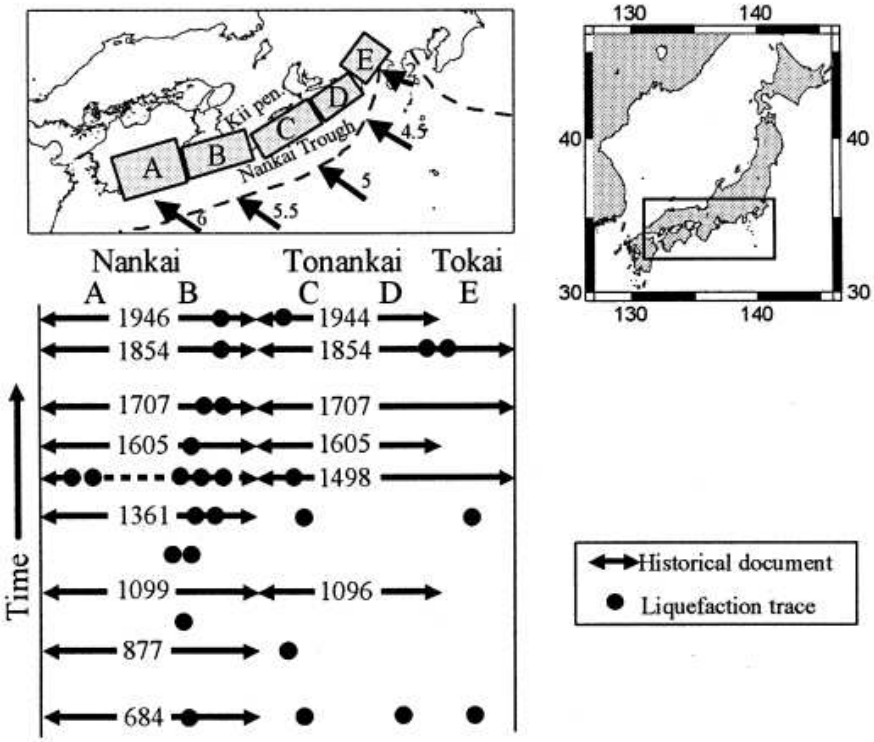

Figure 1.16 Space and time distribution of great earthquakes along the Nankai Trough in southwest Japan; A-E correspond to the segments that have ruptured during the historical earthquakes along Nankai Trough (Mitsui *and* Hirahara, 2004).

1.5.1 The Asperity and Barrier Model

Early asperity models for earthquakes were developed using rock friction experiments

(Byerlee, 1967; Scholz *and* Engelder, 1976), suggesting that faults are held together by strong asperities, where the stresses at asperities were typically higher than elsewhere around.

If a spatial heterogeneity is seen along a fault as the spatial variation of the failure stress (Figure 1.17, up), weak and strong regions can characterize the fault. This is useful to understand the difference between the asperity and barrier models (Figure1.17, middle and bottom respectively). While, the asperity model states that the largest co-seismic displacement occurs in the strong regions, the barrier model states that the displacement occurs at week regions. Both models have a spatial variation in the seismic moment release, and consequently a temporal variation in the moment release (Beck *and* Ruff, 1984).

In the asperity model, a small earthquake represents the failure of one asperity, resulting in a region pinned at both ends by adjacent asperities with an effective width and amount of slip relatively small; while, a large earthquake represents the failure of several asperities (Kanamori *and* McNally, 1982).

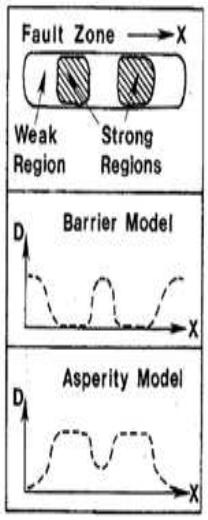

Figure 1.17 The image represents the coseismic behavior with the asperity and barrier models. Along the fault zone are found both weak and strong regions; D is the coseismic displacement, and X corresponds to the distance along fault strike (Beck *and* Ruff, 1984).

1.5.2 Seismic Gap Hypothesis

The essence of the Seismic Gap hypothesis of Sykes (1971), Kelleher *et al*. (1973), and McCann *et al.* (1979) is that seismic gaps are the most likely segments for future large earthquakes.

According to Jackson *and* Kagan (2011), a seismic gap is a fault segment for which the time since the previous characteristic earthquake approaches or exceeds the average recurrence interval. Cloos *and* Shreve (1996) suggest that some seismic gaps may exist simply because the trench axis sediment is locally thin, subduction erosion occurs, and therefore shear-zone thickening downdip of the inlet precludes subducted seamounts from becoming seismogenic asperities. The seismic gap hypothesis has to be taken with caution, since studies as that by Kagan *and* Jackson, (1999) show that large earthquakes increase the probability of all magnitudes earthquakes (Kagan, 2012).

1.5.3 Slow Slip Events and NVT (non-volcanic tremors)

Slow slip events (SSE) are slip episodes that initiate in or near the seismogenic zone, but do not radiate elastic/seismic energy (Schwartz *and* Rokosky, 2007) and they can last from days to months; This type of events has been detected with continuous GPS networks in several places such as Ecuador with a 6.0-to-6.3-Mw SSE (Vallée *et al.,* 2013), Japan (Obara *et al*., 2004), Mexico (Lowry *et al,* 2001), New Zealand (Douglas *et al.,* 2005). For a long time, the aseismic component of plate motions was primarily the steady state creep; however, now slow slip events can help to provide a better quantification of the moment release (Schwarttz *and* Rokosky, 2007).

According to Schwarttz *and* Rokosky, (2007), an abrupt change in the stress on a fault segment as result of earthquake slip on adjacent segment may initiate other modes of strain release, such as slow slip events. Similarly, they consider that slow fault slip may increase or relieve stress on an adjacent fault segment, bringing it close to or farther from earthquake failure.

On the other hand, non-volcanic tremor corresponds to long duration (minutes to hours) of high-amplitude seismic signal, without clear body wave arrivals (Schwarttz *and* Rokosky, 2007). This type of events is generally identified by coincidence of high-amplitude envelopes on several nearby stations (e.g., Outerbrigde *et al.,* 2010). The concurrence of non-volcanic tremor with slow slip events in Japan and Cascadia provides new insight about the seismic cycle; however, possible implications and underlying physics of long-term tremor migration and its relationship with slow slip remains not well understood. Ghosh *et al., (*2010) consider that small changes in static stress due to slow slip events in a section of a fault cause slip and non-volcanic tremor activity in the adjacent segment. They suggest that the resulting progressive along-strike transfer of stress is responsible for the long-term tremor migration during a slow slip event.

1.6 Subducting Topography

The rupture length of megathrust earthquakes is limited by the characteristic strength of the subduction interplate surface, and by lateral variations in its mechanical properties. Topographic features such as seamounts and ridges affect these properties and either trigger the earthquake rupture or stop its propagation, being either considered as an asperity or a barrier (Bilek, 2007; Sparkes *et al.,* 2010). For this reason, it is important to better understand the structural and mechanical effects of subducting topography on the convergent margins and in particular on the inter-seismic coupling and co-seismic slip.

1.6.1 Seamounts

Seamounts are omnipresent features of the seafloor (Chapel *and* Small, 1996), which can present different shapes (Figure 1.18). As plate tectonics goes on, seamounts are bound to be transported into subduction zones (Figure 1.19) affecting the morphology and internal structure of the wedge (Figure 1.20, 1.21) (Dominguez *et al.,* 1998; Watts A. *et al,* 2010) and probably affecting the fluid circulation (Dominguez *et al*., 1998). According to Isozaki *et al.,* (1990) seamount fragments are incorporated in exhumed ancient subduction zones. Deep seismic reflection has permitted to identify coherently subducted seamounts at different depths: in Nankai as deep as 7-8 km (Bangs *et al.,* 2006) and 10-15 km (Kodaria *et al.,* 2000); and in Sumatra a seamount is interpreted around 30-40 km in depth (Singh *et al*., 2012).

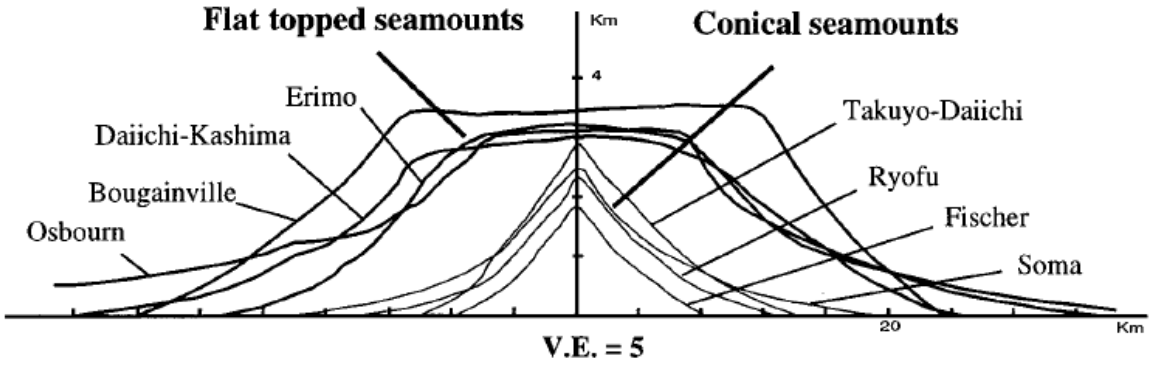

Figure 1.18 Morphologic comparison of Seamount (Dominguez et al., 1998), varying from small conical to large flat-topped seamounts, with a vertical exaggeration of 5.

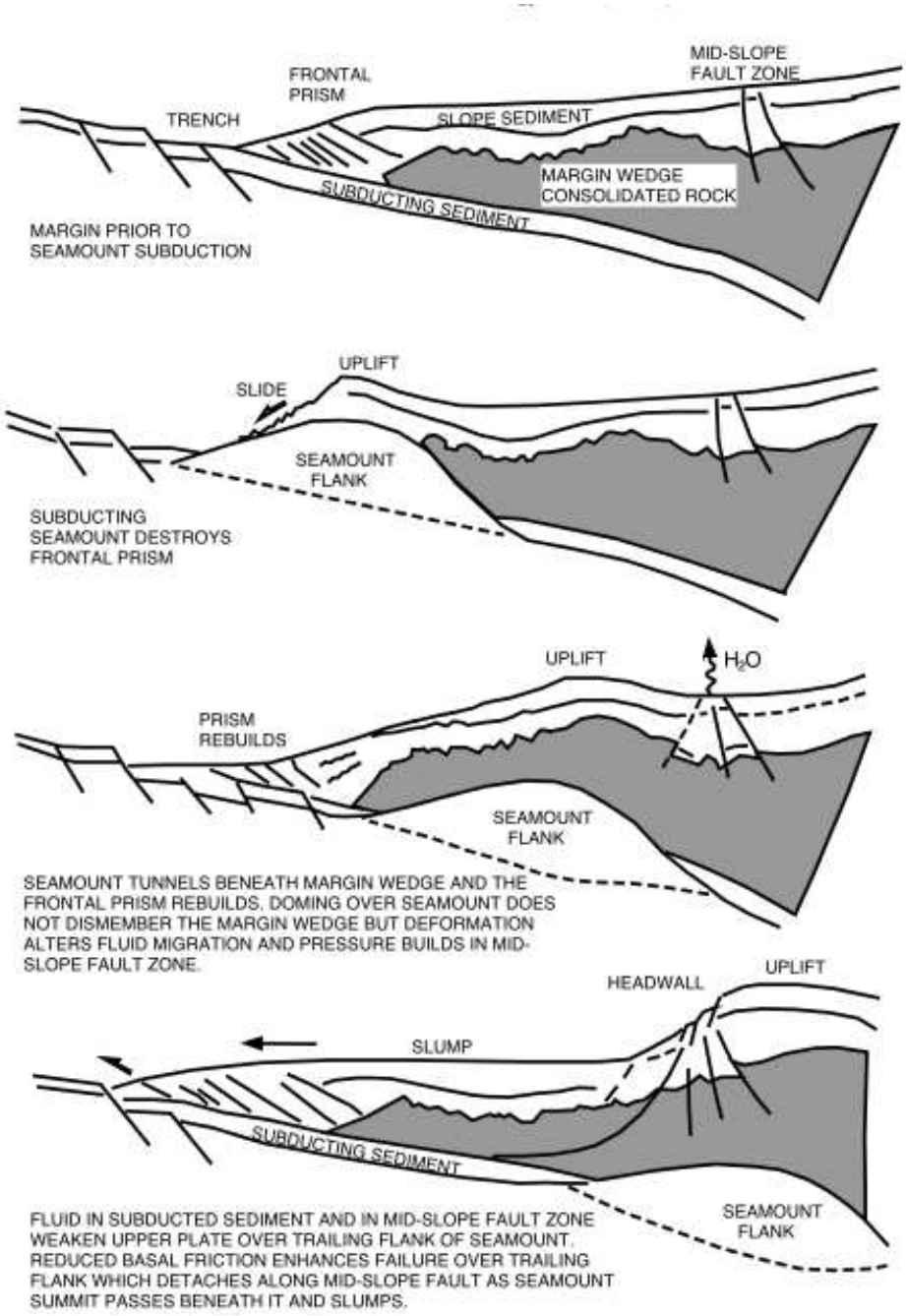

Figure 1.19 Diagrammatic sections across the Nicoya Slump showing a sequence of seamount slide development. The process starts with the destruction of the frontal prism and uplift of the seafloor, and then the tunneling beneath the wedge and the rebuild of the frontal prism; apparition of normal faulting and slumps (von Huene, 2004).

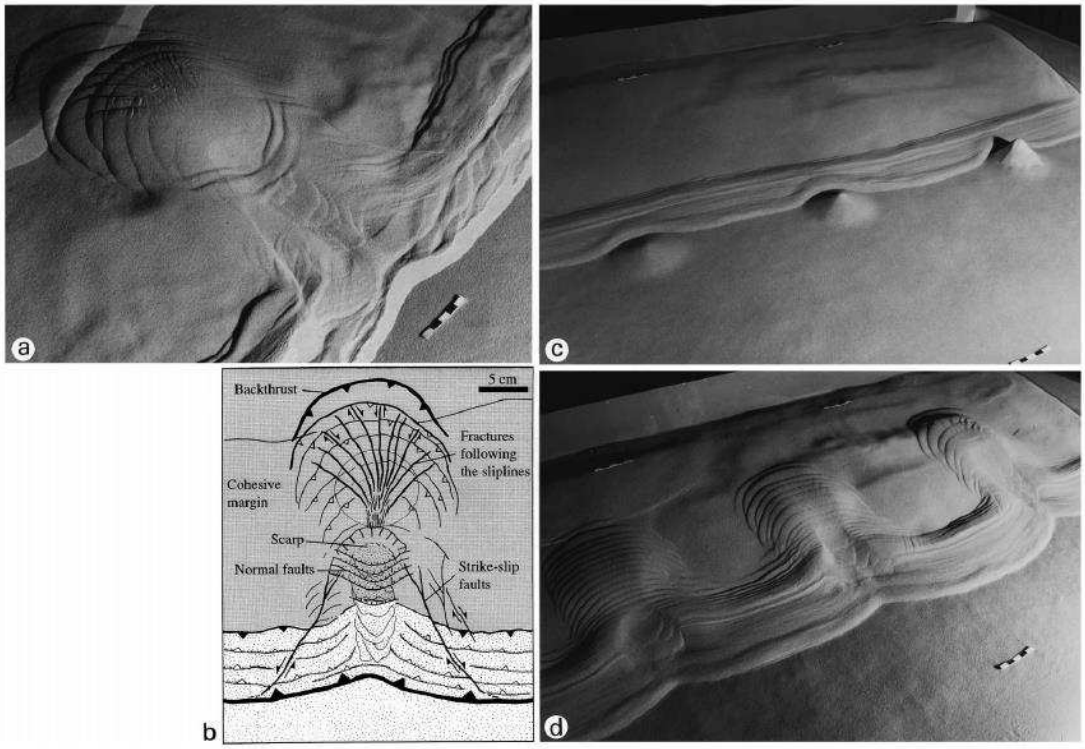

Figure 1.20 Conical seamount subduction experiment (Dominguez et al., 1998); a) fracturing in the wedge; b) structural interpretation; c) and d) views showing the relations between slip-line, backthrust development and differing-high subducting seamount.

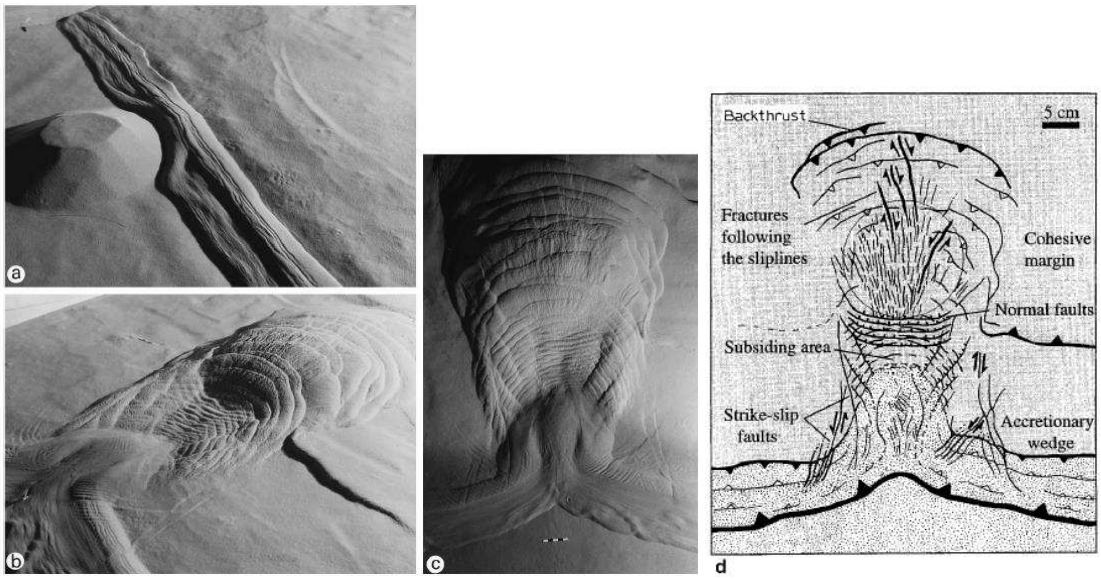

Figure 1.21 Flat-topped seamount (guyot) subduction experiment (Dominguez et al., 1998); a,b,c) subduction of the seamount and the resulting fractures; d) structural interpretation of the seamount subduction.

A widely held expectation is that subducting topographic features can locally increase the inter-seismic coupling and produce great earthquakes (Cloos *and* Shreve, 1996; Kelleher *and* McCann, 1976; Scholz *and* Small, 1997). In contrast, Wang *and* Bilek (2011) suggest that seamounts subduct aseismically producing numerous small earthquakes, and large thrust earthquakes result from the rupture of several asperities. Despite of these studies, the real conditions that control seamount subduction, deformation, shearing-off, decapitation and accretion to the forearc, and to which depth seamounts are subducted without being fully sheared, are poorly known.

Subducted seamounts can act as a rupture barrier or as an asperity (Nishizawa *et al.,* 2009; Das and Watts, 2009), depending on their height-to-width ratio (Yang *et al.,* 2013) and on their position within the subduction zone (Yang *et al*., 2012). According to Yang *et al*, (2012) seamount-induced barriers can turn into asperities on which megathrust earthquake can nucleate at shallow depths and rupture the entire seismogenic zone. This suggests that a strong barrier patch may not necessarily reduce the maximum size of an earthquake. Yang *et al*, (2012) further consider that depending on the stress condition, seamounts can stop or nucleate large thrust earthquakes when seamounts are located up-dip of the nucleation zone; whereas seamounts outside of the seismogenic zone have little effect on large thrust earthquakes. Yang *et al*. (2013) suggest that for a wide range of seamount-normal-stress conditions, subducted seamounts may stop earthquake ruptures including the case of mega-thrust fault lubricated by seamount-top fluid-rich sediments.

On the other hand, the presence of a seamount made up with low permeability rocks may act as a blockage for fluid flow that leads to an increase of fluid over-pressure and a low effective stress zone immediately in front of the seamount, the fluid diverts around the blockage. However, although observations and calculations made by Schlotz *and* Small (1997) and models by Cloos (1992) and Christensen *and* Lay (1988) support that seamount subduction will enhance the local seismic coupling, the correlation between a buried seamount and a highly coupled zone has not been demonstrated yet.

For the 2011 Mw 9.0 Tohoku-Oki, Duan (2012) used a hybrid parallel finite element method for spontaneous rupture and seismic wave propagation simulations; he considers that the failure of a ~70-km-by-23-km-size seamount located up-dip of the hypocenter helped to propagate the rupture to shallow depth, resulting in a significant slip near the trench. He further considers that this seamount was characterized by higher static friction, lower pore-fluid pressure, and higher initial stress than the surrounding regions.

1.6.2 Oceanic Aseismic Ridge

The subduction of oceanic aseismic ridges (Figure 1.22), and magmatic plateaus is a process commonly observed worldwide (Gerya *et al*., 2009) This process is considered to be responsible of dramatic changes in the dynamics and kinematics of the subduction zone and the development of strike-slip faults (Rosenbaum *and* Mo, 2011). Relief on a subducting plate is initially accommodated in the subduction zone by aseismic underthrusting (Melnick *et al*., 2009; Sparkes *et al.,* 2010). High fluid pressure along the plate interface reduces friction and allows the aseismic character of the zone (von Huene *and* Ranero, 2009). As the relief travels deeper down the subduction zone, a net volume of the fluid in the aseismic zone is lost, thus progressively increasing interplate friction to a level where seismogenic behavior occurs (Ranero *et al*., 2008).

According to Collot *et al*. (1992), the sweeping of a subducting ridge along a trench produces thrust faults on the leading flank of the ridge. In the wake of the ridge, the wedge undergoes subsidence, large mass wasting and strong tectonic erosion (Collot *et al.*, 1992; Hampel *et al*., 2004) characterized by normal faults and slumps scarps.

Many authors suggest that enhanced plate coupling in areas of aseismic ridge subduction increases the normal stresses (Rosenbaum *et al.,* 2011); this increase reduces potentially small and intermediate seismicity and can generate large earthquakes (Cloos, 1992; Scholz *and* Small, 1997; Kodaira *et al.,* 2000). In contrast, some authors consider that large magnitude seismicity is inhibited by the subduction of ridges, because ridges are weaker than normal oceanic crust (Vogt *et al.,* 1976) or because the accumulation of elastic strain energy is prevented by margin basement fracturation and enhanced erosion (Cummins *et al*., 2002). Perfettini *et al*. (2010) suggest that the influence of Nazca Ridge seems to promote aseismic sliding and hence a locally low inter-seismic coupling, what is opposite to the assumption that subducting bathymetric features increases seismic coupling. Their finding contradicts the common assumption that subducting seamounts or ridges increase inter-seismic coupling.

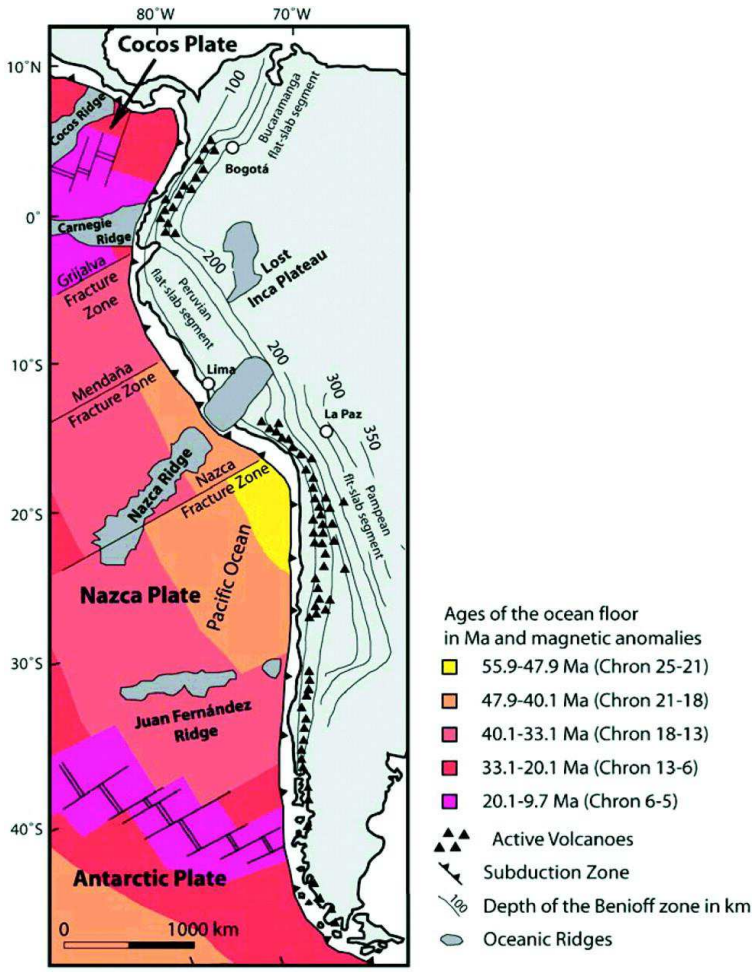

Figure 1.22 Aseismic ridges of Nazca Plate subducting beneath South America Plate; colors represent the age of the oceanic floor from 9.7 M.a to 55.9 M.a, black triangles represent the active volcanoes (Gerya *et al*., 2009).

1.7 Megathrust earthquakes: Sumatra 2004, Maule 2010, and Tohoku-Oki 2011

Megathrust earthquakes are the world's largest earthquakes, capable of nucleating tremendous tsunamis (e.g., Tohoku-Oki 2011 in Japan, Maule 2010 in Chili, and Sumatra 2004). For a longtime, it was thought that: 1) the interplate rupture produced by deep generated EQ could not reach the trench because a negative stress drop will occur if the EQ propagates into the up dip stable zone, resulting in a large energy drop that will stop the propagation (Scholz, 1998); and 2) megathrust EQs most likely occurred in regions with relatively young oceanic crust subducting at high convergence rates (Ruff *and* Kanamori 1980) as documented for both the 1960 Mw 9.5 Chile and 1964 Mw 9.2 Alaska earthquakes.

The 2011 Mw 9.0 Tohoku-Oki, 2010 Mw 8.8 Maule, and 2004 Mw 9.2 Sumatra-Andaman earthquakes showed that these widely held considerations about earthquake nucleation must be revisited, taking in account that **mega-thrust earthquakes can nucleate where old crust subducts with a slow convergent rate** as documented for 2004 Mw 9.2 Sumatra-Andaman earthquake (Subarya *et al.,* 2006), and that the seismic and tsunami threats were underestimated because **large near-trench co-seismic slip can occur and reach the trench** as documented for the 2011 Mw 9.0 Tohoku-Oki earthquake (Ide *et al*., 2011; Simons *et al*., 2011; Tsuji *et al* 2011; Lay *et al.,* 2011), the 2010 Mw 8.8 Maule (Vigny *et al*., 2011) and possibly the Sumatra-Andaman Mw 9.2 earthquake (Subarya *et al.,* 2006), although their model includes both co-seismic and substantial after slip (Shearer *and* Burgmann, 2010);

1.7.1 Tohoku-Oki earthquake

According to Lay *et al.* (2011), this earthquake ruptured a 200 km wide megathrust fault, appearing to extend from near the trench to near the Honshu coastline. The rupture would be constrained to grow outward on the fault relative to hypocenter at 1.5 km/s to a distance of 100 km and then at 2.5 km/s until it reaches the margin. This earthquake had two modes of rupture (Lay *et al.,* 2011; Ide *et al*., 2011; Simons *et al*., 2011): a shallow, relatively quiet rupture, where the co-seismic fault slip exceeded 30 m in places (Ide *et al.,* 2011), concentrated in the shallowest part of the fault near the trench (Figure 1.23 and 24); and a deep rupture, which radiated high-frequency seismic waves produced at several kilometer of depth. According to Simons *et al*. (2011), the Tohoku earthquakes was deficient in high frequency seismic radiation compared to the Mw 8.8 Maule earthquake; they attribute this characteristic to the relatively shallow depth of Tohoku earthquake.

From ocean bottom pressure gauge installed before the earthquake near the tip of the Japan margin, Ito *et al.,* (2011) measured average instantaneous displacements of 58 m east and 74 m east- southeast at the frontal wedge that they modeled to estimate a huge 80-m slip along the main décollement fault near the trench.

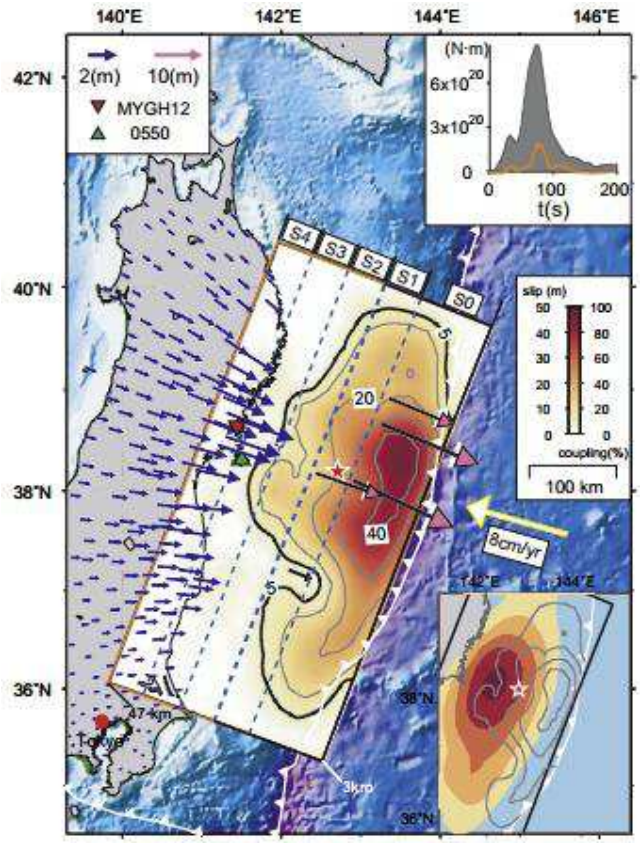

Figure 1.23 Slip model of the Tohoku-Oki earthquake. Map view of the slip model divided into 5 segments indicated by the dashed blue lines. The co-seismic geodetic horizontal displacement vectors are displayed in white while the synthetics fits are presented in blue (inland) and pink (offshore). The heavy black and gray lines indicate the slip contours. The lower corner inset shows the inter-seismic coupling model assuming deep coupling only (Loveless *and* Meade, 2010) and the coseismic slip model (gray contours). The upper right inset displays the moment rate function. The red star indicates the epicenter (Wei *et al*., 2012).

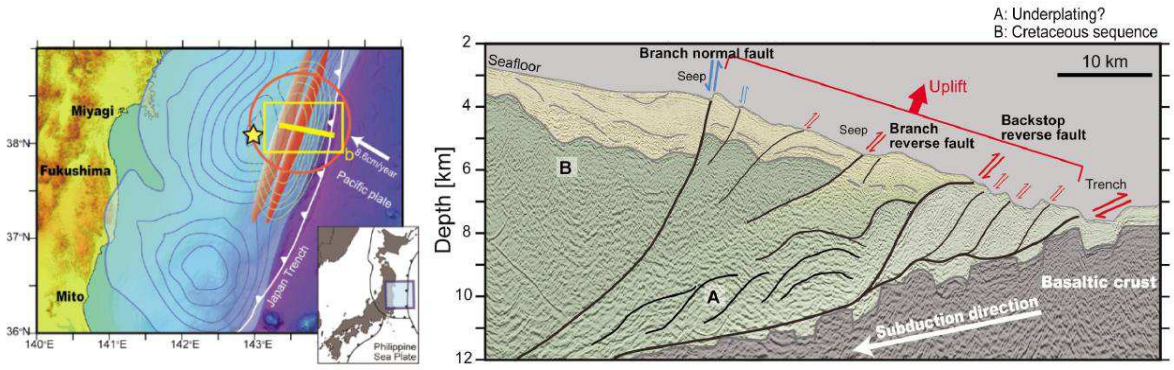

Figure 1.24.A The image is an interpretation of a seismic reflection profile from Tohoku-Oki earthquake left) map showing the location of the line; b) a line showing a large normal fault extends for about 10 km down dip (Tsuji et al., 2011); the fault system is located at the seaward edge of the rupture area (Yagi, 2011).

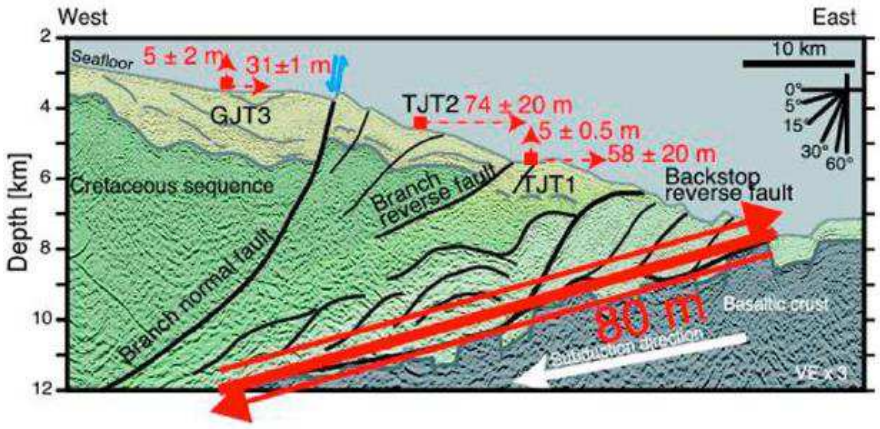

Figure 1.25.B: Two - dimensional décollement fault model along the cross-section perpendicular to the trench axis projected on the seismic section of Figure 1.24A. Red arrows indicated the observed displacements at TJT1, TJT2, and GJT3. The thick red line indicates the fault model with estimated 80 m displacement (Ito et al., 2011)

1.7.2 The Maule Mw 8.8 earthquake

According to Moreno *et al.* (2012) the Maule earthquake affected ~500 km of Nazca-South America plate boundary in Chile producing spectacular crustal deformation; they consider that the co-seismic slip was concentrated north of the epicenter with up to 16 m of slip, whereas to the south it reaches over 10 m within two minor patches, closing a mature seismic gap. The earthquake's rupture (Figure 1.25) reached shallow depths and extended likely up to the trench, similar to Tokoku earthquake, (Vigny *et al*., 2011). To obtain these results, Vigny et al. (2011) used cGPS and GPS data from before, during and after the Maule earthquake in order to determinate the deformation of earth's surface close to the earthquake's rupture. Hicsk *et al*., (2012) used data from the aftershocks of Maule earthquake to obtain 3-D seismic velocity model of the central Chile fore-arc; they found a 25-km-depth high Vp/Vs anomaly along the mega-thrust; they consider that the 2010 Maule earthquake likely nucleated at the up-dip boundary of this anomaly. Moreno *et al.* (2012) consider that the rupture propagation was not affected by bathymetric features of incoming plate; instead, splay faults in the upper plate seem to have limited rupture propagation in the up-dip and along-strike directions. They further suggest that persistent tectonic features may control strain accumulation and releases along subduction mega-thrusts.

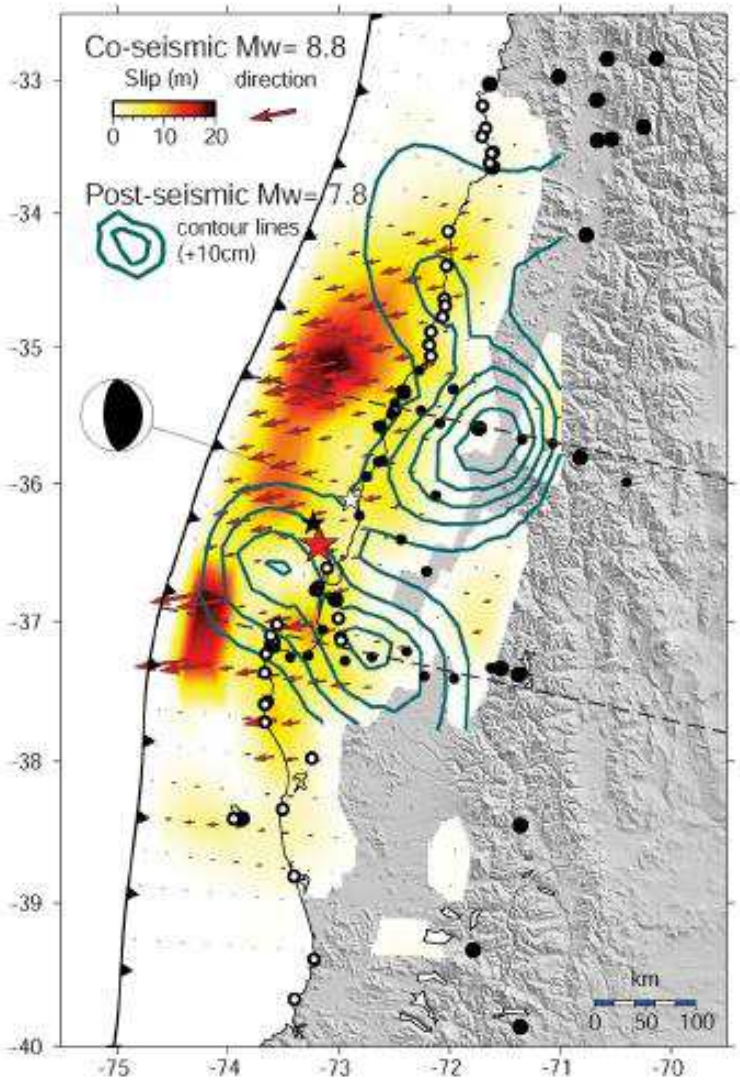

Figure 1.26 Image showing the coseismic and 12-days afterslip source models of Maule 2010 earthquake. Dots show localization and data type used in the inversion (black dots for GPS and open dots for land-level data from natural or anthropogenic marker (Vigny et al. 2011).

1.7.3 The 2004 Mw 9.2 Sumatra earthquake

Sumatra earthquake (Figure 1.26) was the first Mw>9 event recorded by a global network of broadband seismic stations and regional GPS stations, leading to a new understanding of mechanics of megathrust earthquakes and the associated tsunamis (Ammon *et al.*, 2005; Geist *et al.*, 2007). Despite significant earthquakes along the Sunda subduction zone in the past, the structure and morphology of this plate boundary system and its potential for generating large tsunamis are poorly understood (Waldhauser *et al.*, 2012). Waldhauser *et al.* (2012) found that most aftershocks

represent thrust motion on the interplate contact and on northwest-striking imbricate faults that cut through the accretionary wedge. They inferred the position of a master splay fault that branches off the interplate contact at ~55km depth and 190 km from the trench and cuts through the fore-arc to an inferred surface location at the western border of the fore-arc ridge ~100 km from the trench. One of the lessons left by this earthquake is that no matter the convergence rate of a subduction zone, it should be considered dangerous in terms of producing tsunamigenic earthquakes (Bird *and* Kagan, 2004).

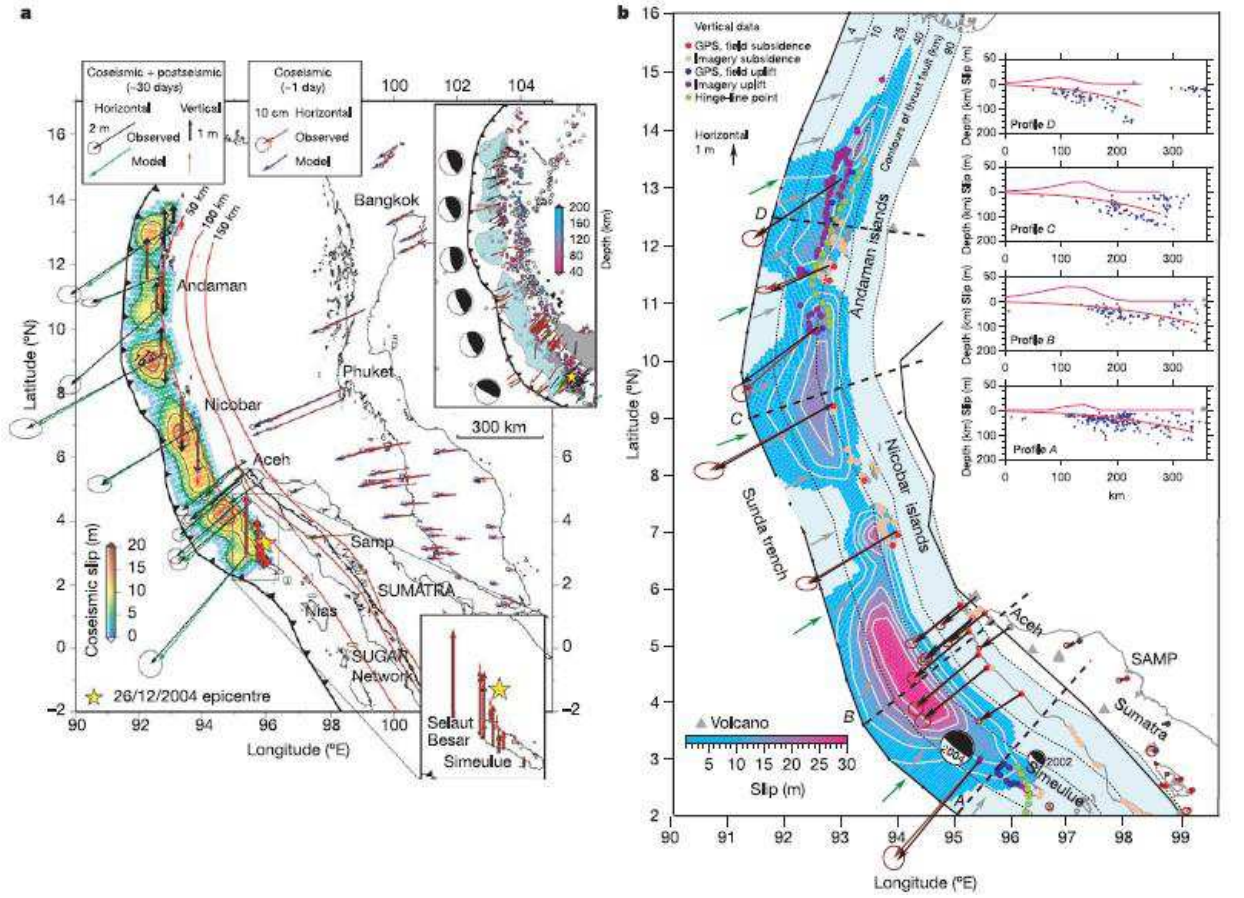

Figure 1.27 Image showing the rupture zone of the megathrust Mw=9.2 Sumatra earthquake; left: co-seismic slip and the direction of the slip using coseismic and post-seismic data of 30 days, the small maps show the focal mechanism and the uplift of Sumatra earthquake; right: (Subarya et al., 2006).

CHAPTER 2

GEOLOGICAL BACKGROUND OF THE ECUADORIAN CONVERGENT MARGIN

2.1. Kinematics of the Ecuadorian margin

The architecture of the **Ecuadorian convergent margin** is mainly controlled by the interaction between Nazca and South America plates (Figure 2.1). The Nazca plate underthrusts eastward the northern part of South America plate at rate of 5.8 cm/yr eastward with respect to South America (Kendrick *et al.,* 2003; Trenkamp *et al*., 2002). At the north-west part of the South America Plate lies the North Andean Block (NAB), a micro-plate limited by the subduction of Caribbean Plate in the north, the Nazca Plate subduction to the west, and to the east several systems of faults that form a transpressive dextral fault system called the Dolores-Guayaquil Megashear (Pennington, 1981). However a recent kinematic model proposed by Nocquet *et al.,* (2014) on the basis of numerous new GPS measurements redefines the eastern boundary of the NAB (or North Andean Sliver). The fault system, which has produced large crustal historical earthquakes (*e.g*. the 1797 Riobamba Mw ~7.6 (Beauval, *et al*., 2010), cuts obliquely trough the Andes, and runs along the foot of the Eastern cordillera with a 7.5-9.5 mm/yr velocity (Figure 2.1; Nocquet *et al*., 2014)

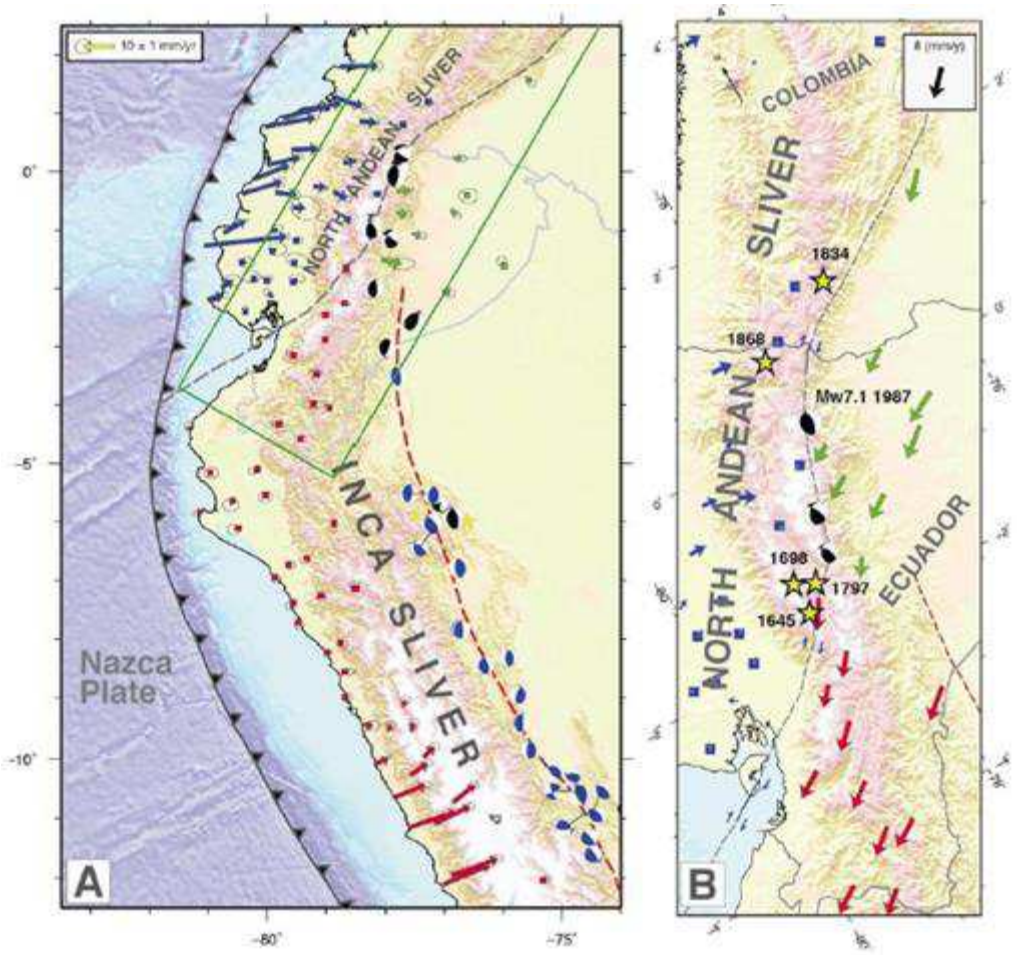

Figure 2. 1 North Andean and Inca slivers boundaries (a) Red and blue arrows represent velocities with respect to the North Andean and to the Inca sliver, respectively; and green arrows are velocities in the subandean domain with respect to South America. Square indicate < 1mm/yr velocities. Focal mechanisms for earthquakes with magnitude larger than 5.5 are displayed along the sliver proposed boundaries. Green box represents the zoom of the North Andean sliver in B. (B) Velocity field along the North Andean sliver. Yellow stars are the major historical events with their dates (Nocque et al., 2014).

2.1.1. Nazca Plate

The Nazca Plate results from the splitting of Farallon Plate that took place ~23-27 M.y. (Handschumacher, 1976; Hey, 1997; Lonsdale *and* Klitgord, 1978). This splitting occurred along of a preexistent fracture (Pacific-Farallon Fracture) along which lies the Cocos-Nazca Spreading Center (CNSC) that separates the new Cocos plate at the north from the Nazca plate to the south (Hey, 1997; Lonsdale *and* Klitgord, 1978).

The two remarkable structural features of Nazca Plate that interact with the Ecuador

subduction zone are: the **Carnegie Ridge and the Grijalva Fracture Zone (GFZ)**. Grijalva Fracture Zone is associated with two other NE-oriented fractures zones: the Alvarado and Sarmiento FZ. The Grijalva FZ has a scarp of 700 m and intersects with the trench at ~3°S (Lonsdale *and* Klitgord, 1978). GFZ represents an important structural limit that separates two oceanic lithospheres with differing ages: at the north of GFZ the ~22-24 M.yr Nazca plate (Handschumacher, 1976) and at its south the >34 M.yr old Farallon plate (Barckhausen *et al*., 2001; Lonsdale *and* Klitgord, 1978). Alvarado and Sarmiento fracture zones lie south of Grijalva fracture, and they enter in subduction beneath the Peruvian margin.

2.1.2. The Carnegie Ridge

The Nazca Plate carries the Carnegie Ridge (CR), a major 2-km-high east–west trending volcanic ridge (Figure 2.2). CR results from the interaction between the Galapagos Hot Spot and the Cocos-Nazca Spreading Center (CNSC) (Sallares *and* Charvis, 2003). The evolution of the Carnegie Ridge together with Malpelo and Cocos Ridges from ~20 Ma to the present is illustrated in the Figure 2.3. CR has been subducting since at least 1.4 M.y (Graindore *et al.,* 2004) and possibly since 8 Myr (Gutscher *et al*., 1999)

The sedimentary layers of the Carnegie flanks are constituted mainly of carbonates aged from the Upper Miocene to the Upper Pleistocene (Site 157 from DSDP, van Andel *et al.,* 1973). This sedimentary coverture contains a 70% to 80% of the pelagic sediments dominated by nannofossil ooze with discrete ash levels (Sites 1238 and 1239, from Leg 202 Preliminary report, 2003).

According to Sallares *et al*., (2005), the 19 km-thick Carnegie Ridge (CR) is consistent with the oceanic plateau proposed by Lonsdale (1978) and Sallares *et al*. (2003). Graindorge *et al*. (2004) suggest that, in our study zone, CR that is 14 km-thick comprise three layers: **layer 1** has a thickness of 0.2-9.9 km and velocities from 2.4 km/s at the top to 2.8 km/s at the base (van Andel, 1973); **layer 2** comparable to the oceanic layer b2 has a thickness of 2.8 km and velocities of 4.8 km/s at the top and 5.5 km/s at the bottom; **layer 3** has velocities between 6.4 km/s at the top and 7.3 km/s at the bottom and it is comparable to the typical oceanic layer 3 (White *et al*, 1992)

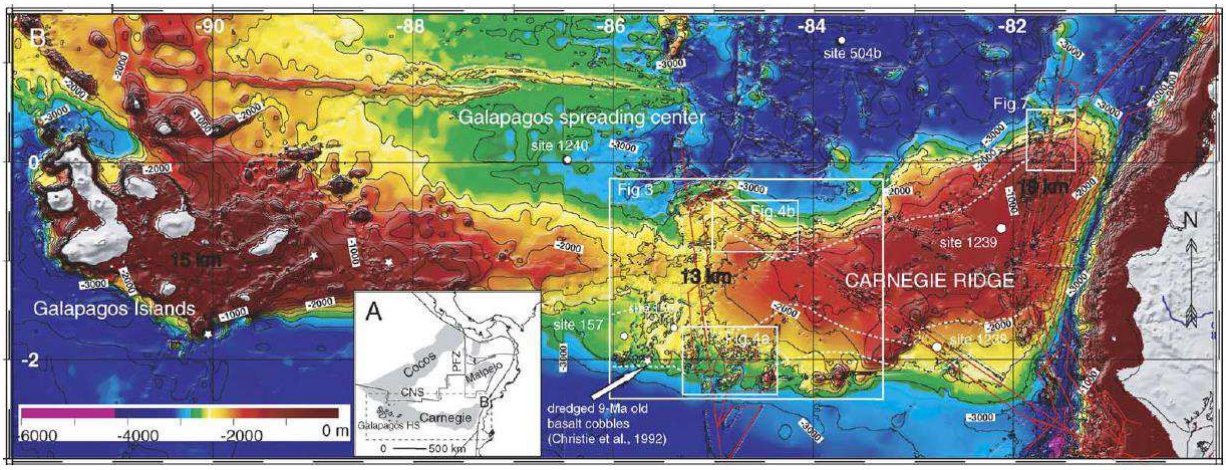

Figure 2. 2 General geodynamic setting of the Carnegie Ridge (CNS=Cocos–Nazca Spreading Center; HS=Hotspot; PFZ=Panama Fracture Zone); bathymetric map of the Carnegie Ridge, grid size 300 m (Michaud et al., 2005).

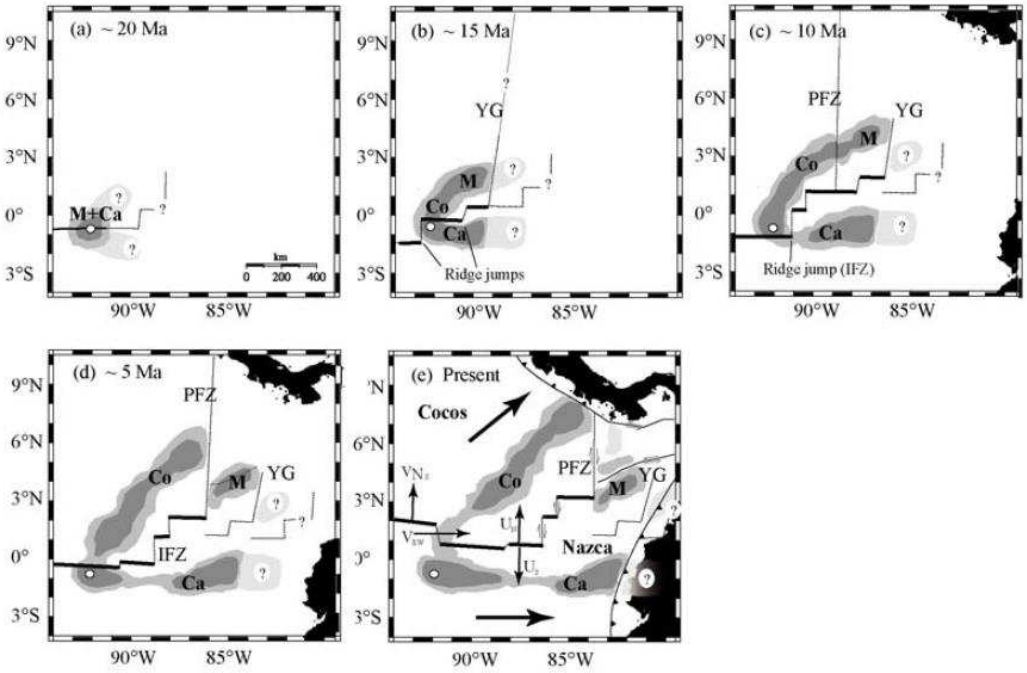

Figure 2. 3 Evolution of Carnegie and Cocos Ridge from 20 M.y. to the present; Ca= Carnegie Ridge, Co= Cocos Ridge, M= Malpelo Ridge, YG= Yaquina Graben, and PFZ= Panana Fracture Zone, Un and Us = expansion directions (Sallares and Charvis, 2003).

2.1.3. Age of initiation of Carnegie Ridge subduction

The uncertainty about the age of the CR subduction corresponds to the difficulties associated to the reconstruction of tectonic plate kinematics and the geometry of the subducted segment of the Carnegie Ridge (CR).

Michaud et al. (2009) consider that the deformation of the margin toe and the uplift of the Ecuador coast are not necessarily related to the CR subduction, and that in the absence of a flat slab (Guillier et al., 2001), which would indicate the presence of the CR as suggested by Gutscher et al., (1999) the normal bending geometry of the slab cannot be used to define the continuation of CR at depth. Michaud et al. (2009) further suggest that the adakitic signal can be explained with an alternative model (Kay, 2005), which does not require the subduction of CR. Thus, they conclude that there is no a clear segmentation of the deformation of the margin toe that can be linked with the CR subduction or with its landward prolongation at depth. On the other hand, Collot et al. (2009) propose a reconstruction of the timing of the Carnegie Ridge (CR) subduction (Figure 2.4) based 1) on the kinematics between the Nazca plate and NAB, and 2) on the Ridge imprint left in the outer-wedge morphology as a result of the ridge sweeping along the margin. They suggest that the CR has been subducting for ~4-5 Ma. Morphology and Geology of Continental Ecuador

2.1.4. Coastal, Andean, and Oriental regions

Ecuador comprises three main morpho-structural regions (Figure 2.5): the coastal region (fore-arc); the Andean region (volcanic arc) constituted by the Cordilleras Occidental and Real (Oriental); and the Oriental or sub-andean region (back-arc). All of these regions are related to the active subduction of the oceanic Nazca Plate beneath the continental South America Plate. The general geologic and tectonic framework is a product of a complex geologic history involving several accretionary processes that have produced spatial and temporal overlay of different tectonic terranes (Eguez *et al.,* 1993). The morpho-structural regions appear to be controlled by conspicuous NNE-SSW trending fault systems (Eguez *et al*., 1993).

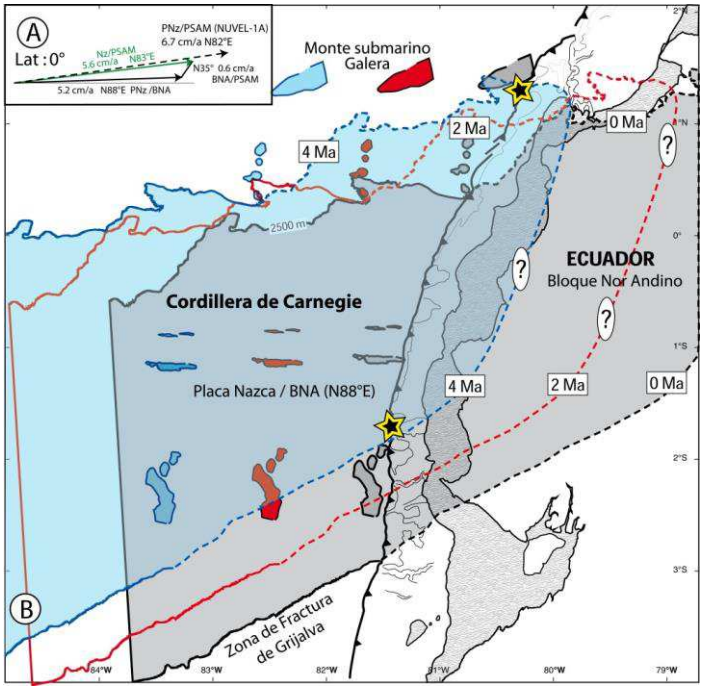

Figure 2. 4 Reconstruction of Carnegie Ridge (CR) location at ~2 My and ~4 My; (a) kinematics frame, Nazca plate vector/ North Andean Block (b) The north flank of Carnegie Ridge was obtained using the 2500-m contour line, the stars correspond to the intersection between the trench axis, and the Grijalva Fracture Zone and the north flank of CR (Collot et al., 2009).

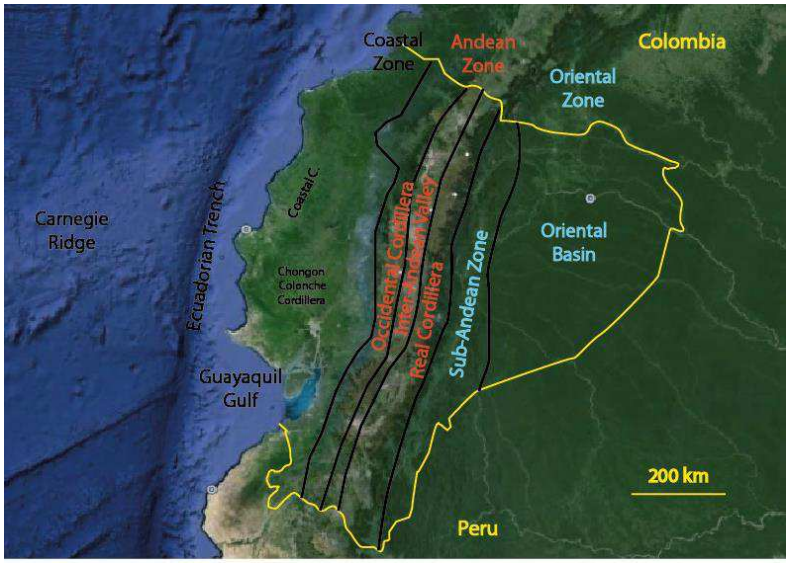

Figure 2. 5 Ecuadorian main structural domains; Ecuador shows three main regions: Coast Z., Andean Z., and Oriental Z. The principal features in the Coastal Z. are: Chongon-Colonche and Coastal Cordilleras; the Andeas Z presents the Occidental and Real Cordilleras separated by the Inter-Andean Valley; and the Oriental region principal divisions are the Oriental Basin and the Sub-Andean Zone

The Ecuadorian margin (Figure 2.6) is composed of cretaceous oceanic and island arc terranes (Goosens *and* Rose, 1973; Henderson, 1979; Feininger *and* Bristow, 1980, Lebras *et al.,* 1977, Reynaud *et al.,* 1999). Jaillard *et al*., (2009), consider that the three main oceanic terranes that are identified in Ecuador were accreted between Late Campanian and Late Paleocene times. They suggest that the first one "The San Juan terrane" is made of an Early Cretaceous oceanic plateau, accreted during the Late Campanian (~75 Ma); the second one, "the Guaranda terrane" compose of a Coniacian oceanic plateau (~90 Ma) overlain by either Campanian–Maastrichtian island arc products or Santonian–Maastrichtian pelagic cherts was accreted dunring the Late Maastrichtian, ~68 Ma; and the last one, the "Piñon–Naranjal terrane" comprises of a Late Cretaceous oceanic plateau overlain by Late Cretaceous island arc suites, and was accreted during the Late Paleocene (~58 Ma). They further propose that the Macuchi island arc rests on the Piñon– Naranjal oceanic plateau is of Late Maastrichtian–Late Paleocene age, and was accreted during the Late Paleocene).

2.1.4.1. The Coastal Region

The Coastal region corresponds to the Ecuadorian fore-arc. It is characterized by topography with an average height of 300 m that does not exceed 600 m in the Coastal Cordillera trending parallel to the margin, and the Chongón-Colonche Cordillera (N110°E) in the south. The principal structures that control the coastal morphology follow the cordilleras orientation, NNE-SSO along the coast, and NO in the south (Eguez *et al*., 2003).

The Coastal region is formed by three allochtonous oceanic terrains that were accreted to the continental margin during the Upper Cretaceous and the Middle Eocene (Feinninger *and* Bristow, 1980; Jaillard *et al.,* 1995, 1997). In the Coastal region, three sedimentary basins have formed (Figure 2.7): the Borbón, Manabí and Progreso basins (Deniaud, 2000); however, three other basins can be found offshore: the Manta-Bahía, Valdivia and Guayaquil Gulf basins.

The sedimentary fill may reach up to 10 km (Font *et al.,* 2013); and the seismic p-wave velocities within the fore-arc basins increase with the sedimentary thickness, reaching about 5 km/s for a thickness of about 8 km. Gravity modeling suggest that the North Andean Block (NAB) crustal thickness varies between 22 km (near the coast line) to 30 km (western flank of the Andes), thinning locally beneath the Coastal Cordillera (Case *et al.* 1973; Feininger *and* Seguin 1983).

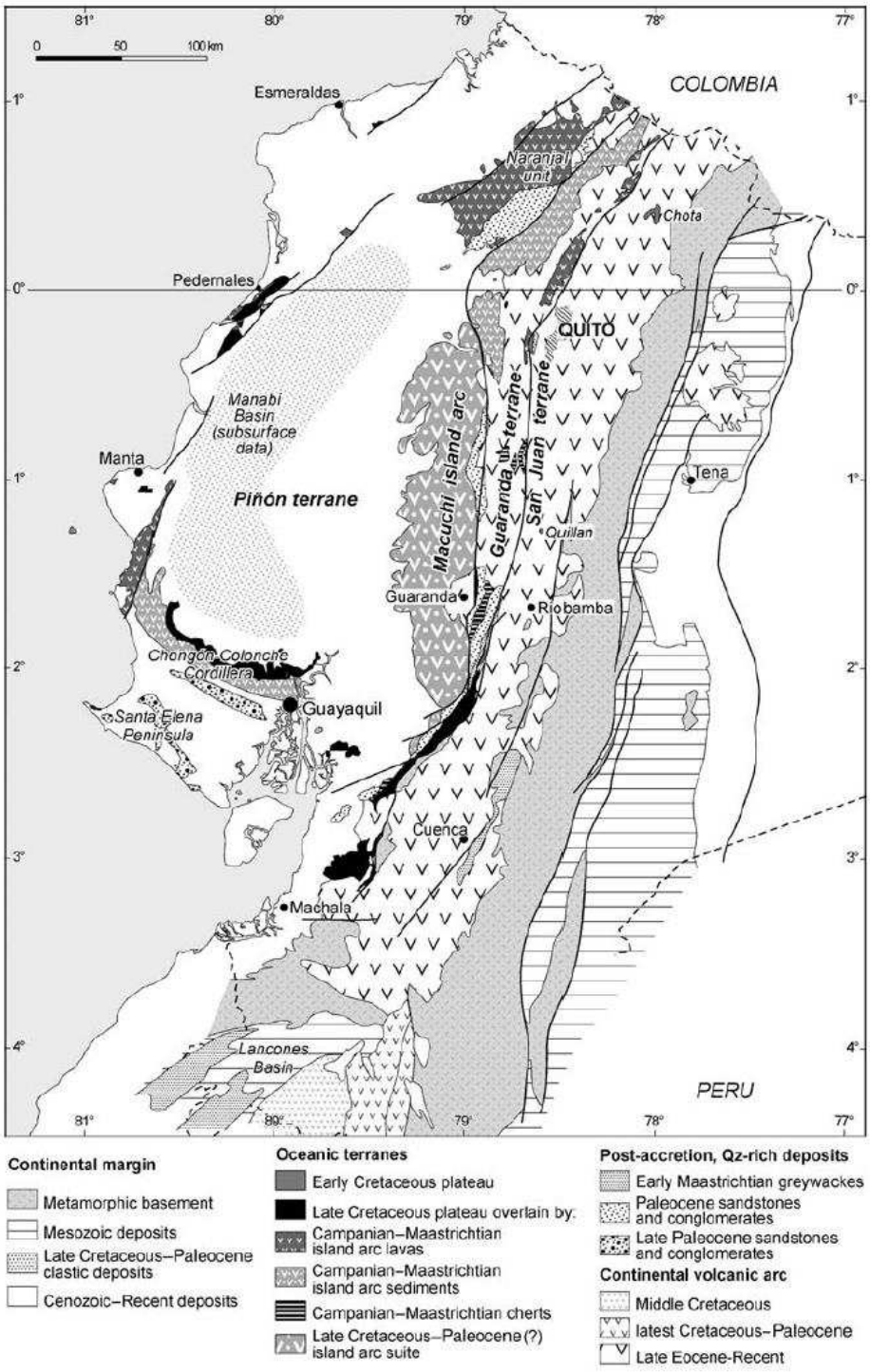

Figure 2. 6 Geological map of western Ecuador showing the continental margin rocks, oceanic

terranes and post-accretion deposits (Jaillard et al., *2009)* .

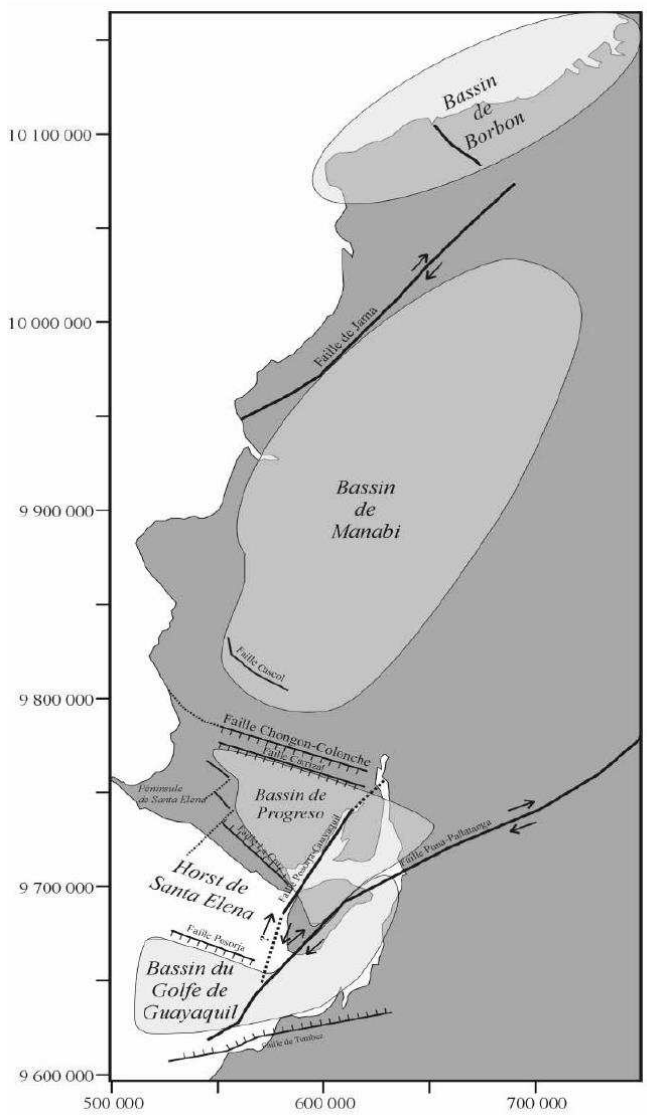

Figure 2. 7 Ecuadorian Neogene basins emplaced in the Coastal region; Borbón and Manabí in the north, and Progreso and Guayaquil Gulf Basin in the south (Deniaud, 2000); showing the main structures: Puná-Pallatanga and Jama faults and Santa Elena horst are shown.

2.1.4.2. The Andean Region

The Andean Range consists of the two parallel Real and Occidental Cordilleras, which are oriented NNE-SSW and separated by the Inter-Andean Valley (Figure 2.5). The Inter-Andean valley forms a depression generated by reverse faults (Winter *et al.,* 1993). The Andean region has a width of 150 km and 650 km of length, and it is oriented NNE-SSW parallel to the trench.

The Real Cordillera consists mostly of sub-linear belts of Paleozoic to Mesozoic metamorphic rocks, affected by different phases of deformation and metamorphism before being successively accreted to the paleo-continental margin since the Mesozoic (Bladock, 1982). These rocks are attributed to magmatic periods that occurred from the Upper Triassic to the Lower Jurassic (200 - 220 M.y), the Middle Jurassic to the Upper Jurassic (190 - 150 M.y), and the Upper Cretaceous (85 - 65 M.y) (Figure 2.6); Basement rocks of the Real cordillera are covered by Cenozoic to modern volcanico-sedimentary units. The Occidental Cordillera is a volcanic arc that was emplaced after the accretion of the oceanic terrains that form the substratum of the Coastal Region (Hughes *and* Pilatasig, 2002). Both Cordilleras are separated by the Inter-Andean filled by Pliocene to Qaternary, 5000-m-thick-volcano-sedimentary cover (Lavenu *et al*., 1995). Feininger and Seguin (1983) suggest that the basement underlying the Inter-Andean zone consist of Real Cordillera rocks.

Although no strong Moho discontinuity has been imaged, seismology and gravity modelling agree with a crust thickness reaching 50 to 66 km (Ocola *et al*., 1975; Leeds, 1977; Feininger *and* Seguin, 1983; Guillier *et al*., 2001).

The Ecuadorian Andes have at least 25 potentially active volcanoes, mainly distributed along the two mountain chains. These volcanoes are the highest peaks in the Ecuadorian Andes (Chimborazo 6268 m); besides, there are volcanoes in the Inter-Andean Valley and Sub-Andean Region. The volcanic activity in Ecuador is important, both historical and in recent periods. The magmatism associated to the activity of Ecuadorian volcanoes is typically andesitic and dacitic. However, some volcanic edifices in the Ecuadorian Chain, such as the Antisana (Bourdon, 1999), the Guagua Pichincha (Bourdon, 2001), the Quimsacocha (Beate, 2001) are adakitic as result of fusion of the oceanic crust (Kay, 1978).

2.1.4.3. The Oriental Region

The Oriental region (Figure 2.5) consists of the Upper Amazon basin dominantly formed by sedimentary series floored by the Guiana shield; the Sub-Andean zone (Napo and Cutucu foothills) appears at the margin of the Andean Cordillera: this zone includes folded Mesozoic sedimentary rocks and is bounded by thrust systems on the east that shows significant Neogene motion as mentioned by Eguez *et al*., (1993).

The thickness of this basin reaches 10 km (Thomas *et al.,* 1995) and is characterized by a

velocity gradient between ~2 to 5.5 km/s (Font *et al.,* 2013). Feininger *and* Seguin, (1983) using gravity modeling estimated an average continental crust thickness between 30 and 35 km.

The sub-Andean region has an altitude that never exceeds 2000 m and it is limited to the east by the fault zone Cutucú-Galeras that separates it from the hinterland (Benitez, 1995). The Oriental Basin is little deformed zone and has low altitude. Related to the Andean orogeny, the basin subsided during the Tertiary (Baby *et al.,* 1999).

2.1.5. The Continental Shelf and outer margin wedge.

Analyzing the northern segment of the Ecuador trench, Marcaillou *et al*. (2006) found that North of the Ecuadorian margin, the trench is locally disrupted and filled by ~3 km of turbidites. According to Ratzov *et al.,* (2010) the northern Ecuadorian trench close to Punta Galera is isolated from major continental sediment input; thus, the mass-transport deposits (MTDs) and turbidites found here are considered of local origin, and they contribute to short-term frontal erosion. They found that: 1) seven MTDs were emplaced in distinct trench sub-basins since ~23 kyr, and 27 kyr, whose 6 derived from the margin; 2) turbidites were deposited in the southernmost trench sub-basin since ~4.9 kyr; 3) the dissociation of gas hydrates during the last 8 kyr-stage of slow sea-level rise might have contributed to trigger the three youngest MTDs.

Collot *et al*., (2009) divided the Ecuadorian margin in 3 segments (Figure2.8): the Manglares segment, the Central segment, and the Southern Segment. They consider that the morphology of the central Ecuadorian margin is characterized by a generally steep slope, intensive mass wasting and a small frontal prism that is compatible with an erosive margin and negative mass transfer; whereas that tectonic accretion occurs in the southern and northern margin segments in the form of Guayaquil and Colombia accretionary wedges, where a positive mass transfer contributes to the continental growth. They further suggest that sediment transfer from the Andes to the trench is accommodated through the Guayaquil canyon across the southern margin segment and across the northern margin segment by the Esmeraldas and Patia-Mira canyon systems; this provides 0.8 km and 2.0-4.8 km trench fill, respectively. In contrast, less sediment is deposited in the shallow trench of the central margin segment (Figure 2.9). Areas with eroded margin slope are present between Cabo Pasado and the Galeras seamounts and between Puerto Lopez and the Guayaquil canyon, all resulting from the southward migration of Carnegie Ridge flanks along the Ecuadorian trench.

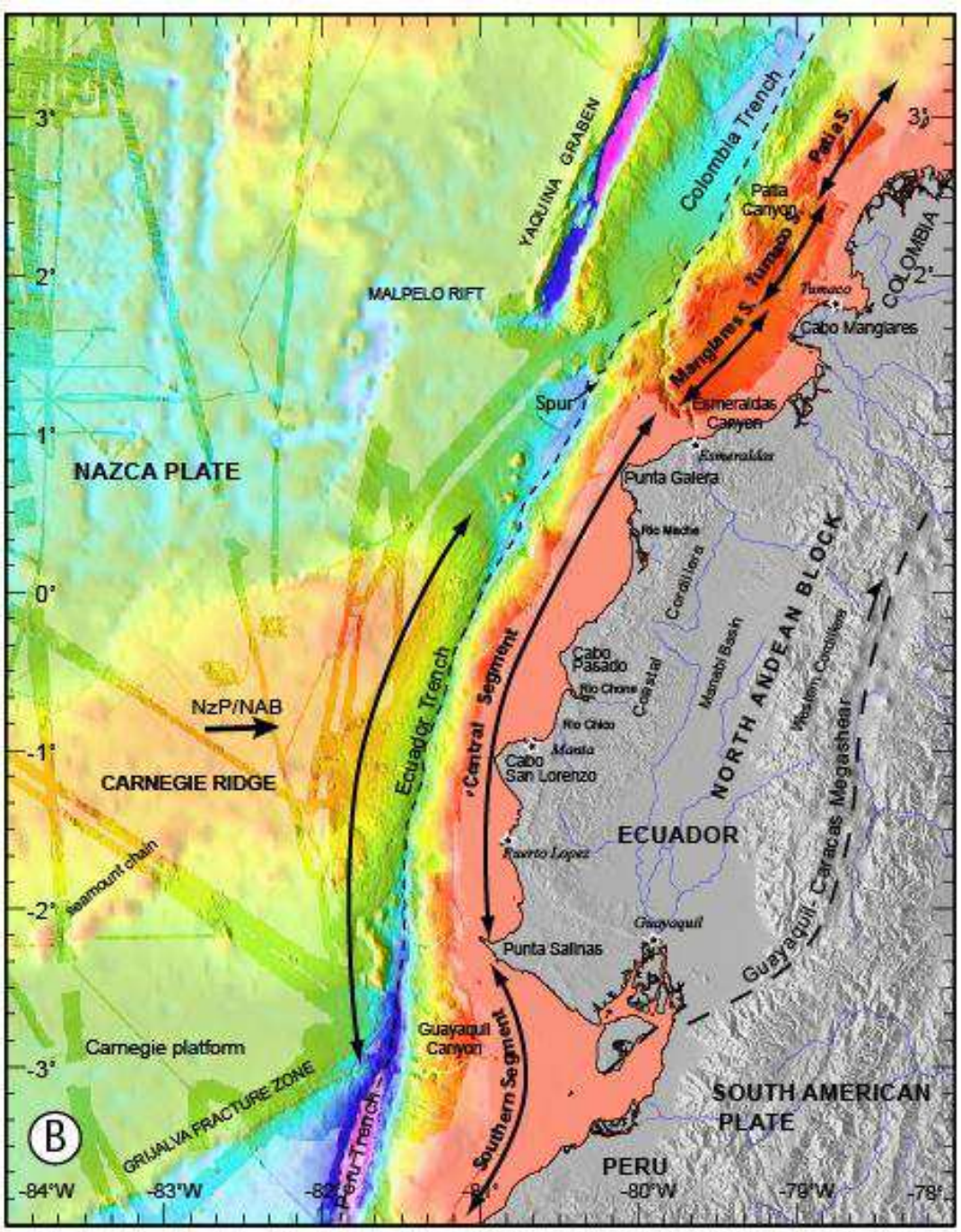

Figure 2. 8 The map shows the bathymetry and topography of Ecuadorian subduction margin and south of Colombia (Michaud et al., 2006, Collot et al., 2009).

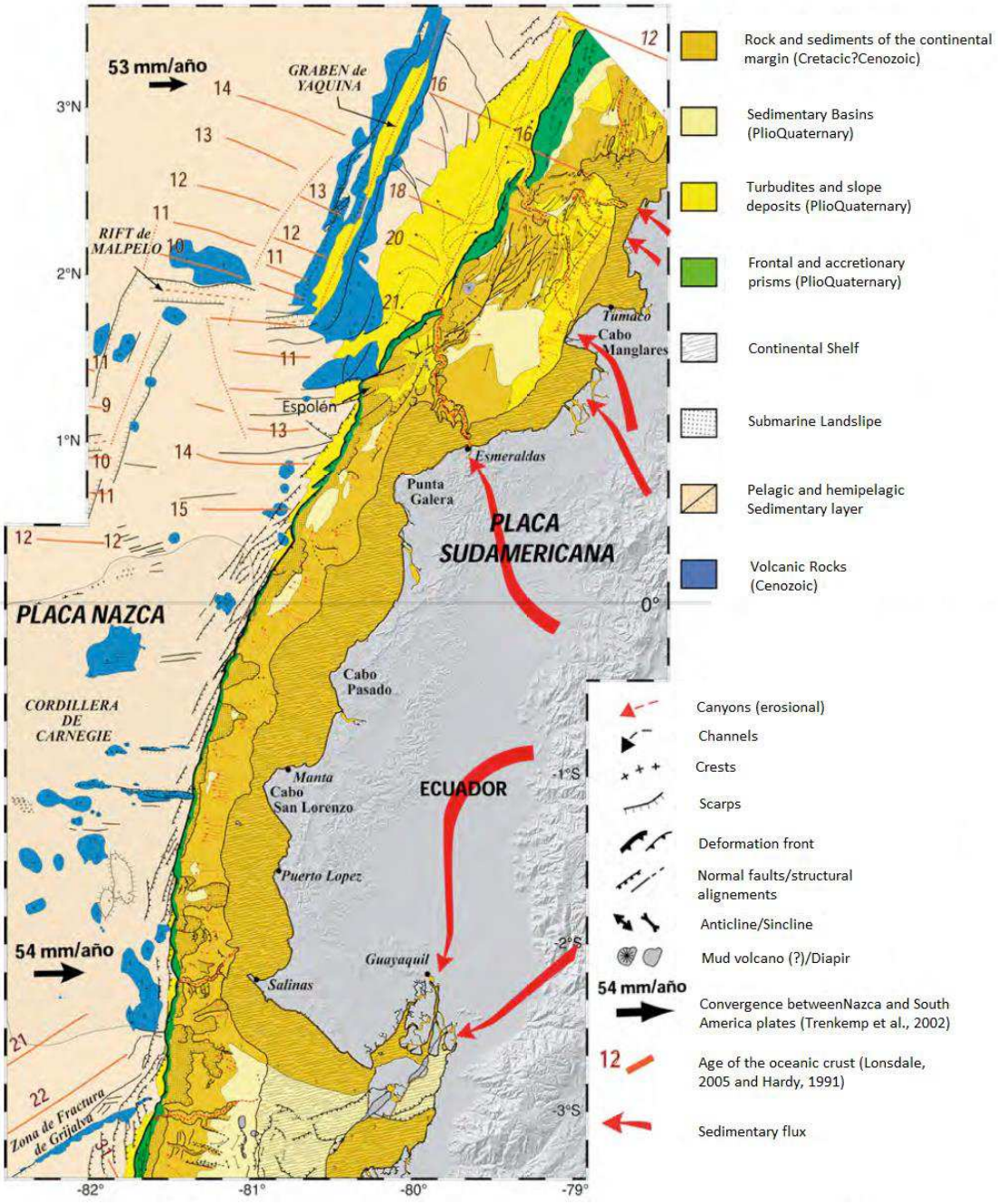

Figure 2. 9 Geologic and structural interpretation of convergent Ecuadorian-South Colombia margin (Collot et al., 2009).

2.1.6. Margin segmentation and crustal structures (seismo-tectonic)

In Ecuador, the seismicity and the volcanism show a high degree of segmentation along strike of the Andes (Gutscher *et al.,* 1999); and the subduction of Carnegie Ridge (CR) has been suggested as responsible of this segmentation (Gutscher *et al.,* 1999; Collot *et al*., 2004). In this erosional margin, the seismogenic segmentation is likely caused by transverse faults (Figure 2.10), some of them correlate with the limits of the megathrust earthquake co-seismic slip zones that have occurred over the last century (Collot *et al.,* 2004). Collot *et al.* (2004) identified the offshore extension of these faults using Multichannel seismic reflection and bathymetric data acquired during the SISTEUR cruise (2000). They propose a model of weak sub-vertical transverse faults that decouple adjacent margin segments, which are strongly coupled along the plate interface, thus limiting the along-strike size of the rupture and therefore the earthquake magnitude. These faults: Manglares, Esmeraldas and Jama-Quininde are showed in Figure 2.10. In the region of the 1958 earthquake rupture, these authors propose that the seaward extent of the rupture was controlled by a splay fault (Figure 2.11).

According to Collot *et al.* (2004), **Manglares fault** is a N106°E trending crustal transfer fault that separates the strongly shortened and uplifted margin segment at north, and a poorly deformed and subsiding segment at south; 2) **Esmeraldas fault** systems is another structure segmenting the northern margin and its offshore projection lies along the upper course of the Esmeraldas canyon; 3) and the **Jama-Quininde fault** system is a major upper plate mechanical discontinuity that divides the margin obliquely and outlines the southern extremity of both the 1906 and 1948 earthquake ruptures.

Agudelo *et al.* (2009) obtained an optimal blocky velocity model (Figure 2.12) that revealed several structural characteristic about the northern Ecuadorian margin: 1) fine-scale sediments lateral velocity variations across the trench and the frontal margin slope for lithological variations, tectonic compaction, and mass wasting processes; 2) the existence of a major sub-vertical splay fault (SF) that cuts the two-layer velocity structure of the inner wedge margin basement; 3) the outer wedge basement has lower velocities (4.0-5.5 km/s) than the inner wedge basement (4.0-6.6 km/s) (Gailler *et al.,* 2007); 4) a lower-velocity zone (3.8-5.0 km/s) associated with a major landward dipping splay fault that likely results from tectonic shearing and fluids migration along the fault.

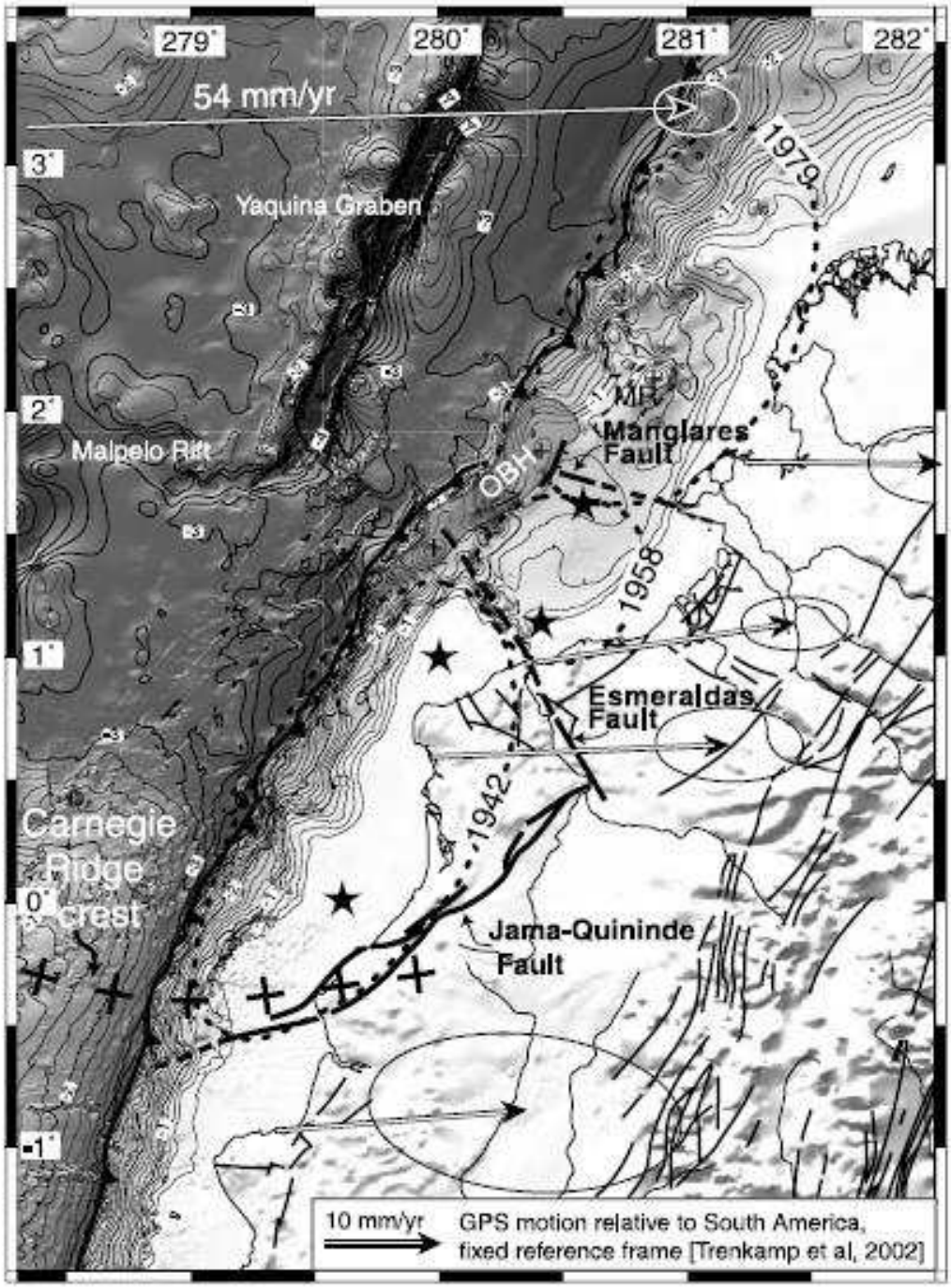

Figure 2. 10 Map shows the structural relationships between transverse crustal faults and great

earthquake rupture zones in the northern Ecuadorian margin (Collot et al*., 2004).*

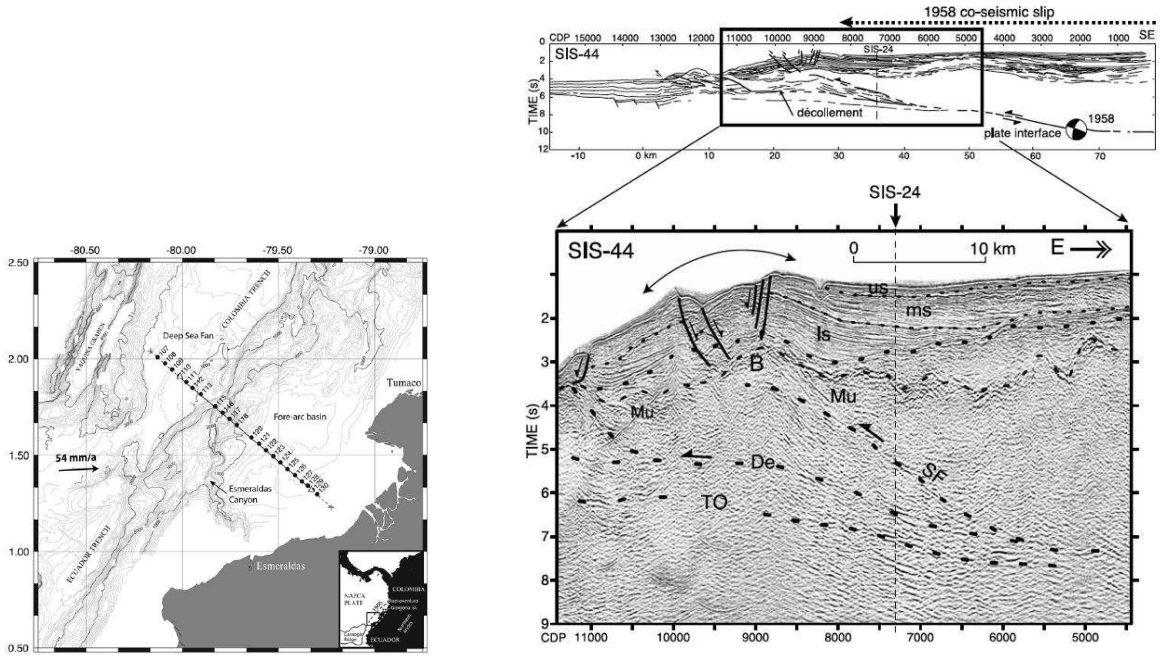

Figure 2. 11 left) localization of the profile SIS44; right) Close-up of time migrated image from line SIS44, showing focal mechanism of 1958 earthquake, the basin summit graben, and Splay fault SF (Collot et al*., 2004).*

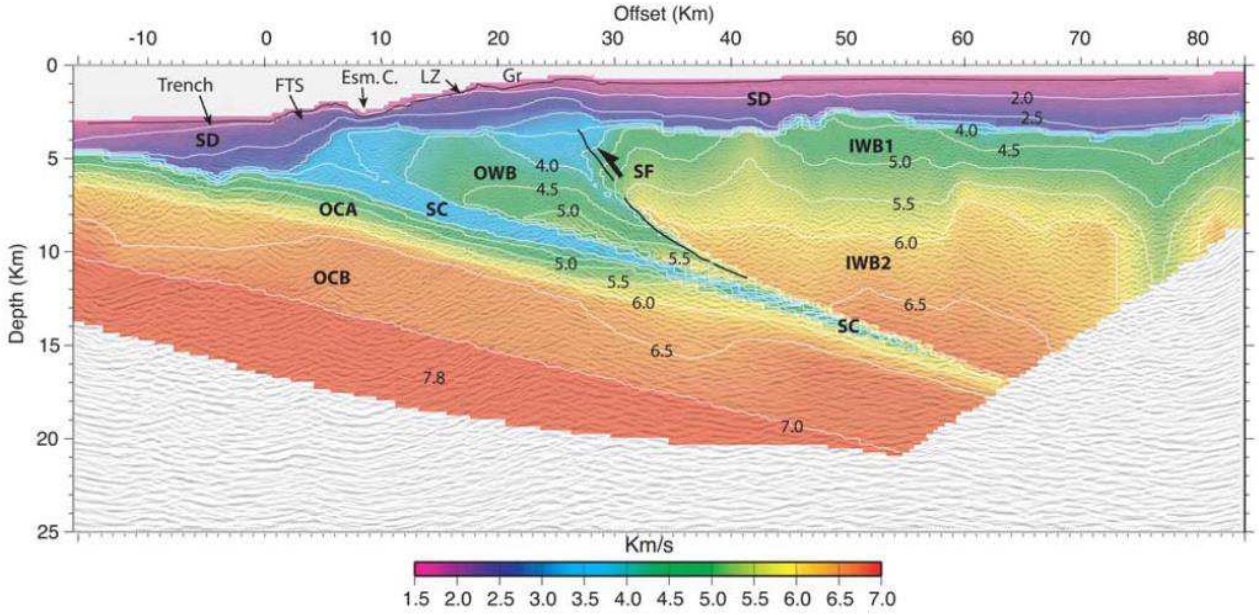

Figure 2. 12 Velocity model of profile SIS44; it is result of superimposing the blocky model and PSDM image; SC: subduction channel, SF= splay fault, SD: sedimentary cover, IWB1: upper inner wedge basement, IWB2: lower inner wedge basement, OC: oceanic crust, OCA: oceanic crust layer A, OCB: oceanic crust layer B, FTS: frontal tectonic sliver, Esm C: Esmeraldas canyon, LZ: zone of landslide, Gr: summit graben; while lines are the iso-velocity contours in Km/s (Agudelo et al., 2009).

2.1.7. Seismicity along the Ecuadorian margin

2.1.7.1. Regional Seismicity

Gutscher *et al.,* (1999) showed (Figure 2.13) that the focal mechanisms of earthquakes in this region are consistent with the plate tectonic model of the area and they distinguished several types of earthquakes: 1) shallow dextral strike-slip in the active Panama FZ (1–5); 2) shallow normal faulting in the active Panama Rift (6, 7; 3) shallow underthrusting in the subduction zone (8–16); 4) shallow normal faulting in the flexural bulge east of Yaquina Graben (17–21); 5) shallow thrusting and dextral strike-slip events in the upper plate (27–42); and 6) deeper, commonly normal faulting events in the down-going slab (43–52).

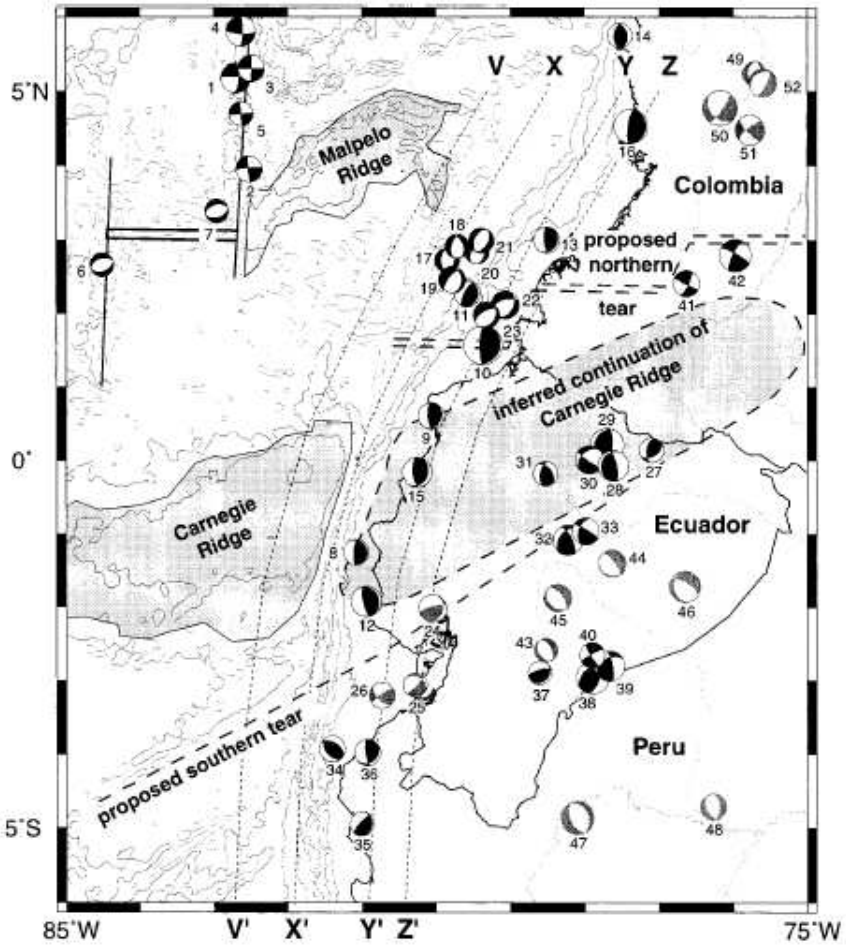

Figure 2. 13 Map shows the inferred continuation of Carnegie Ridge and the focal mechanics of different type of earthquakes from 1976 to 1997 (Gutscher et al., *1999); shallower events < 50 km in shaped black and deeper events >50 km in gray.*

According to Guiller *et al.* (2001), the major tectonically active structures in the Ecuadorian Andes have been reactivated by the present day compression and correspond to Late Jurassic to Early Tertiary East-dipping sutures. They found elements favoring a crustal thickness of about 40-50 km under the coastal plain and 50-70 km beneath the Andes and they consider that the deformation is concentrated beneath the Andes, while the Coastal plain acts as a buttress transmitting the stress to the Andes.

Segovia *and* Alvarado (2009) identified several seismic sources using the local seismic network (RENSIG), which are characterized by: earthquakes located in interplate contact; earthquakes linked to internal deformation and relative displacement of the two continental plates (North Andean Block and South America Plate), both with shallow depth; and earthquakes related to the deformation within the subducted oceanic plate. Off-shore, they observed extensional and compressional regimes, both with near W-E orientation; in the fore-arc, there is a great variation of the stress, oriented from N13° to N130°; in the north Ecuadorian Andean zone, the stress directions vary between N93° and N119° and at the south the stress direction is N125°.

Font *et al.* (2013) show a map (Figure 2.14) with the epicenters (from the 1994-2007 RENSIG catalog, for 3.8< Mw< 6.5 earthquakes) and rupture zone of the large Ecuadorian subduction earthquakes, and the regional seismicity from 0 to 30 km depth. They further suggest the existence of four areas; two of them with differing seismicity patterns identified as eventual asperities that might be accumulating stress (the 1958 rupture zone area and the Jama cluster); the third area close to Manta, which appears almost aseismic on a spherical domain of ~30 km of radius; and the last one, where a slow-slip event and seismic swarms have been observed but no large historical earthquakes are known (Vallée *et al.* 2013).

The Ecuadorian margin shows a highly variable seismic behavior characterized by large earthquakes north of Manta to an almost aseismic area in the central and southern margin segments, south of Manta.

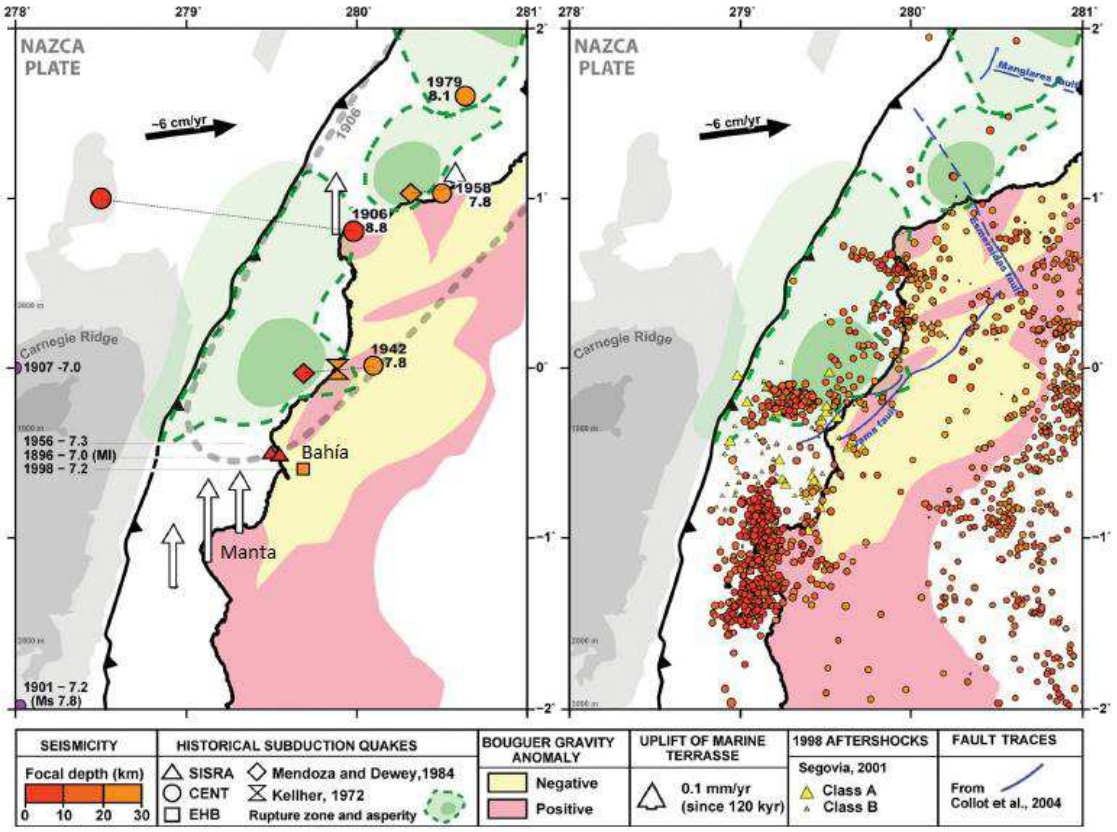

Figure 2. 14 Historical earthquake epicenter's map (1994-2007 RENSIG catalog) (Font et al, 2013) using the 3-D-MAXI catalogue from 0 to 30 km of depth; this map shows the earthquakes' asperity (dark green), the rupture zone (light green) (light green; Kanamori and McNally 1982; Beck and Ruff 1984; Swenson and Beck 1996) , the Simple Bouguer gravity anomalies (Feininger and Seguin, 1983): positive (red) and negative (yellow), and the marine terraces uplift (white arrows) from Pedoja et al., 2003, 2006.

The north Ecuador and south Colombia margin has been affected by four thrust earthquakes Mw > 7.7 along the last century (Figure 2.15), some of them triggered devastating tsunamis that reached even far locations as Hawaii or Japan. The first of these events, the January 31, 1906 earthquake had a Mw 8.8 and a rupture length (*L*) of 500 Km (Kelleher, 1972; Kanamori *and* McNally, 1982). The same area was ruptured in three smaller segments: 1) the 1942 earthquake, Mw 7.8, L=200 Km; 2) the 1958 earthquake, Mw 7.7, L=50 Km; and, the 1979 earthquake, Mw 8.2, L=180-230 Km, (Kanamori *and* McNally, 1982; Mendoza *and* Dewey, 1984; Swenson *and* Beck, 1996).

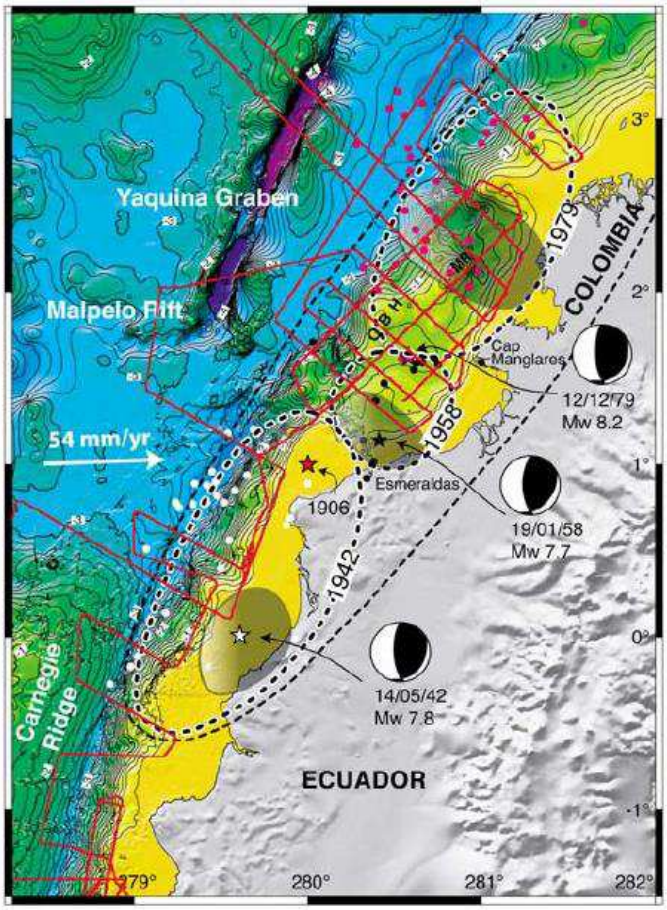

Figure 2. 15 Location of the 20th century great subduction earthquake rupture zones of northern Ecuador–SW Colombia (dashed ellipses), epicenters (stars), and their associated relocated 3-month aftershocks of mb > 4.8 (white, black, and red dots) (Mendoza and Dewey, 1984), seismological asperities (gray shaded elliptic areas) and focal mechanisms (Kanamori and Given, 1981; Kanamori and McNally, 1982; Swenson and Beck, 1996; Herd et al., 1981; Beck and Ruff, 1984). Bathymetry map in km has been compiled from NGDC and the R/V Nadir SISTEUR cruise single beam bathymetric data (red lines) and swath bathymetry from the R/V l'Atalante Pugu cruise and the R/V Sonne Salieri and SO162 cruises. OBH is outer basement high; MR is middle ridge. Open arrow shows Nazca–South America relative plate motion vector, derived from Trenkamp et al. (2002) GPS study (from Collot et al., 2004).

2.1.7.2. The January 31, 1906, Earthquake

The January 31, 1906, event had an estimated Mw 8.8, and rupture length (L) of 500 Km and was the largest event recorded in the area (Kelleher, 1972; Kanamori *and* McNally, 1982). It occurred at 10:30 a.m. (UT-5) with three large foreshocks at 9:06, 9:25, and 9:40 a.m. (UT-5) (Rudolf *and* Szirtes, 1911). This event was analyzed by Kanamori *and* McNally (1982) using old seismograms, and it is a thrust event which rupture propagated in NE direction, what was confirmed

by the severe destruction over 100 km inland. Few minutes after the earthquake, a tsunami swept the coast from Rio Verde (Esmeraldas) forward to the north, killing among 1000 to 1500 people; in La Tola town at the north of Esmeraldas, 23 houses were destroyed, and the Esmeraldas River flooded the low parts of Esmeraldas city. The tsunami reached also Bahía de Caráquez city where the water height was around 80-100 cm in 20 minutes and left in ruins several towns and plantations (Soloviev, 1975; Rudolph *and* Szirtes, 1911). Jama-Quininde fault (Figure 2.10) could have stopped the 1906 and 1942 earthquake rupture zones,

2.1.7.3. The May 14, 1942, Earthquake

After the 1906 earthquake, the largest event in the region was the 1942 thrust earthquake (Mw 7.8, L=200 Km, and depth=19.7 km) and occurred at 7:13 a.m. UT (+5 local time) near the subducting Carnegie Ridge off the coast of Ecuador (Kanamori *and* McNally, 1982; Swenson *and* Beck, 1996; Mendoza *et al.,* 1984). Collot *et al.,* (2004) found that the Jama-Quininde fault system divides the margin obliquely and that this fault system coincides roughly with southern limit of the 1942 and 1906 earthquake rupture zones. They consider that higher interplate pressure due to the buoyancy of the bulk of the subducted ridge would be responsible for stopping the 1906 and 1942 rupture zones propagation near the subducted ridge crest and Jama-Quininde fault system.

No tsunamis at teleseismic distances were reported for the 1942 event No long-period seismogram is available for the 1942 event. However, the size of the aftershock area determined by Kelleher (1972) suggests that this event had about the same size as the 1958 earthquake.

2.1.7.4. The January 19, 1958, Earthquake

The 1958 earthquake occurred at 2:07 p.m. UT (+5 local time) with Mw 7.7, L=50 Km and a depth=29.8 km, and asperity's length of 25 km (Beck *and* Ruff, 1984; Mendoza *et al*., 1984). This thrust earthquake had a lack of aftershocks near to the trench; however, it has an intense aftershocks activity in the boundary between the 1958 and 1979 (Mendoza *and* Dewey, 1984). Collot *et al*. (2004) propose that the seaward limit of the 1958 earthquake rupture zone was associated with the splay fault imaged on line SIS44 (Figure 2.12). This fault accommodated the coseismic elastic slip, and produced the seafloor deformation that was the main source of the 1958 tsunami. They also consider that a relative seafloor high, involving small-sized seamounts and oceanic horst, extends between the trench and Malpelo rift, suggesting that minor oceanic relief is being subducted

beneath the margin segment ruptured in 1958 (Collot, *et al*. 2004); however, seismic reflection data do not provide support for a large subducted seamount near the Manglares fault (Marcaillou, 2003).

2.1.7.5. The December 12, 1979, Earthquake

The 12 December 1979 event (Mt=8.2, Mw=8.2, L=180-230 Km), the last large rupturing sequence, occurred at 7:59 a.m. UT (+5 local time) and it was located at latitude 1.62°N and longitude 79.42° W with a depth of 24.3 Km, and had a rupture direction of N40°E (Kanamori *and* Given, 1981; Kanamori *and* McNally, 1982; Mendoza *and* Dewey, 1984; Engdahl *and* Villaseñor, 2002). The 1979 event was recognized as an interface thrust earthquake (Figure 2.5) on the basis of its body and surface wave's radiation patterns (Herd *et al*., 1981; Kanamori *and* Given, 1981).

This earthquake began with the failure of the barrier that arrested the 1958 rupture; and its main shock hypocenter was located at the boundary between the 1958 and 1979 aftershock zones (Mendoza *and* Dewey, 1984). The 1979 earthquake had less aftershock activity than the 1942 and 1958 events; it may imply that the subduction zone in this region was under lower stress or experiencing lower strain rate (McGarr, 1976; Mendoza *and* Dewey, 1984).

Beck *and* Ruff (1984) assumed a rectangular fault (divided into three segments) with a uniform width of 100 km, a shear modulus (μ) of $5x10^{10}$ N/m^2 and using the theoretical equation of the seismic moment ($Mo = \mu * D * A$) in order to calculate for each segment of the fault the displacement. This rupture area consists of 3 segments from south to north, whose displacements were 1.75 m, 5.9 m, and from 1 m to 2m. They concluded that the asperity that ruptured in the central segment was essentially locked between the 1906 and 1979 earthquakes..

2.1.7.6. The 4 August, 1998, Earthquake

According to Segovia, (2001), the 4 August earthquake (Mw=7.2) struck the Ecuadorian coast at latitude 0.5°S, with an intensity of VII in Bahía de Caráquez city (Figure 2.16); this thrust event (CMT catalog) had two foreshocks of Mw=5.4 and 5.7 that warned the population; even though, this event did not generate any tsunami, the water receded 30 min after the earthquake.

The zone that generated the 1998 earthquake and 2 other events (Mw>7 occurred in 1886 and 1956) may correspond to a small local asperity of strong inter-seismic coupling, and the rest of the area behaves mostly aseismically by steady creep or slow slip events (Font *et al.,* 2013).

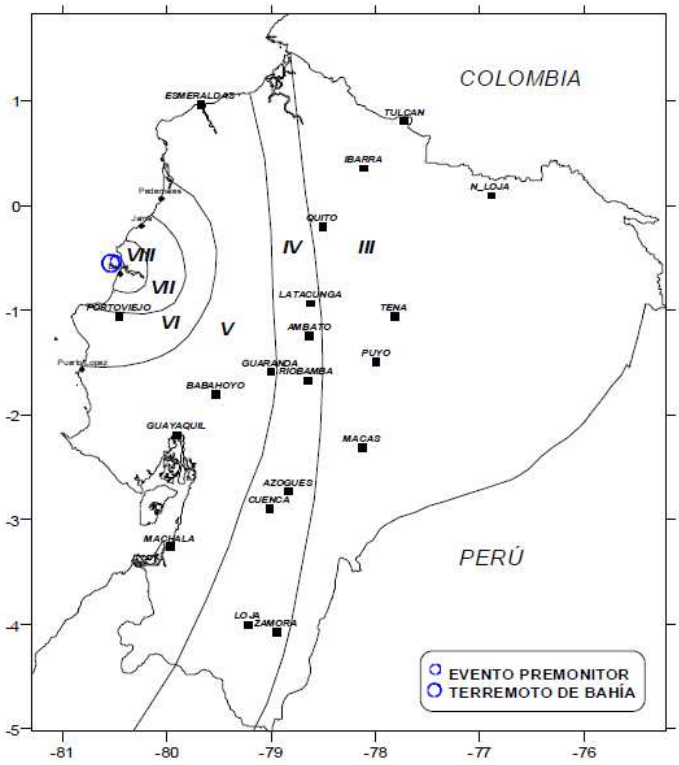

Figure 2. 16 Isoseismal map of the Bahía de Caráquez's earthquake of 1998 (Egred, 1998); intensity VII was reached at Bahía de Caráquez city.

2.1.1. Inter-seismic coupling variations along the Ecuadorian Margin

Chlieh *et al.,* (submitted) using an Inter-seismic coupling model that provides a robust framework to explore more realistic seismic models from simple forward static model, found that in the rupture area of the great 1906 Mw=8.8 earthquake, the inter-seismic coupling is very heterogeneous and mainly concentrated in the first 30-km depth of the interplate. Their models indicate 5 large asperities distributed along the Ecuadorian interplate contact (Figure 2.17), 4 of which fall within the ruptures of large earthquakes of the last century. South of the 1906 rupture area, the Carnegie ridge crest subducts and coincides relatively well with a 50-km wide creeping corridor between Manta and Bahia de Caráquez) that may have acted as persistent barrier to the large seismic ruptures. Southward, a highly locked asperity is observed below La Plata Island.

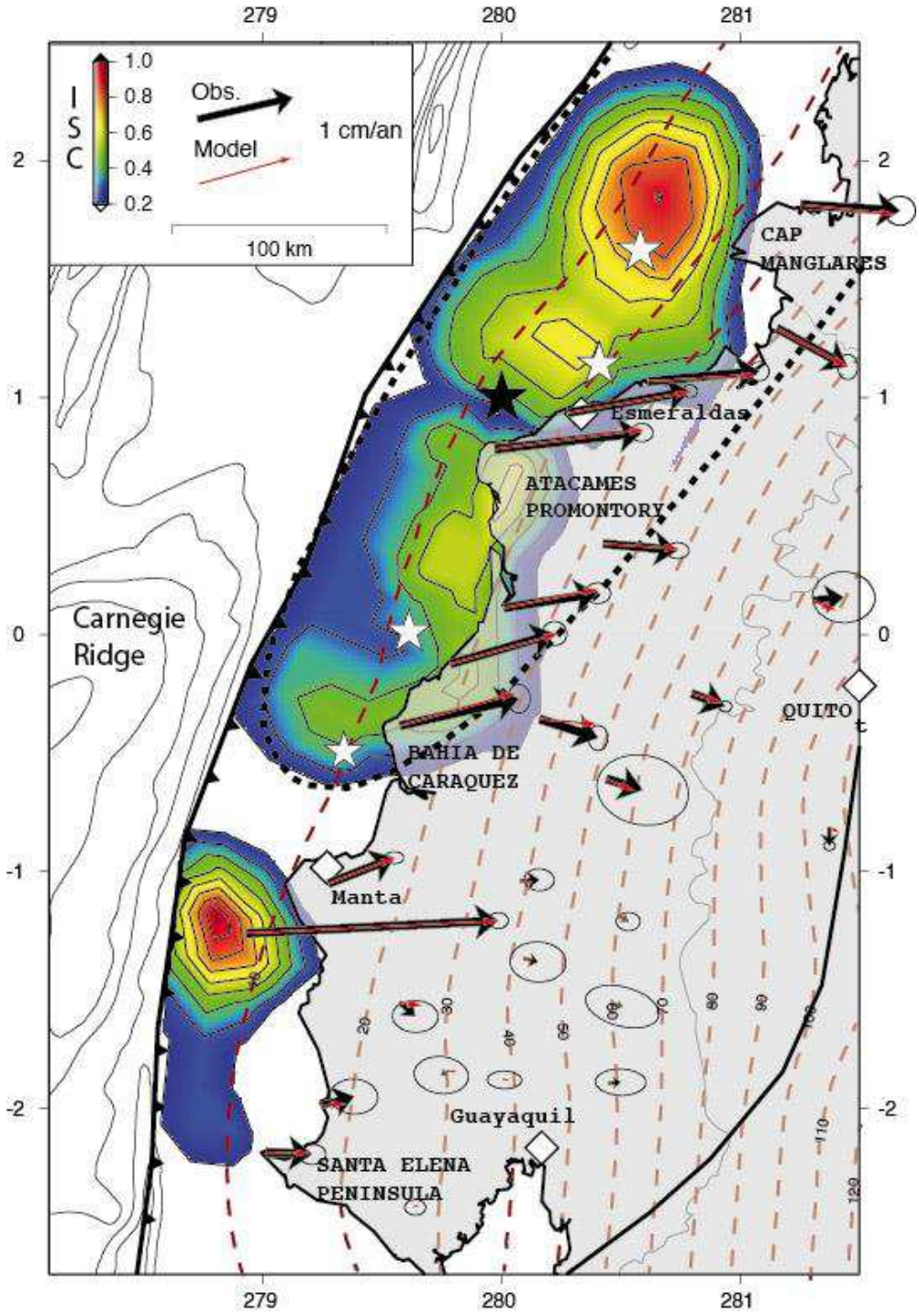

Figure 2. 17 Distribution of the inter-seismic coupling along the Ecuadorian subduction zone derived from the inversion of the inter-seismic GPS velocities. The yellow-red areas indicate highly locked zone since green-blue and white areas between Bahia de Caraques and Santa Elena represent creeping regions of the megathrust interface, and dashed lines indicate the depth of the expected interplate contact (Chlieh et al.*, submitted).*

2.1.2. Marine Terraces along the Ecuadorian margin

The Ecuadorian coast is part of the Talara Arc, a 1000-km-long structure bordered by concave subduction zone to the west and the base of the Andes to the east, which includes the continental shelf and the coastal region (Pedoja *et al.* 2006a). According to Pedoja *et al.*, (2006a), a marine terrace is an uplifted landform and associated deposits, separated from each other by steep scarps that represent relict sea cliffs formed by a single sea-level oscillation; marine terraces provide useful markers for assessing the presence, rates and pattern of coastal deformation; whereas a sequence of uplifted Pleistocene marine terraces corresponds to the geologic and geomorphic records of repeated glacioeustatic sea-level high stands superimposed on a rising coastline (Ota, 1986).

Emerged Pleistocene marine terraces located along the Talara Arc have been documented by several autors (*e.g*., Cantalamessa *and* DiCelma, 2004; Pedoja *et al.,* 2001, 2003, 2006a, 2006b). In this region, the coastal uplift is generally related to the subduction of Nazca (Macharé *and* Ortlieb, 1992) and Carnegie aseismic ridges (Gutscher *et al.,* 1999; Pedoja *et al*., 2001, 2003, 2006a, 2006b). According to Pedoja *et al*., (2003), the strongest uplift is observed in front of the subduction of the Carnegie Ridge in the Manta Peninsula, and it tends decrease towards the northern and southern ends of the Talara Arc; they described 7 sequences of marine terraces along the Talara Arc, in the Ecuador and northern Peru (Figure 2.18); and they used Infra-Red Stimulated Luminescence (IRSL), a common method for dating soil sediments on sands as old as ~330 ka, and C14 and U-series from fossil shells for geo-chronological cross control. Three of these sequences (I, II, III) lie in Ecuador:

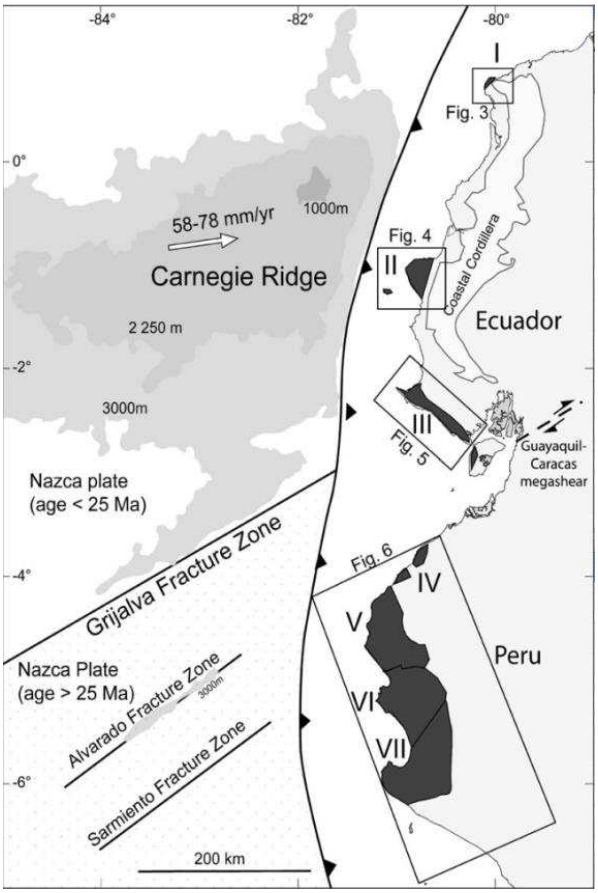

Figure 2. 18 Image shows the geodynamical context and marine terrace distributed in 7 sequence from I to VII, along the Talara Arc from (Pedoja et al.*, 2006); Ecuador: I Northern coast: Galera Point, II Central Coast: Manta Peninsula, La Plata Island. III Gulf of Guayaquil: Santa Elena Peninsula, Puna Island. Peru: IV Cancas, V Mancora: Los Organos, Lobitos, Talara, VI Paita Peninsula, VII Illescas Peninsula and paleo-bay of Bayovar Pedoja et al., (2006).*

2.1.2.1. Sequence I, Ecuador Northern coast:

According to Pedoja *et al*., (2006), at Punta Galera (Figure 2.19) there are three marine terraces **T1** (98 ± 23 ka, with IRSL), **T2** (220 ± 42ka, with IRSL) and **T3** (it was not sampled for dating, but extrapolating back in time an uplift rate of 0.30 mm/yr , provides an age ranging between 320 and 350 ka). These terraces are carved in the Onzole Formation (Upper Miocene–Lower Pliocene) and tare locally covered by 2–3 m thick, marine sediments and limited by the NE–SW trending Galera Fault.

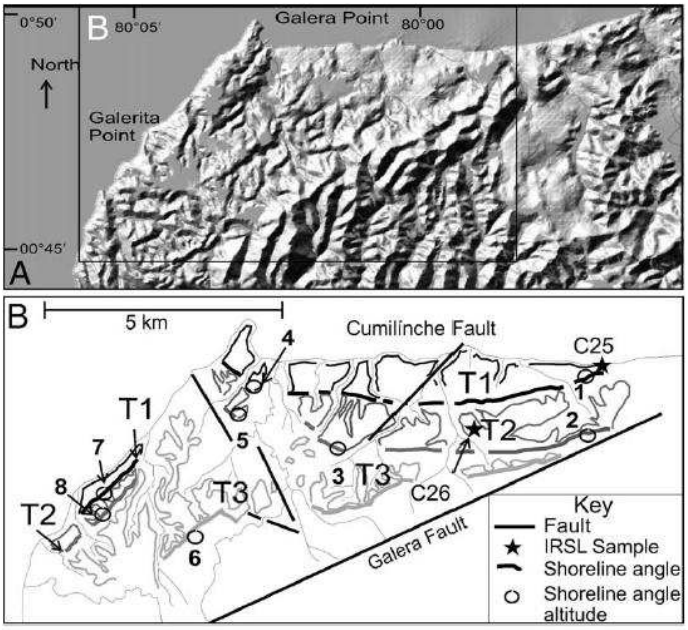

Figure 2. 19 Sequence I at Point Galera; (A) DEM of the studied area; (B) Marine terraces on Galera Point. T1: 1: 20±1 m, 4: 46±2 m, 7: 43±4 m; T2: 2: 53 ±3 m, 3: 65±3 m, 5: 61±3 m, 8: 64±4 m; T3: 6: 101±3 m (Pedoja et al.*, 2006).*

2.1.2.2. Sequence II, Manta Peninsula and La Plata Island

Pedoja *et al*., (2006) found that marine terraces are relatively well preserved on the Manta Peninsula, where the geometric disposition of the two highest terraces (T4 and T5) shows that the Manta Peninsula was originally an island before connecting to the continent, during the uplift and the formation of marine terrace T3. They attribute the differences in elevation for the same marine terrace north and south of the Manta Peninsula to movements along the Montecristi Fault (DGGM, 1970) (Figure 2.20).

The age for the marine terraces of sequence II are (Pedoja *et al.,* 2006a): **T1** has an age of 76 ±16 ka (IRSL) and an age of 85 ± 1.2 ka with U/Th; samples from **T2** have with IRSL ages of 232 ± 35, 212 ± 3 and 203 ± 32 ka, and with U/Th a minimum age of 187±3.7 ka; and **T3** deposit has a corrected age of 272 ± 28 ka; On Manta Peninsula, extrapolations of the Late Pleistocene uplift rates from the northern of the Peninsula show ages from 643 to 710 ky for **T4** (203 ± 10 m) and ~1Ma for **T5** (300±10 m).

La Plata Island is also part of the sequence II (Figure 2.20). It is located 25 km southwest off

the Manta Peninsula and presents a sequence of four marine terraces carved in Cretaceous basaltic basement rocks, with a thin discontinuous sedimentary cover (Pedoja *et al*., 2006). Cantalamessa *and* Di Celman (2004) describe the marine terraces of the La Plata Island as Plata 1 (T4, the oldest), Plata 2 (T3), Plata 3 (T2), and Plata 4 (T1, the youngest): Plata 1 has a very limited aerial extension and covers the northernmost part; Plata-2, the second terrace joins the paleo–sea cliff that separates it from Plata-1, and drops gradually southeastward to approximately 150 m at its southernmost rim; Plata-3, a less prominent step, present exclusively on the eastern part of La Plata Island, in the neighborhood of Punta Escalera; Plata-4 the fourth occupies the entire southern part of the Isla de la Plata. Along the remaining portion of coast, Plata-4 is found as small remnants or a white horizontal line on the sea cliff. They suggest that La Plata Island was produced by tectonic uplift on the order of 0.4 mm/yr and glacio-eustatic variations dated at least 500 ka. By comparing the marine terrace sequence T1 to T4 between the Northern Manta Peninsula and La Plata Island, and considering a mean uplift rate of 0.3 mm/yr, Pedoja *et al*., (2006) provide a T4 age on La Plata Island ranging between 643 and 710 ka.

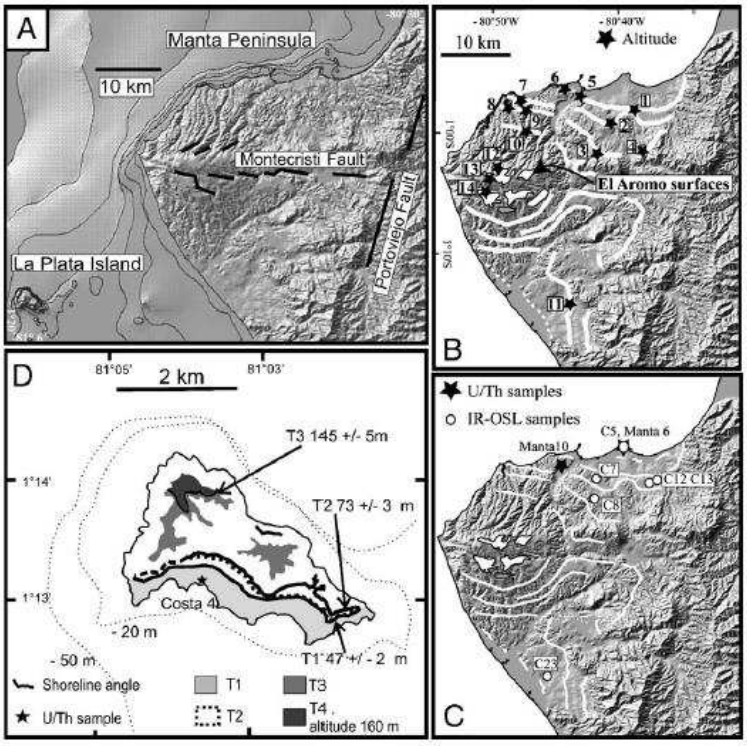

Figure 2. 20 The image shows the sequence II in the central coast of Ecuador. (A) DEM of the studied area (B) Marine terraces on the Manta Peninsula (C) Location of the U/Th and IRSL samples on the Manta Peninsula (D) Marine terraces on La Plata Island (Pedoja et al.*, 2006).*

2.1.2.3. Sequence III, Santa Elena Peninsula

Previous geological studies described the presence of three marine terraces T1, T2 and T3 on the Santa Elena Peninsula (Hoffstetter, 1948; Marchant, 1961), and their extension eastward along the northern margin of the Gulf of Guayaquil to Puna Island (Bristow *and* Hoffstetter, 1977; Dumont *et al*., 2005).

Pedoja *et al*., (2006) analyzed this sequence of three marine terraces (Figure 2.21) observed along the coastal stretch of the Santa Elena peninsula, and they found that the altitudes of the same shorelines are similar over long distances. Besides, they noticed that on the peninsula, La Cruz Fault and the Estancias hills separate the marine terraces from the Progresso Basin, and faults perpendicular to the shore have not been active since the terrace formation. Pedoja *et al*., (2006) propose ages for the terraces: **T1**, **in northern part** of the peninsula, yielding minimum ages of 111 and 136 ka; and **in southern part**, ages of 98 and 95 km, both using U/Th. Assuming constant uplift through time, they calculated the ages of **T2** (between 400 and 500 ka) and **T3** (between 600 and 900 ka), which implies a relatively slow uplift.

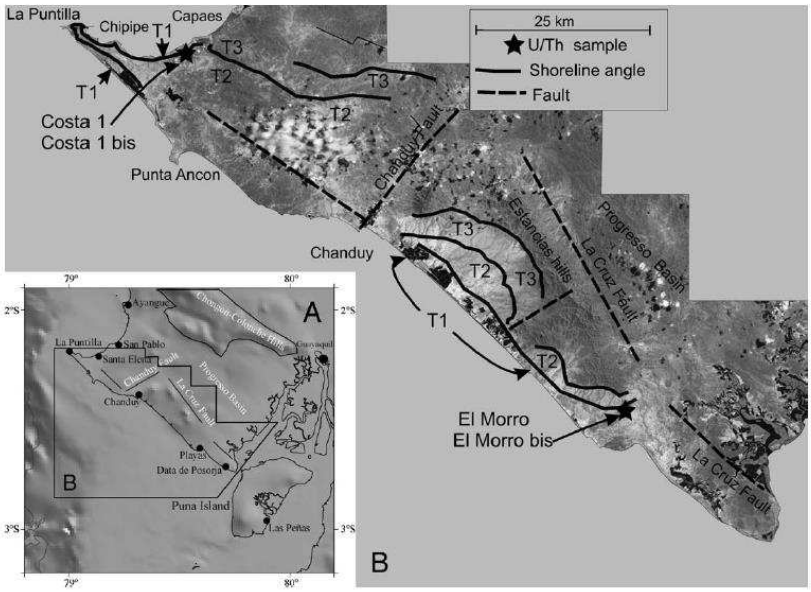

Figure 2. 21 Image shows the sequence III, Santa Elena Peninsula; a) DEM of the studied area; b) Marine terraces on the Santa Elena Peninsula (Pedoja et al*., 2006).*

CHAPTER 3

THE STUDY AREA: The Central Ecuador margin between Manta and Salinas

3. Introducción

The central Ecuadorian margin extends between Manta and Salinas (Figure 3.1). This margin segment was chosen as our study area because, to date, it shows unique structural, mechanical and seismogenic characteristics that truly differ from those of the northern Ecuadorian margin described in the previous chapter. The central Ecuadorian margin presents a lack of great subduction earthquakes (Mw >7.7). In contrast, it is the place of either earthquake swarms (Mw <6.2) and slow slip events near La Plata Island, or a lack of seismicity further south (Font *et al,* 2013). Recent GPS studies (Vallée *et al.,* 2013, Chlieh *et al.,* sub. Nocquet *et al*., 2014) show this margin segment to be weakly coupled with the exception of a highly coupled patch associated with La Plata Island.

These characteristics, together with the outer-wedge morphology and known internal structures that are described hereafter in the following paragraphs, provide this margin segment with a specific mechanical behavior, which we are going to investigate from a grid of multichannel seismic data and Vp velocity models derived from previous Wide angle seismic studies.

3.1. Morphology of the Carnegie Ridge and the trench

In our study area, the subducting southern Carnegie Ridge flank (Figure 3.1) carries seamounts of different shapes (Figure 3.2). The first group of seamounts presents seamounts with a flat topped morphology that does not exceed 0.5 km of height (Figure3.2.a). The second group of seamounts is situated few kilometers west of the southern segment of the trench (Figure 3.2.b), and is formed by: 1) two conical seamounts (about 10 km in base diameter) and an average height of 1 km; and by 2) one larger and NNW-SSE elongated seamount with a size of 35km x 12 km and a 1.2-km-average height. Both groups will enter subduction in ~210 kyr (using a convergence velocity of 47 mm/yr) and will affect the outer-wedge slope depending on their sizes.

Along the trench axis of our study zone, it is possible to identify two different trench

morphologies. North of latitude 01°30, the trench is 3.2 km-deep, and only 8 km-wide; whereas south of latitude ~1°30, the trench is broader (~30 km) and deepens southward down to 3.8 km in our study zone (Figure 3.1)

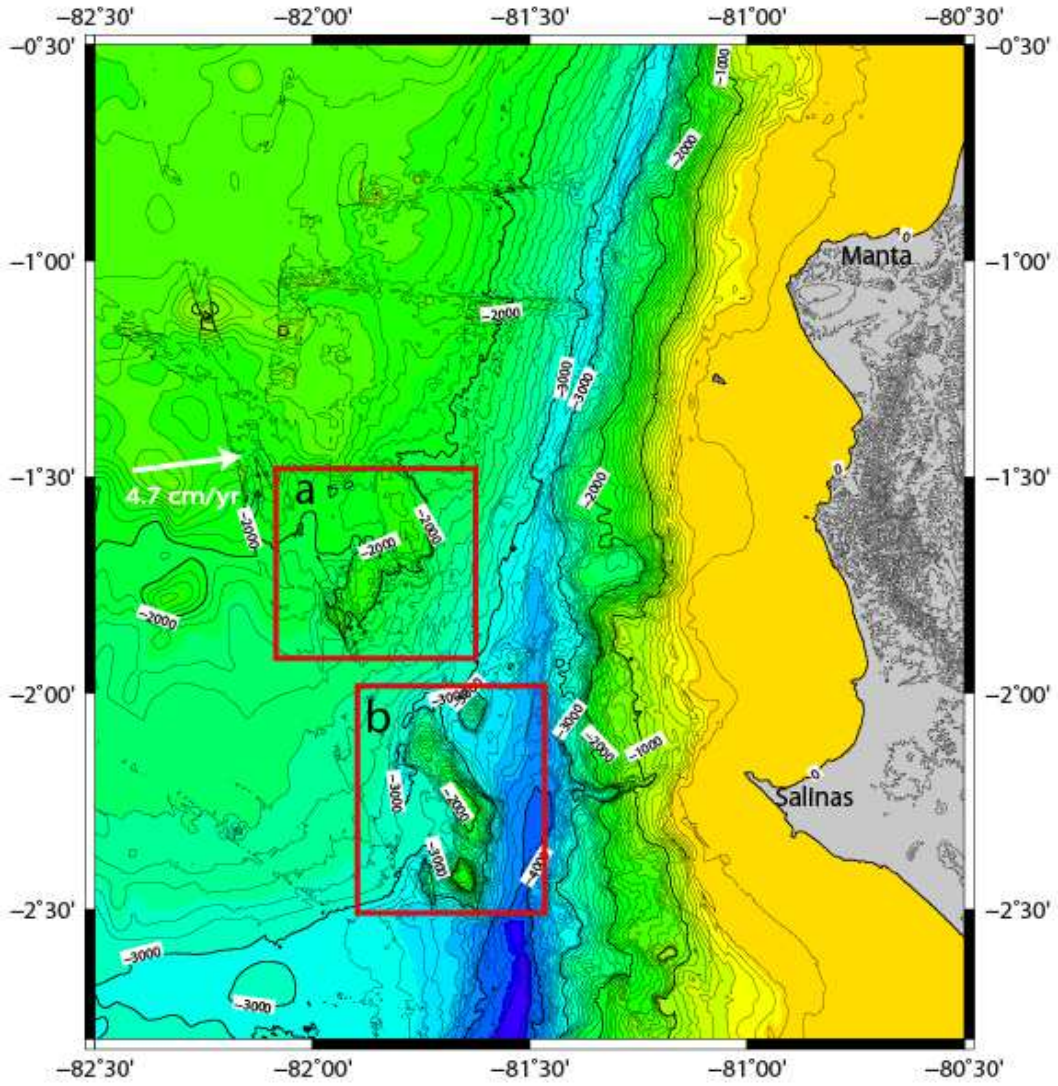

Figure 3.1 Map of the study zone between Manta and Salinas. Seafloor of the Carnegie Ridge spotted with differing-size seamounts, in special fronting the trench off-shore of Salinas; contour lines indicate the seafloor depth each 1000 meters; orange and light green: shallower depths and dark blue: deeper depths; the shore line marked with 0 m and the coast in gray; white arrow indicates the Nazca plate/NAB convergence rate (Vallée et al., 2013).

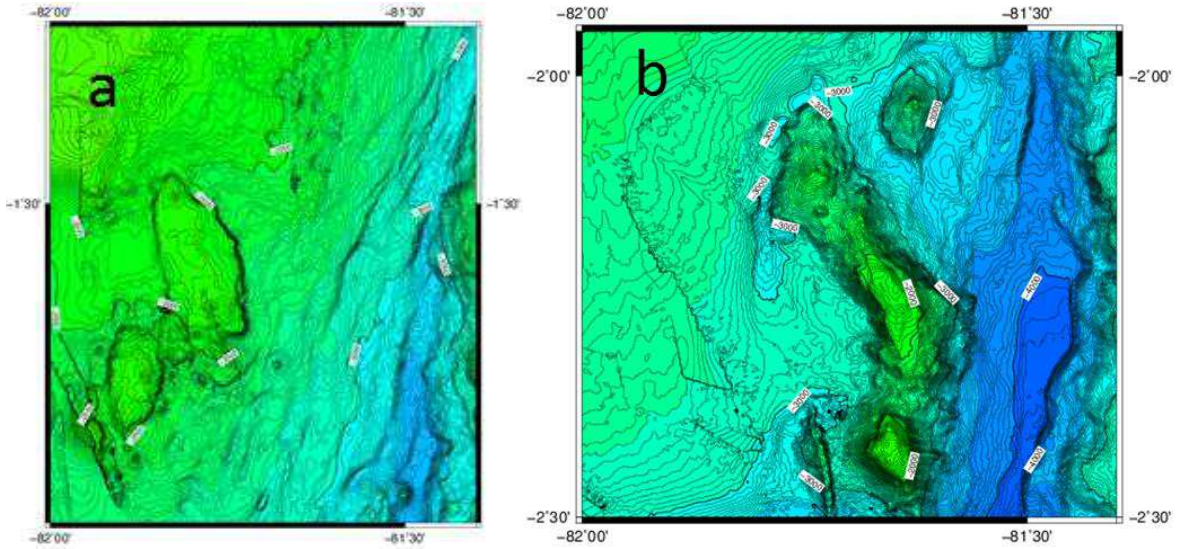

Figure 3.2 Various Seamounts morphologies on the Carnegie Ridge close to our study area; a: Seafloor of the Carnegie Ridge spotted with flat-morphology seamounts fronting the northern trench segment ; b: Segment of the Seafloor of the Carnegie Ridge spotted with Conical and elongated massive seamounts. Contour lines indicate the seafloor depth each 50 meters; light green: shallower depths and dark blue: deeper depths.

3.2. Morphologic segmentation of outer-margin wedge slope

The outer-margin wedge seafloor morphology changes dramatically at latitude ~1'30ºS and it can be divided in two segments: 1) a northern segment (north of ~1'30º) with smooth outer wedge slope; and 2) a southern segment (South of ~1'30º) with a rough outer wedge slope.

In the northern segment (Figure 3.3), the outer wedge slope dips with a ~6º average angle, and shows a remarkably smooth morphology. In this segment, the continental shelf has a width of ~40 km and it is narrowest off-shore of Manta (~20 km), and the wedge presents 3 morphologic re-entrants (E0, E1, and E2 in figure 3.3). The re-entrant E0 scallops the shelf edge, ~15 km north of La Plata Island. Re-entrant E0 is ~20-km-long and 10-km-wide and does not exceed ~500 m in depth. The ~30-km-long and 8-km-wide embayment E1 is located at depths between 2 km and 3 km, where the lower slope shows a gentle dip-angle. The third embayment E2 is located ~25 km westward of La Plata Island at a depth between 2.2 km and 3 km. It has a ~50 km-length and ~10 km width, and cuts through the southern part of E1, indicating that E2 postdates E1.

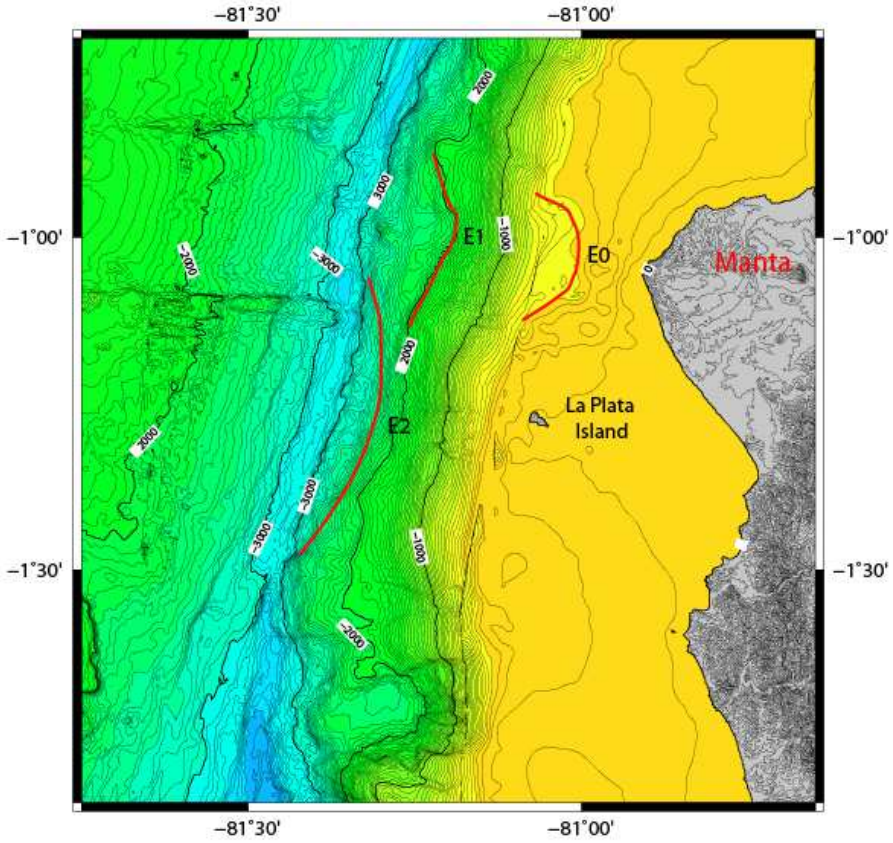

Figure 3.3 Bathymetric Map of the northern margin segment of our study area showing the generally smooth seafloor morphology (after Michaud et al., 2006); contour lines indicate the seafloor depth each 100 meters; in yellow: shallower depths and in light blue: deeper depths (3500m). Red lines mark re-entrants E0, E1, and E2.

In contrast the southern segment (Figure 3.4) shows a rough morphology characterized by large embayments (E3 and E4), a seafloor high (A), Santa Elena canyon (C1). The 15-km-wide and 30-km-long re-entrant E3 is the largest and deepest re-entrant of our study area; it has a height of ~2.5 km and reaches the continental shelf edge. This re-entrant is flat at 2000 m depth and extends for ~20 km in the dip direction; whereas E4 is a 25-km-long and 15-km-wide re-entrant with a height of ~2 km, which sharply incises the front outer wedge. A is the only high observed along the outer wedge in our study zone, and it lies immediately landward of the re-entrant E4. Off-shore Salinas, the 4-km-wide Santa Elena canyon (C1) extends from the trench at a depth of 3 km for at least 20 km.

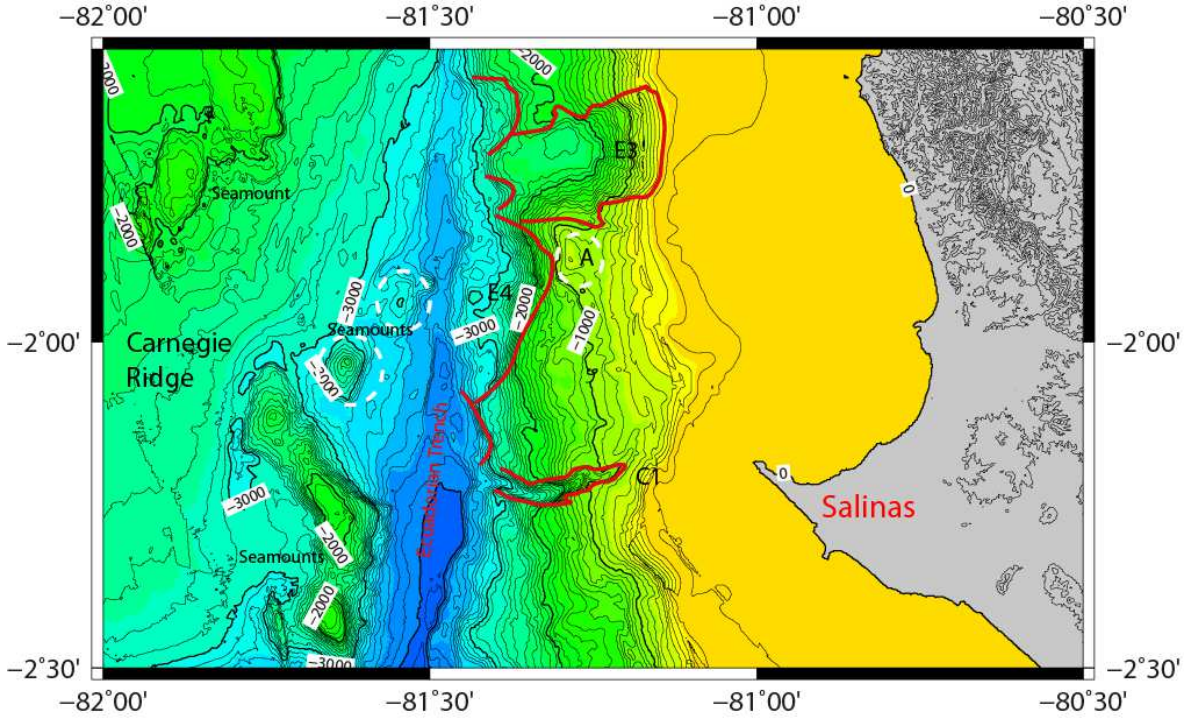

Figure 3.4 Map of the southern margin segment showing the rough morphology that characterizes this segment. E3 and E4 are re-entrants likely resulting from subducted seamounts. White-dashed circles are: seafloor margin high A, and conical seamounts spotting the Carnegie Ridge seafloor; C1 is Santa Elena submarine canyon. Contour lines indicate the seafloor depth each 100 meters; yellow: shallower depths and dark blue: deeper depths; in gray, the Coast around Salinas.

3.3. La Plata Island and its 4 marine terraces

La Plata Island is an important marker for our study because: 1) it is located only ~35 km from the trench and reveals the geologic nature of the margin basement in our study zone; and 2) its quaternary marine terraces (see section 2.1.2.2) help to better understand the uplifting history of this margin segment.

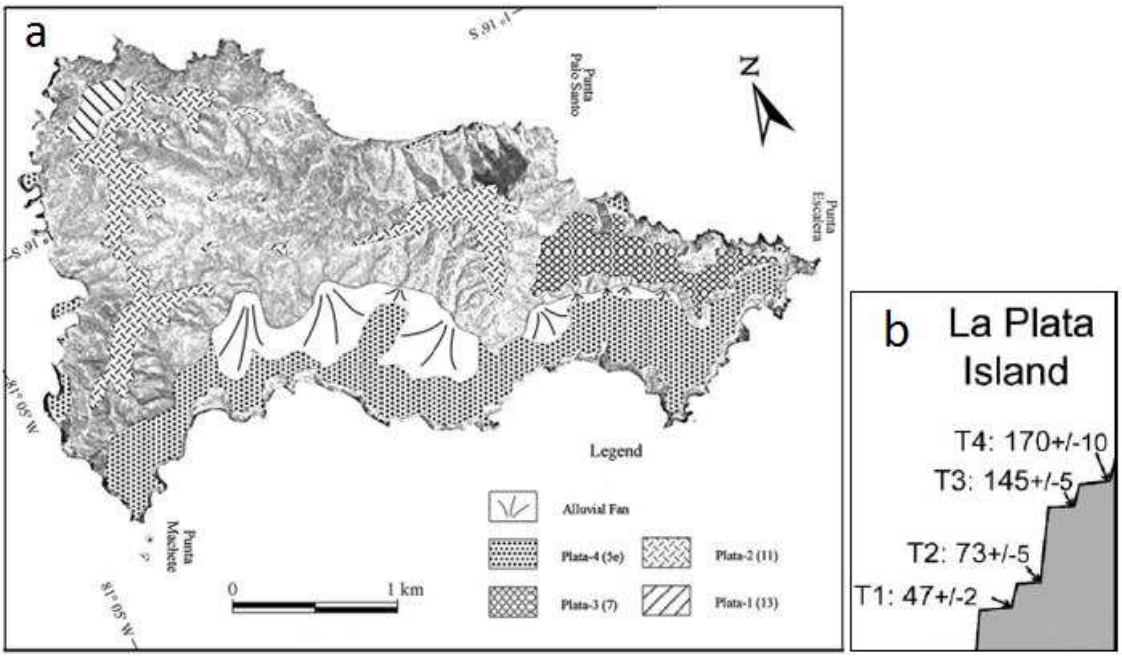

Figure 3.5 Marine Terraces of La Plata Island; a) map of La Plata Island showing the distribution of its 4 marine terraces: Plata 1-4; several alluvial fans (Cantalamessa and Di Celma, 2004); b) the heights of the marine terraces T1-T4 of La Plata Island (modified from Pedoja et al., 2006)

3.4. Inter-Seismic Coupling

According to Chlieh *et al.* (submitted), a highly heterogeneous pattern of inter-seismic coupling was modeled from GPS data along the upper (shallow 30 km depth) plate interface between the Nazca Plate and the North Andean Block (NAB). As indicated in Figure2.17, from Bahia de Caraquez to Cap Manglares the interplate is coupled down to 25-30 km whereas in our study zone (Figure 3.6 from Chlieh *et al.* submitted) from northern Manta to the south of Salinas, the inter-seismic coupling is very weak (ISC <0.2) from 10-15 km down dip, and bounded to the North by a 50-km wide creeping corridor, which presumably acted as a barrier for the large 1906 and 1942 seismic ruptures.

In the La Plata Island region, GPS inversion demonstrates the presence of a highly-coupled patch (ISC >0.9) beneath and seaward of the island i.e. beneath the outer margin wedge, indicating that the interplate fault is locally fully locked up to very close to the trench axis. Immediately south of the highly locked zone and down to the region offshore Salinas, the shallow interplate fault is poorly coupled (SC 0.2-0.3), whereas its deeper section deeper than 10-12 km is nearly free sliding.

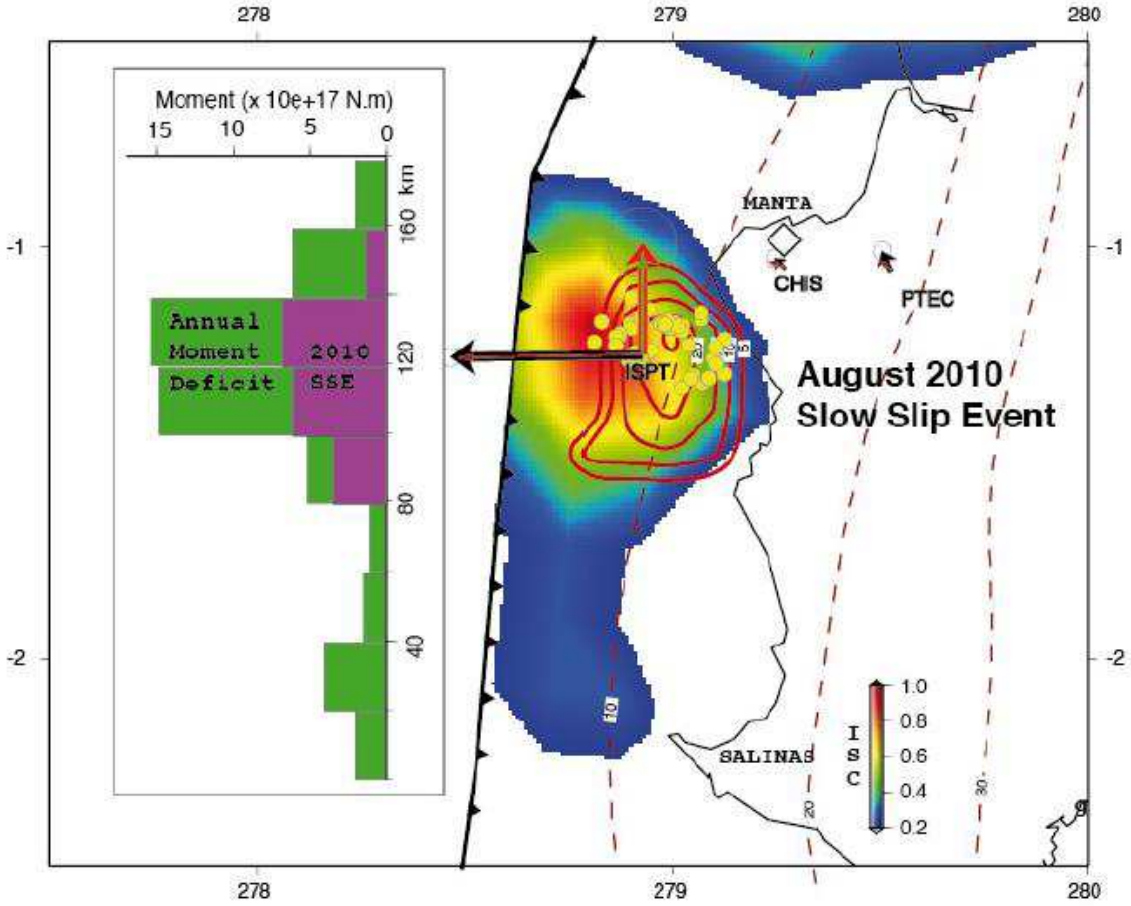

Figure 3.6 The La Plata Island locked patch and the August 2010 slow slip event (SSE). Distribution of the inter-seismic coupling along the Ecuadorian subduction zone between Salinas and Manta (study zone) derived from the inversion of the inter-seismic GPS velocities (Chlieh et al., submitted 2014). The yellow-red areas indicate the highly coupled zone (up to 90% nW of ISPT) whereas green-blue areas represent poorly coupled to creeping regions of the megathrust. The 2 cm seaward horizontal vector (thick black) and 1 cm vertical vector (thick red) are GPS motions that occurred during that SSE and synthetics are the overlapping thin arrows. The SSE distribution (red contours, each 5-mm) overlaps very well the 3D relocation of the micro-seismicity (yellow dots) reported by Vallée *et al*. (2013). The SSE overlaps also the La Plata asperity and its down-dip coupled-uncoupled transition zone.

3.5. Seismicity

Font *et al*. (2013) show that the seismicity (Figure 3.7) from 0.75°S to 1.5°S (northern segment of our study zone) and over the 1994-2007 time period is mainly organized in earthquake swarms over time (Figure 3.8) such as in 1998, 2002, and 2005 (Segovia, 2009; Vaca *et al.,* 2009); whereas the southern segment between 1.5°S and 2.5°S is rather aseismic over the same time period. However, a poorly documented earthquake with a potential Mw=7.2 occurred in this region in 1901

(Askew *and* Algermissen, 1985; Engdahl *and* Villasenor, 2002) and 13 others occurred (EHB catalog, from 1960 to 2008) beneath the southern margin segment (see Figure 1 in Vallée *et al.,* 2013). Font *et al*., (2013), found that the micro-seismicity close to La Plata Island extends parallel to the trench covering an area of 80 km long and 30 km wide, and that the hypocenters are distributed from the interplate contact up to the surface. They consider that the focal mechanism of the largest earthquakes of the 1998 and 2005 swarms present thrust motion, suggesting that the past swarms occurred on or close to the subduction interplate contact.

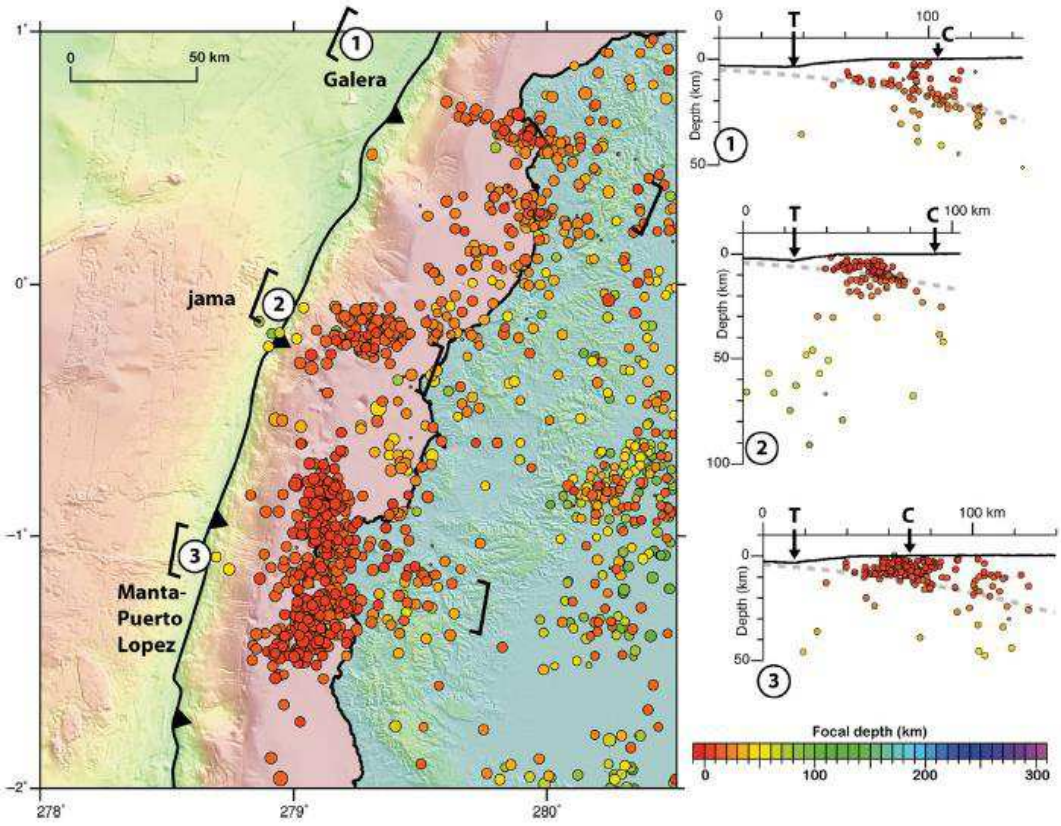

Figure 3.7 Map of Seismicity of the Ecuador Margin using the RENSIG catalog (1994-2007); left: earthquake hypocenters with focal depth according to color; right: three cross-sections in the vicinity of the interplate seismogenic zone, results from the 3-D approach and P-wave arrivals. Sections 1, 2, and 3 refer to the Galera, Jama and Manta clusters, respectively. The sections are marked by the brackets on the map (Font *et al.,* 2013).

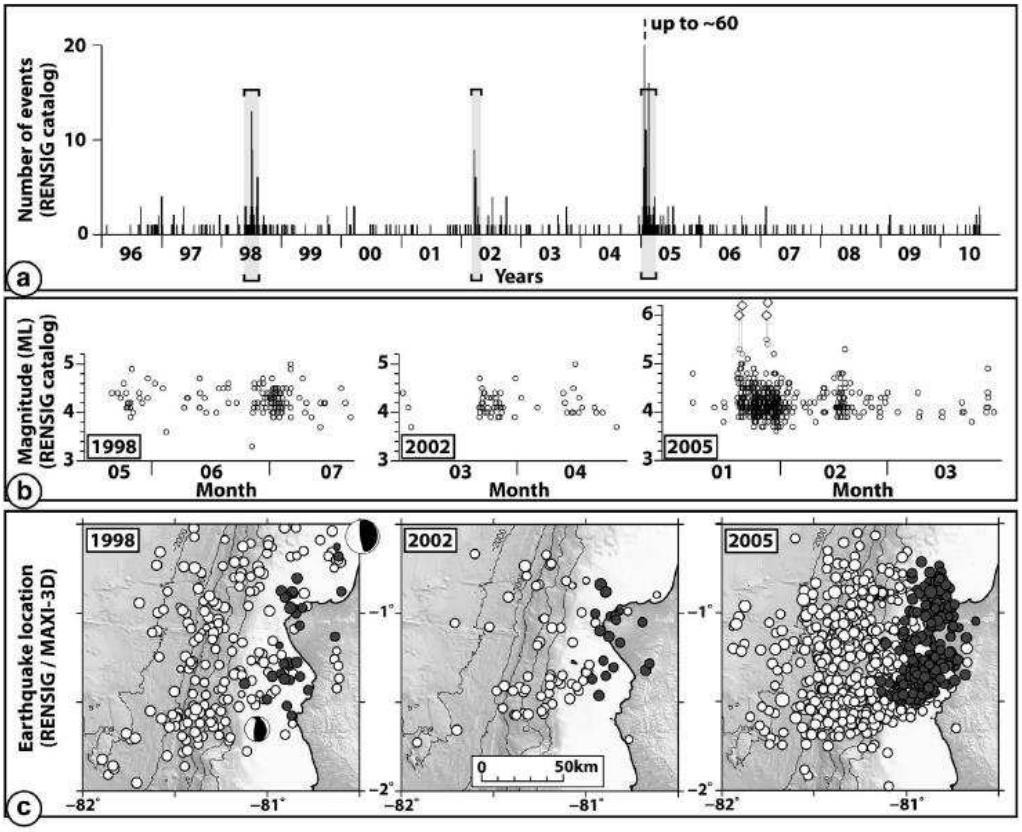

Figure 3.8 Earthquake occurrence characteristics in the La Plata – Manta region (from Vallée *et al*., 2013); a) Histogram of earthquake occurrence (RENSIG catalog) from 1996 to 2010 (bin is 1 day). b) Earthquake magnitude versus time for the 3 main periods of activity. ML is represented by circles (from RENSIG) and Mw by diamonds (Vaca *et al*., 2009). c) Epicentral locations (RENSIG) of earthquakes presented in b) are shown by white circles. Relocations in a 3D model (MAXI-3D catalog; Theunissen *et al*., 2012; Font *et al*., 2013) are shown by grey circles. Focal mechanisms of earthquakes with magnitude above ~5.5 are from Global CMT (Ekström *et al.,* 2012).

3.6. Slow Event close to La Plata Island

Besides of the swarms observed in the regions of La Plata Island, Vallée *et al*. (2013) documented a week-long slow slip event (SSE, Figure 3.9) with an equivalent Mw of 6.0–6.3, which occurred in August 2010 below La Plata Island at an inferred depth of about 10 km. The SSE occurred within the down-dip part of the shallow (<15 km) isolated, highly-coupled patch along interplate contact, and had a maximum slip of 10 to ~40 cm. The slow slip sequence was accompanied by a sharp increase in local seismicity with more than 650 earthquakes (50 events with Mw between 1.8 and 4.1). The observations indicate that the stress increment induced by the episodic aseismic slip may lead to both sudden seismic moment release and to progressive rupture within small locked patches.

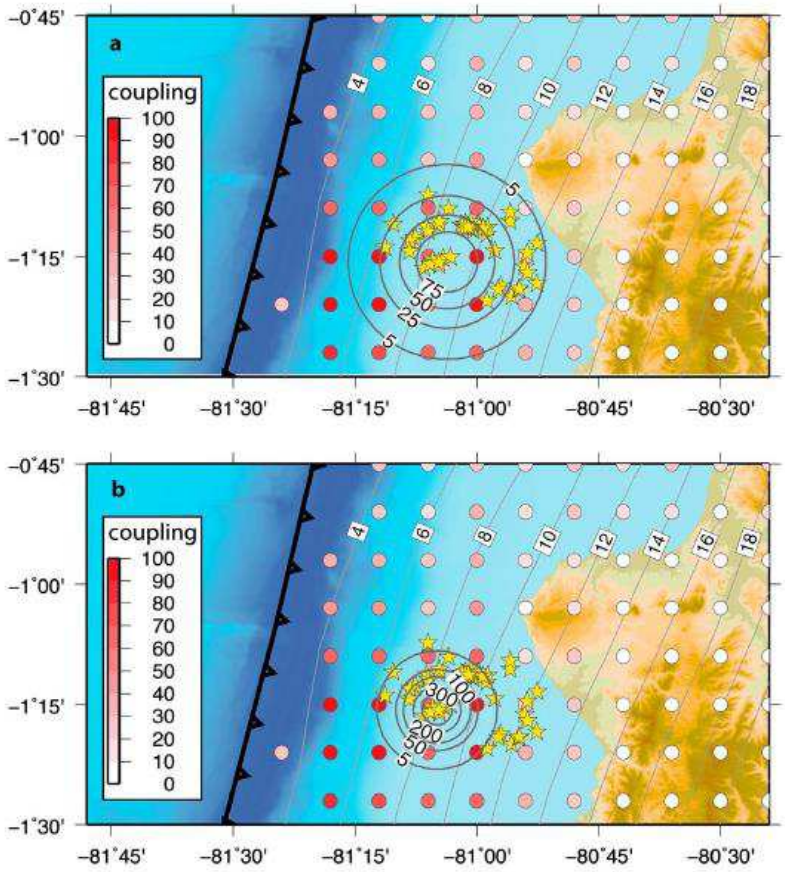

Figure 3.9 Map view of the slow slip models from Vallée et al., (2013), with the observed seismicity during the slow slip event; epicenters (yellow stars), isovalues of slip in mm (numbers along the concentric circles), iso-depth of the interplate surface (Graindorge et al., 2004; Font et al., 2013) and coupling spatial distribution. Map "a" corresponds to the upper bound of the slow slip spatial extension with a maximum slip of 10 cm, all the seismicity is located inside the slow slip area. Map "b" corresponds to the lower bound of the slow slip area with a maximum slip of ~40 cm, only the easternmost events are located outside the slow slip area.

3.7. Crustal structures of the central Ecuadorian margin from published SISTEUR data.

Deep penetration multichannel seismic reflection (MCS) and wide-angle seismic (WA) data have been collected across the Ecuador-Colombia margin during the SISTEUR cruise (Collot *et al.*, 2002). Among this data set, MCS profiles SIS12 and SIS64 (Figure 3.10) were processed to PSDM to reveal the overall structure of a narrow segment of the central Ecuador margin (Sage *et al*., 2006). Moreover, wide-angle seismic data collected along OBS lines SIS 01, 02 and 04, which

are coincident with MCS lines SIS09, SIS07 and SIS05 (Figure 3.10) have allowed to construct Vp velocity models of the central Ecuador margin (Graindorge *et al.,* 2004; Gailler, 2005; Gailler *et al.,* 2007). Down below, we summarize the results of the MCS SIS12 and SIS64 profiles.

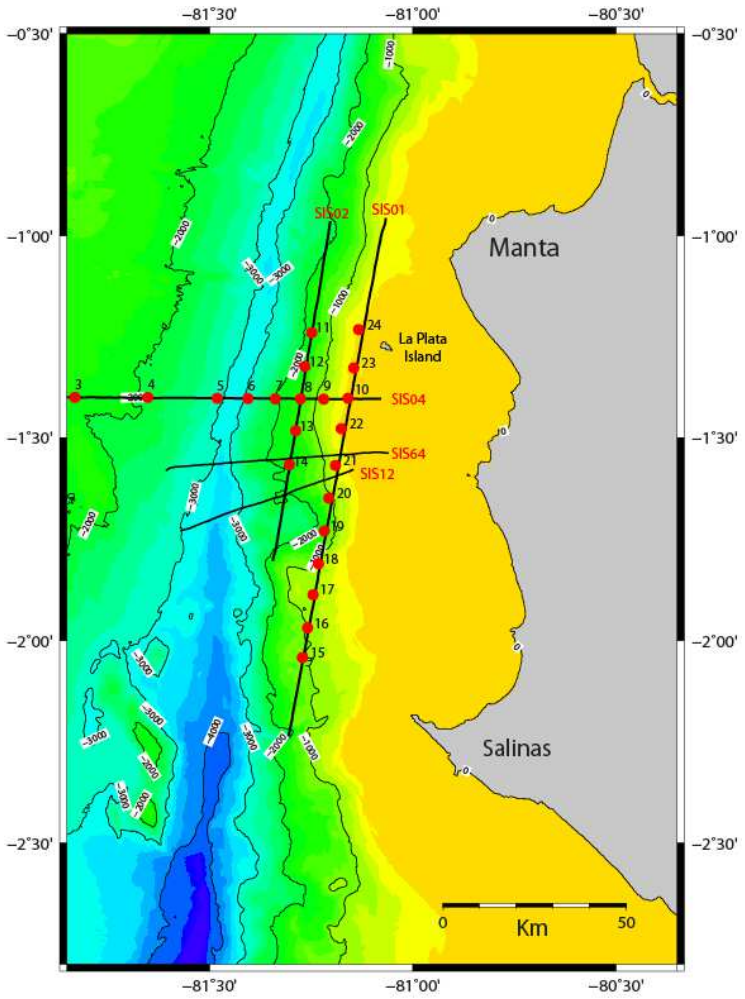

Figure 3.10 Map showing the Ecuadorian bathymetry, the SISTEUR MCS profiles (black lines) and OBS position (red points) of the SISTEUR cruise.

3.7.1. Profiles SIS12 and SIS64

Sage *et al*., (2006) established several structural characteristics of the central Ecuadorian margin using profiles SIS12 and SIS64 (Figure 3.10): 1) the margin basement thins rapidly trenchward, and this thinning is associated with seaward-dipping normal faults (SIS64, Figure 3.11) caused by basal erosion and margin collapse; 2) near the margin front, time-variable interplate mechanical coupling leads to the superposition of compressional and extensional faults systems; this temporal superposition constitutes an efficient long-term erosional process for basement apex

breakup, and subducting seamounts (SIS12, Figure 3.12) reinforces it locally; 3) enhanced seismic reflectivity at the base of the upper plate suggests damaged basement rocks caused by over-pressured fluids delivered from the subduction channel; 4) a 600-m-thick lens of 2.2-2.5 km/s low-velocity subducting sediments (with respect to 3.8-4.2 km/s velocity of the overlying basement) implies an interplate patchiness, suggesting strong variations in mechanical coupling across the plate boundary.

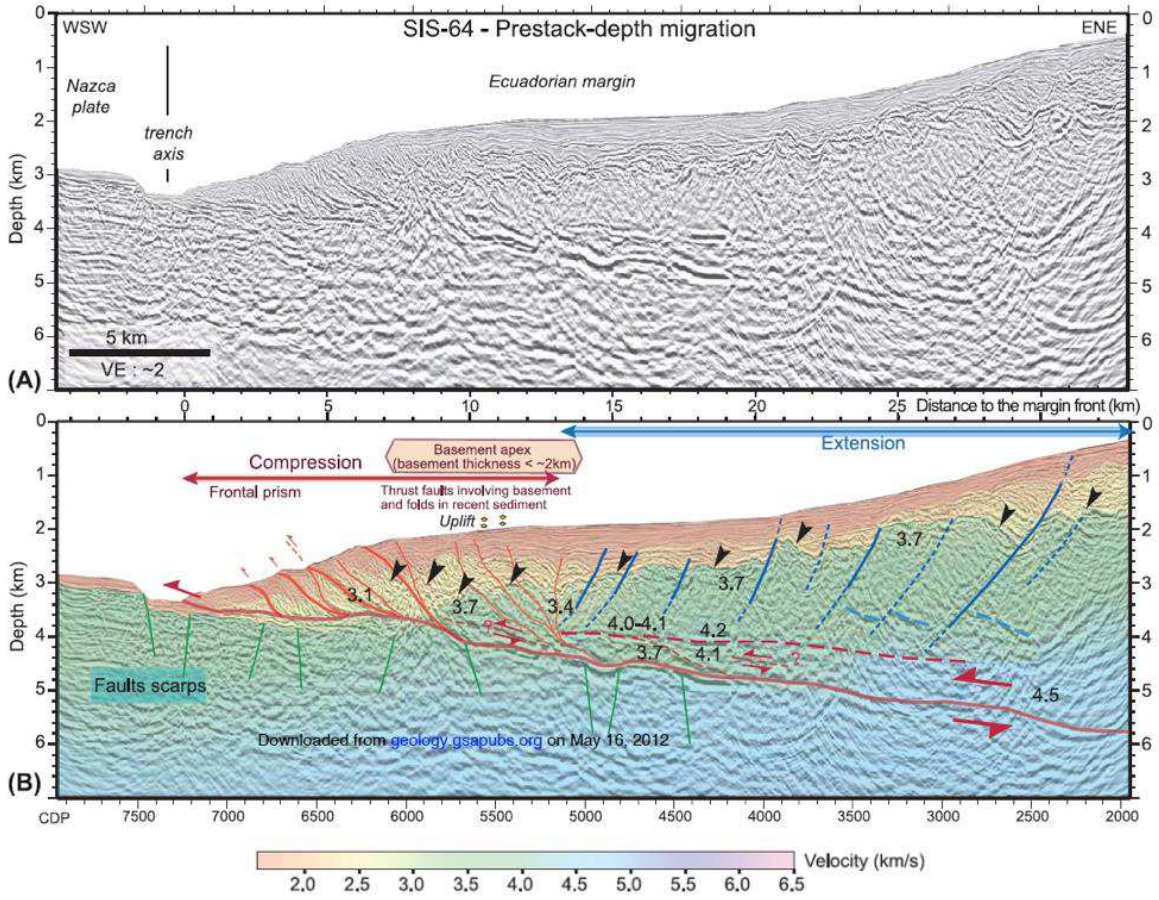

Figure 3.11 Up) Pre-stack depth-migration image of profile SIS64; down) Interpreted PSDM profile SIS64; red dashed line represent the top of the highly-reflective layer; blue lines: normal faults in the upper plate; red lines: thrust faults and plate interface; green lines: normal faulting in the under-riding plate; numbers indicate the p-wave velocity in km/s; the compressional and extensional zones are identified using the type faulting observed in the zone (Sage et al., 2006).

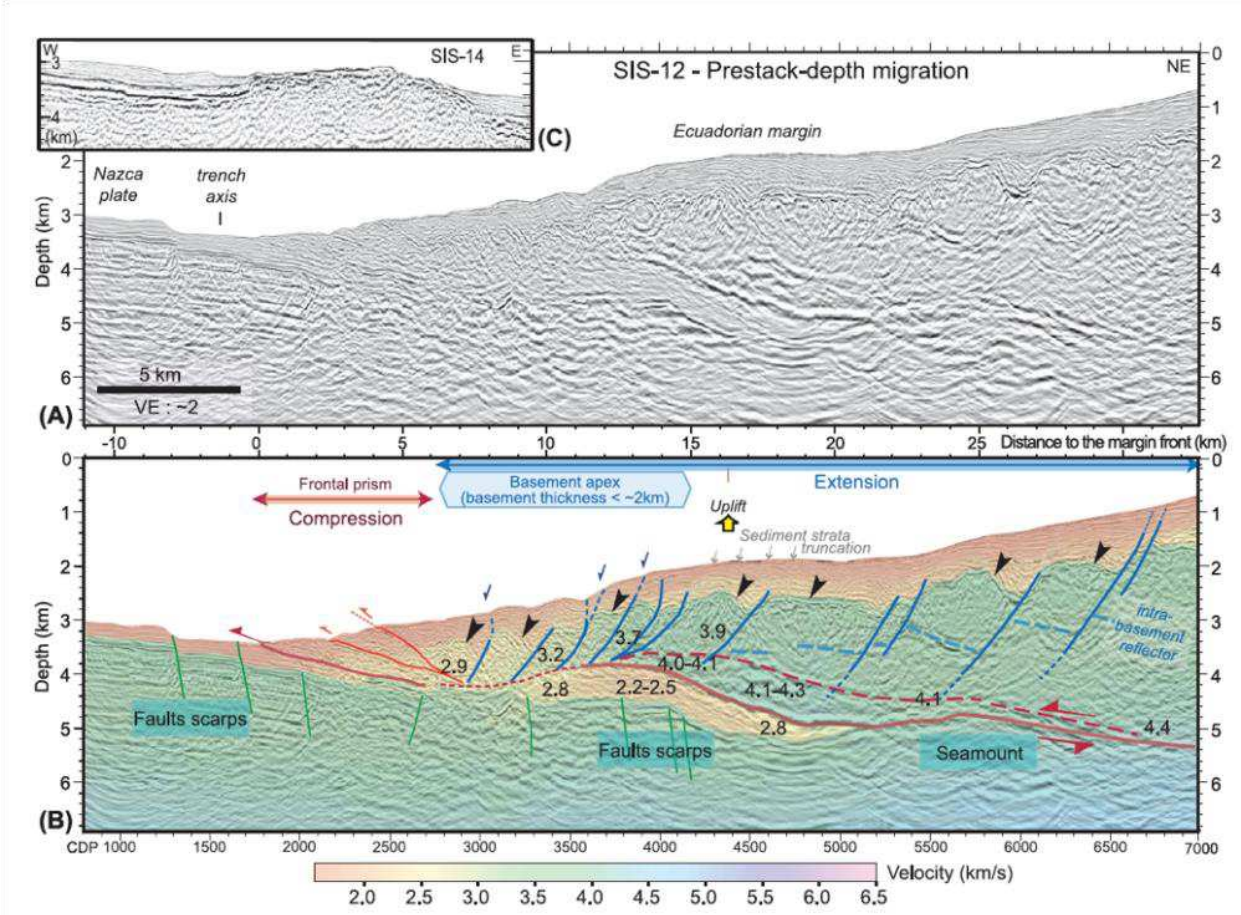

Figure 3.12 Up) Pre-stack depth-migration image of profile SIS12; down) interpretation of PSDM of profile SIS12, black arrows represent the top of the high-velocity margin basement; blue lines: normal faults in the upper plate; red lines: thrust faults and plate interface; green lines: normal faulting in the under-riding plate; numbers indicate the p-wave velocity in km /s; the compressional and extensional zones are identified using the type faulting observed in the zone (Sage et al., 2006).

3.7.2. Wide-angle profiles SIS01, SIS02, and SIS04

3.7.2.1. WA Velocity model (uncertainty, shadow zone)

Graindorge *et al*. (2004) and Gailler (2005) employed wide angle-seismic data from SISTEUR cruise (2000) to obtain velocity models of profiles SIS01, SIS02 and SIS04 (coincident with MCS profiles SIS09, SIS07 and SIS05, respectively). Along profile SIS04, Graindorge *et al*. (2004) used 9 OBS and two land stations to build a velocity model using an automated forward modeling approach (Zelt *and* Smith, 1992) (Figure 3.18); whereas for profiles SIS01 and SIS04, Gailler (2005) obtained velocity models using the first-arrival traveltime tomographic inversion (Korenaga et al. 2000). According to Gailler (2005), the central part of the velocity models of profiles SIS01

and SIS02 corresponds to the region with the highest density of ray tracing (Figure 3.13, and 3.14) with low uncertainties values in order of 0.1-0.15 km/, which depends on the geometry of the acquisition. The lack of ray tracing at the extremities and deep part of the models produce higher uncertainties (0.15-0.20 km/s). The velocity zones that lies beneath the OBS until depths 20 km are well constrained; whereas the extremities and parts deeper than 20 km in depths of the model keep a strong dependence of the initial velocity model, and are not representative of real structures.

It must be considered that this tomography does not allow to access to the detailed structure of the margin, because it only uses the first arrival times of refracted waves and is affected by the footprint of initial velocity model.

Graindorge *et al.,* (2004) and Gailler (2005) identified shadow zones in the OBS seismic records from SISTEUR (2000) (Figures 3.15 to3.17). Graindorge *et al.,* (2004) modeled the shadow zones observed in the OBS section (SIS4-OBS04, Figure 3.17) as a low velocity zone consisting of a thin layer of underthrust sediments and the 3-km-thick Carnegie Ridge (CR) layer 2, whose velocity (5.1 km/s) is slower than that of the margin wedge (layer C, 6.1 km/s to 6.4 km/s).

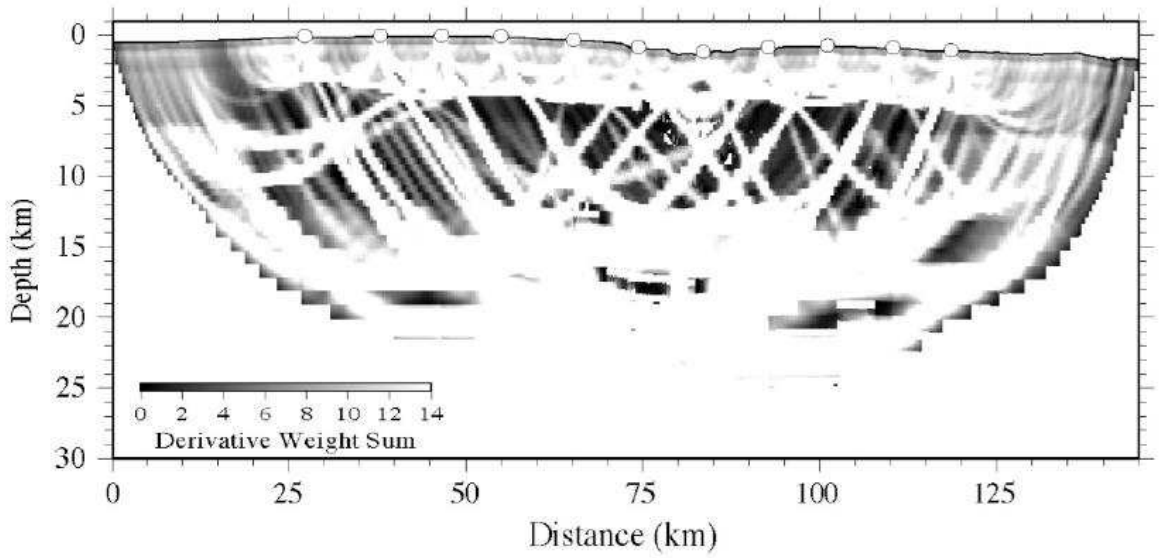

Figure 3.13 Ray tracing for the final velocity model of SIS01; white zones are well controlled and black zone are expected to be less controlled; the white circles represent the OBS (Gailler, 2005).

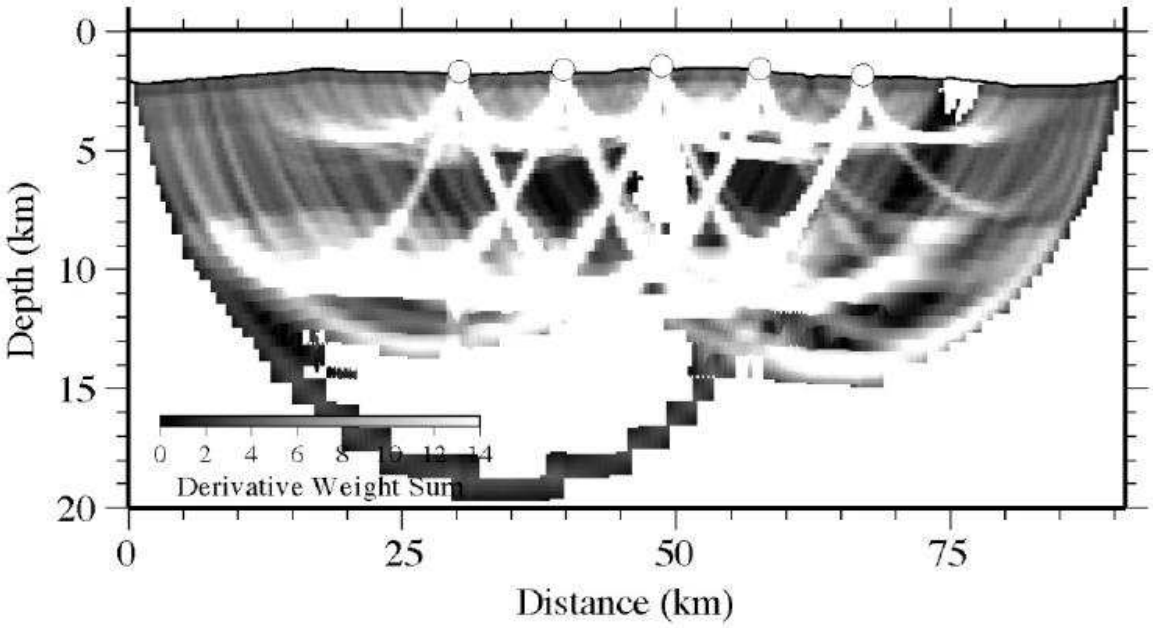

Figure 3.14 Ray tracing for the final velocity model of SIS02; white zones are well controlled and black zone are expected to be less controlled; the white circles represent the OBS (Gailler, 2005).

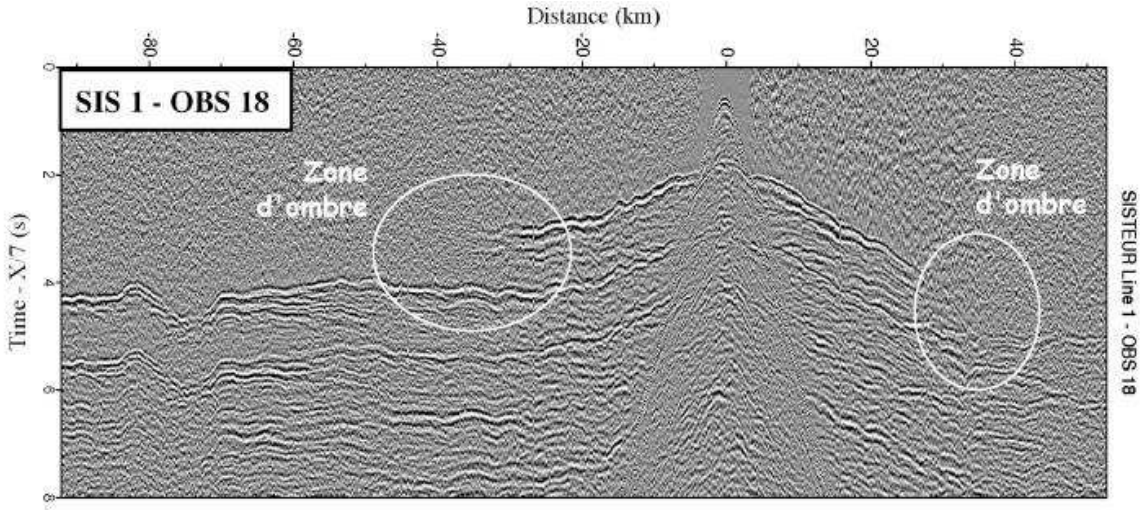

Figure 3.15 Section of the OBS 18 of profile SIS01. The figure show two dark zones (Gailler, 2005)

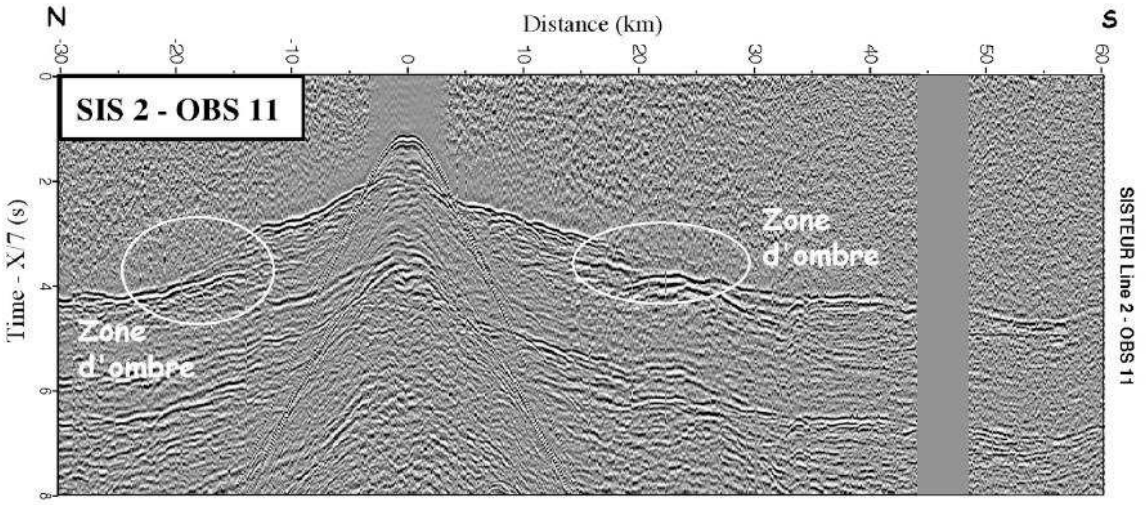

Figure 3. 16 Section of the OBS 11 of profile SIS02 location in Figure 3.10; the figure show two dark zones (Gailler, 2005)

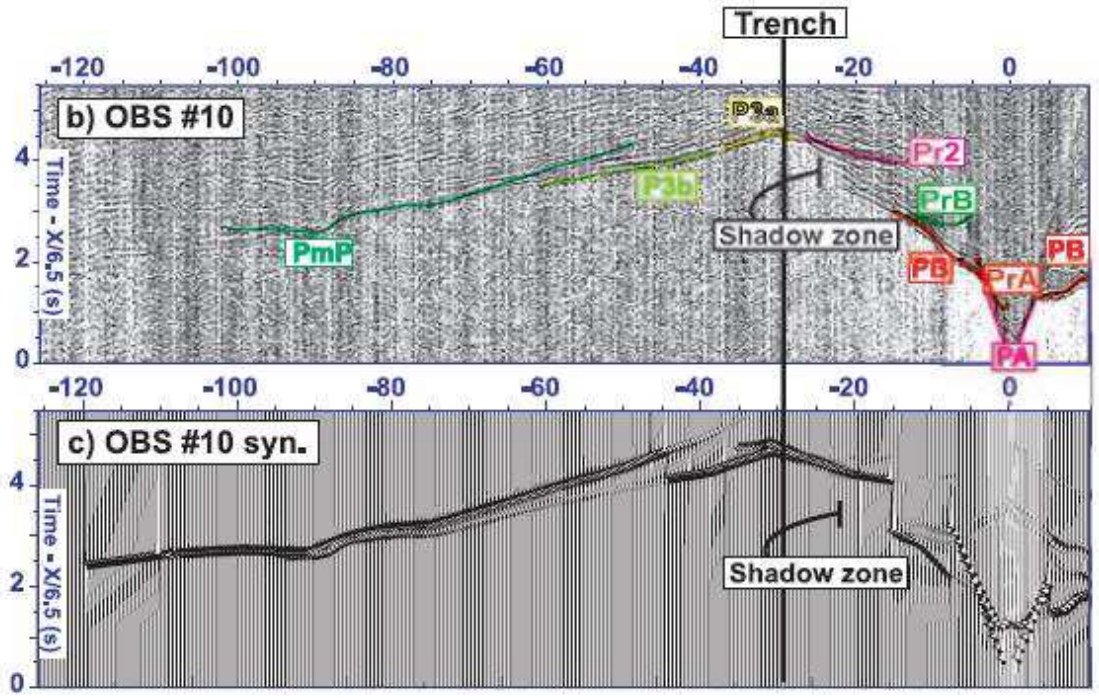

Figure 3.17 Wide-angle seismic record sections SIS04-OBS 10 (b) the different phases observed are labeled: 1) PmP reflection from oceanic Moho, 2) P3a and P3b, waves refracted within oceanic layer 3. 3). Reflected phases are designated by Pr2 from the base of layers 2. For OBS and land stations located on the upper plate, seismic records show additional phases at short offset: 1) PA refracted phase within shallow margin sediments 2) PB phase corresponding to turning rays within a second crustal layer with higher seismic velocity (B). Reflected phases from the base of layers A and B have also been observed and modeled (PrA and PrB). Records from seismometers located on the margin show a shadow zone which increases landward from 0.3 s to 1.1 s. (c) For comparison a synthetic seismogram of seismic section recorded by OBS 10 is calculated from the final crustal model with comparable plotting parameters.

3.7.2.2. Profile SIS04

Based on the velocity model of Profile SIS04, Graindorge *et al.,* (2004) interpreted three layers A, B, and C for the **margin rocks** (Figure 3.18): **layer A** shows velocities that range from 1.9 to 2.2 km/s, and a thickness of 0.8 km suggesting sediment rocks. In contrast, **layer B** shows higher velocities that range between 3.8 km/s and 5.1 km/s. Layer B would be the upper section of the Piñón Formation, which is interpreted as Upper Cretaceous volcano-clastics (Baldock, 1983) known onshore on the La Plata Island (Jaillard *et al.,* 1997). The deeper **layer C** shows velocities ranging from 6.1 km/s to 6.4 km/s; they are interpreted as the deeper section of the magmatic Piñón formation. Graindorge *et al.,* (2004) further proposed three layers (layer 1, 2, and 3; see chapter 2.1.2) for the subducting Carnegie Ridge oceanic crust with a local maximum thickness of 14 km.

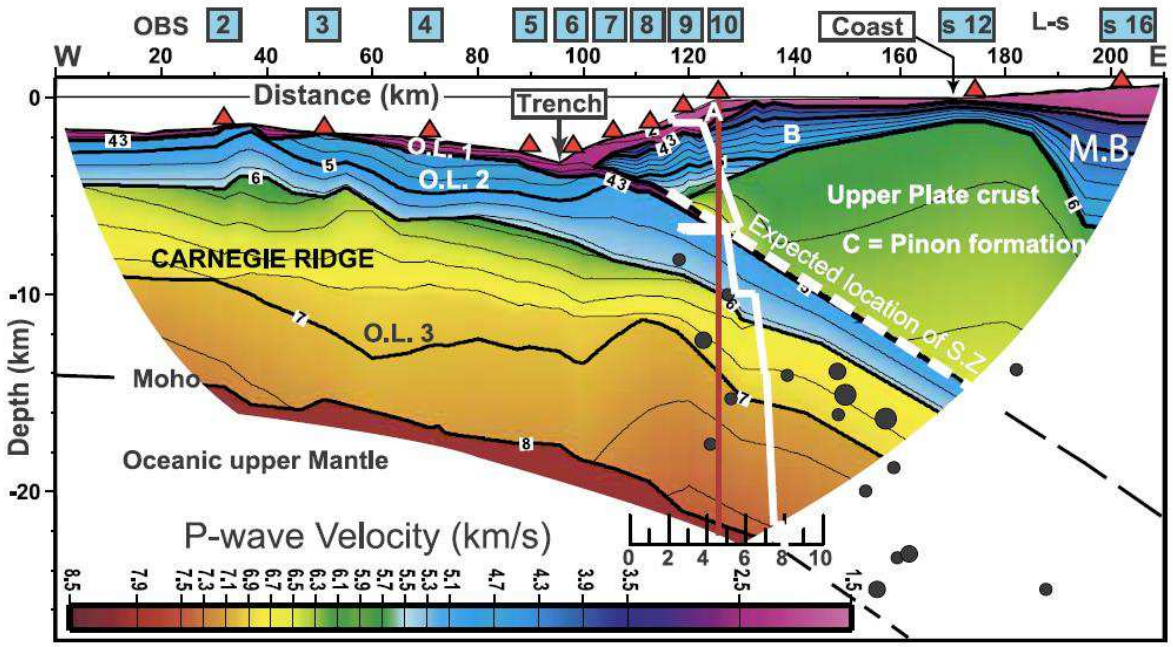

Figure 3.18 Velocity model for SIS04 (MCS profile SIS05); M.B: Manabi Basin, S.Z.: subduction zone, O.L.: oceanic layers, L-s: land stations, black circles indicate position of earthquakes from Engdhal's catalogues; red triangles represent the OBS and two land stations (Graindorge et al.*, 2004). OL2 is the cause for the Low Velocity Zone beneath layer C of the margin basement.*

3.7.2.3. Profile SIS01

Gailler (2005) identified **a high velocity Body (HVB)** along profile SIS01 between km 25 and

km 115 (Figure 3.19) that has P-wave velocities locally higher than 5.5 km/s attributed to the Piñón formation. This HVB overlies **a low velocity zone (LVZ)** with velocities that range from 5.0 km/s to ~5.5 km/s (P-wave velocity inversion zone) that Gailler attributed partially to the **footprint of subduction channel**. The extremities of the model are not well controlled by the OBS. The LVZ observed at the south of the HVB could be related to the slight obliquity of profiles SIS01 that samples lower velocities along its shallower southwestern part than along its deeper northeastern section. According to Gailler (2005), the low velocities at the north of the HVB could have a tectonic origin.

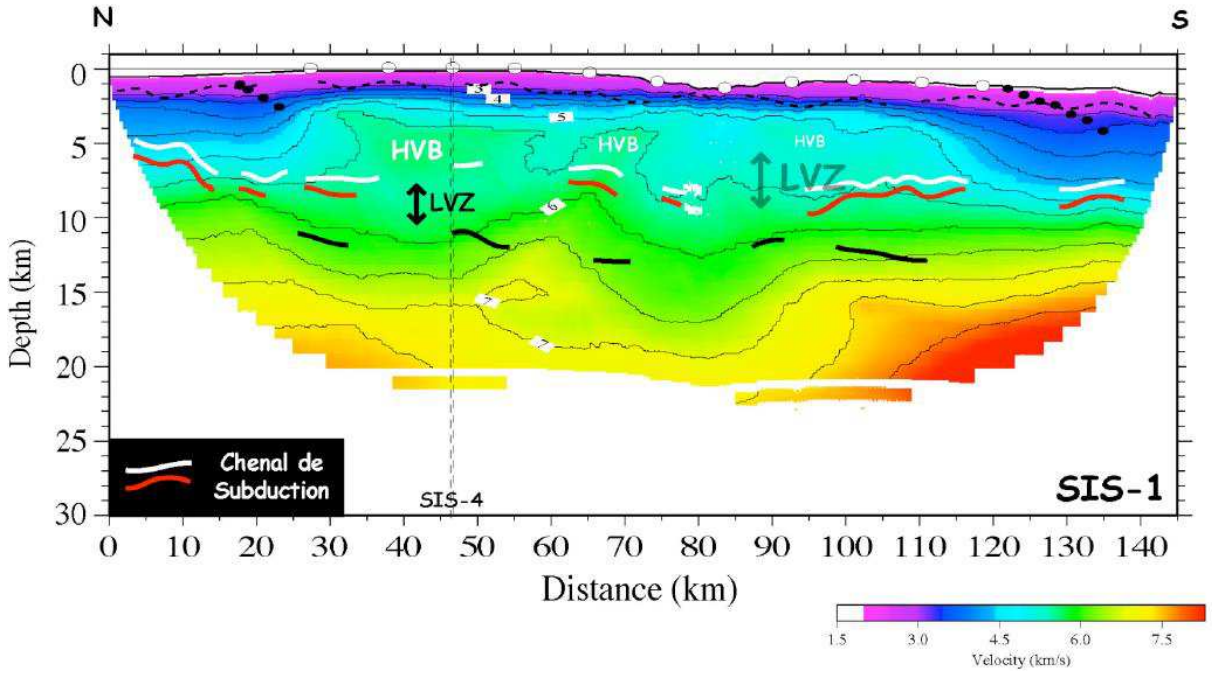

Figure 3.19 Velocity model from the tomographic inversion of profile SIS01, located 30 km landward from the trench (Gailler, 2005); this line cuts across the shelf edge in its middle part and shows progressively outer-wedge velocity structures towards both line extremities according to Fig 3.10. LVZ: low velocity zone; HVB: high velocity body; white line is the top of subduction channel (SC), and the red line is the bottom of the SC; white circles represent the OBS position; black lines represent the layered seismic facies in the downgoing oceanic crust.

3.7.2.4. Profile SIS02

The Profile SIS02 cuts through the margin tip ~17km from the trench (Figure 3.20). According to Gailler (2005), the overriding plate corresponds to a very shallow part of the SIS02 velocity

model with a ~3 km thickness. Gailler (2005) considers that the HVB presents in profile SIS01 is absent in profile SIS02, which in turn shows a margin tip with relative homogeneous velocities (~4.5-5.0 km/s). Gailler further considers that the interplate contact is marked by a velocity inversion zone (LVZ) (~ -0.4 km/s) that she correlates with the subduction channel (SC) and the top of the oceanic crust (TOC); the identification of the top and base of the SC was obtained from the interpretation of the coincident MCS profile SIS07. Gailler (2005) found that beneath the velocity inversion zone, the upper part of the under-riding plate shows a vertical velocity gradient of ~0.65 km/s for values from 5.2 km/s to 6.5 km/s at depths of 6 km and 8 km, respectively.

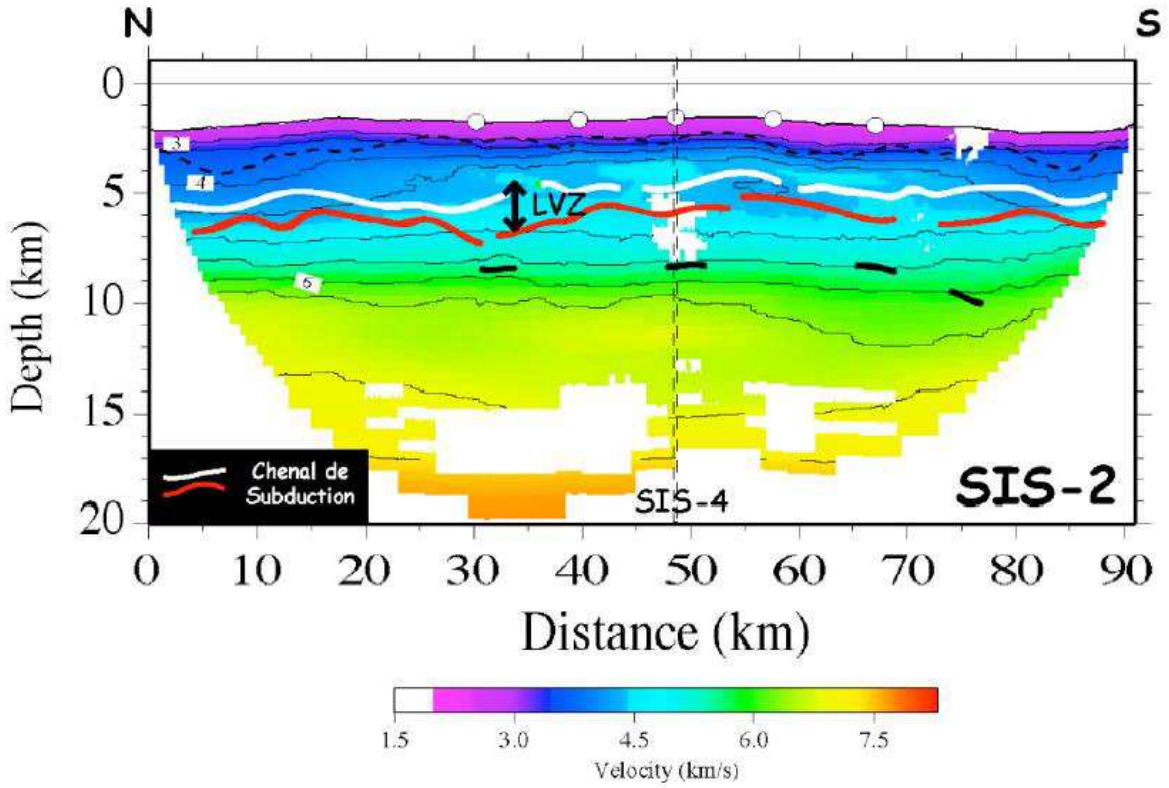

Figure 3.20 Velocity model obtained from the tomographic inversion of SIS01, located 17 km from the trench axis (Gailler, 2005). LVZ: low velocity zone; white line is the top of subduction channel (SC), and the red line is the bottom of the SC; white circles represent the OBS position; black lines represent the layered seismic facies in the downgoing oceanic crust.

CHAPTER 4

SEISMIC PROCESSING IN TIME DOMAIN

4. SEISMIC PROCESSING GENERALITIES

4.1. Introduction

Today, 3-D seismic and 2-D sections are routinely used for exploration purposes in offshore environments because the data can now be acquired quickly. New processing techniques and improved visualization tools add clarity to the data, helping to provide a realistic view of the subsurface (Yilmaz, 2001). From the seismic records, it is therefore possible to estimate the speed of propagation of waves in complex media (Figure 4.1) and deduce information on other physical properties such as structural geometry, porosity, or density (*e.g.*, Collot *et al.,* 2004; Bang *et al*., 1996, Sallares *and* Ranero, 2005). Multichannel seismic reflection (MCS) and wide-angle seismic data are commonly used to study the active margin structures, including accretionary wedges (Westbrook, 1988), backstop structures (Christeson *et al*., 2003), splay faults that branch on the interplate fault (Park *et al.,* 2002; Nakanishi *et al.,* 2008), and the subduction channel (Calahorrano *et al*.,2008).

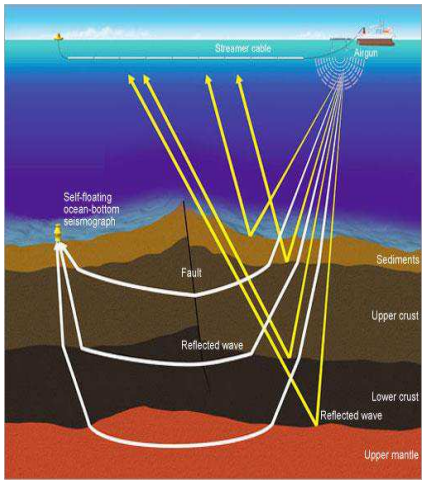

Figure 4. 1 Seismic reflection profiler measures the vertical layers beneath the seafloor. Sound waves from a surface-towed transducer are received by a separate hydrophone array after they bounce off different rock or sediment boundaries; white lines are the wide angle seismic waves recorded by the OBS, and yellow lines (reflection seismic) are recorded by the streamer (Japan Agency for Marine-Earth Science and Technology).

The seismic acquisition is based on the emission, the propagation and reception of waves, and

they use: a seismic source (Figure 4. 2) that produces seismic waves; a propagation medium, normally unknown; and receivers that will record the arrival times. In marine seismic, the receivers are hydrophones, which are sensitive to pressure variations in water.

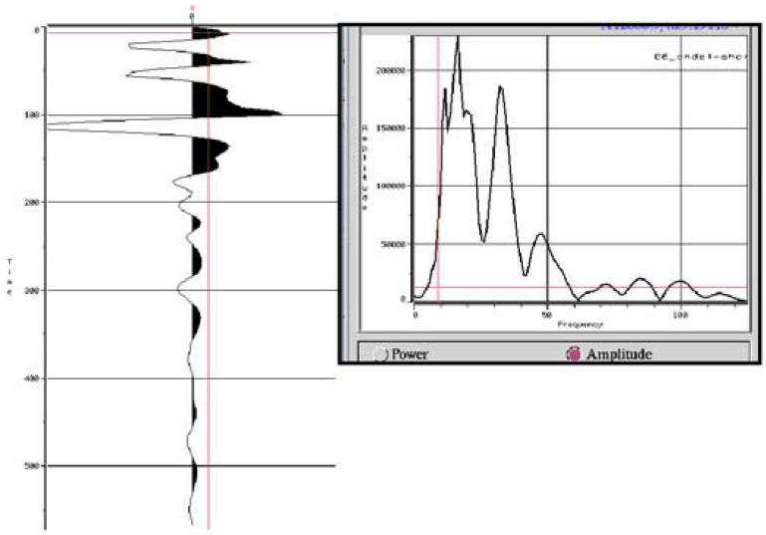

Figure 4. 2 Example of a seismic source; SISTEUR seismic source modeled by IFREMER-GENAVIR from the signal (left) registered, and the signal spectrum of the source (right) (Calahorrano, 2005).

4.2. Seismic Methods

4.2.1. Seismic Reflection, Multichannel seismic data (MCS)

In seismic reflection (Figure 4.1), a recorded seismic trace contains the reflection of different underground interfaces and noise. In order to obtain several reflected traces in a same point (mirror point), a multiple coverture device (streamer with several active traces) is employed (Figure 4.3). The seismic source selection will constrain the resolution and the signal penetration (see section 4.4 below); thus, the source must be selected according to the survey. One important point in seismic reflection is that the distance source-receiver remains constant during the acquisition.

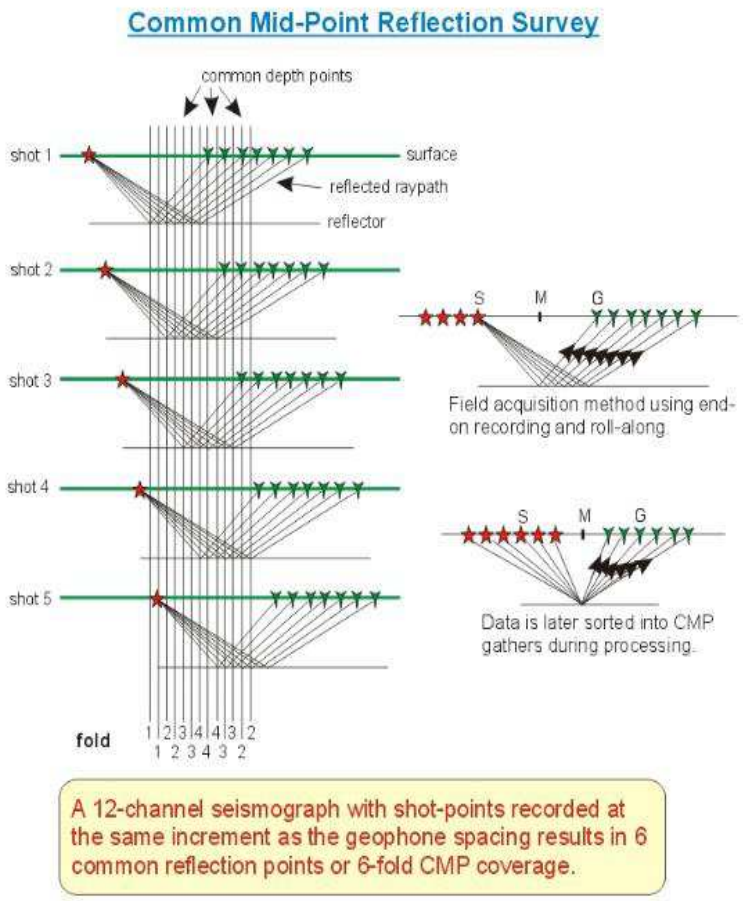

Figure 4. 3 Principle of acquisition of marine seismic reflection data using multiple coverage from shot 1 to shot 5. CMP gathers are the most common technique used in seismic processing, by setting a large number of geophones over a line (streamer) (from Geoscience Survey Ltd).

4.2.2. Seismic Refraction

Seismic refraction is a technique more used to image deep structure (Figure 4.4). In contrast to seismic reflection, the wave are recorded by fixed reflectors (OBS, oceanic bottom seismometers, Figure 4.5) deployed on the seafloor, where the distance source-receiver varies along the profile. The acquisition geometry permits to obtain distance source-receiver greater than that of seismic reflection. Besides, it permits to record deep waves both refracted and reflected.

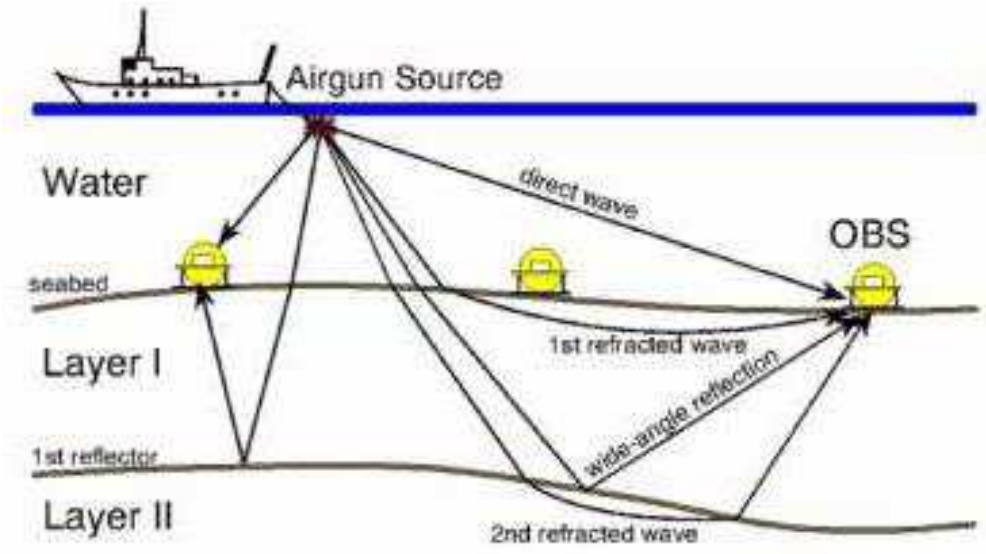

Figure 4. 4 Principle of measure in seismic refraction. (www.geopro.com); the wave travels from the air-gun source through the water and layer I and II until arrive to the OBS; the direct wave is also registered by the OBS.

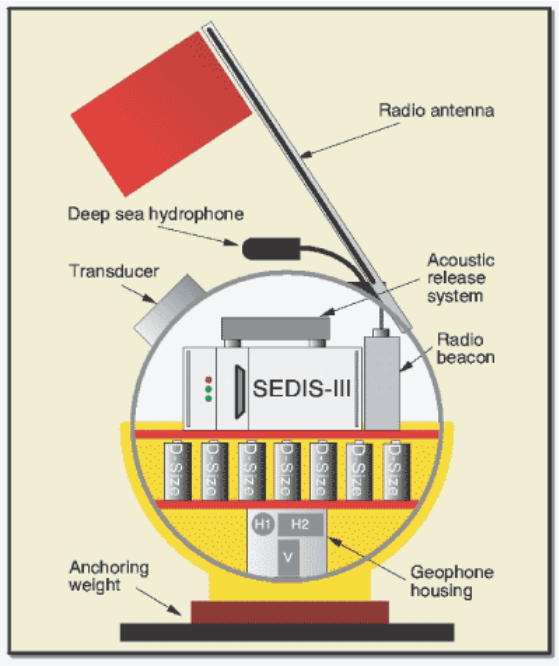

Figure 4. 5 Ocean bottom seismographs (OBS). GeoPro GmbH Hamburg (GeoPro) (www.geowarn.ethz.ch).

4.3. Standard Processing Sequence of Seismic Reflection data in time domain

Conventional processing of reflection seismic data (Yilmaz, 2001) yields an earth image represented by a seismic section (Figure 4.6) that can be displayed in time or in depth.

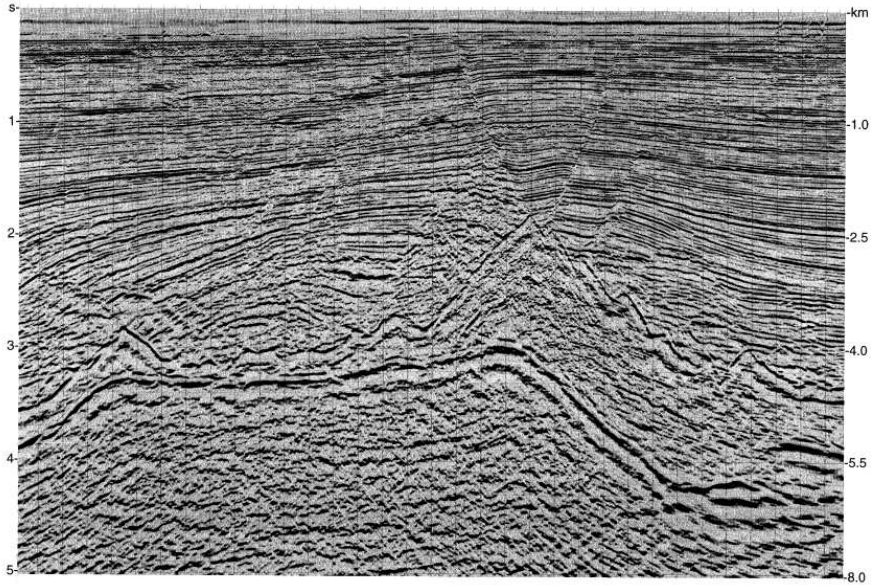

Figure 4. 6 Example of a seismic section from the Gulf of Mexico (Yilmaz, 2001), with a length of around 40 km and 5 seconds along the vertical axis.

An important goal in seismic data processing is to improve the low signal-to-noise quality typical of seismic data. In acquisition, this is the primary motivation in deploying as many receivers per shot as feasible and collecting data that are redundant to some degree. Common-mid-point (CMP) recording is the most widely used seismic data acquisition technique (Yilmaz, 2001). By means of this, redundancy is provided, improving the signal quality. Seismic data processing strategies and results are strongly affected by field acquisition parameters and surface conditions (especially in land). Seismic data recorded in digital form by each channel of the recording instrumental are represented by a time series, on which Fourier transform are applied (Yilmaz, 2001).

Seismic Processing requires an orderly approach to convert raw field data into meaningful information about the subsurface geology. The major steps are presented in Figure 4.7, where the three main processes in seismic processing are: deconvolution, CMP stacking, and migration (Yilmaz, 2001).

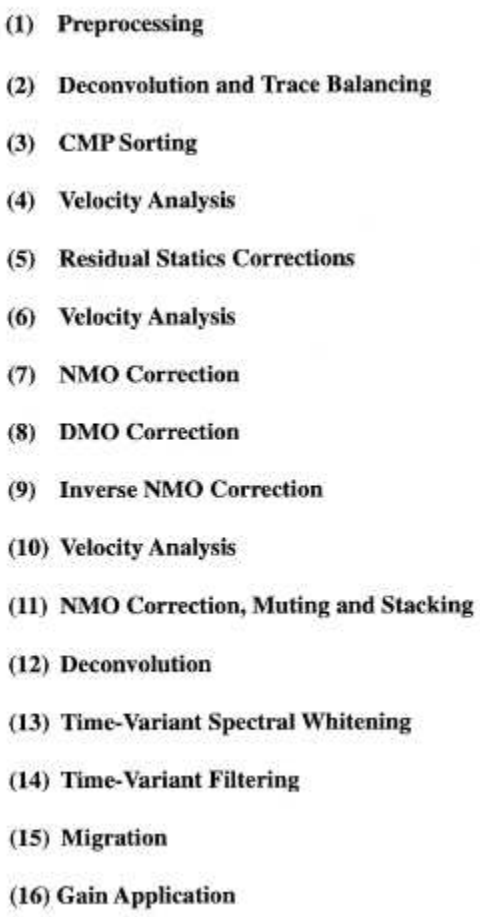

Figure 4. 7 Example of a processing flowchart; it shows the main steps employed to obtain a seismic image (Yilmaz, 2001).

4.3.1. Data initialization

In order to process old field data, which is recorded in multiplexed form (*i.e.*, order by sample time), is necessary to put the data in trace or channel order by using a process called de-multiplexing (Gadallah *and* Fisher, 2009); modern data are normally in de-multiplexed form.

In traditional processing sequence (Yilmaz, 2001), a collection of seismic traces which share some common geometric attribute (*i.e.*, gathers) are sorted from field records to examine the dependence of amplitude, signal/noise, move-out, frequency content, phase, and other seismic attributes, on offset, incidence angle, azimuth, and other geometric attributes that are important for data processing and imaging. Shot gathers (Figure 4.8) are sequentially recorded from the sensors for a single shot experiment.

Normally, the measurement for one source at one receiver location is called a trace, which is a time series of reflections; and the offset is defined as the distance from source to receiver. Data are stored in the recording instrument and then put onto a magnetic tape, record by record. If it has several traces reflected in one point, these tracks can be added; the signals, which arrive in phase one each other, can be added up constructively, while the noise, distributed randomly on the track, tends to vanish. The number of traces recorded for each reflection mirror point is called coverage. To have multiple traces reflected in a mirror point. In the multiple coverage, the streamer (data acquisition device) is used to improve the low signal-to-noise quality typical of seismic data (Yilmaz, 2001). Besides for every shot, the seismic streamer is shifted a whole number of mirror-points, so each mirror point is recorded by several successive shots. In CMP processing, seismic traces are grouped into CMP gathers on the basis of shared source-receiver midpoint bins; CMP velocity functions are interpolated throughout a survey area to construct a velocity model of the subsurface. This velocity model is used to perform normal move-out (NMO) corrections throughout the survey (Yilmaz, 2001).

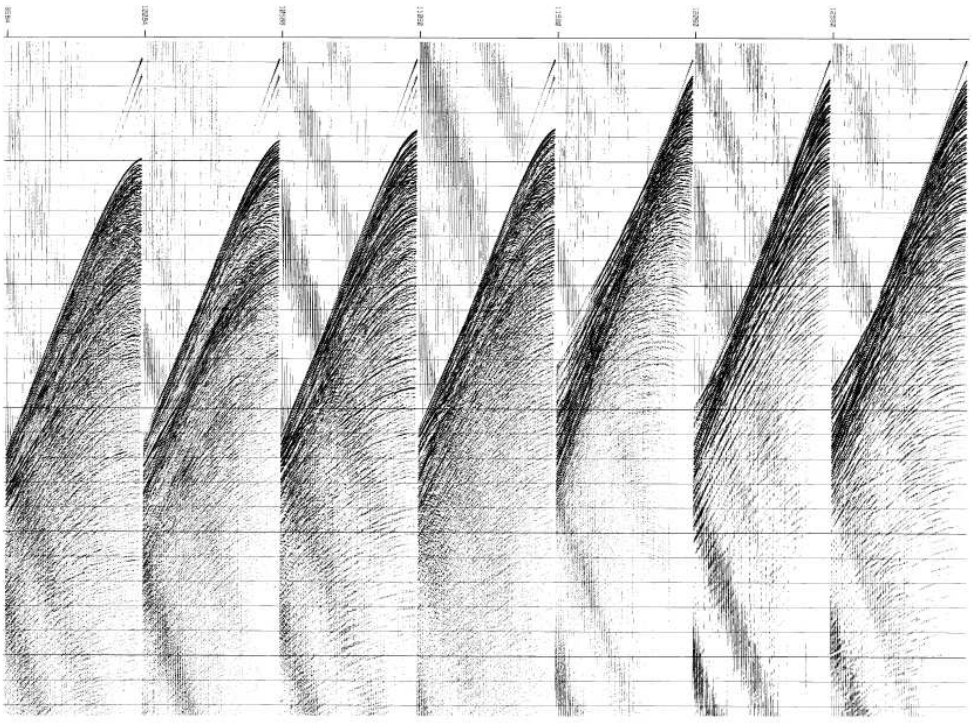

Figure 4. 8 Common-shot gather after extracting the data (Yilmaz, 2001).

4.3.2. Normal Move-Out

Normal Move-Out (NMO) is a non-linear stretching of the seismic time axis to remove the travel time component due to source-receiver offset and it is effectuated using a primary velocity function (Yilmaz, 2001). This correction is applied to each trace in a gather so that the reflection travel times on all traces approximate that of a trace with zero source-receiver offset. The relationship between arrival time and offset is hyperbolic and is the principal criterion used to decide whether an event is a reflection or not (Yilmaz, 2001). NMO correction can be used as a seismic processing tool to powerfully distinguish between reflections and other events such as refractions, diffractions and multiples.

If an accurate NMO correction has been applied, reflections will appear as straight horizontal lines (Figure 4.9), refractions will now appear as inverse curves and diffraction and multiple arrivals will retain some curvature.

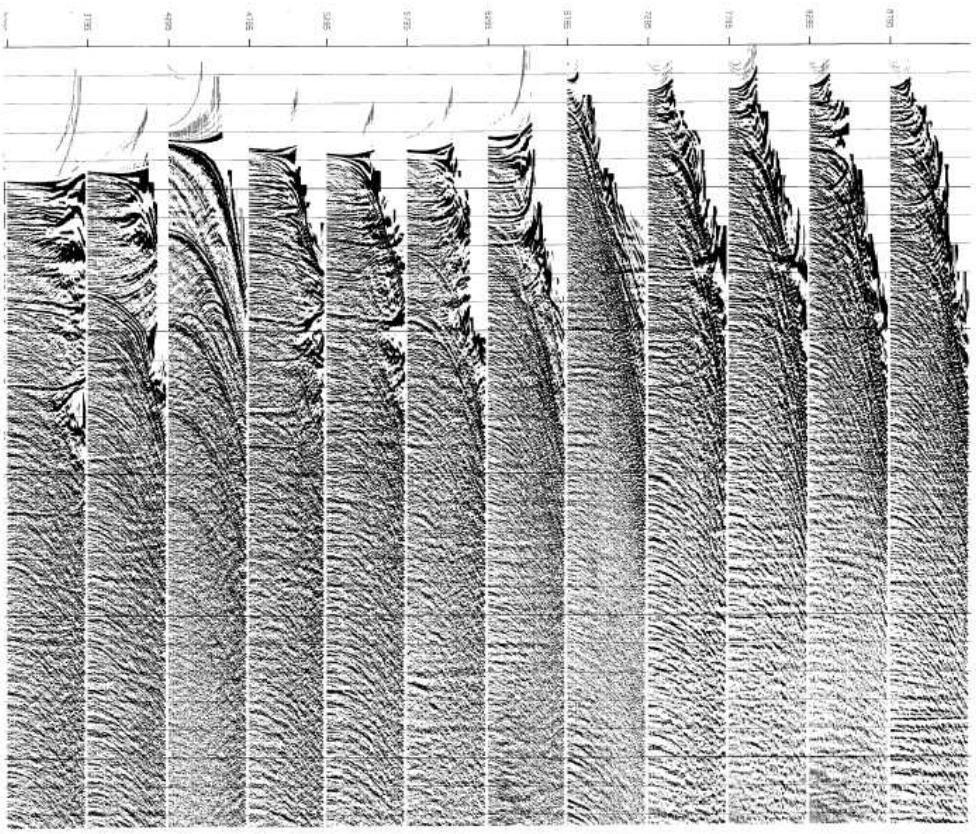

Figure 4. 9 Common-shot gather after applying NMO correction; refractions appear as inverse curves and diffraction and multiple arrivals retain some curvature (Yilmaz, 2001).

4.3.3. Migration methods

According to Gadallah *and* Fisher, (2009), there are two general approaches to migration: post-stack and pre-stack. Post-stack migration (PSM) is acceptable when the stacked data has zero-offset. If there are conflicting dips with varying velocities or a large lateral velocity gradient, a pre-stack partial migration is used to resolve these conflicting dips. The Post-stack Migration uses only two basis approaches: the hyperbolic summation and downward continuation; whereas Kirchhoff algorithm uses the hyperbolic summation and the finite difference, and Stoltand Gazdag's Phase Shift algorithms use downward continuation approach.

Kirchhoff Migration (Diffraction migration) is a statistical approach technique, based on the observation that the zero-offset section consists of a single diffraction hyperbola that migrates to a single point Migration involves summation of amplitudes along a hyperbolic path (Gadallah *and* Fisher, 2009).

F-K Domain Migration uses Stolt and Phase-Shift migrations, whose Phase shift migration is considered to be the most accurate method of migration but is also the most expensive (Galladah *and* Fisher, 2009). F-K migration is a deterministic approach via the wave equation instead of using the finite difference approximation using mainly the 2-D Fourier transform. A 2-D Fourier transform over time and space is called an F-K (or K-F) transform where F is the frequency (Fourier transform over time) and K refers to wave-number (Fourier transform over space). The space dimension is controlled by the trace spacing and (just like when sampling a time series) must be sampled according to the Nyquist criterion to avoid spatial aliasing. In the F-K domain there is two-dimensional amplitude and phase spectrum but usually only the former is displayed for clarity with color intensity used to show the amplitudes of the data at different frequency and wave-number components. Several noise types such as ground roll or seismic interference may be more readily separated in the FK amplitude domain than the time-space domain and therefore will be easier to mute before the inverse transform is applied.

4.3.4. Filtering

On the other hand, at various stages of treatment, filters are applied filters (in frequency and in the field FK) to eliminate or reduce noise.

4.3.4.1. Band-pass filtering

Filtering is designed to pass signal and reject noise (Figure 4.10). A filter scan is generated from the data in which many different narrow, band-pass filters are applied and the results displayed for analysis (Gadallah *and* Fisher, 2009). The important part is to let pass the frequency containing the coherent energy (reflections) and to reject the noise included in the some frequencies.

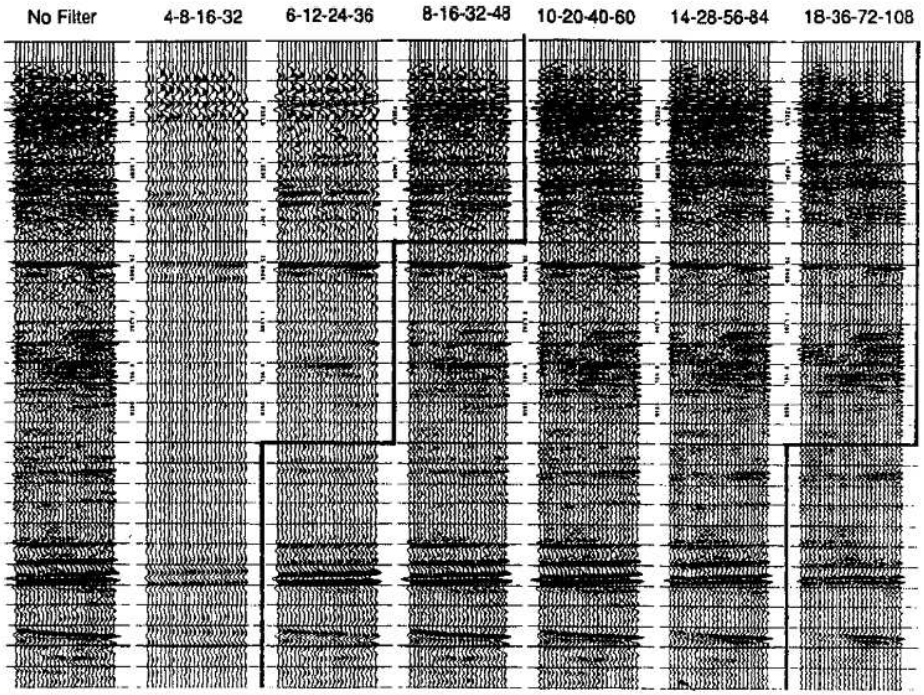

Figure 4. 10 Example of filter test to design time-variant filters (Galladah and Fisher, 2009). Here, the signal (at the left) has been filtered with different band-pass filters to choose the best filter.

4.3.4.2. F-K filter

In the case of a frequency-wave (F-K) filter applied to data, internally the f-k filter converts the data to the F-K domain. The data is converted from time and space (T-X) sampled traces to the F-K domain by a two-dimensional Fourier Transform. Once the data is filtered, this is converted back to the T-X domain by the inverse Fourier.

4.3.5. Deconvolution (Pre-Stack)

Typically, pre-stack Deconvolution (Figure 4.11) is aimed at improving temporal resolution by compressing the effective source wavelet contained in the seismic trace to a spike (Yilmaz, 2001),

which is called spiking deconvolution. Deconvolution is applied before stack and seeks to eliminate the source wavelet to obtain a stronger signal pulse and therefore a better vertical resolution, and sometimes to remove the effects of multiples (Figure 3.12). Deconvolution usually is applied to pre-stack data trace by trace; however, it is not uncommon to design a single deconvolution operator and apply it to all the traces on a shot record (Yilmaz, 2001).

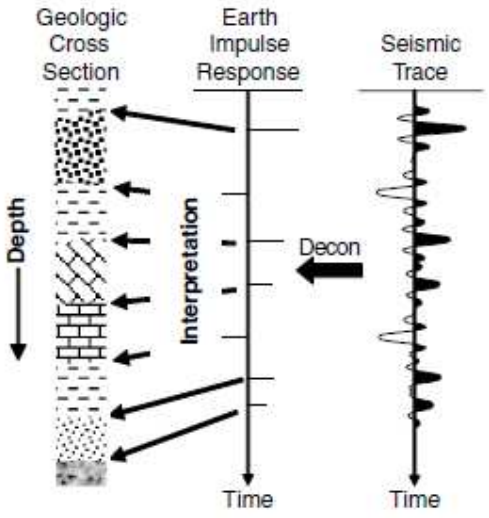

Figure 4. 11 Process of applying the deconvolution on a seismic trace (Gadallah and Fisher, 2009).

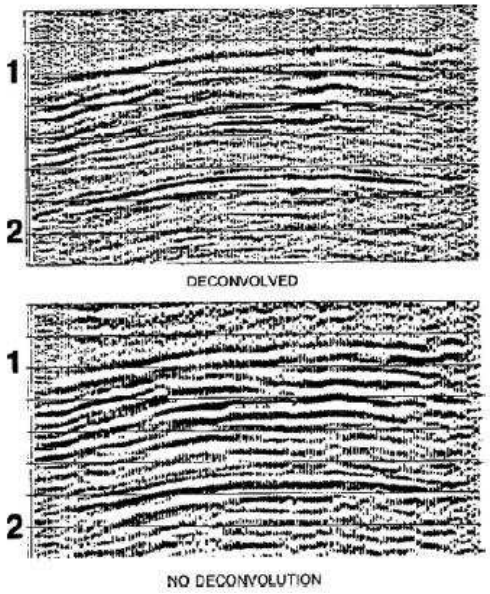

Figure 4. 12 Deconvolution vs no deconvolution. Note that the reflection widths are decreased and a number of events are removed or greatly attenuated in the deconvolved record compared to the one not deconvolved; these events are likely multiple reflections (Gadallah and Fisher, 2009).

4.3.6. Stack

Stacking reduces the effects of random signals or enhances the signal-to-noise ratio by using data redundancy in each reflection point (Yilmaz, 2001). Common-midpoint stacking is the most robust of the three principal processes. The redundancy in CMP recording, allows us to attenuate uncorrelated noise significantly by increasing the source/noise ratio of the stacking. The main problem with CMP stacking is the assumption of the hyperbolic move-out, which may be violated in complex structural areas. Besides, multiple can be attenuated during the stacking, because they have larger move-out than primaries, then they are uncorrected and attenuated (Yilmaz, 2001).

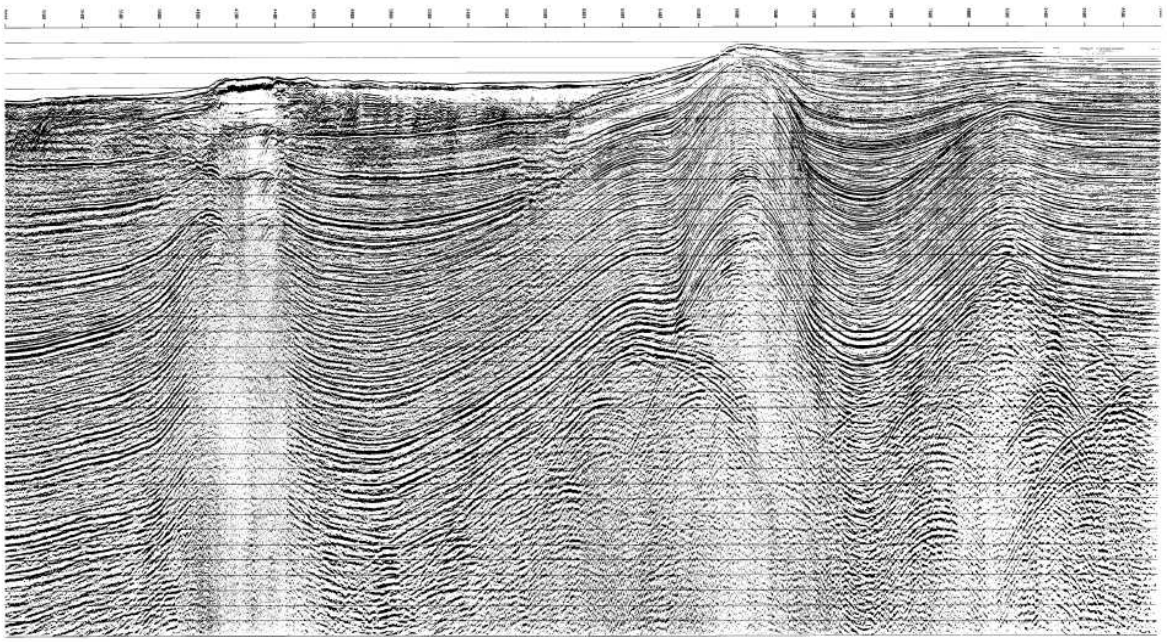

Figure 4. 13 Example of CMP stack associated to same data of Figure 3.8 (Yilmaz, 2001).

4.3.7. *Post-Stack Deconvolution and Wavelet Processing*

Following the CMP stack, there still remains some reverberatory energy that can be removed to obtain a better image (Figure 4.14). A type of predictive deconvolution, where the second-zero crossing of the auto-correlation function of the trace, is used as the predictive "gap", prior to the application of the second-zero crossing deconvolution. Additionally, to further increase temporal resolution, wavelet processing can be applied using the variable norm deconvolution method (Gray, 1979).

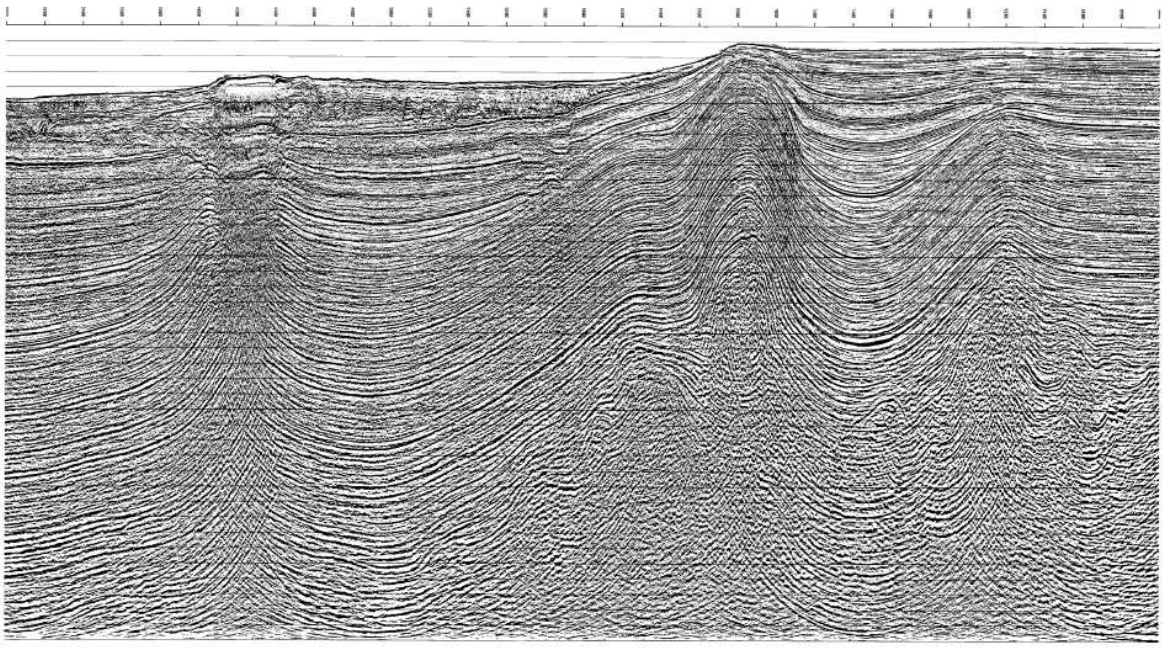

Figure 4. 14 Example of Example of CMP stack after post-stack spiking deconvolution, time-variant filtering, migration, AGC scaling (Yilmaz, 2001).

4.3.8. Interpretation

The interpretation is the final step to obtain a final product of seismic processing steps. Conventional seismic interpretation implies picking and tracking laterally consistent seismic reflectors for the purpose of mapping geologic structures, stratigraphy and reservoir architecture. In seismic interpretation some techniques can be used: Modeling, Tomography, AVO, and VSP interpretation (Gadallah *and* Fisher, 2009).

4.4. Seismic Resolution

Seismic Resolution is the ability to distinguish separate events. Combined approaches are used, in particular when well logs are available. Two types of resolution can be estimated: lateral and vertical that are controlled by signal bandwidth (Yilmaz, 2001).

4.4.1. Vertical Resolution

Vertical resolution controls the thickness of the bed we can resolve using seismic reflections.

According to Yilmaz (2001), the criterion for vertical resolution is the dominant wavelength, which is the wave velocity divided by dominant frequency. Deconvolution can increase the vertical resolution by broadening the spectrum, thereby compressing the seismic wavelet. The dominant wavelength of seismic waves is given by the relation between velocity and the dominant frequency.

4.4.2. Horizontal Resolution

Horizontal resolution refers to how close two reflectivity points can be located horizontally and yet be recognized as two separated points rather than one. According to Yilmaz (2001), the criterion for lateral resolution is the Fresnel zone, a circular area on a reflector whose size depends on the depth to the reflector, the velocity above the reflector and, again, the dominant frequency; besides, migration can improve the lateral resolution by decreasing the width of the Fresnel zone, thus separating features that are blurred in the lateral direction.

4.5. Geophysics Data Acquisition, SISTEUR cruise

Deep penetration multichannel seismic reflection (MCS) and wide angle seismic (WA) data were obtained across the Ecuador-Colombia margin during the SISTEUR cruise (September–October, 2000) on board R/V Nadir (Collot *et al.,* 2002). The 45-fold coverage 360/348 MCS data were recorded using a 4.5 Km long streamer and a 45-l air-gun seismic source tuned in single-bubble mode and fired every 50 m (Figure 4.15) (Collot *et al.*, 2002); whereas 18 fold coverage WA data were obtained using an array of eight 16-1 air-guns, shot at 125 m intervals (Gailler *et al.,* 2007). Some parameters used in acquisition are showed in table 1, 2 and 3.

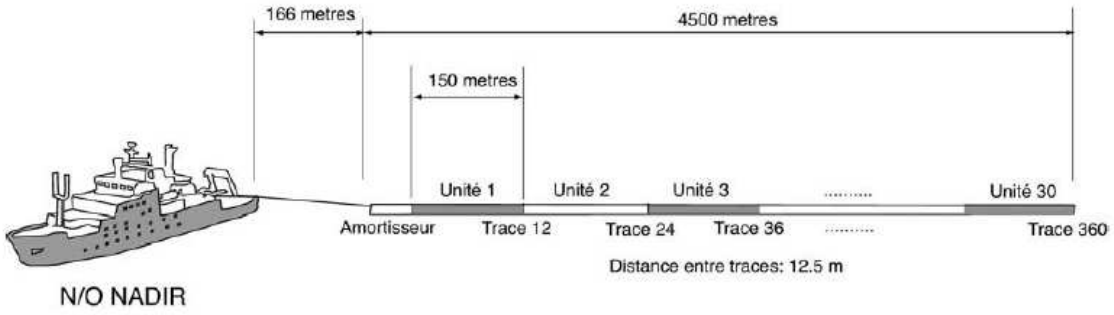

Figure 4. 15 Parameters used in SISTEUR cruise (2000) for the MCS data acquisition (Agudelo, 2005

	Résumé des paramètres d'acquisition sismique						
	Volume (inch / Litre) Pression	Immersion -Canons -flûte	Intervalle de tir (m) Vit navire (nds)	Inter-trace (m)	Nbre de traces	Echantill. (ms), Longueur enregis. (s)	Couv. Multiple
Source réflexion	**2869 / 48** 140b	10-11 m 15 m	**50** 5	**12.5**	**360**	**4 /15**	**45**
Source réfraction	**7814 / 128** 140b	25-30 m 20 m	**125** 4	**12.5**	**360**	**4/15**	**18**

Table 1 Parameters used during the acquisition of SISTEUR data (SISTEUR, 2000).

Type de source	Canons à air
Volume total d'air	45 L
Pression de l'air liberé	14 MPa (140 bars)
Distance entre tirs	50 m
Profondeur des tirs	10 m
Energie libéré par tir	~ 6.0 e+05 N.m
Fréquence source	13 -18 Hz

Table 2 Parameters of the MCS Source of SISTEUR cruise (2000) (Agudelo, 2005).

Type de acquisition	Sismique 2D
Longueur total	4 500 m
Profondeur d'inmersion	15 m
Nombre de traces	360 (profils 1-31) et 348 (profils 32-73)
Distance entre traces	12.5 m
Pas d'echatillonage	0.004 s
Longueur trace	15 s

Table 3 Parameters of the Streamer used in SISTEUR cruise (2000) (Agudelo, 2005).

4.6. Processing on board of the NADIR

During SISTEUR cruise (2000) a set of seismic profiles were obtain along the Ecuadorian margin (Figure 4.16); on board of NADIR ship, velocity analysis and dynamic correction (Figure 4.17) was performed to these profiles using a station SUN Ultra60 and Geovecteur seismic software (version 6.1) to control the data quality, and to obtain a first set of time migrated sections (Figure 4.18) (SISTEUR rapport, 2000).

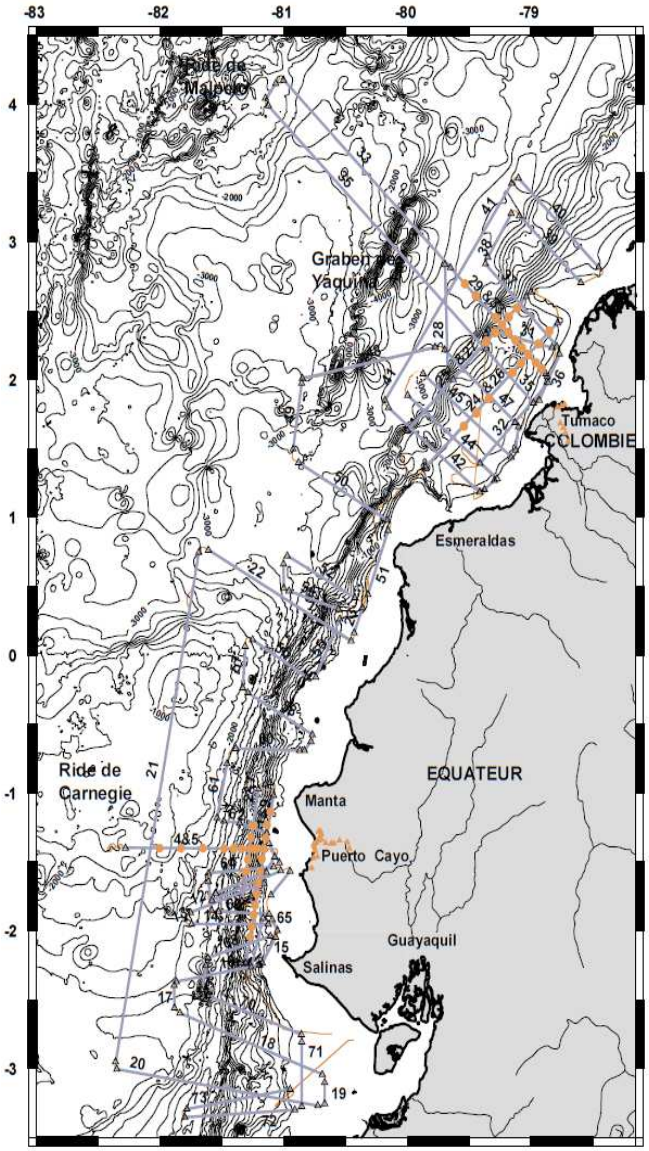

Figure 4. 16 Profiles from SISTEUR cruise (2000) in light blue. Profiles from 5-25 and 32-73 (in light blue) have been acquired with a single bubble seismic source, and from 1-4 and 26-31 with a source of seismic of wide angle (in orange) (SISTEUR cruise report, 2000).

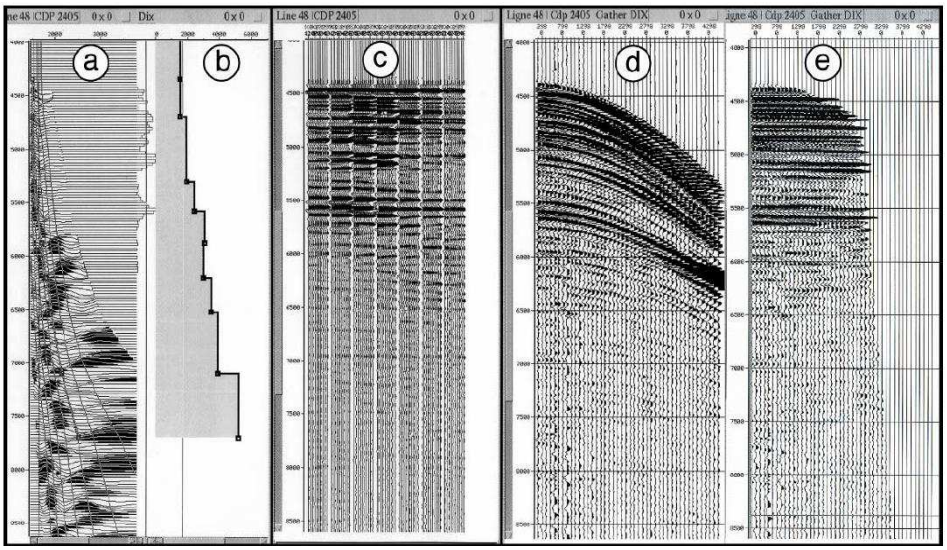

Figure 4. 17 Velocity analysis and dynamic correction (NMO). Profile SIS48-cdp2405; a) Semblance panel (velocity in X, and time in Y) with the velocity law. b) Velocity law pointed in the maximum of energy. c) Mini-stacks of 10 CDP for 7 velocity laws. d) CDP 2405 uncorrected. e) CDP 2405 with the NMO correction in velocity defined in b, and external mute (SISTEUR rapport, 2000).

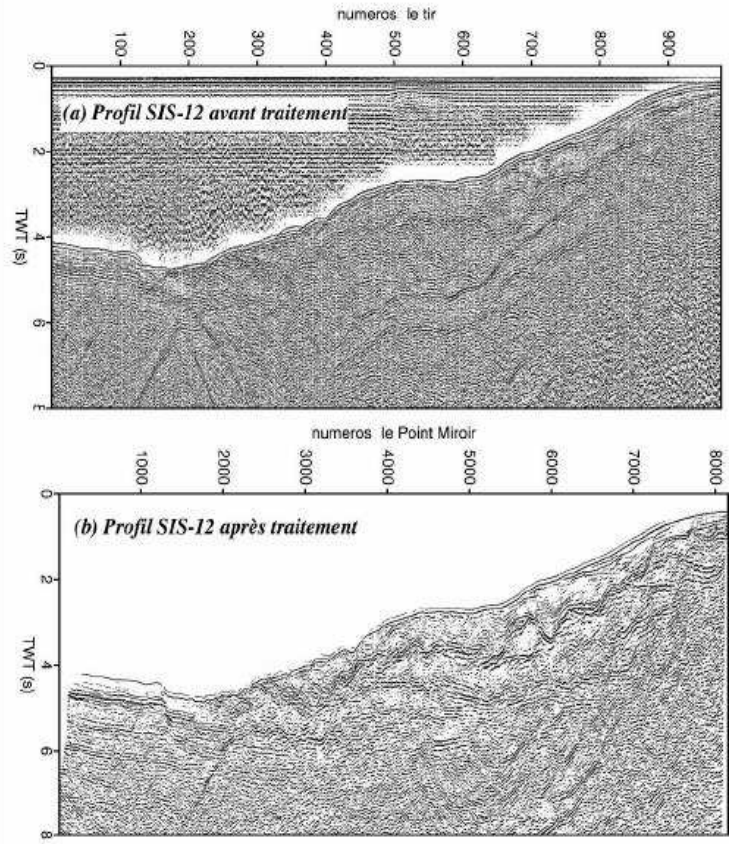

Figure 4. 18 Profile SIS12 from SISTEUR 2000: a) before treatment and b) after treatment with coverage of 45 and migration with a velocity of 1500 m/s (SISTEUR cruise report, 2000).

4.7. Seismic Processing: SISTEUR profiles SIS05, 07, 09, 13, 14, 62, 66 and 68

Several seismic profiles (Figure 4.19) obtained on SISTEUR cruise (2000) were improved implementing a new treatment sequence (Figure 4.20), which allowed to eliminate the multiples, and to refine the spatial resolution of the margin velocity structures, enhancing the reflection coherency, and modeling reflectors as thin layers at the roof and floor of the plate interface.

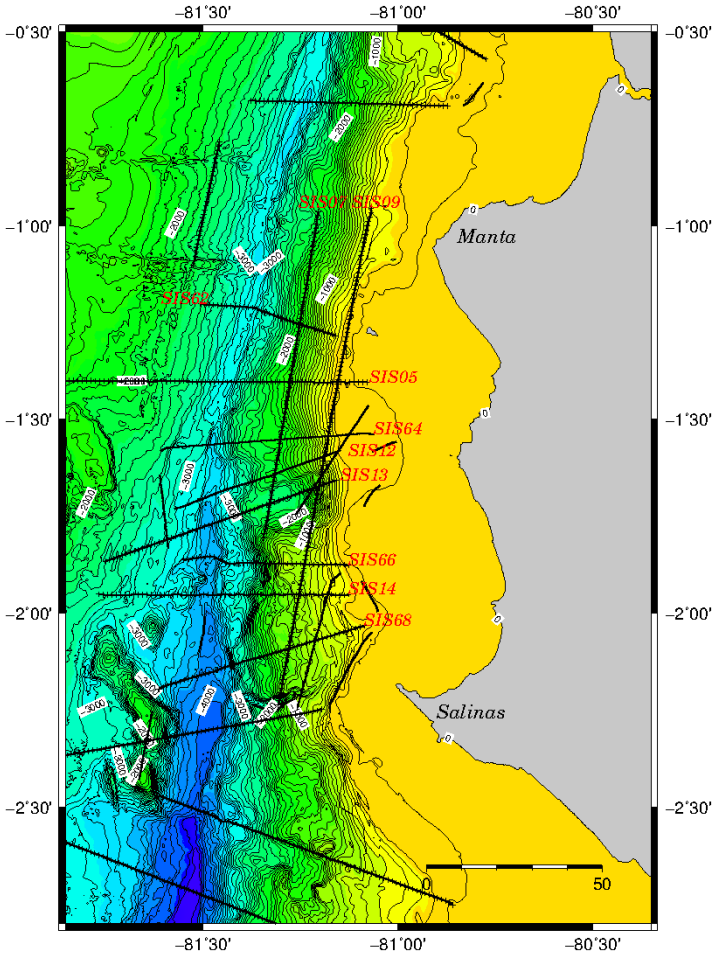

Figure 4. 19 Bathymetric map of the central Ecuador with contoured at 100m intervals (after Michaud 2006), in red showing the multichannel seismic reflection lines SIS05, 07, 09, 13, 14, 62, 66 and 68 from the cruise SISTEUR in 2000.

The new processing (Figure 4.20) was performed using Geocluster seismic processing software, preserving the phase amplitudes and allowed us to obtain better seismic images (Figure 4.21). This processing included: data sorting to 6.25 m CDP; first velocity analysis; band pass filter

(4, 12, 28, 33 Hz) at the beginning and after deconvolution; minimum phase conversion of the signal (WAPCO module); multiple attenuation in the frequency-wave number (FK) domain (FKFIL); normal move-out velocity analysis (FANMO); external and internal mutes (MUTE); spherical divergence correction (SDICO module) and its inverse, to compensate the signal's amplitudes for the deep zones, where the deconvolution and the anti-multiple are not so effective (> 5 s.); predictive deconvolution (TRITA module) to reinforce high frequencies and improves the resolution that also amplified the noise; a second multiple attenuation using Radon transform (RAMUR) to reinforce the main signal masks by the multiples; and inverse NMO correction; a second band pass filter (3, 6, 50, 60 Hz); stack (STACK module) and migration (FKMIG); and sorting of CDP to shot gather.

Depending on the image, we adapted the seismic processing, adding or removing certain modules (e.g., filters, anti-multiples); however, the sequence in all the profiles is relatively similar. The new images are shown in Figure 4.22 to Figure 4.29, the intersections with other profiles is represented by red dashed lines. The vertical axis is in time (ms) and horizontal axis in cdp.

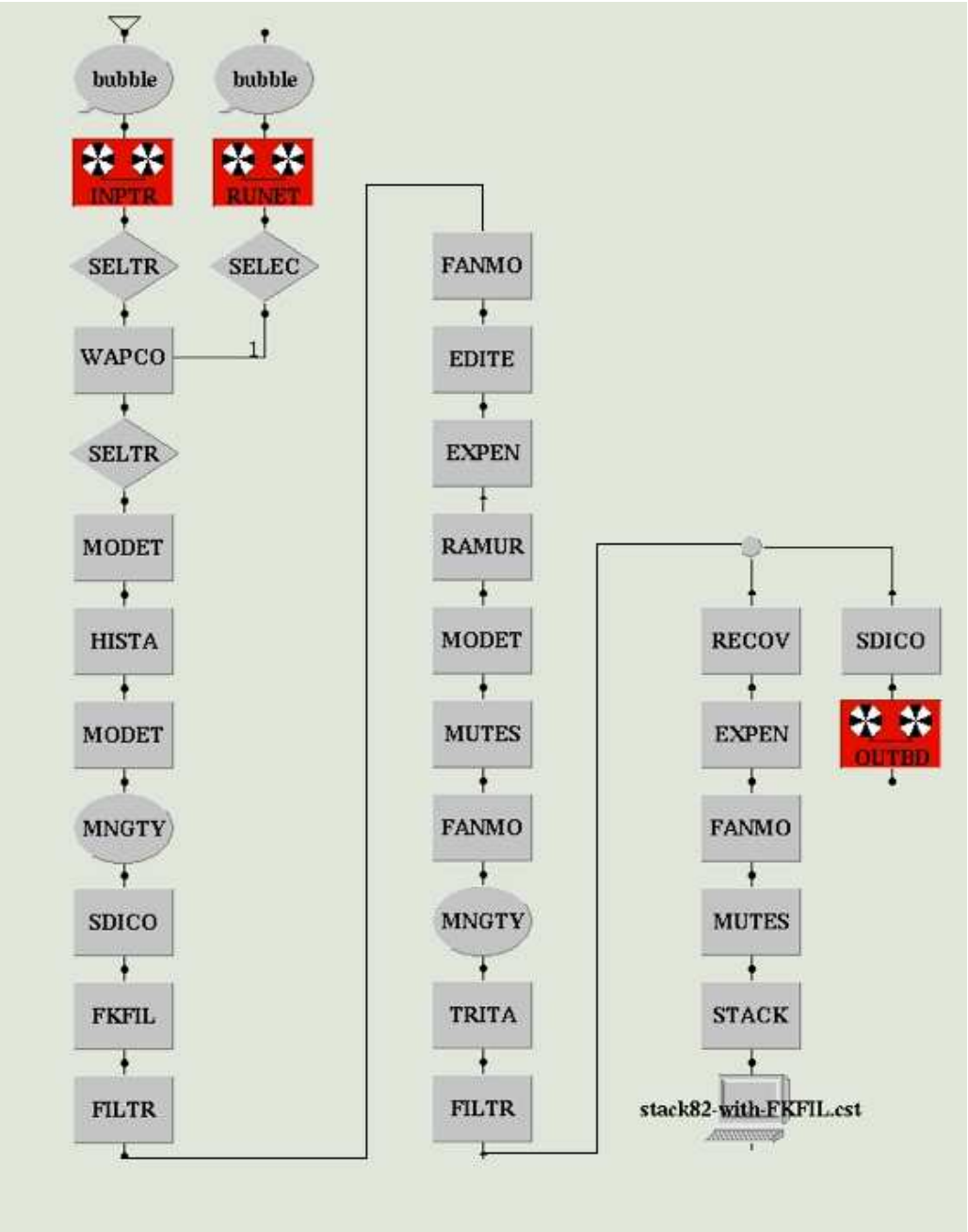

Figure 4. 20 Figure 4.20 Example of a processing sequence applied to the line SIS05 from SISTEUR cruise 2000, using Geocluster. In this sequence several filters (FILTR), mutes (MUTES), anti-multiples (FKFIL, RAMUR), convolution (TRITA), minimum phase (WAPCO), spherical divergence corrections (SDICO) and other modules are applied to prepare the data (INPTR) that will be used during the time-migration (stack82-with-FKFIL.cst) and depth-migration (OUTBD).

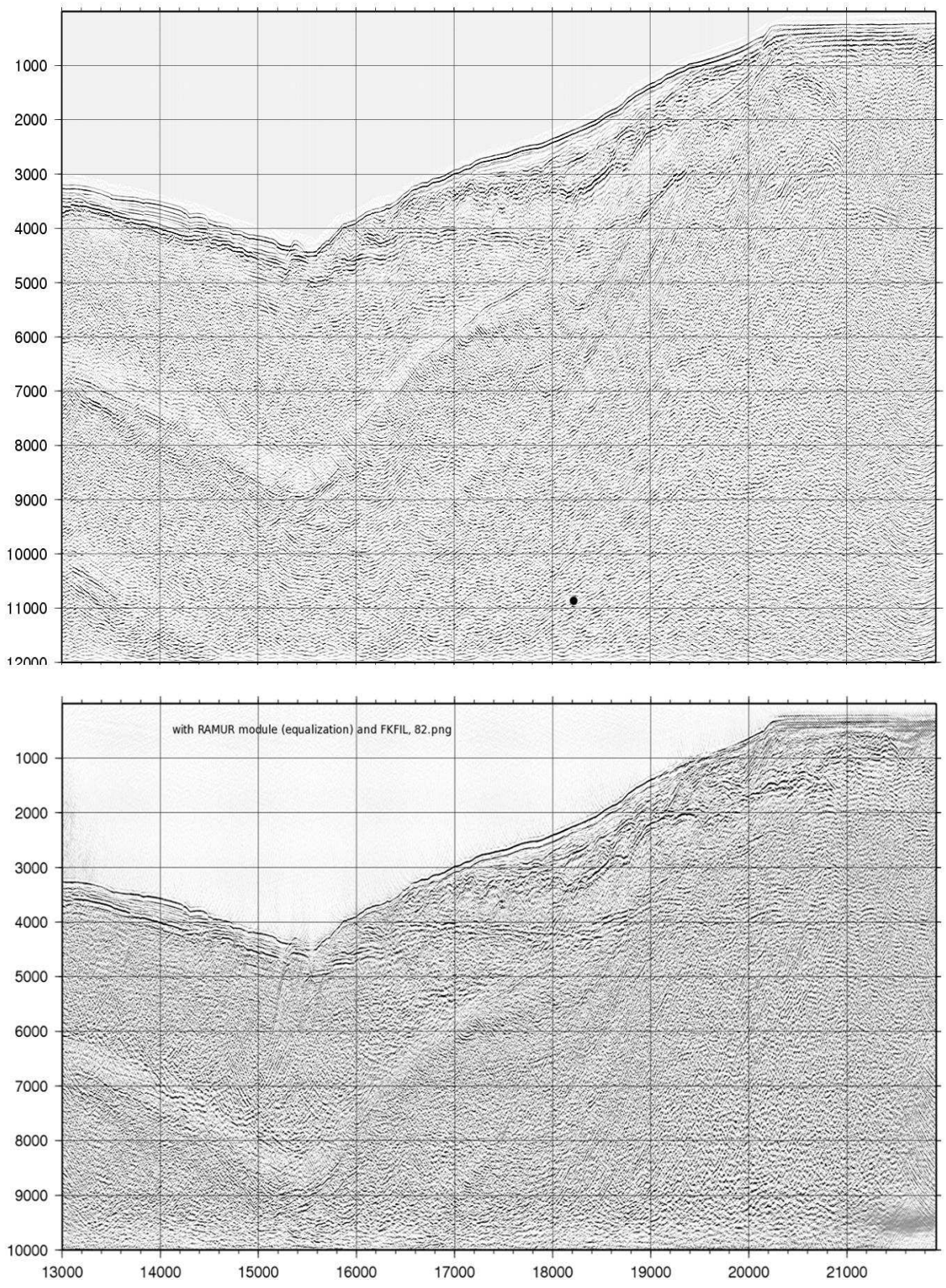

Figure 4. 21 Comparison of two time-migrated images of profile SIS05 from SISTEUR (2000). Top) treatment during SISTEUR cruise; bottom) image with the new processing sequence, using Geocluster and applying RAMUR and FKFIL modules.

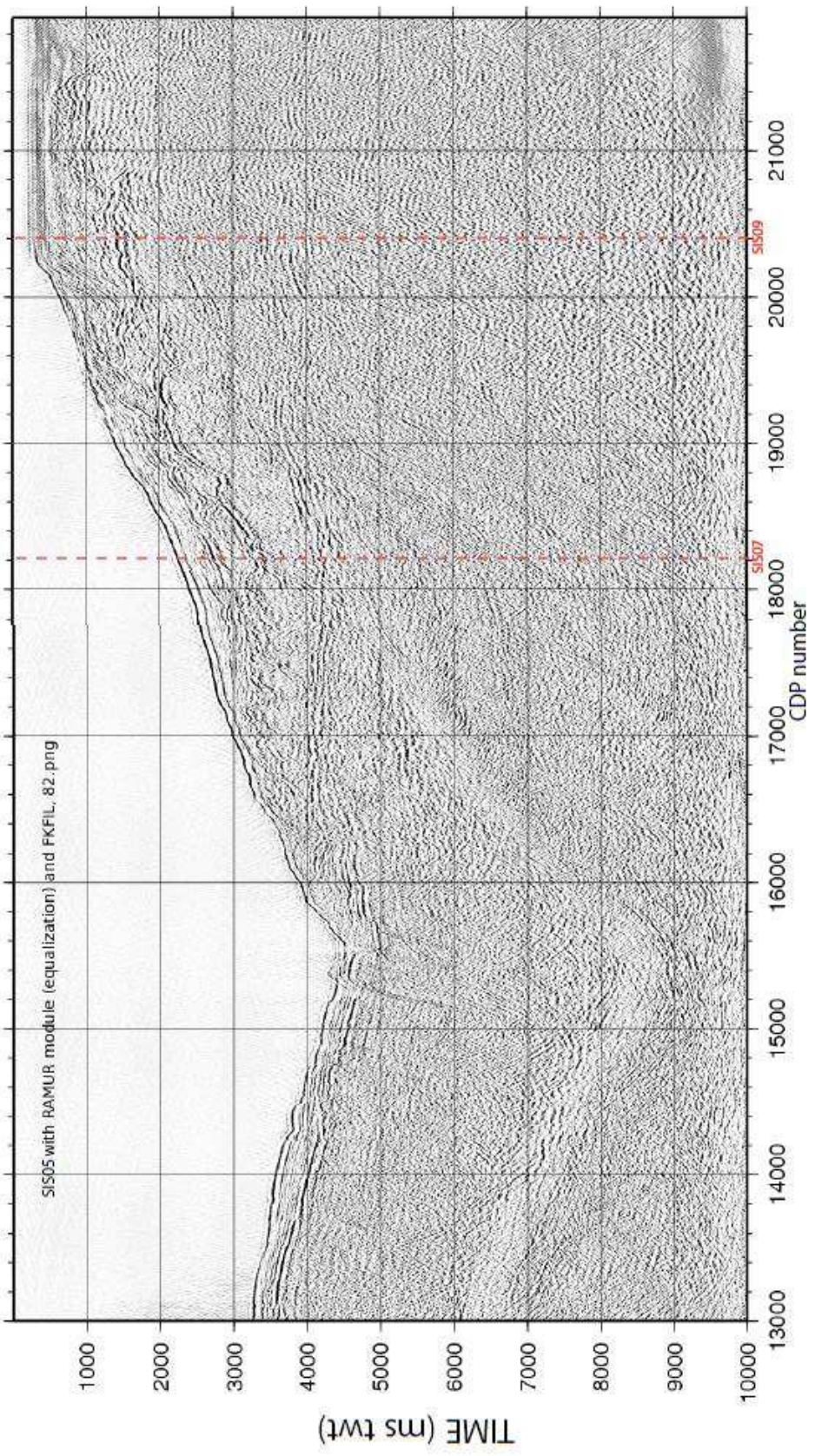

Figure 4. 22 Seismic profile SIS05, using Geocluster with FKFIL and two RAMUR modules; red dashed lines indicate the intersection with the strike profiles SIS07 and SIS09.

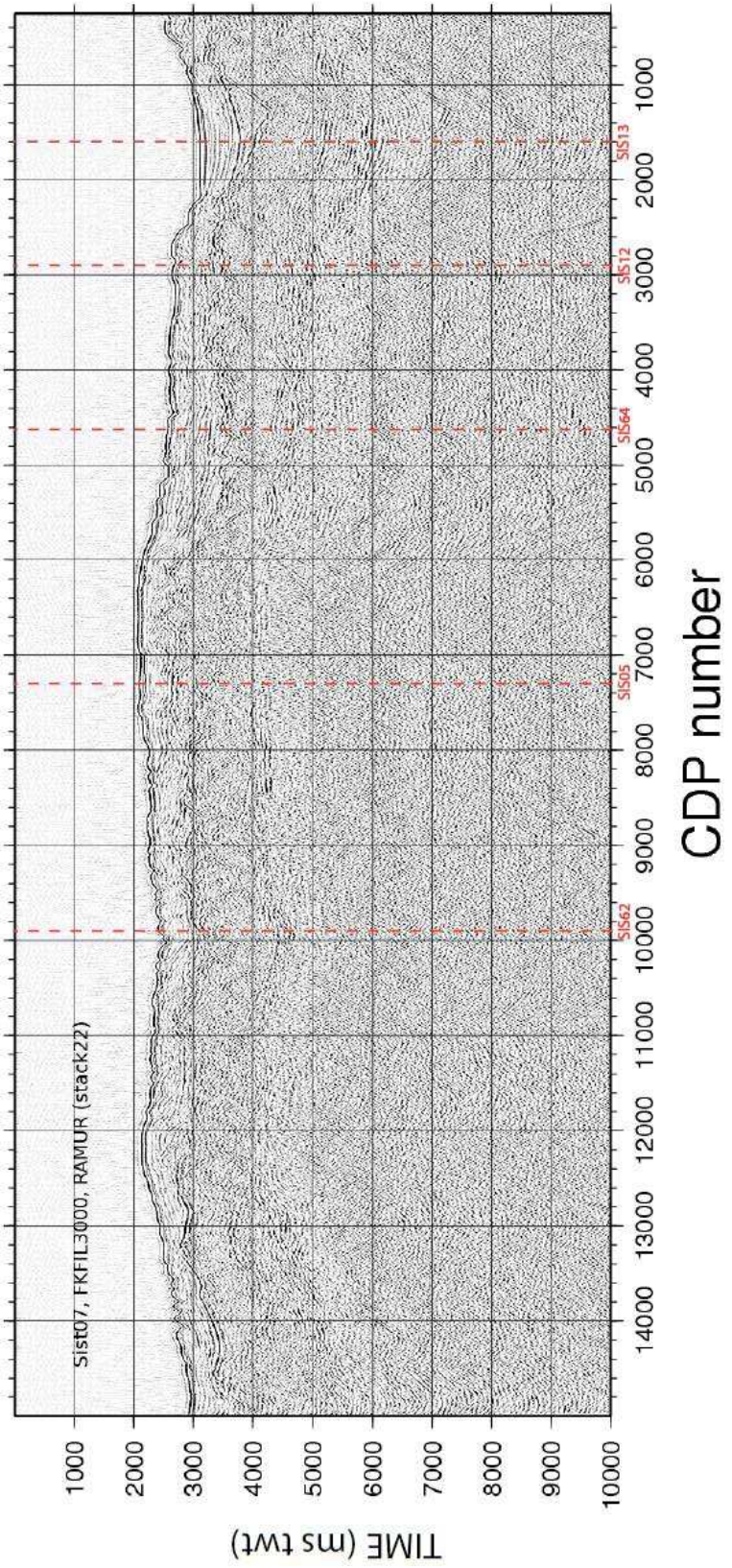

Figure 4. 23 Seismic profile SIS07 from CDP 100 to 14800, using Geocluster with FKFIL and two RAMUR modules; red dashed lines indicate the intersection with the dip profiles.

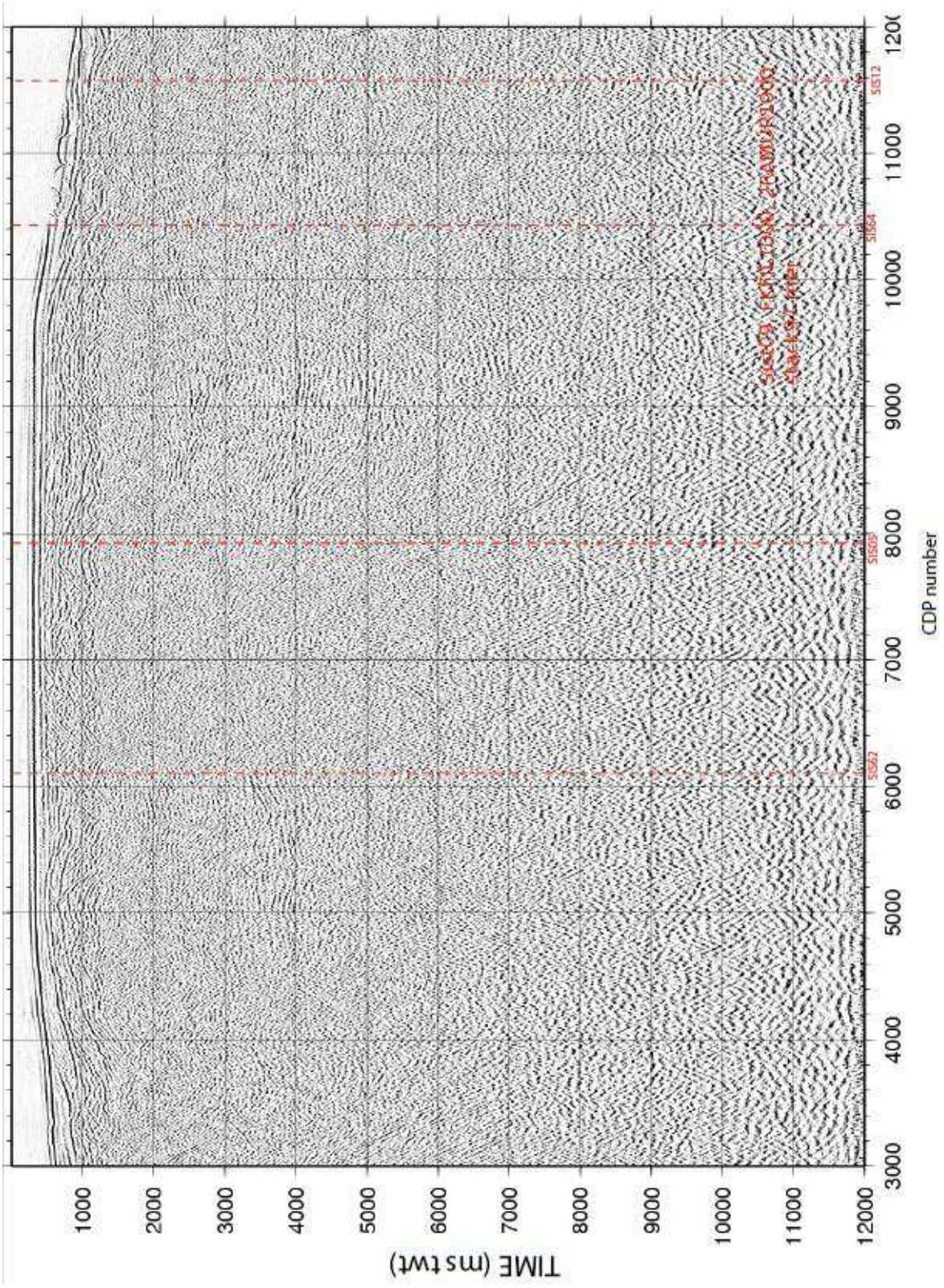

Figure 4. 24 Seismic profile SIS09 from CDP 3000 to 12000, using Geocluster with FKFIL and two RAMUR modules. Red lines represent the intersection with SIS62 and line SIS05; red dashed lines indicate the intersection with the dip profiles.

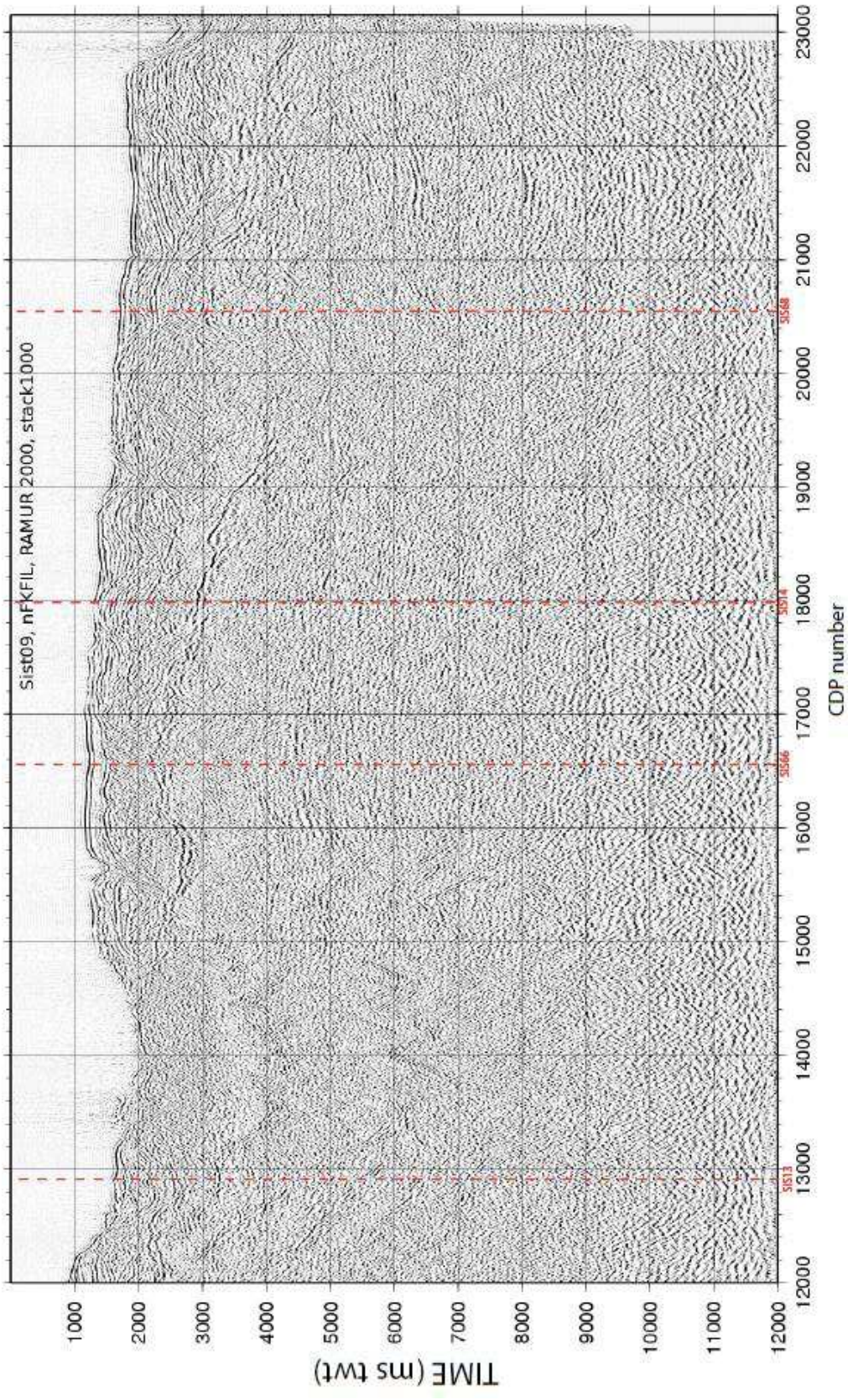

Figure 4. 25 Seismic profile SIS09 from CDP 12000 to 23192, using Geocluster with RAMUR module; red dashed lines indicate the intersection with the dip profiles.

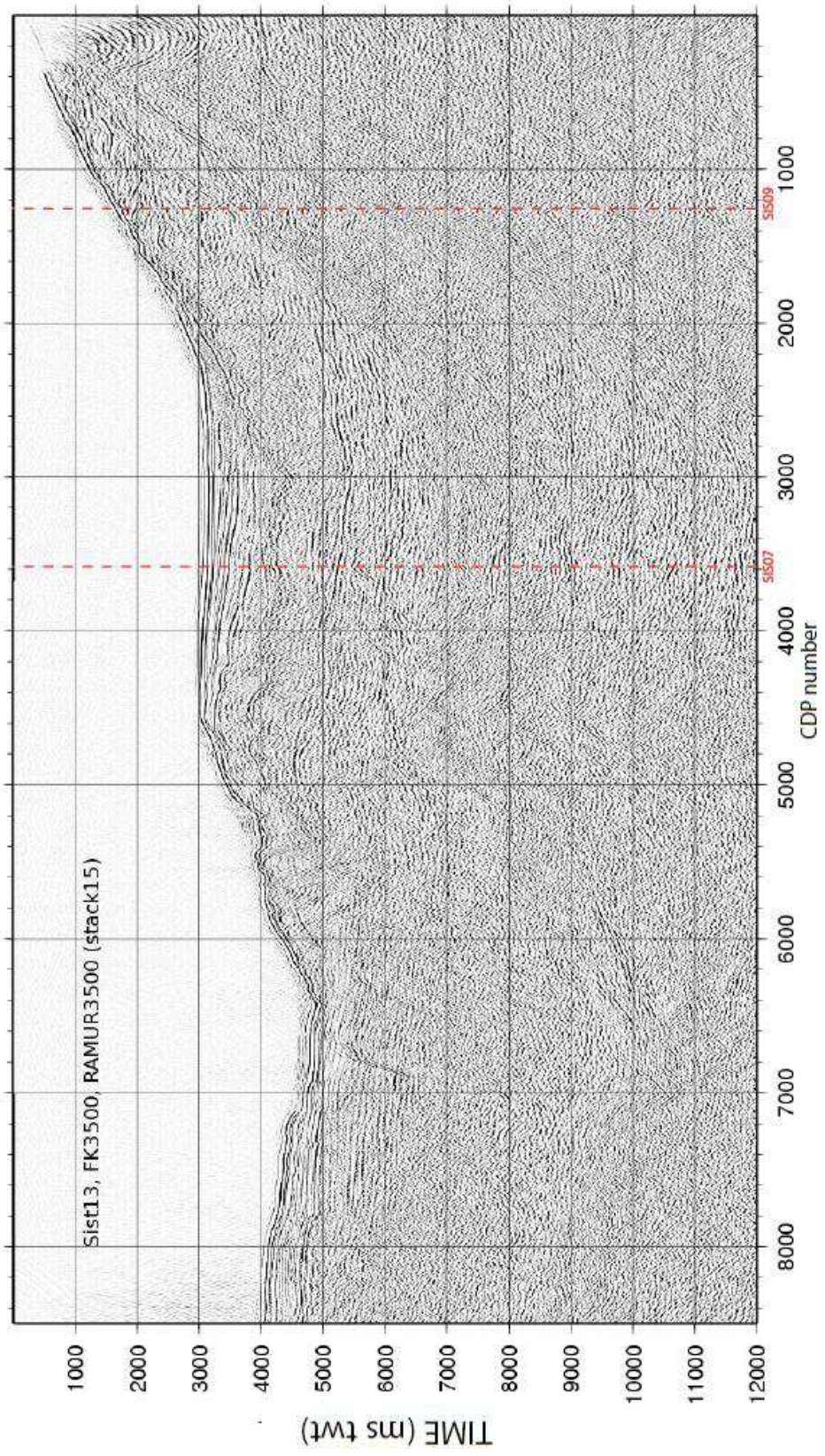

Figure 4. 26 Seismic profile SIS13, using Geocluster with RAMUR module; red dashed lines indicate the intersection with the strike profiles.

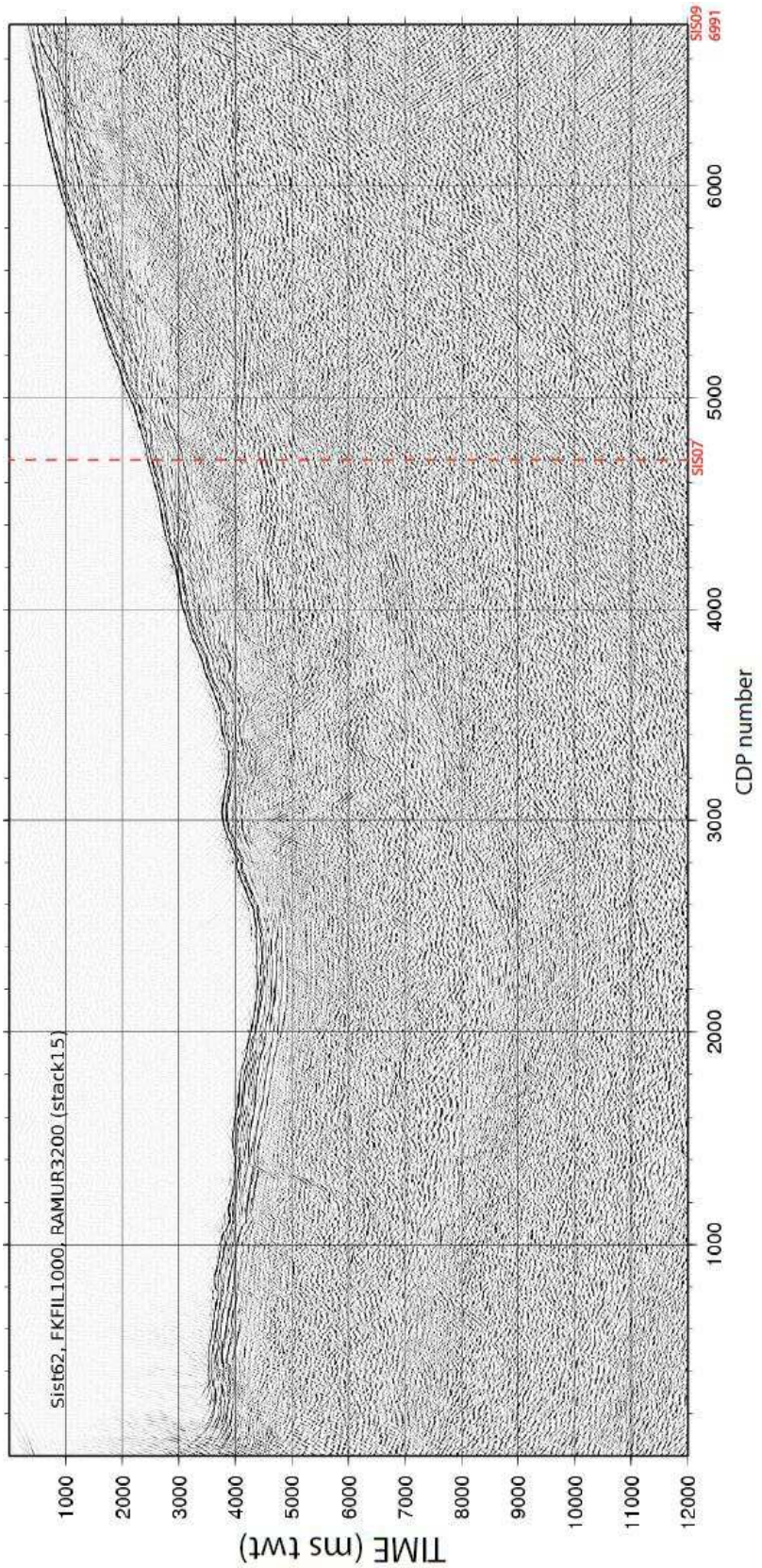

Figure 4. 27 Seismic profile SIS62 processed with Geocluster and applying FKFIL and RAMUR modules; red dashed line indicates the intersection with the strike profile SIS07.

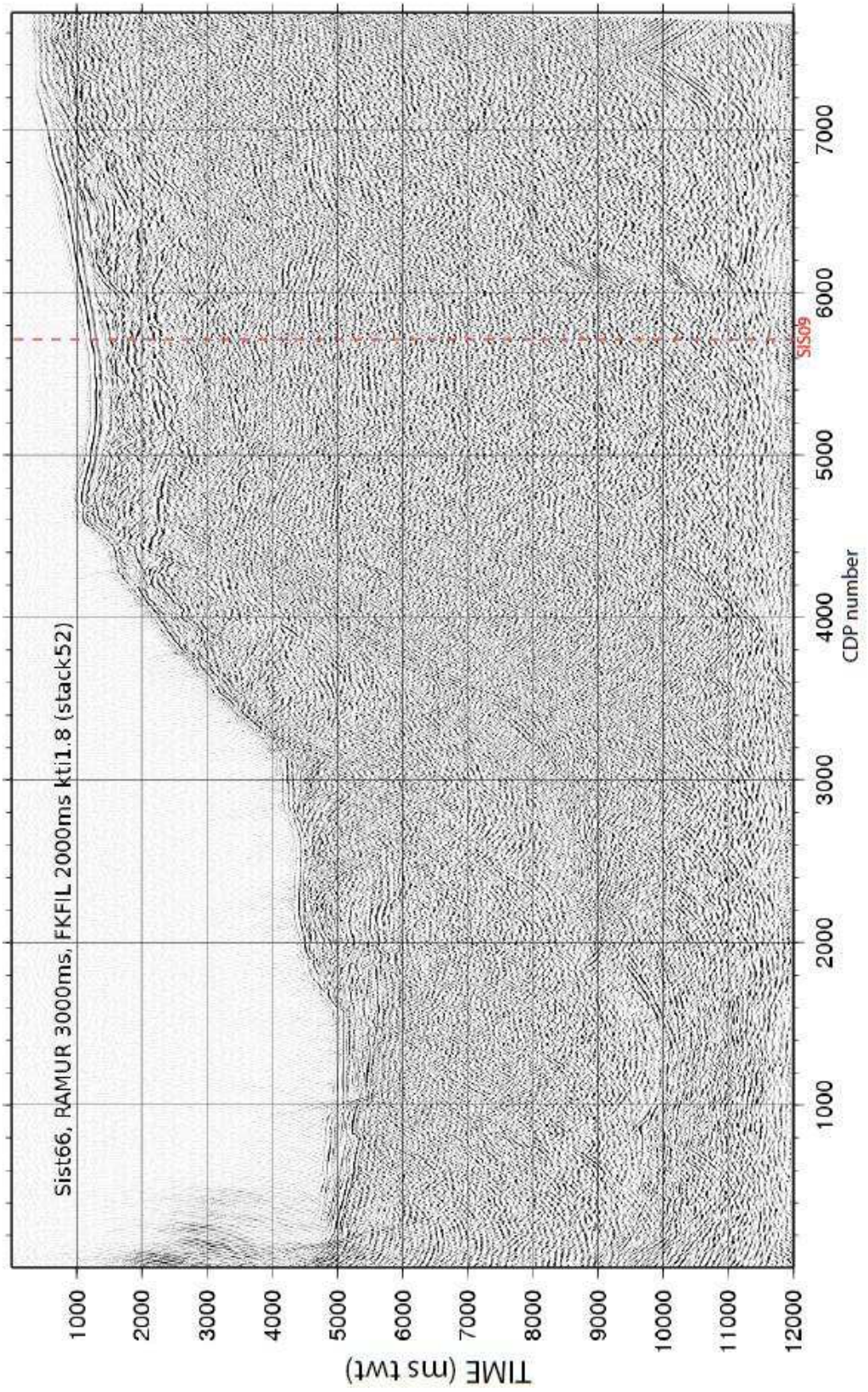

Figure 4. 28 Seismic profile SIS66 processed with Geocluster and applying FKFIL and RAMUR modules; red dashed line shows the intersection with SIS09.

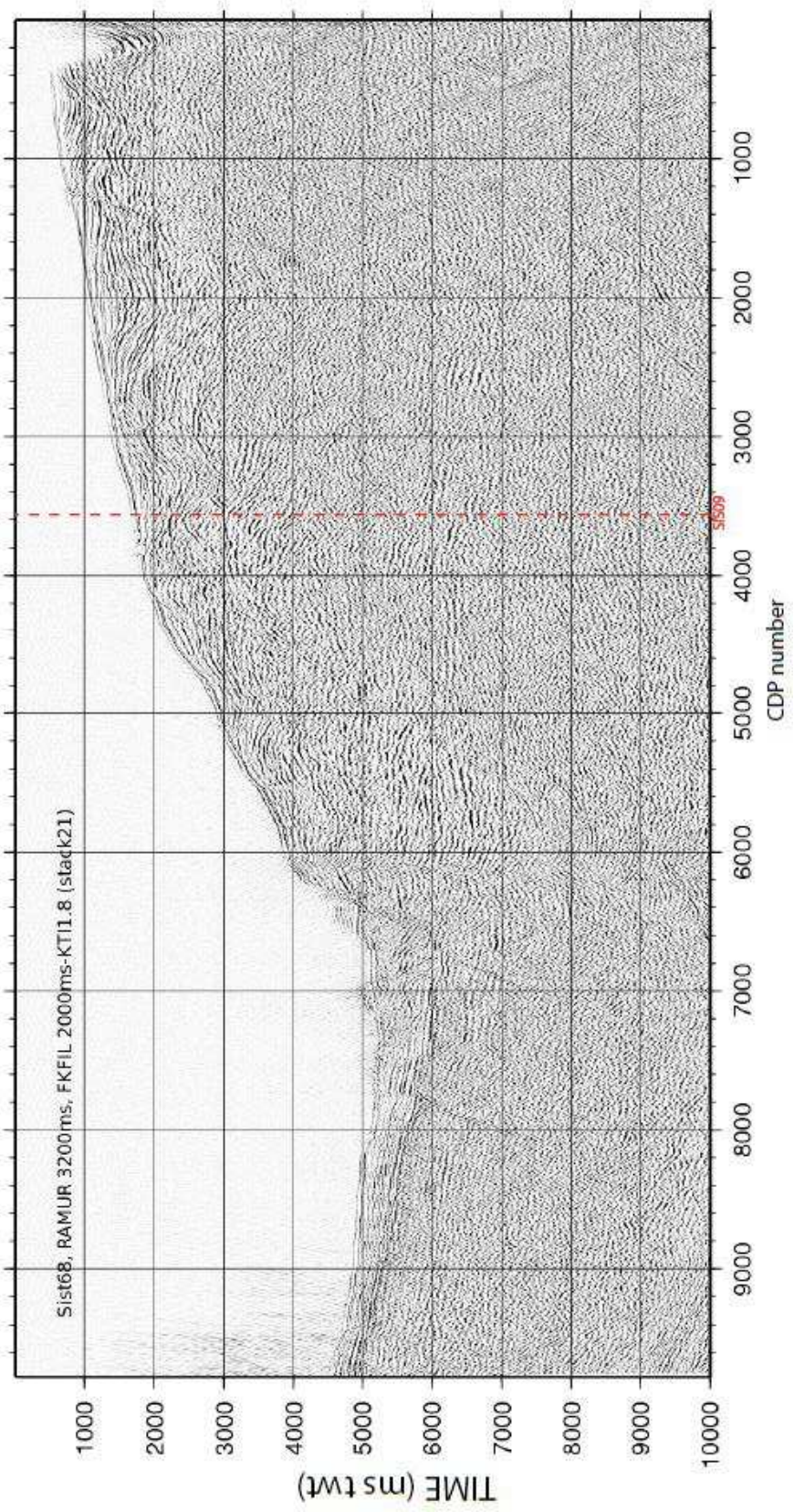

Figure 4. 29 Seismic profile SIS68 processed with Geocluster and applying FKFIL and RAMUR modules; red dashed line indicates the intersection with the strike profile SIS09.

CHAPTER 5

PRE-STACK DEPTH MIGRATION, SISTEUR PROFILES

5. Depth Migration

5.1. Processing Sequence in Depth Domain

Pre-stack depth migration is an interesting tool to study areas where there are significant and rapid lateral or vertical changes in the velocity that would unacceptably distort time migrated images. During the propagation in the Earth the amplitude and phase of the seismic signal are modified, and the classic reflection methods do not take in consideration amplitude modifications. The waveform inversion of seismic signal used in this work (diffraction tomography) allows us to characterize physical properties of the underground as variations in the velocity and to obtain the correct geometry of reflectors, where the initial velocity model is enough accurate (Beylkin, 1985; Jin *et al*., 1992; Lambaré *et al*., 1992).

5.2. Seismic Data inversion

The seismic inversion is the process of transforming seismic reflection data into a quantitative rock-property description of the underground. The inversion methods are sometimes presented as improved migrations (Mora, 1989; Ehinger *and* Lailly 1991; Thierry *et al*., 1995, 1996). In seismology, the modeling or direct problem is concerned to calculate the seismograms using physical parameters of the underground. In contrast, the inversion is the process that consists in determining the physical characteristics of the model by minimization of the misfit between observed data and estimated seismograms, (Beylkin, 1985; Jin *et al*., 1992; Forgues, 1996); in the seismic inversion basically, we try to determining what physical parameters of rocks and fluids can produce the seismic record that we have.

5.2.1. Ray+Born migration/inversion diffraction

The method called ray+Born migration/inversion is known as preserved amplitude pre-stack depth migration (PSDM). This method provides a quantitative depth-migrated image. The method is based on ray +Born waveform migration/inversion (Beylkin, 1985; Jin *et al*., 1992; Lambaré *et*

al., 1992; Ribodetti *et al*., 1998, 2000a; Thierry *et al.,* 1999a; Lambaré *et al.,* 2000, 2003; Agudelo, 2005). The software (Thierry *et al*. 1999) is the acoustic version of an original elastic method proposed by Jin *et al.* (1992), who introduced an attractive asymptotic method for inverting seismic reflection data. Since the technique of Jin *et al.* (1992) was introduced, several applications to two-dimensional (2D) and three-dimensional (3D) datasets have been developed for acoustic modelling (Lambaré *et al.* 1992; Thierry *et al.* 1999; Ribodetti *et al.* 2000; Operto *et al*. 2003). This approach is very sensitive to the initial velocity model estimate. If the model is incorrect, the reflectors are mislocated and the amplitudes of the velocity distributions are biased. To obtain a reliable image (correct geometry and correct velocity perturbations of seismic reflectors) we used a simple and efficient method, proposed by Alyahya (1989) and implemented by Agudelo (2005), to perform a quantitative estimate and correction of the velocity macro-model, through a standard 'migration–velocity–analysis' (MVA) approach. Iso-X panels (or common image gathers (CIGs)) are stored during migration and semblance panels estimated to obtain a local correction function for the velocity-macro model. Confidence in the migrated image is achieved when the Iso-X panels are flat and when the corresponding semblance panels are around 1 (Alyahya, 1989). The velocity macro-model is then iteratively corrected during migration until the semblance panels remain around 1 for all the main reflectors and CIGs are very flat. When such conditions are satisfied, all the CIGs are stacked to obtain the final migrated image.

5.2.2. Workflow to process MCS data

The workflow applied to MCS data consists in a pre-processing that preserves the amplitude and permits to obtain a velocity macro-model using the velocity model from the velocity analysis. This new velocity model is converted to RMS velocity with the Dix equations, interpolation and smoothing (Agudelo, 2005). All the parameters (travel-time, amplitude, diffraction angle) required for the migration are calculated from a dynamic ray tracing (Lambaré *et al*, 1996).

To verify whether the velocity macro-model is accurate or not, the migration velocity analysis in depth domain is performed. This analysis consists in calculating partial migrations for constant diffraction angles (Xu, 2001), where the final images (ISO-X panels, or common image gather CIG) will permit to evaluate the accuracy of the reference velocity model. For each Iso-X panel, each reflector for all angles should be flat; if not (curved reflectors appear on the iso-x panels) corrections using the semblance gamma function (factor gamma) are applied (Al-Yahya, 1987; Agudelo, 2005). After several iterations, the true amplitude of the velocity perturbations and the

correct geometry is recovered when the reflectors are flat and the gamma functions are around 1.

The workflow of this methodology is summarized in (Figure 5.1) and includes an iterative correction of the Vp velocities macromodel, and it provides a 2D quantitative migrated image. These tools, developed by S. Operto, A. Ribodetti and W. Agudelo, are available at Geoazur.

Using this technique we observe between 0 to 5 km very flat CIGs, suggesting a minimum error for the velocity model; as a consequence depth locations of seismic events have uncertainties of less than 20-30m. Errors in velocity estimation grow quickly for depths greater than the maximum offset of the streamer (for our MCS data is 4.5 km) (Lines, 1993; Ross, 1994).

5.3. Pre-Stack Depth-migration images: SISTEUR profiles

The profiles SIS05, 07, 09, 13, 14, 62, 66 and 68 (*e.g.*, Figure 5.2) were depth-migrated using the procedure described in the previous section. When the velocity model is not accurate enough, several iterations (AN01, AN02, AN03, etc.) must be performed, consuming a lot of time, both to prepare the iteration (2 days) and to run it (1 day), depending on the profile's length. In our case, running more than 3 iterations does not certify that the result will converge, or that the image will be good enough to be used (as happened for line SIS09). Thus, it is important to begin with a velocity model accurate enough in order not to run more than 3 iterations.

Following the above-mentioned procedure, a macro-model (velocity for AN01) was prepared for each line, and a first pre-stack depth-migration (PSDM-AN01) was performed. The horizontality of the reflectors (*e.g.,* Figure 5.3, 5.4) and their gamma functions) were used to control the quality of each image. When the results are not estimated well; we carry on improving the gamma correction, and a new iteration is run until obtaining a more accurate and improved PSDM image. The PSDM images with their respective iso-x panels or semblance are shown from Figure 5.5 to Figure 5.9.

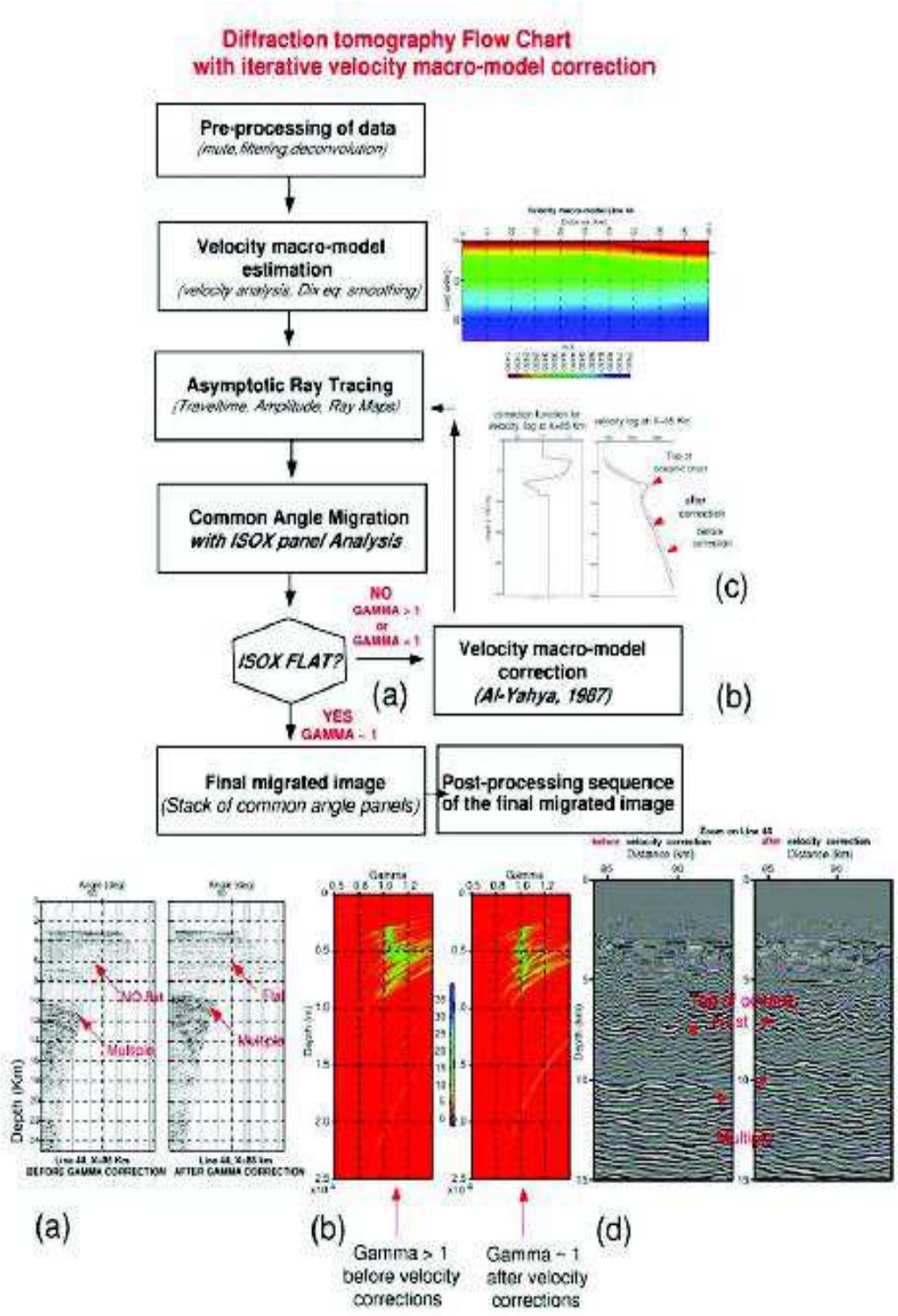

Figure 5. 1 Workflow applied on our seismic profiles. MCS processing for the profile SIS44 (Agudelo, 2005); (bottom) a) example of ISO-X panels sorted during the step; b) example of gamma functions; d) example migrated image before and after CIGs correction; (top) (a) of the workflow (b) velocity model corrections (c): example of the gamma function (left) and of a velocity log before and after correction (Agudelo, 2005).

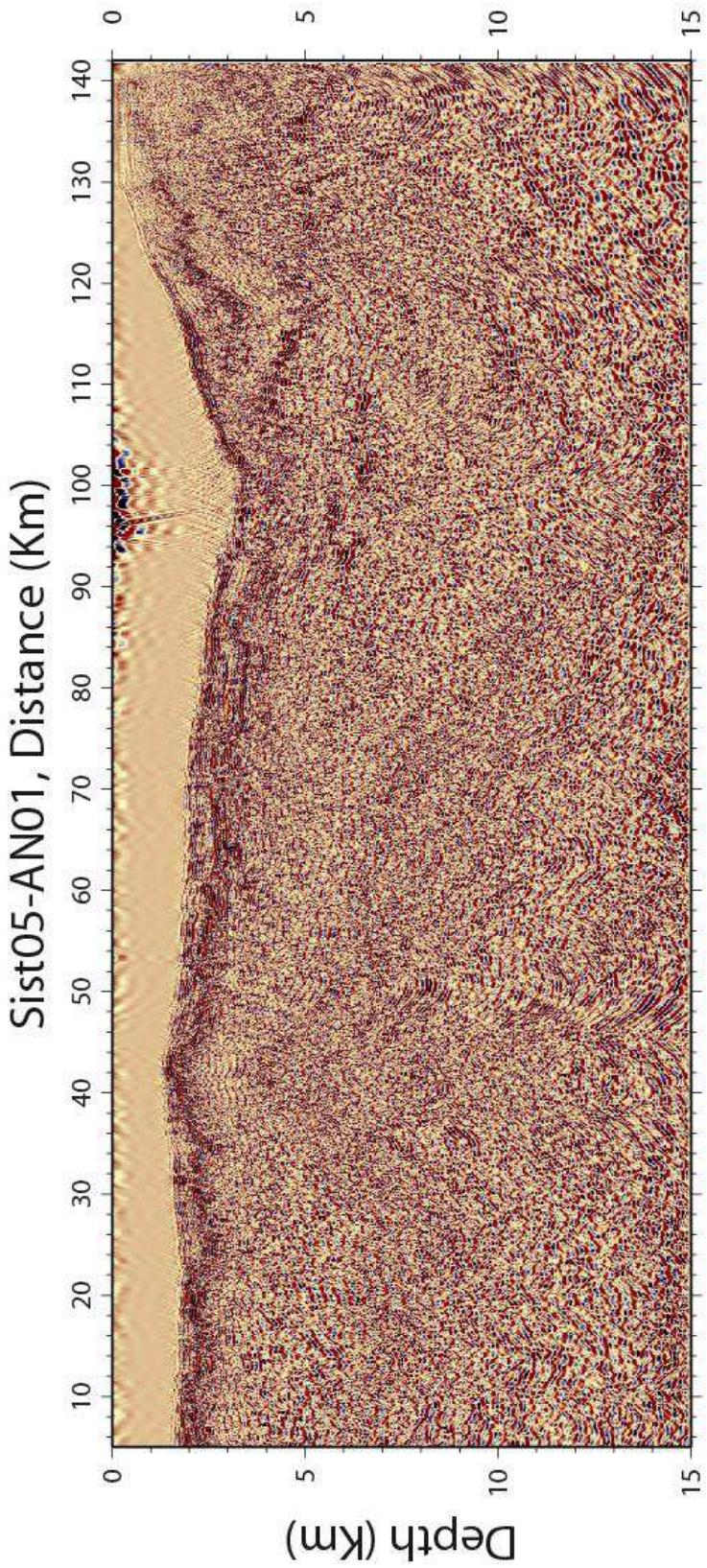

Figure 5. 2 Example of Pre-Stack-Depth-Migrated image of the seismic profile SIS05.

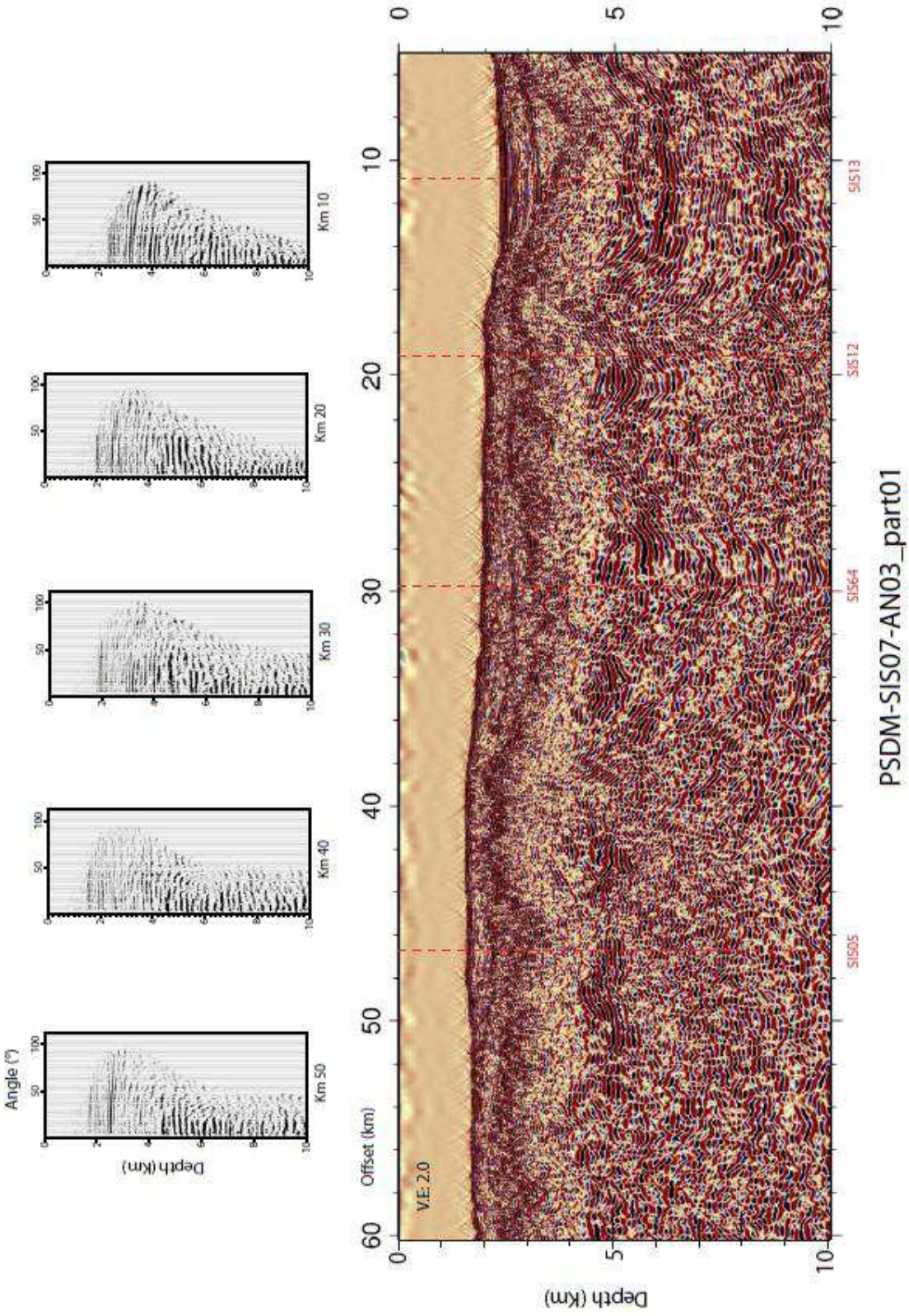

Figure 5. 3. Examples of quality and accuracy control of the Pre-Stack-Depth-Migrated image of the seismic line SIS07 iteration 02 from 5 km to 60 km (part 01); top); several common images gathers and semblances; bottom) the pre-stack depth-migrated image for line SIS07.

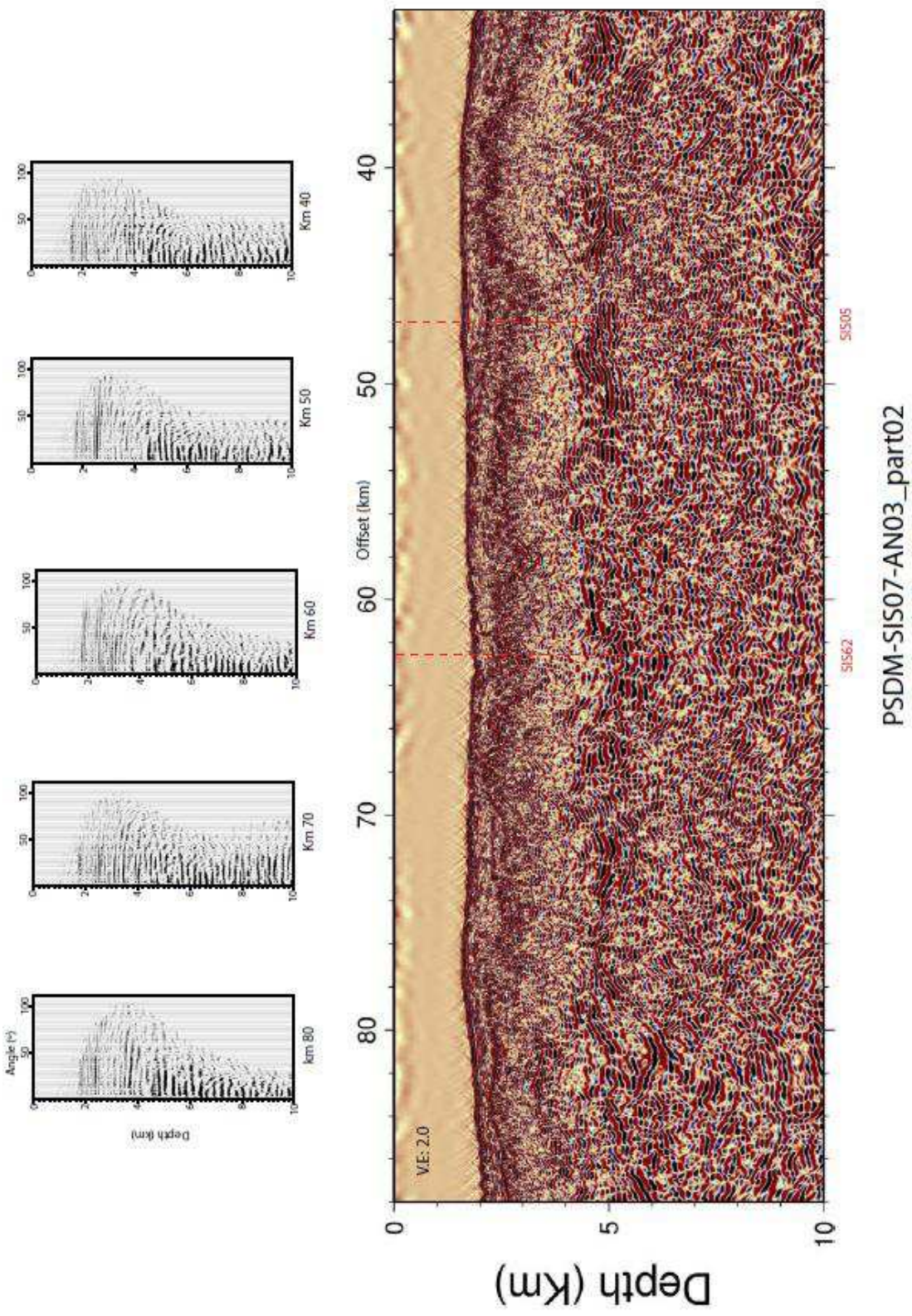

Figure 5. 4. Examples of quality and accuracy control of the Pre-Stack-Depth-Migrated image of the seismic line SIS07 iteration 02 from 32 km to 88 km (part 02); (top) several common images gathers; (bottom) the pre-stack depth-migrated image for line SIS07 .

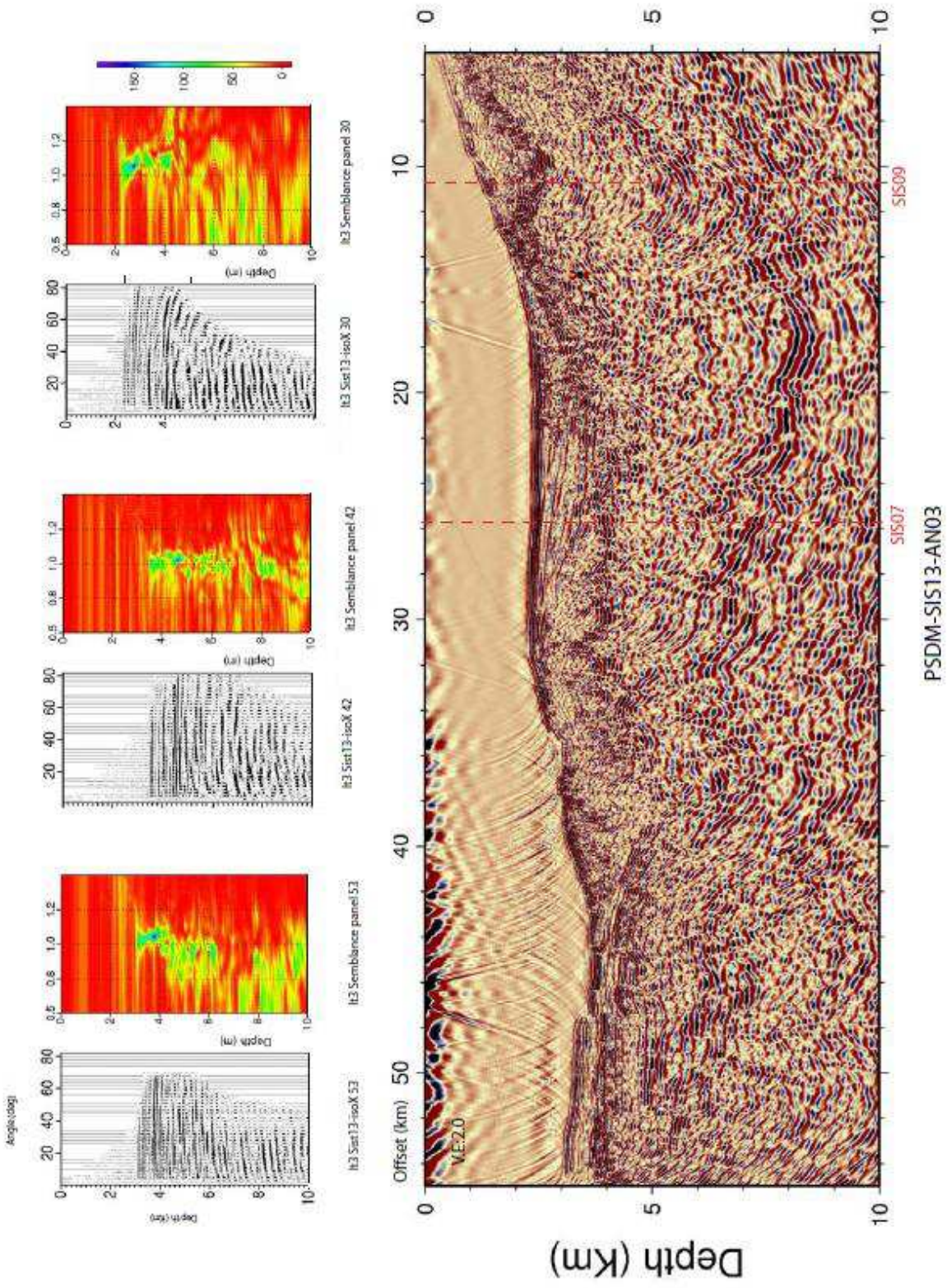

Figure 5. 5 Examples of quality and accuracy control of depth-migrated seismic line SIS13; top) Common images gathers and semblances for the kilometers 30, 42 and 53, the maximum semblance is blue; bottom) pre-stack depth-migrated image for profile SIS13

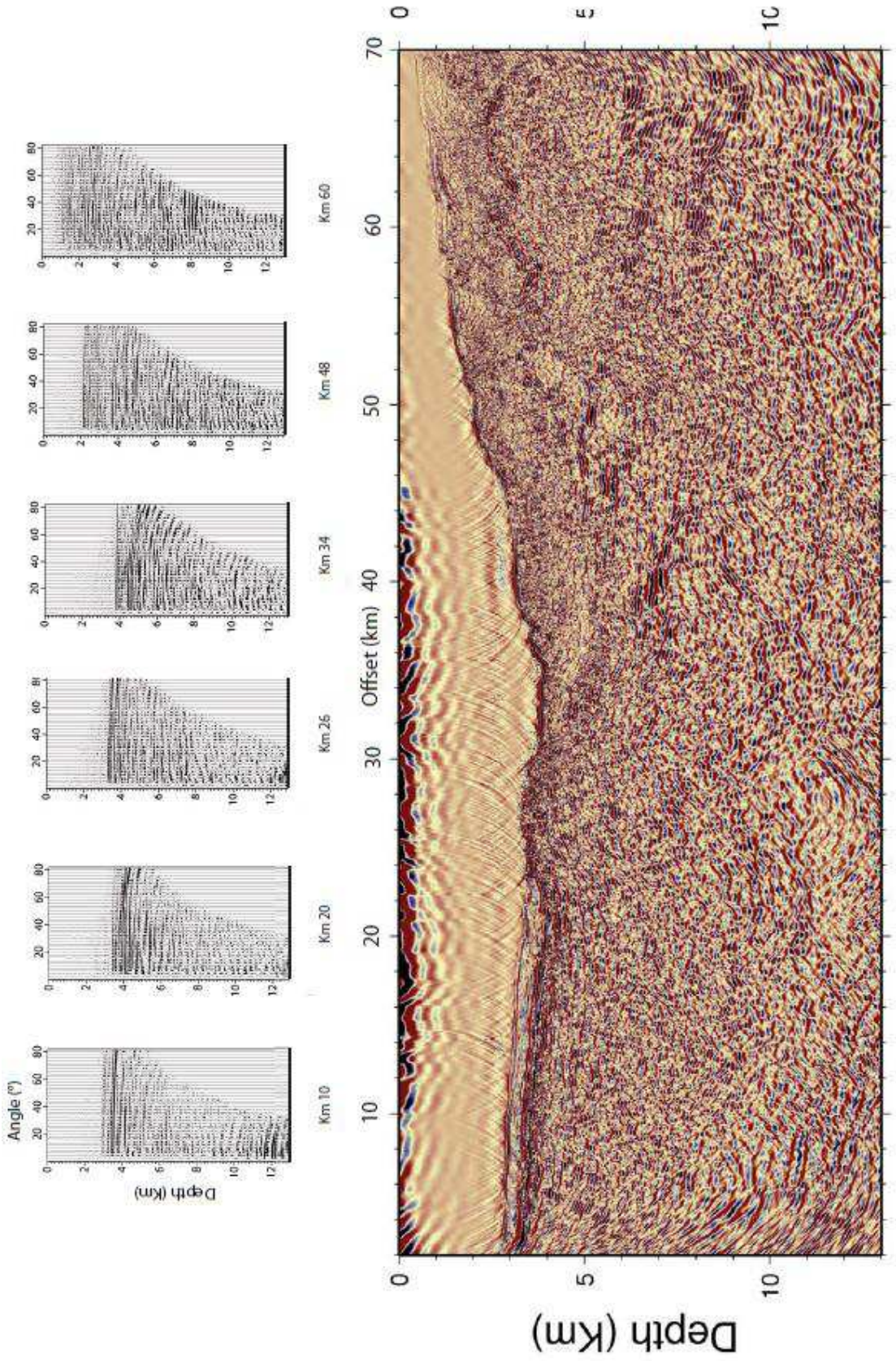

Figure 5. 6 Examples of quality and accuracy control of depth-migrated seismic line SIS14; top) Common images gathers; bottom) pre-stack depth-migrated image for line SIS14.

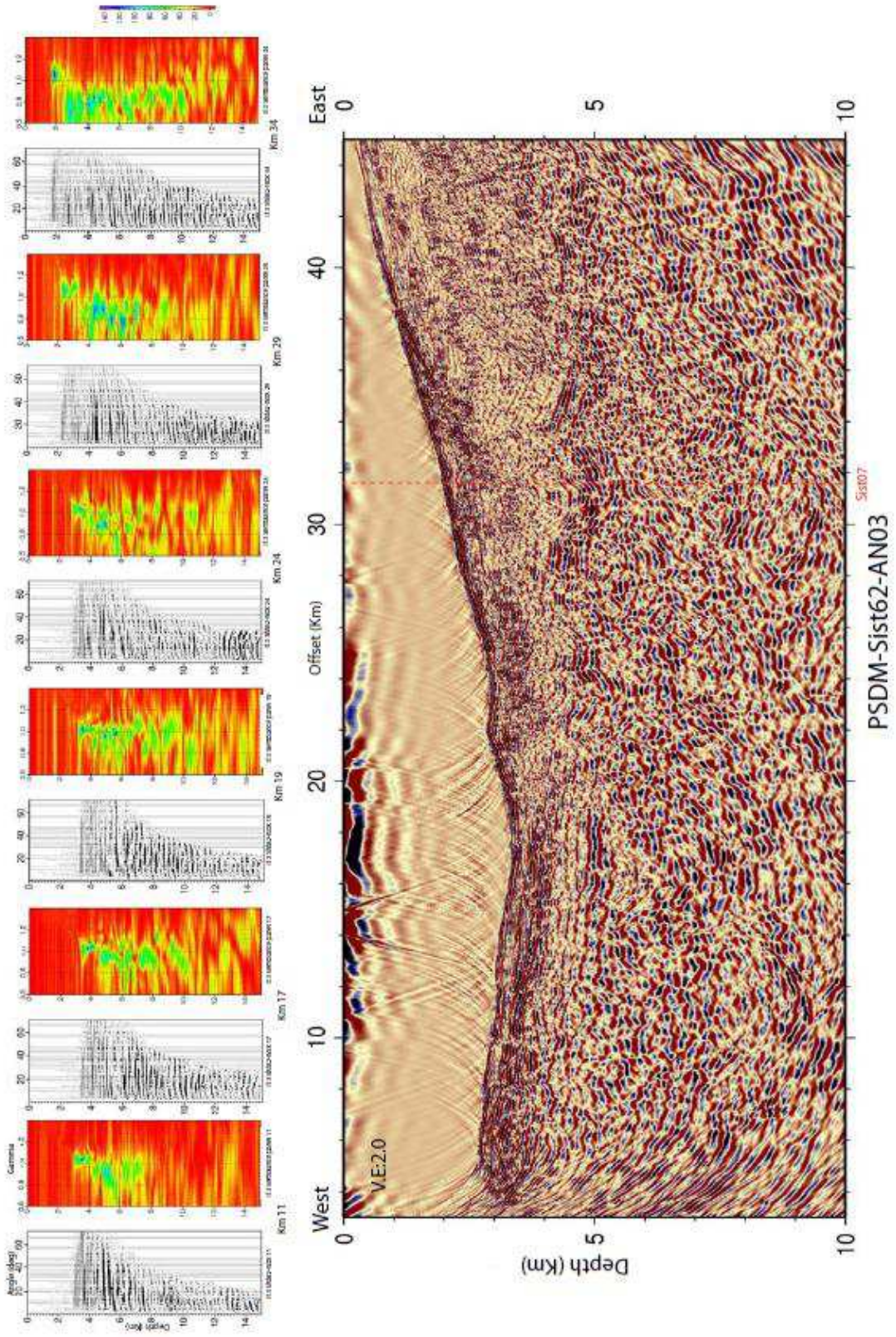

Figure 5. 7 Examples of quality and accuracy control of depth-migrated seismic line SIS62; top) several common images gathers and semblances, the maximum semblance is blue; bottom); the pre-stack depth-migrated image for line SIS62, iteration 3 (AN03).

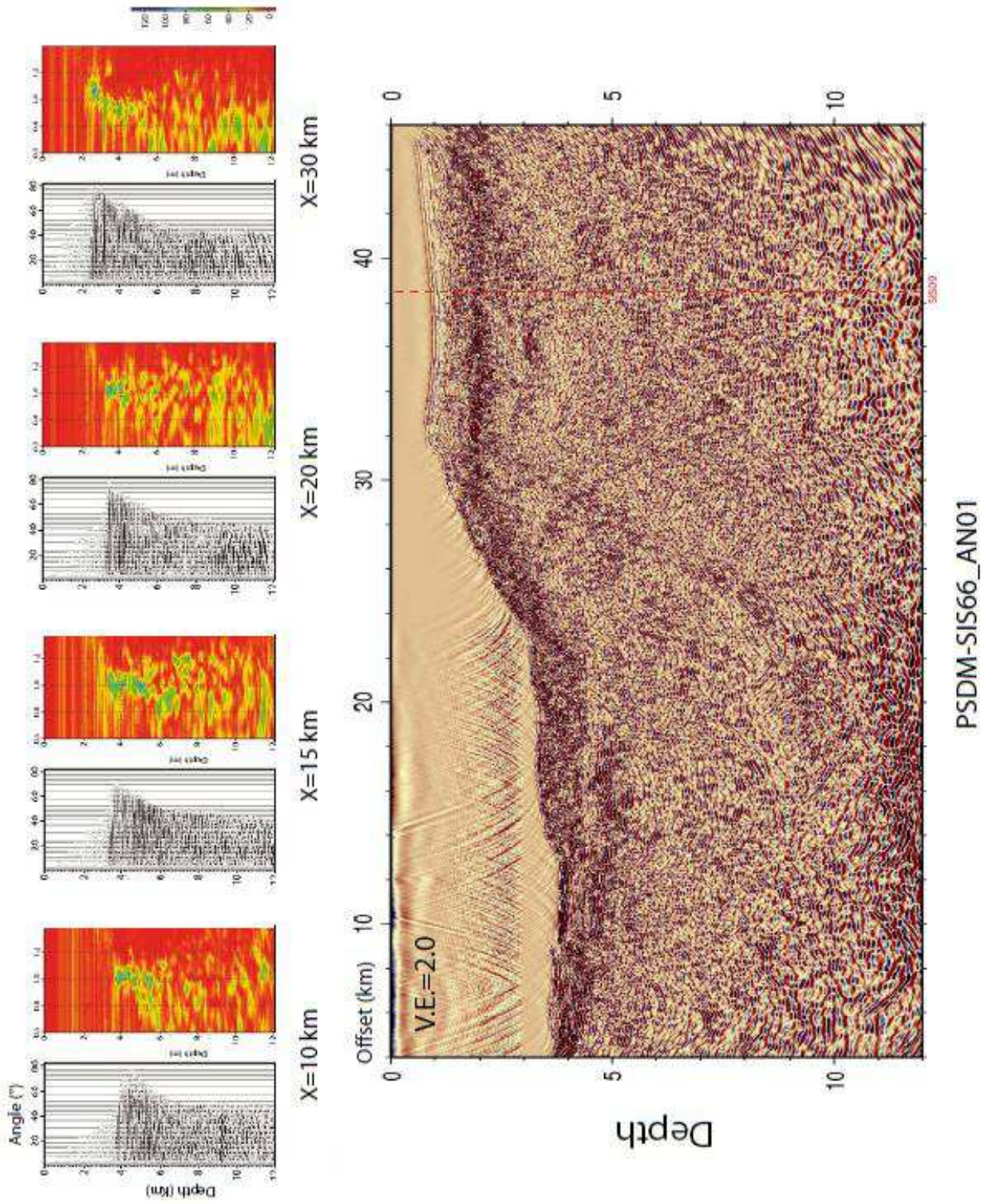

Figure 5. 8 Examples of quality and accuracy control of depth-migrated seismic line SIS66; top) several common images gathers and semblances, the maximum semblance is blue; bottom); the pre-stack depth-migrated image for line SIS66, iteration 1 (AN01).

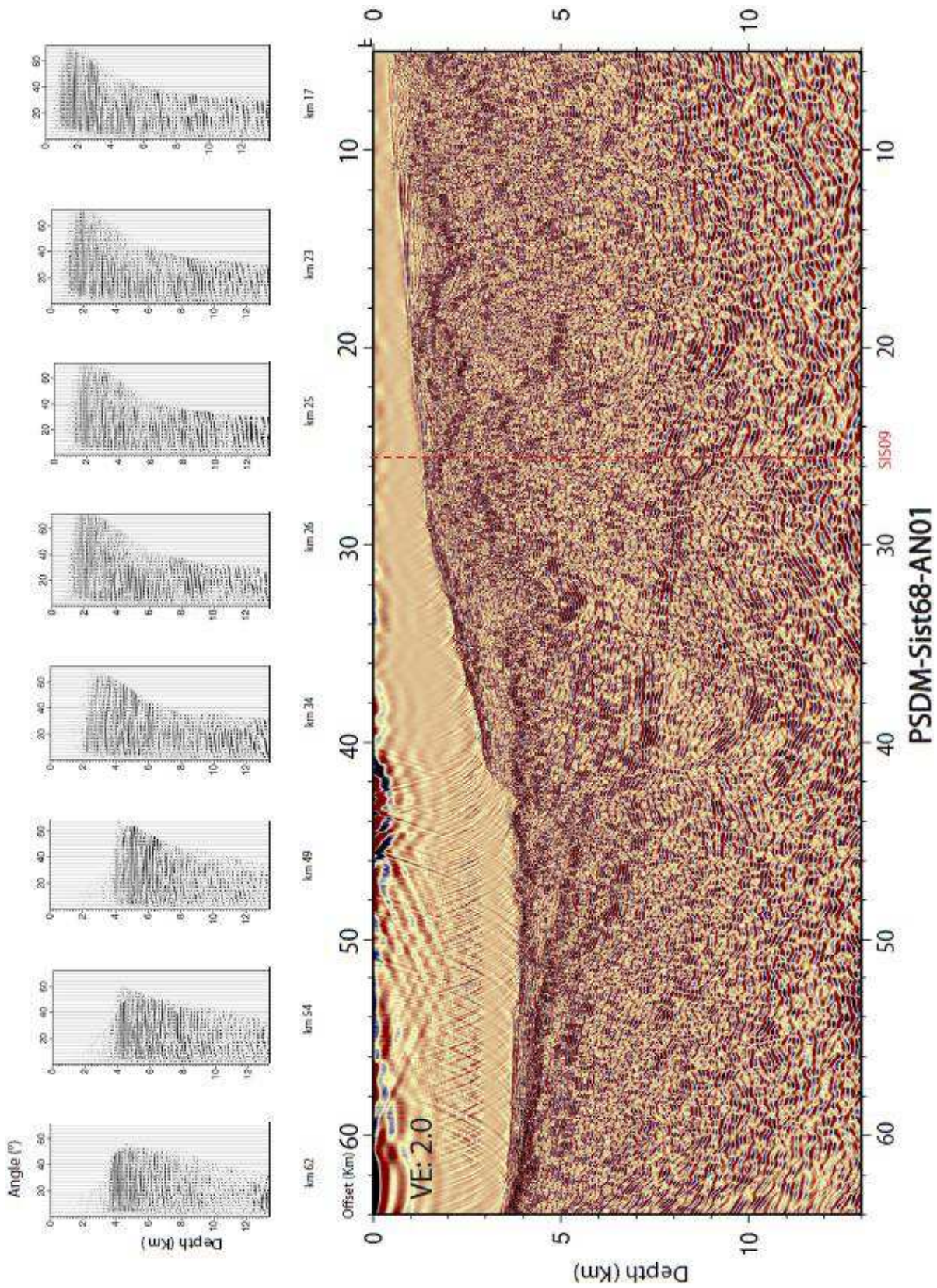

Figure 5. 9 Examples of quality and accuracy control of depth-migrated seismic line SIS68; top) several common images gathers; bottom) the pre-stack depth-migrated image for line SIS66, iteration 1 (AN01).

5.4. Wide-Angle Seismic and Mixed Models

5.4.1. Wide-Angle Seismic

The wide-angle refers (WA) to the incident angle near the critical angle for the seismic P wave. According to seismic theory and practices, the reflection is very strong when the seismic wave interfaces with the wide incident angle; this is very used to explore the structure of the Earth's crust (Wang *et al.,* 2007). The WA seismic (Figure 5.10) is used to measure the travel time of seismic waves between a source and a receiver using a variable offset (receiver distance from the start of the line). The target is to define the seismic velocities in the materials and the geometry of the different layers using essentially P waves (Figure 5.11; 5.12) (e.g., Pi, PmP (reflection from oceanic Moho), Pn, PiP).

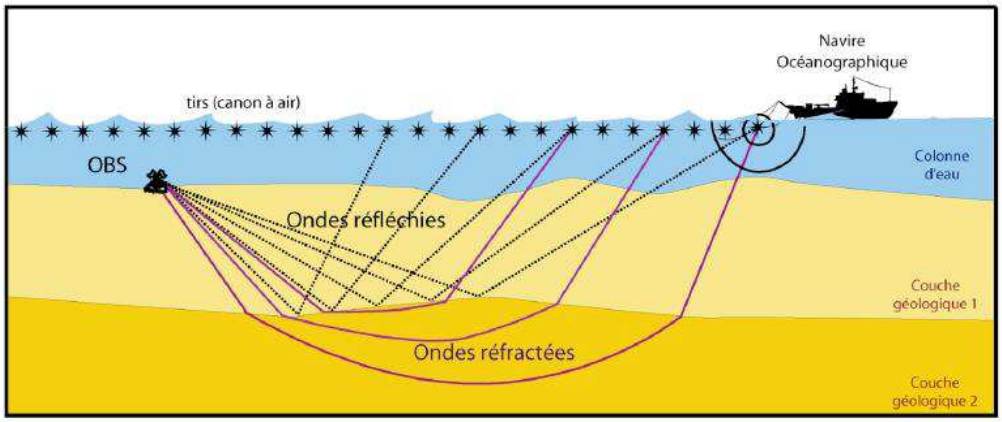

Figure 5. 10 Wide-Angle seismic and the different type of recorded seismic waves

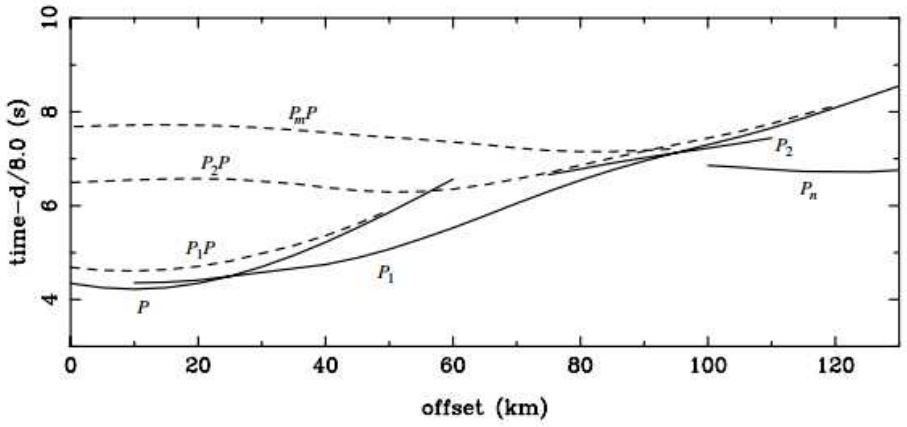

Figure 5. 11 Traveltime curves of arrivals from source located at (x,y)=(55, 25) km recorded by receivers that lie along the line x= 15 km. PiP= reflection from the i-th interface, P'= refractions that turn beneath interface i (Pi); P corresponds to the direct arrival; (Rawlinson et al., 2001).

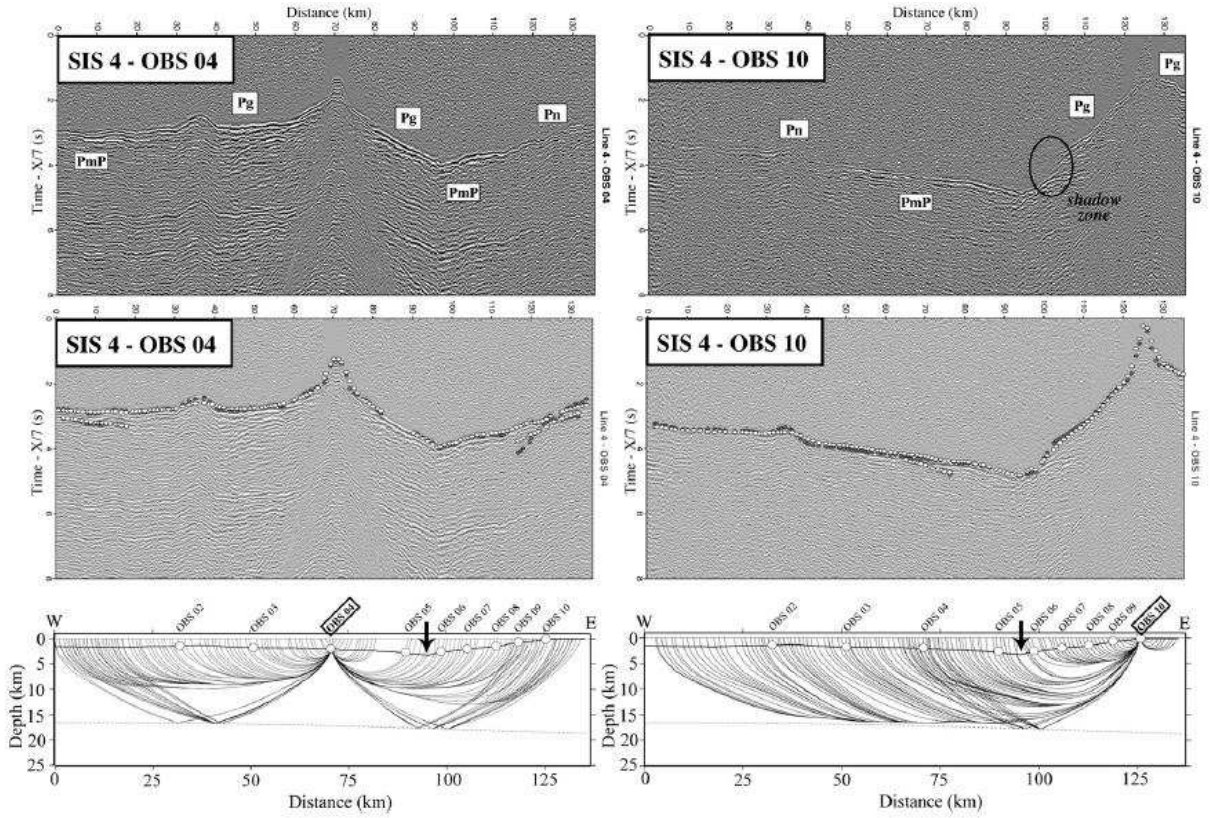

Figure 5. 12 Example of wide-angle seismic data for the OBS 04 and 10 from line SIS04 (SIS05), showing the calculated travel times (top), the picked (middle), and their corresponding ray paths (bottom) for the best velocity model; first arrival times (Pg and Pn) and refraction from the Moho (PmP) are indicated in the upper images (Gailler et al., 2007).

5.4.2. Acquisition, SISTEUR Cruise

Wide-angle seismic data were acquired during the SISTEUR cruise (2000), using a source of eight 16-1 air-guns, shot at 125 m intervals; here, 24 OBS were deployed with a configuration showed in Figure 5.13. The OBS prepared in the laboratory of INOCAR, were shipped on Orion and deployed along the Ecuadorian margin between 2°20'S et 1°S in order to characterize the deep structure of the margin and explore the seismogenic zone. The data will help us to prepare mixed velocity models that will be used to obtain Pre-Stack-Depth-migrated images between the Peninsula of Manta and Salinas. Wide-angle data for profiles SIS05, SIS07, SIS09 are available and were used to improve our velocity models.

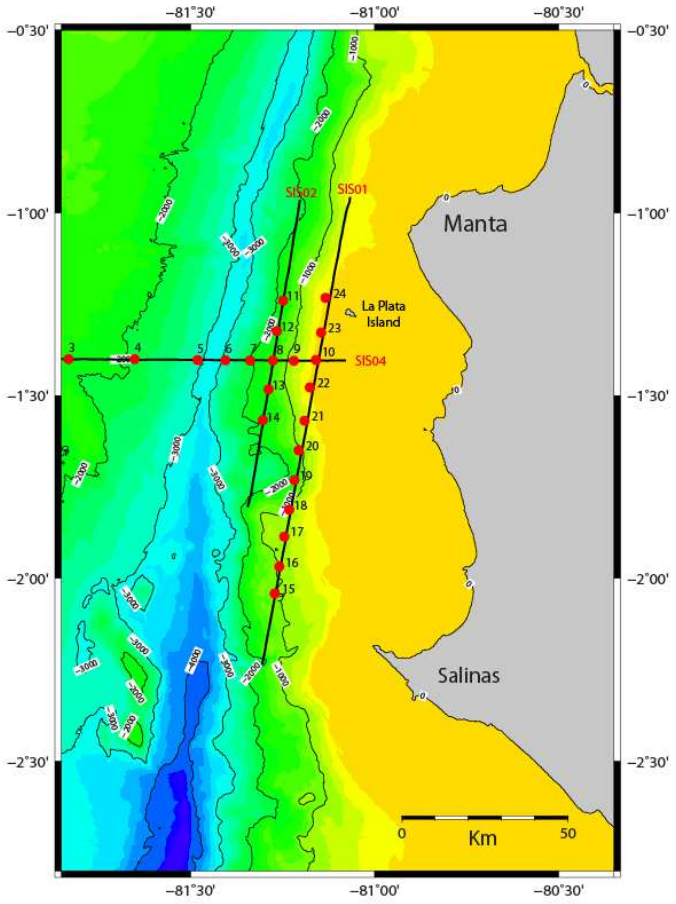

Figure 5. 13 Map showing the Ecuadorian bathymetry, the profiles (black lines) and OBS position (red circles) of the SISTEUR cruise.

5.4.3. PSDM using Mixed Velocity Models

One way to improve deep reflector imaging is to increase the offset/depth ratio. Because of high-resolution MCS acquisition geometry fails to accurately image deep level structures, and low-resolution WA acquisition geometry provides good constraints on deep level structures, we use an integrated processing work flow applied to coincident MCS and WA data sets to develop PSDM images and using mixed velocity models, methodology that have already applied by Agudelo *et al.,* (2009) to a seismic transect consisting of coincident MCS and OBS seismic data collected across the north Ecuador–SW Colombia convergent margin.

This methodology, described in Agudelo *et al.,* (2009) and Agudelo (2005), consists in combining the deep velocity structure inferred from first-arrival travel-time tomography of WA data with the shallow velocity model inferred from MCS to build a mixed velocity macro-model

appropriated for PSDM to image the crustal structure. At large depths (z > 5 km), the information coming from with wide-angle data is used to estimate a "mixed" velocity model. In mixed models, the MCS velocity macro-model corresponds to the shallow part; whereas wide-angle tomographic velocity model corresponds to the deeper part of the mixed model. A transition part is established between the MCS and the wide-angle velocity models. This mixed model should provide a better resolution in depth, where the resolution of MCS is not so high (Agudelo, 2005, Agudelo *et al.,* 2009).

5.4.4. PSDM of profile SIS05

A blocky velocity model for SIS05 was developed by Graindorge *et al*., (2004), through a combination of travel-time inversion and amplitude modeling of observed arrivals. They applied the ray-trace modeling to get a starting model, and inverted the travel times of refractions and reflections phases using the ray trace-based inversion scheme of Zelt *and* Smith (1992).

We combined a smoothed version of the blocky velocity model (Figure 5.14.c) with the shallow velocity model inferred from MCS data (Figure 5.14.a) to build a mixed velocity macromodel (Figure 5.14.e), using a transitional zone between 6 and 8 km of depth. This macromodel is further refined by joint inversion of normal incidence travel-times picked on stack sections, and refraction/wide-angle reflection travel-times picked on OBS gathers.

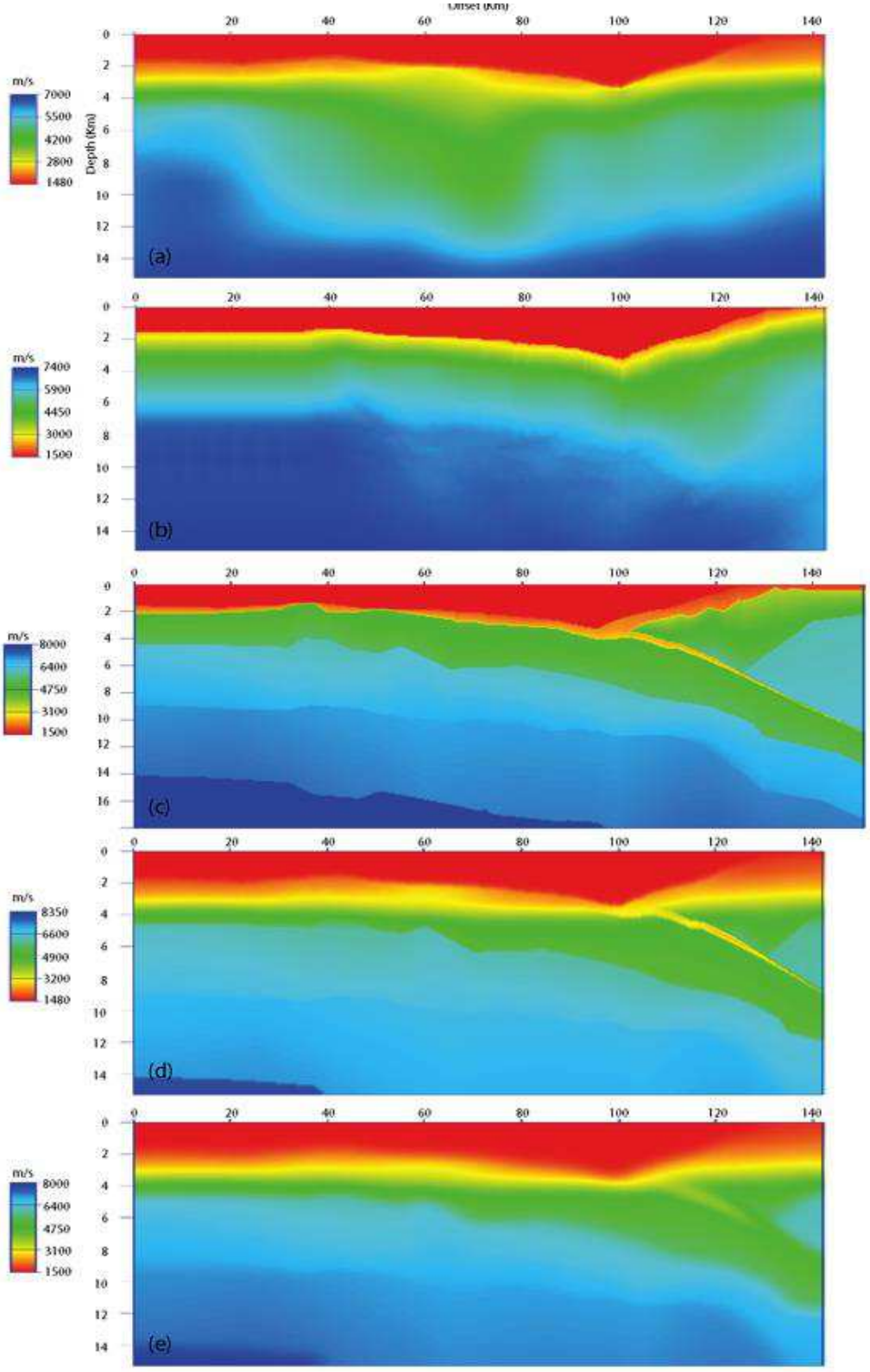

Figure 5. 14 Velocities models for the SIS05: (a) third iteration using Al-Yahay's Method to correct the macro-model; (b) tomographic model (Gailler, 2005); (c) model Zelt; (d) result of mixing model "a" and "c" with a transitional zone between 3 and 5 km of depth; (e) model d with a smooth tau=5000. An inversion is appreciable for, model "c" to "e".

Figure 5.14.b corresponds to the tomographic model (Gailler, 2005), which does not show the velocity inversion, and Figure 5.14.d is the macro-model without any smoothing. An initial smoothing (tau=5000) on the velocity model (Figure 5.14.e) produced a white band on PSDM image, which was attenuated by increasing the smoothing of the velocity model to a value of 10000; thus, we obtained a more suitable velocity model (Figure 5.15) that was used to obtain the final PSDM for profile SIS05 (Figure 5.16)

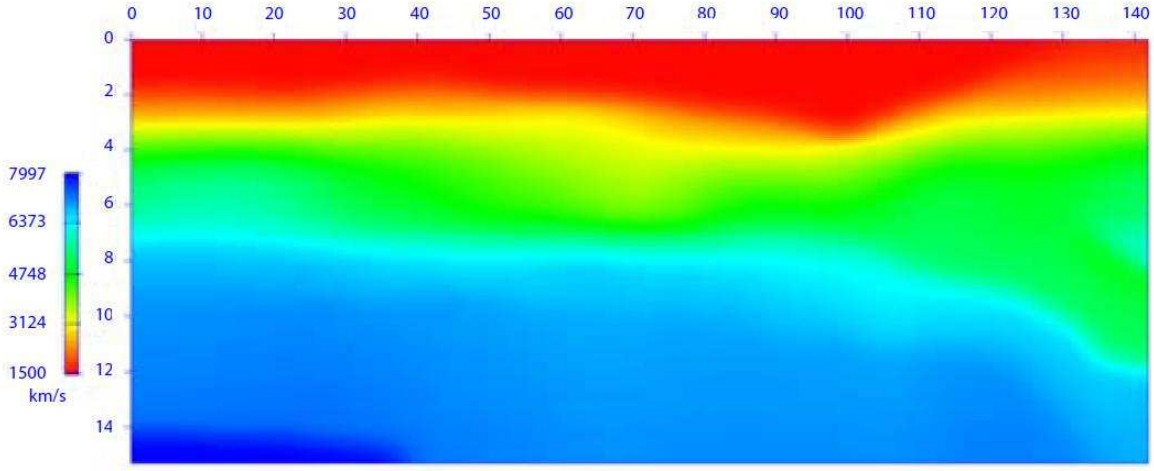

Figure 5. 15 Mixed velocity model of profile SIS05. This model is result of mixing our MCS model with Zelt model of Graindorge et al. (2004). The horizontal and vertical axes are in km, and the scale of colors represents the velocity in m/s.

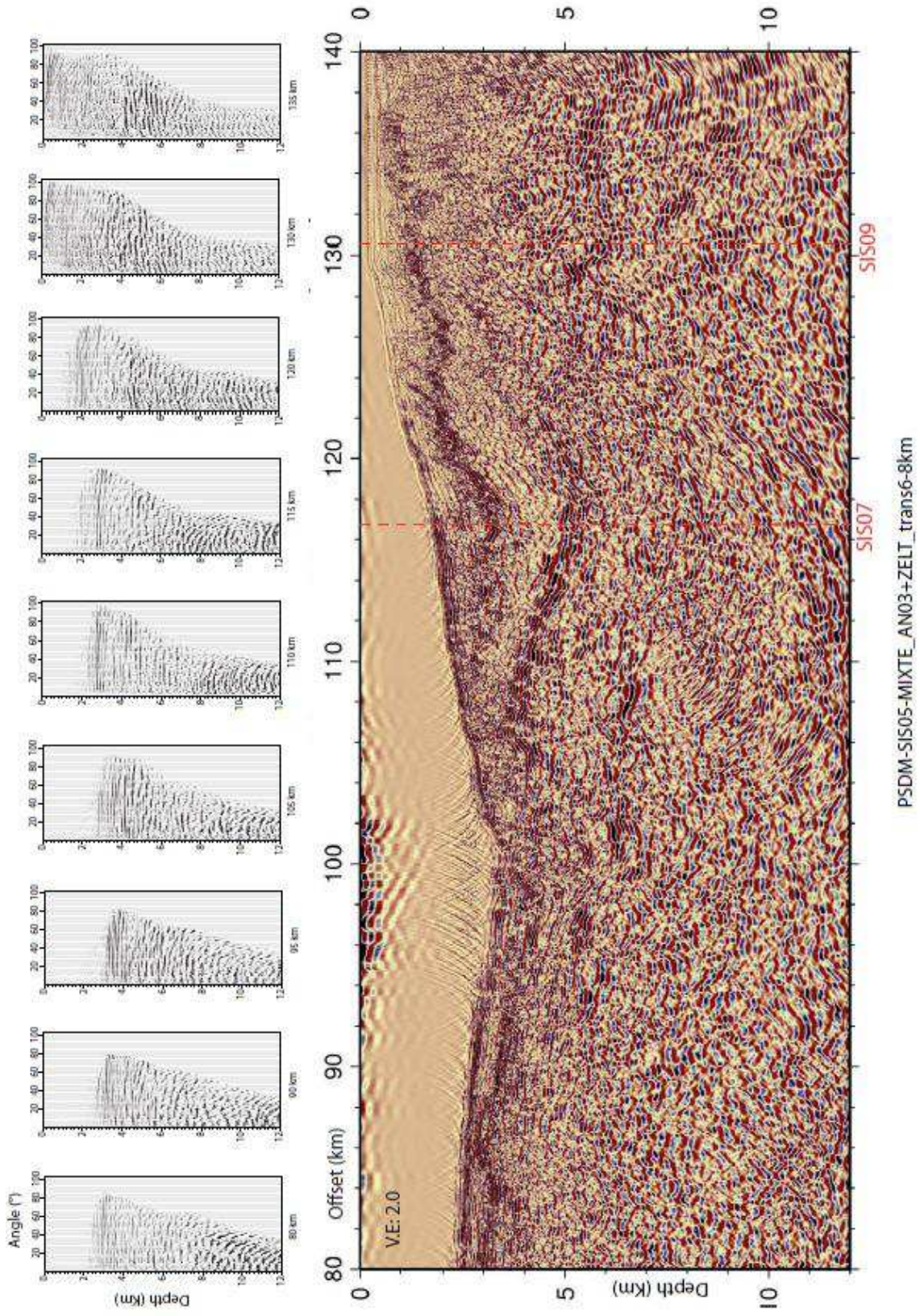

Figure 5. 16 Examples of quality and accuracy control of depth-migrated seismic line SIS05 using the mixed velocity model; (top) several common images gathers; bottom) the pre-stack depth-migrated image for line SIS05 cut from 80 to 140 km.

5.4.5. PSDM of profiles SIS09 and SIS07

Using the same methodology applied for SIS05 (SIS04), we mixed the WA velocity model of SIS09 from Gailler (2005) with our respective MCS velocity model to obtain a final mixed velocity model (Figure 5.17). For the PSDM of SIS07, we started with a velocity model provided by Agudelo *and* Ribodetti. They mixed WA velocity model from Gailler (2005) with a MCS model, and they obtained a final mixed model (Figure 5.18). The MCS model and the data used for the PSDM of SIS07 had a different processing that did not eliminate completely the multiples.

The PSDM of SIS09 and SIS07 obtain with these velocity models (Figure 5.17 and 5.18) all with a vertical exaggeration of 2 and their respective ISO panels (SIS09, Figure 5.19-5.22) and (SIS07, Figure 5.23).

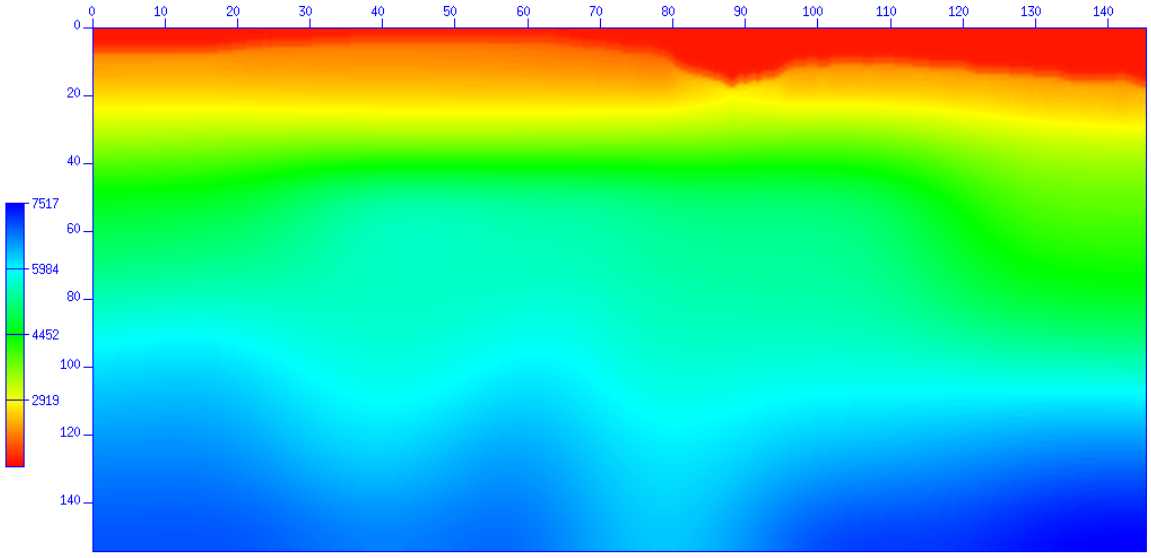

Figure 5. 17 Mixed velocity model of profile SIS09; this model is result of mixing our MCS model with OBS model of Gailler (2005); the horizontal and vertical axes are in km, and the scale of colors represents the velocity in m/s.

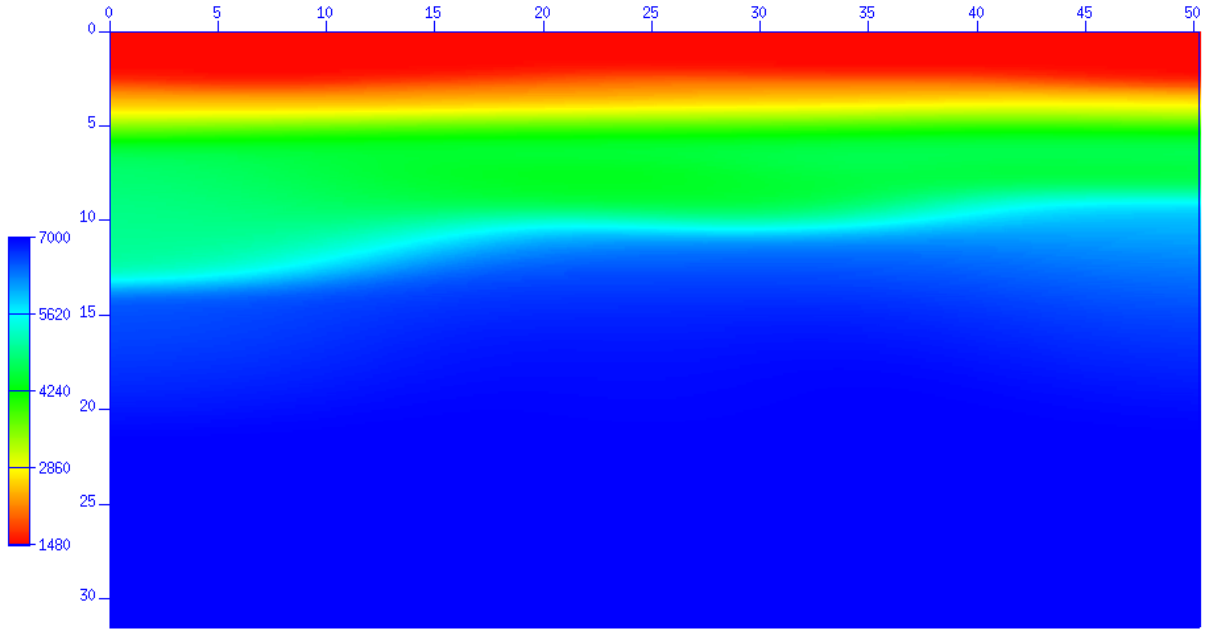

Figure 5. 18 Mixed velocity model of profile SIS07 provided by Agudelo and Ribodetti; this model is result of mixing a MCS model with OBS model of Gailler (2005). The horizontal and vertical axes are in km, and the scale of colors represents the velocity in m/s.

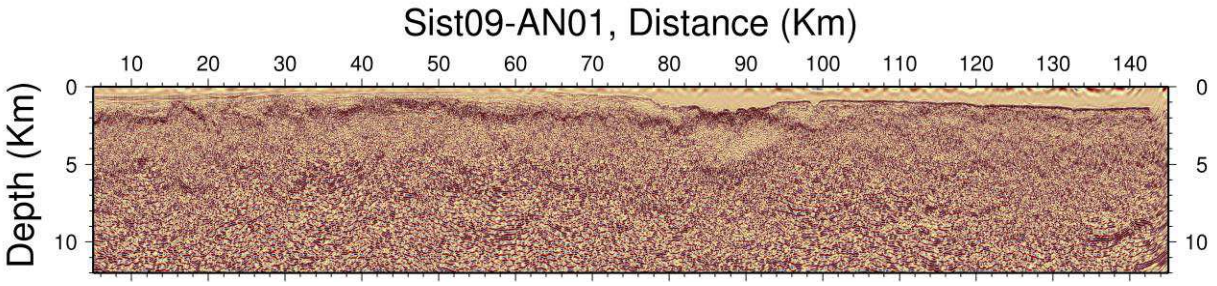

Figure 5. 19 PSDM of Profile SISIS09 with a mixed velocity model. Zooms are shown in figures 5.20, 5.21 and 5.22, with their Iso-X panels .

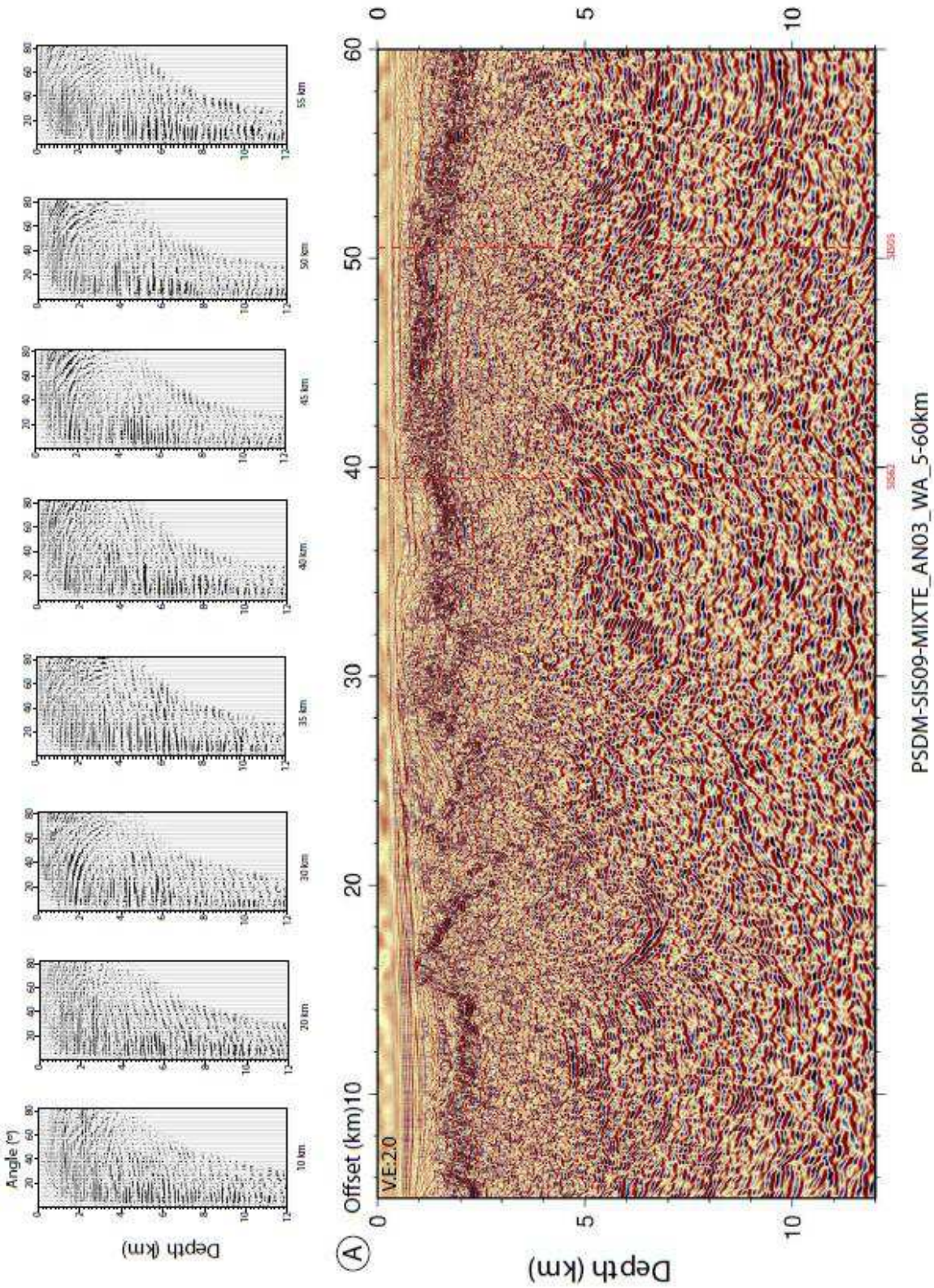

Figure 5. 20 Examples of quality and accuracy control of depth-migrated seismic profile SIS09 using a mixed velocity model; (top) several common images gathers; bottom) the pre-stack depth-migrated image of Figure 5.19 from km 5 to km 60.

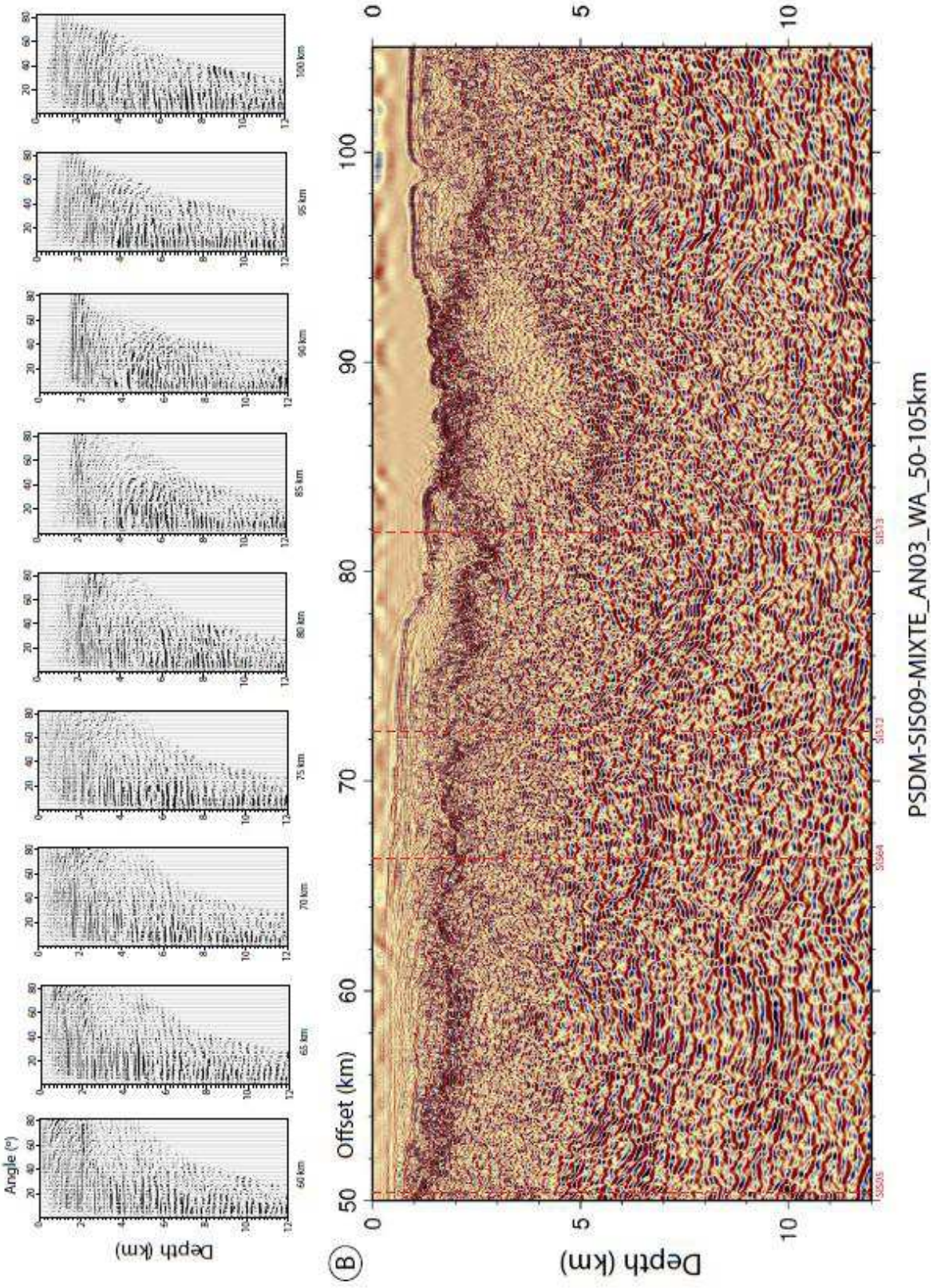

Figure 5. 21 Examples of quality and accuracy control of depth-migrated seismic profile SIS09 using a mixed velocity model; (top) several common images gathers; bottom) the pre-stack depth-migrated image of Figure 5.19 from km 50 to km 105.

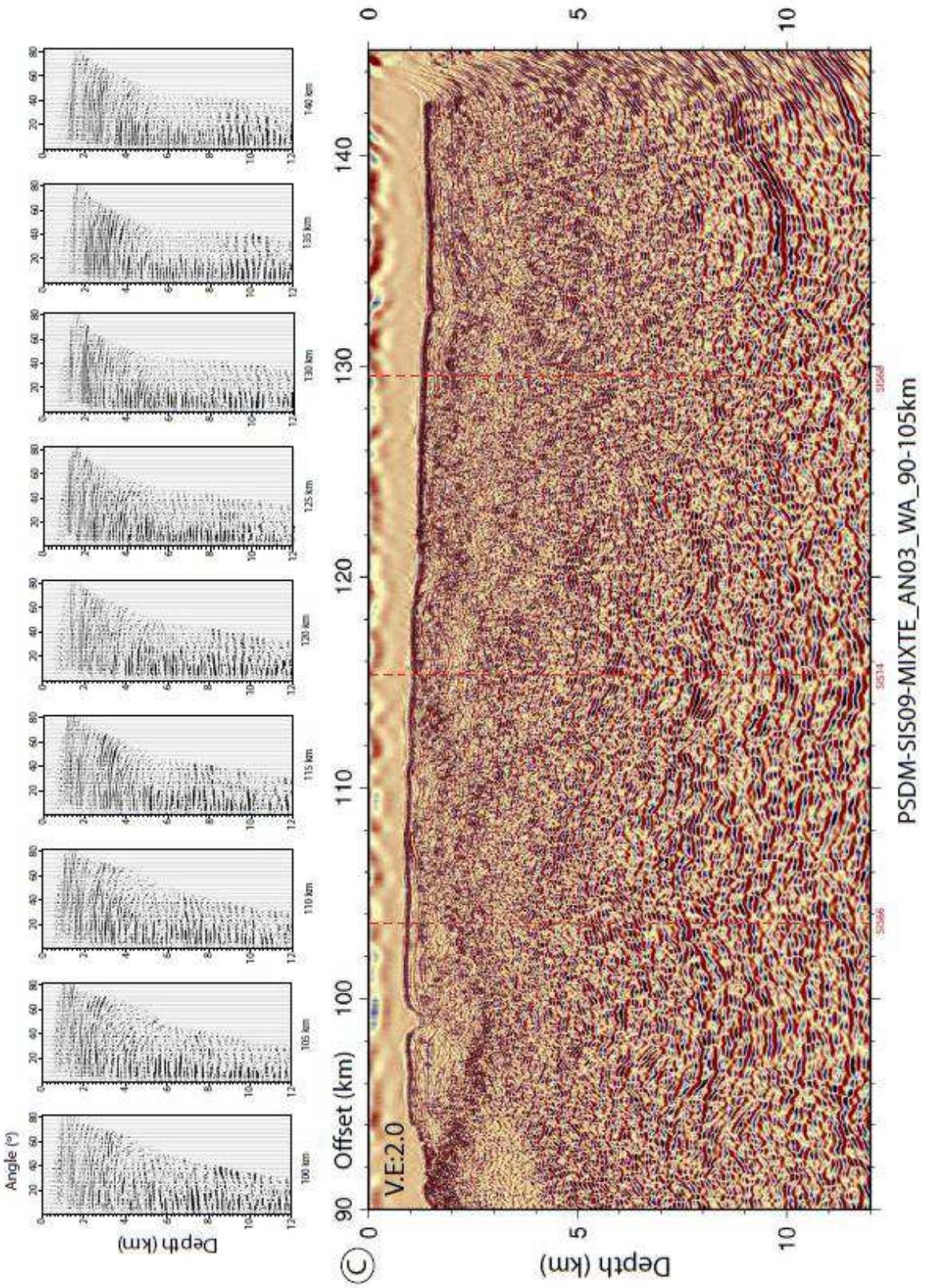

Figure 5. 22 Examples of quality and accuracy control of depth-migrated seismic profile SIS09 using a mixed velocity model; (top) several common images gathers; bottom) the pre-stack depth-migrated image of Figure 5.19 from km 90 to km 145.

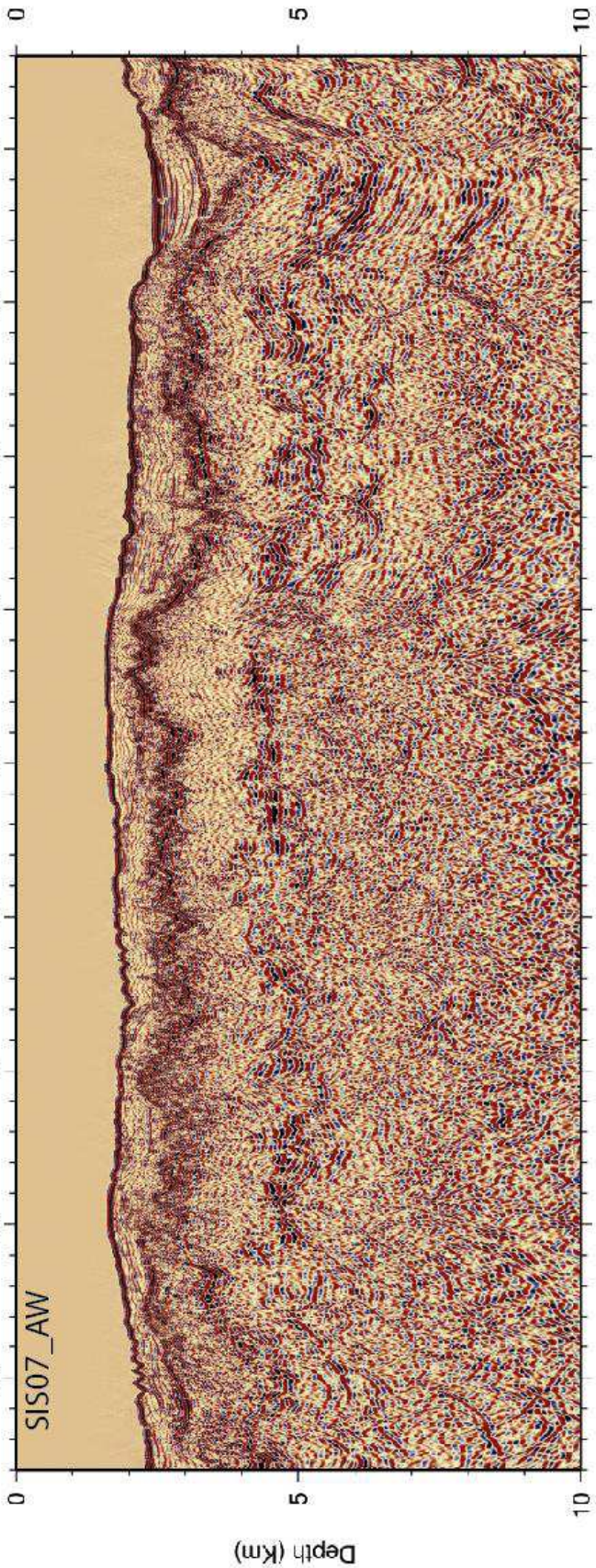

Figure 5. 23 PSDM image for profile SIS07 using the mixed model of Figure 5.18.

CHAPTER 6

RESULTS AND INTERPRETATIONS

The smooth and linear outer-margin wedge slope in the northern part of the study area changes to a morphologically rough slope, south of latitude 1º35'S. This drastic morphologic change likely reflects structural changes within the basement margin. We choose to present the seismic reflection results from North to South according to the morphologic changes along strike the margin, from the smooth (Figure 6.1) to the rough morphology (Figure 6.4).

6.1. Margin structures beneath the smooth outer wedge slope: Profiles: SIS62 and SIS05

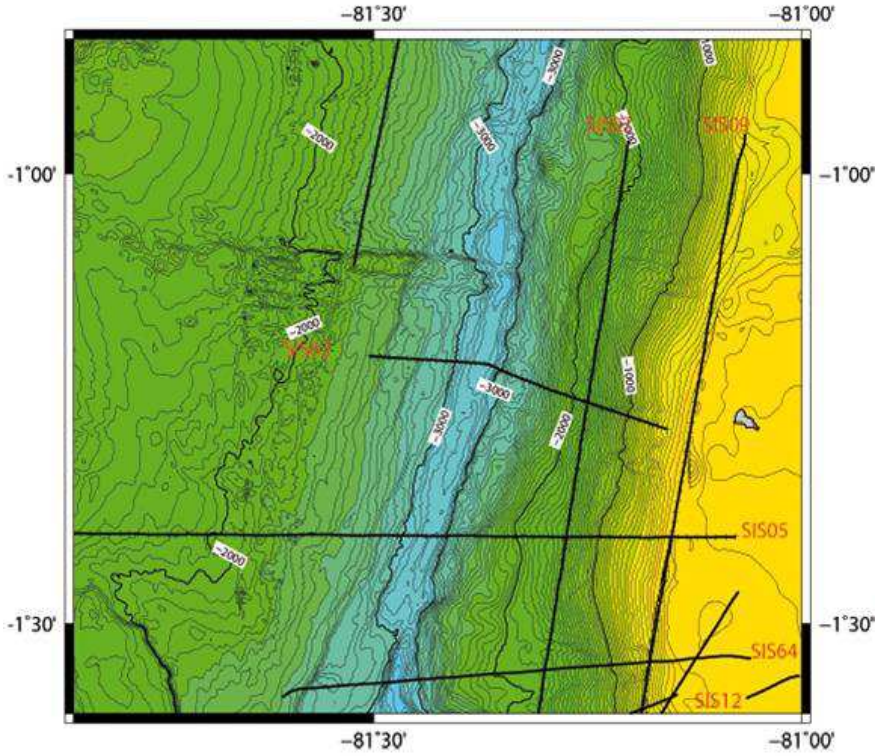

Figure 6. 1 Bathymetric map of the northern segment of our study zone close to La Plata Island (After Michaud et al., 2006); contour lines indicate the seafloor depth each 50 meters; in yellow: shallower depths and in light blue: deeper depths; black lines indicate the position of Multichannel Seismic profiles from SISTEUR (2000), in red their respective names .

We will first present Profile SIS05 because it represents the most complete section across the smooth outer-wedge reaching the continental shelf up to a distance equivalent to the trench- La Plata Island distance. Besides, it is the only perpendicular-to-the-trench depth profile obtained with a mixed velocity model (Chapter 5, Figure 5.14).

6.1.1. Profile SIS05

Profile SIS05 (Figure 6.2) images crustal structures of the convergent margin from the subducting Carnegie Ridge to the continental shelf. Along the profile, the sea-floor reaches ~3.3 km and 0.15 km depth respectively across the trench and the continental shelf. From the continental shelf edge (km 129.5) to the trench axis, the outer wedge slope dips with a 6º angle and shows a remarkably smooth morphology, only disturbed by a small-amplitude, long-wavelength seafloor bulge, at km 123.

Along this profile, the Carnegie Ridge (CR) seafloor gently dips trench-ward and shows east-facing scarps between km 90 and km 100. The dipping seafloor is underlain conformably by well-stratified, 0.6-1-km-thick, ~2.1 km/s Vp velocity sedimentary layer (**S1**). The layer overlies, more or less in conformity, a strong reflector that we interpret as the Top of the Oceanic crust (**TOC**), which according to the mixed-velocity model (Figure 5.14) has a velocity of ~4.0 km/s. Both TOC and S1 are offset vertically by small-throw normal faults associated with the seafloor scarps. At the seismic scale, no unconformable turbidite trench fill can be interpreted in the trench, which is therefore considered devoid of terrestrial sediment.

Deeper in the Carnegie Ridge crust, at 5 to 6 km depths where Vp velocity reaches ~4.6 km/s, a group of strong reflectors (**DR**) underlies the fault zone and dips landward beneath the margin. According to ODP Site 1238 (Mix *et al*., 2003, site 1238) located farther seaward on the CR, layer S1 can be interpreted as dominated by nannofossil ooze with discrete ash levels. However, layers enriched with hemi-pelagic sediment may be encountered near the summit of the layer.

Both layer S1, and TOC reflector extend landward beneath the margin tip. However, layer S1 is sharply truncated and overlain by a small frontal prism no more than 5 km wide. In contrast, TOC reflector, whose amplitude is locally enhanced, extends beneath the margin, up to the landward termination of the line at a depth of ~6 km. This reflector that dips landward with a very shallow average slope of **~4º** is characterized by a series of three ~1 km-high peaks (Pk17, 18, and

19, in Figure 6.2). According to our mixed-velocity model (Figure 5.14), the peaks are characterized by Vp velocities ranging between ~4.7 and ~5.5 km/s.

The outer wedge thins from ~6 km at the continental shelf edge to ~1 km at the frontal prism (km 117), extending over a distance of ~30 km from the trench. The Top of the Basement, indicated by strong reflector **TB**, dips from below the continental shelf and terminates against the frontal prism. This reflector is highly disrupted and separates well-stratified, 0.5-1.5 km-thick layer **S2** from the underlying basement. Both the basement and reflector TB are deformed by normal faults, defining small grabens (km 115 and 123). The faults increase in density, seaward, across the wedge tip. Only fault **F1** appears to cuts layer S2 and slightly deforms the seafloor, suggesting that the fault is active and extensional.

Basement units **B1** and **B2** are identified based on their differing reflectivity and contrasting Vp velocities 2.6-4.0 km/s and 2.3-4.9 km/s, respectively. They are separated by intra-basement reflector **IB**. Unit B1 shows continuous and poorly reflective layers forming a syncline. Unit B1 comes into contact with the TOC, where the trench-ward flank of the syncline parallels the TOC and shows enhanced reflectivity. We interpret this contact as the décollement thrust "De". Unit B2 underlies B1, and shows semi-continuous, strongly reflective, and highly deformed strata, which lay in contact with the undulated segment of the TOC/De décollement between km 122 and the landward end of the profile.

In conclusion, profile SIS05 is characterized by a remarkable smooth morphology, a very shallow dipping Décollement De (~4°), no detectable subduction channel and three ~1-km-high peaks. The normal faults density increases seaward, cutting the highly disrupted top of the basement and margin basement. The basement shows two differing reflectivities and velocities that permit to differentiate units B1 and B2.

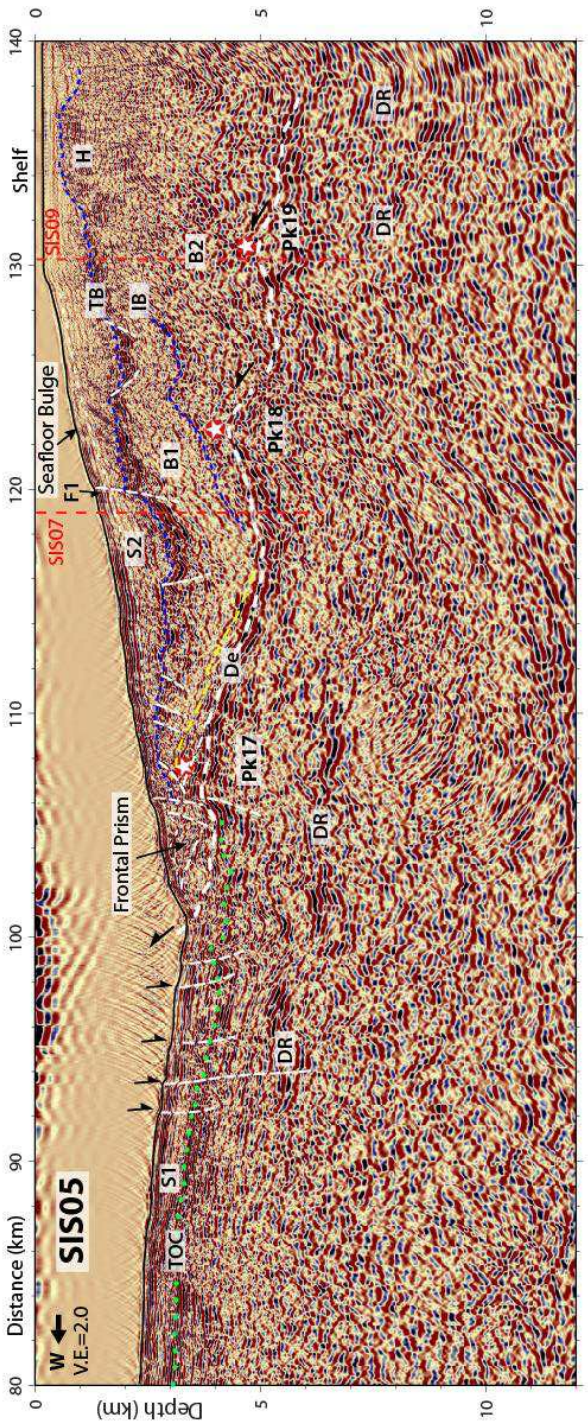

Figure 6. 2 Interpretation of the Pre-Stack-Depth Migration (PSDM) image of profile SIS05. Localization is shown in Figure 6.1. This profile is characterized by a remarkably smooth morphology, a very shallow average dipping angles of ~4°, and three ~1-km-high peaks (Pk17, 18, and 19). TOC: top of the oceanic crust (green dashed line); S1-S2: sedimentary layers; S1 is dominated by nannofossil ooze with discrete ash levels (Mix et al., 2003, site 1238); DR: deep reflector; thin white lines represent faults ; F1: sub-active normal fault; De: décollement (white thick dashed line); TB: top of the basement (blue dashed lines); B1-B2: basement units; IB: intra-basement reflector (in blue); red vertical dashed lines represent the intersection with strike MCS profiles; V.E: vertical exaggeration .

6.1.2. Profile SIS62

Profile SIS62 (Figure 6.3), located north of Profile SIS05, extends over a distance of 60 km from the oceanic crust with a maximum depth of ~3.5 km at the trench to a 0.2-km-depth across the outer wedge, only ~8.5 kilometers from La Plata Island (Figure 6.1). The smooth-morphology seafloor of the outer-wedge slope dips 6º.

The Carnegie Ridge seafloor gently dips landward, and does not show scarps along this profile. Similarly to Profile SIS05, the oceanic seafloor along Profile SIS62 overlies the sedimentary layer **S1**, which is only 0.2-0.6-km-thick above the strong reflector, interpreted as the Top of the Oceanic Crust (**TOC**). Beneath the margin wedge, the TOC that we interpret as the décollement (**De**), as in profile SIS05, reflects the absence of a subduction channel. De dips landward with a very shallow **~2.5º dipping angle**, and extends up to the line termination, at a ~4.8 km depth. The décollement shows an undulated shape with several small amplitude peaks (Pk14, 15, and 16), which may result from the décollement molding over an underlying horst-and-graben structure. The structure is controlled by normal faults cutting downward through the subducting Ridge crust.

Similar to Profile SIS05, unconformable turbidite trench fill cannot be interpreted in the trench. However, a ~4-km-wide frontal prism is identified at km 22, and is cut by several thrusts that extend to the trench seafloor.

Across the outer wedge, layer **S2** is a ~1.2-to-1.5 km-thick monocline separated from basement units B1 and B2 by seaward-dipping and highly-disrupted **TB** reflector. This reflector is vertically offset by normal faults, which are considered inactive because none of them deforms layer S2 and reach the seafloor. **B1** and **B2** units show similar reflectivity characteristics as in Profile SIS05. However, reflector **IB** that separates these units is better defined as a change of reflectivity than as a reflector. Molding of the décollement over the underlying horst-and-graben structure reflects in the internal structure of unit B1, which is depressed over the graben axis at km 31.

In conclusion, profile SIS62 shows a smooth seafloor with an outer-wedge slope of 6°. The top of the oceanic crust dips landward with a very shallow angle of 2.5°, no evidence for a subduction channel, and the décollement presents an irregular shape spotted by three small peaks.

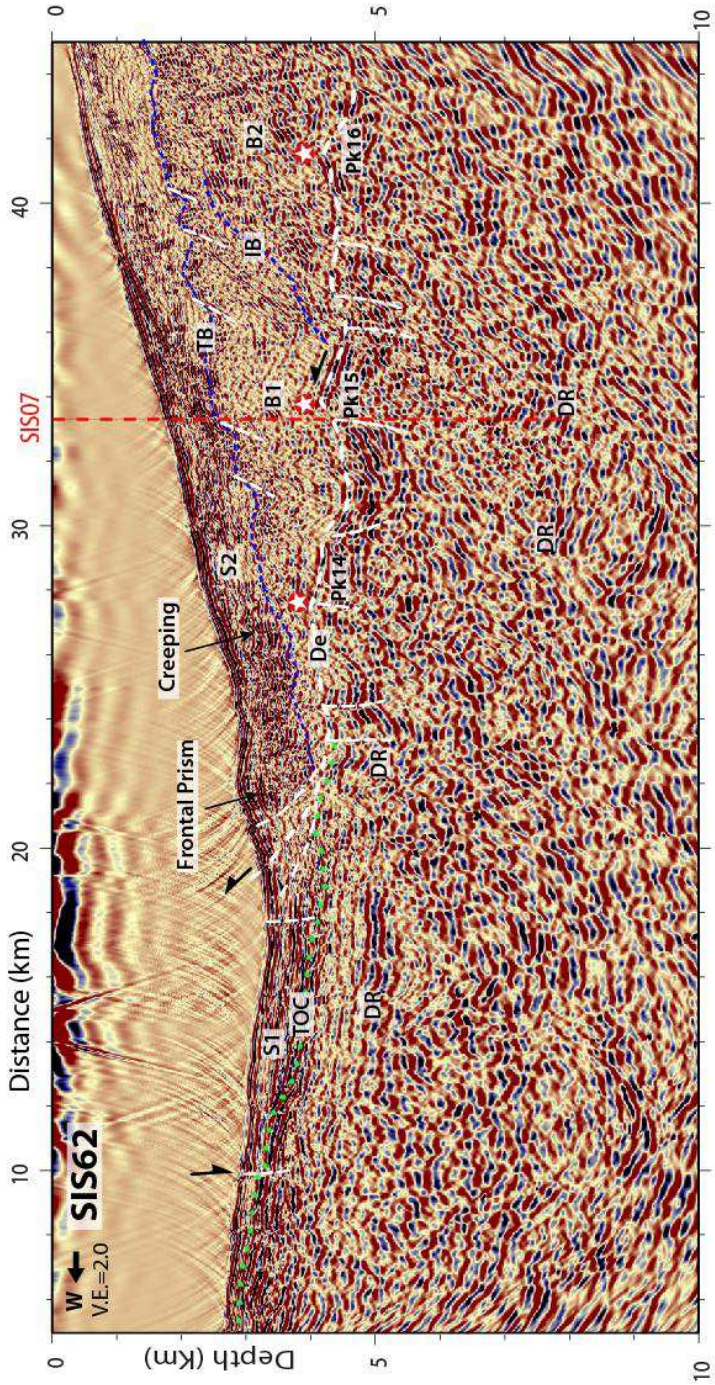

Figure 6. 3 Interpretation of the Pre-Stack-Depth Migration (PSDM) image of profile SIS62. Localization is shown in Figure 6.1. This profile is characterized by remarkable smooth seafloor morphology, a very shallow average dipping angles of ~2.5°, the absence of a subduction channel and undulated décollement that results from a subducting horst-and-graben structure. TOC: top of the oceanic crust (green dashed line); three peaks were imaged along the TOC (stars: Pk14, 15, and 16); S1-S2: sedimentary layers; DR: deep reflector; thin white lines represent faults ; De: décollement (white thick dashed line); TB: top of the basement (blue dashed lines); B1-B2: basement units; IB: intra-basement reflector (in blue); red vertical dashed line represents the intersection with strike profile SIS07; V.E.: vertical exaggeration of 2.0 .

6.1.3. Main observations derived from the interpretation of profiles SIS05 and 62 at the northern margin segment of the study area

Profiles SIS05 and SIS62 are characterized by no large active thrust or normal faults cutting the margin wedge, and a remarkable smooth seafloor morphology. The sedimentary cover reaches values of ~1.5 km in average. The top of the oceanic crust (TOC) in both profiles has an undulated shape with peaks, and presents very shallow average dipping angles, ~4° for SIS05 and ~2.5° for SIS62. The roughness of the TOC and the absence of a subduction channel (<150 m) are similar characteristics in both profiles, suggesting that they are representative of the northern margin segment.

6.2. Margin structures beneath the rough outer wedge slope: Profiles: SIS13, SIS66, SIS14 and SIS68

South of 1º35'S, MCS profiles SIS13, SIS66, SIS14 and SIS68 image the outer wedge structure beneath the morphologically rough margin segment (Figure 6.4).

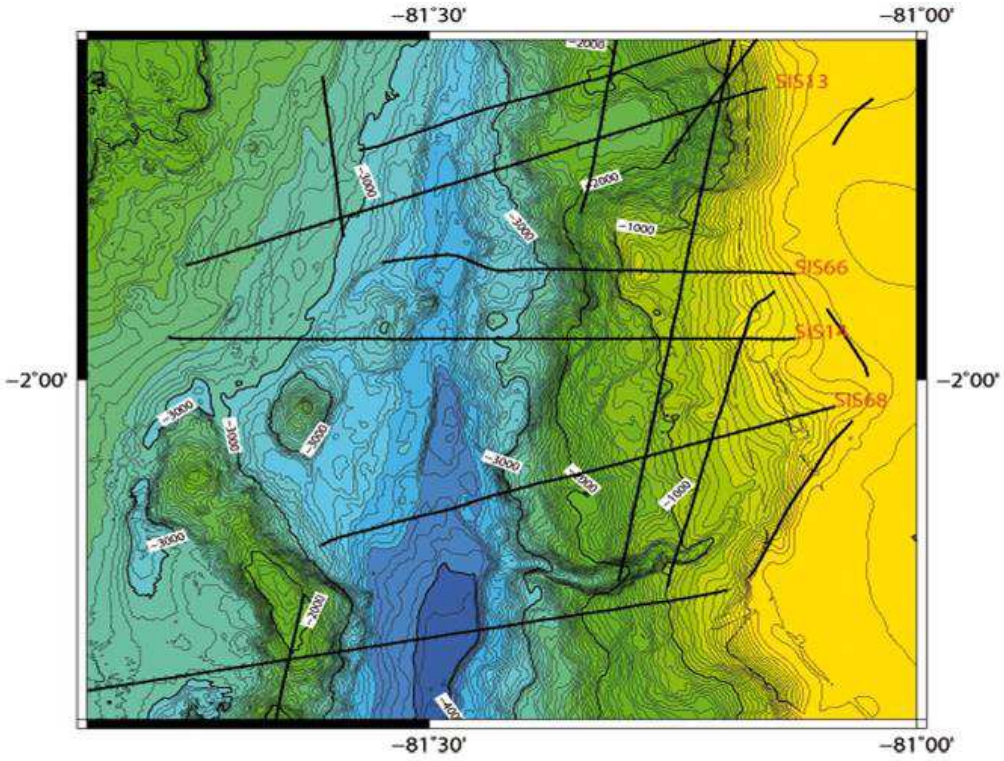

Figure 6. 4 Bathymetric map of the southern segment of the study zone (after Michaud et al., 2006); contour lines indicate the seafloor depth each 50 meters; in yellow: shallower depths and in dark blue: deeper depths; black lines indicate the position of Multichannel Seismic profiles from SISTEUR (2000), in red their respective names .

6.2.1. Line SIS13

Profile SIS13 (Figure 6.5) shows a very different bathymetric section from that of profiles SIS05 and SIS62. This 55 km-long profile extends from the Carnegie Ridge through the 3000m-deep trench axis, across the large outer-wedge morphologic reentrant E3, which forms a slope basin at depths of 2600m, and a steep (6°) margin wedge upper slope.

In the trench, layer **S1** shows a constant 1 km-thickness. Together with the **TOC**, they are disrupted by normal faults, one of them reaching an up to ~300 m-high throw. The group of deep reflectors (**DR**) interpreted as deep as 8 km, may be cut by this fault.

Beneath the frontal prism, the TOC is also disrupted by normal faults, and forms downdip, a ~0.8 km-high and 4-km-wide bump around km 31. The bump is interpreted as a subducted peak (**Pk24**). Two other peaks (**Pk25** and **Pk26**) lie on both side of the intersection with profile SIS09. Layer S1 extends beneath the outer wedge tip and defines a ~15 km-long subducting channel. The subducting channel that is thin (~0.3 km) beneath the frontal prism, thickens up to ~1.1 km on the peak PK24, prior to tapering down at km 28, thus defining a sediment lens. The **lens**, which is floored by the underthrusting Pk24, is roofed by the interplate décollement De. According to the velocity model constructed with the Sirius software (Sage, perso. communication) the lens shows a Vp velocity inversion as low as ~2.2-2.5 km/s with respect to the 4-5 km/s velocity in the overlying margin rocks.

Between the trench axis and km 22, the average dip angle of the décollement (**De**), is **~6º** landward, prior to reverse to ~4.2° seaward, supporting the presence of a deeper subducting seamount with two peaks Pk 25 and Pk 26.

Across the outer wedge, the structure of layer **S2** and the topography of reflector **TB** clearly differ from their equivalent in profiles SIS05 and 62. Layer S2 divides into an upper slope layer **S2a**, a lower-slope layer **S2b,** and a middle-slope layer **S2c** deposited in the slope basin ensconced within the re-entrant. Layer S2a, which extends from near the shelf edge, to km 13, is 0.8-km- thick, stratified and affected by small-throw normal faults delimiting tilted blocks. Two of these faults appear to be still active as they deform the seafloor. Layer S2b lies seaward along the deeper-water segment of the outer-wedge and extends over ~10 km from beneath the slope basin to the frontal prism. Layer S2b shows a chaotic seismic facies and reaches ~0.8 km in thickness. It is floored by

reflector TB and topped by a highly irregular surface. These characteristics support that layer S2b is a **mass transport deposit**. Evidence for thrust faults cutting through both the TB reflector and Layer S2b suggests that the mass transport deposit was deformed by contraction, and uplifted. The deformation was recorded by the fan-shaped layering of layer S2c, which indicates a landward tilt of the slope basin. Below reflector TB, basement units B1 and B2 are identified with similar reflectivity characteristics as along Profiles SIS05 and SIS62.

In conclusion, profile SIS13 cuts large outer-wedge indentation E3 with a sub-horizontal slope basin and has an upper slope angle of ~6°. The sedimentary layer S1 together with the top of oceanic crust (TOC) is affected by normal faults that reach the deep reflector (DR). Thrust faults deform t margin basement unit B1 and the mass transport deposit S2b. The dipping average angle of the décollement is ~6° landward and it reverses to 2° seaward after km 22. A short subduction channel that varies in thickness from 300 m to 1.1km is interpreted as a low velocity sedimentary lens.

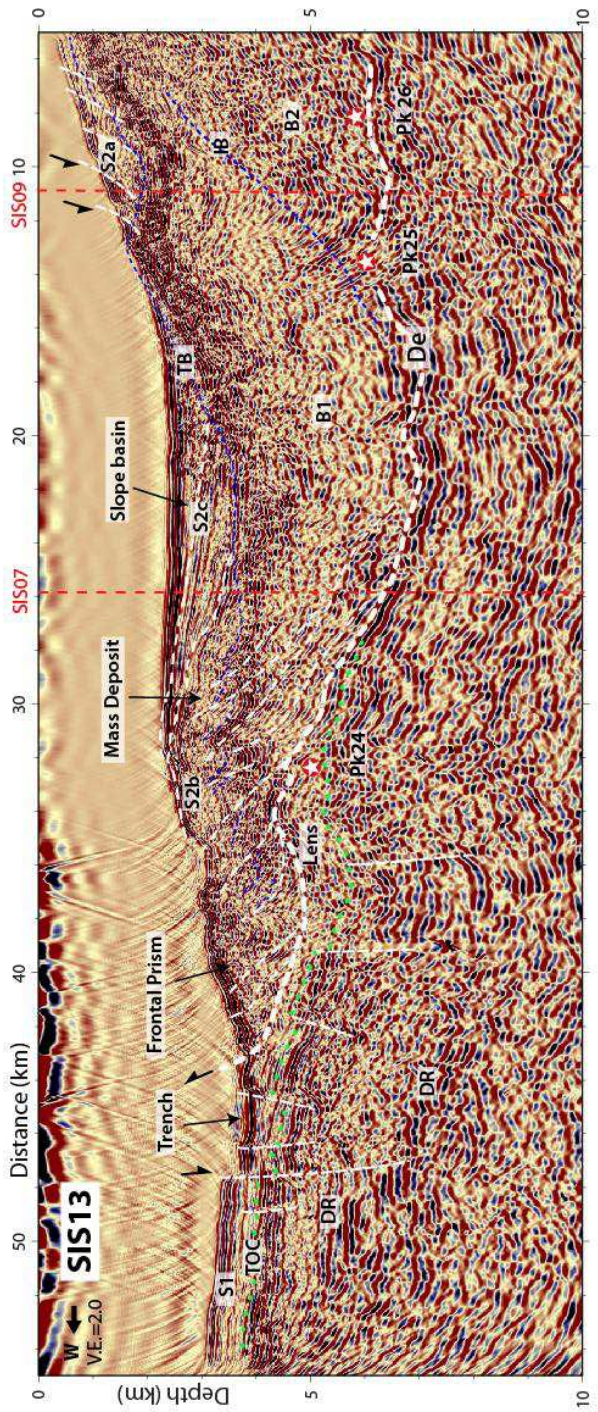

Figure 6. 5 Interpretation of the Pre-Stack-Depth Migration (PSDM) image of profile SIS13. Localization is shown in Figure 6.4. This profile cut the rough outer-wedge margin segment across re-entrant E3 that contains a slope basin. TOC: top of the oceanic crust (green dashed line); the TOC presents three subducted peaks (Pk24, 25, and 26); S1-S2: sedimentary layers, S2 is divided into S2a (upper slope layer), S2b (lower slope layer is a mass transport deposit), and S2c (middle slope layer); S1: Carnegie ridge sediment); DR: deep reflector; thin white lines represent faults ; De: décollement (white thick dashed line); TB: top of basement (blue dashed lines); B1-B2: basement units; IB: intra-basement reflector (in blue); red vertical dashed lines represent the intersection with strike MCS profiles; V.E.: vertical exaggeration of 2.0.

6.2.2. Line SIS66

Profile SIS66 (Figure 6.6) is located south of large indentation E3 crossed by profile SIS13. The profile extends from the 3.7-km-deep trench to the shelf at 0.4 km depth.

The outer-wedge slope presents an unusual morphology broken into three slope segments. The upper slope segment dips only 2° trenchward and terminates downward by a slight slope inversion at a ~ 800-m-deep seafloor high (A at km 32). The middle slope segment, from km 23 to 30 shows a steep, ~10º-dip angle, whereas the lower slope segment dips only 1.5 ° and terminates at the trench.

In the trench, layer **S1** is overlain by a 200-m-thick, strongly reflective horizontal layer suggesting turbidite deposits. Beneath layer S1, the **TOC** is defined by a 0.5 km-thick strongly-reflective layer, which dips **~3º** landward, and can be interpreted as far as beneath the lower slope segment. Together with the TOC, layer S1 extends beneath the lower margin slope, thus, forming a 300-600-m- thick subduction channel (SC). The SC is topped by an unconformity between its relatively well-stratified reflectors and the overlying structurally more complex frontal prism. This unconformity is interpreted as the Décollement (**De**).

Beneath the middle slope, the seafloor multiple prevents interpreting the TOC reflector. However, above the multiple, a 1.5–km-thick set of discontinuous reflectors reverses to seaward dipping instead of dipping landward with the bending oceanic crust. Because the décollement tends to lie dominantly above this set of reflectors, we interpret these reflectors to belong to the down-going plate.

Beneath the upper slope segment, at a 4 to 5-km depth, a downward vertical change in seismic facies from poorly reflective to reflective and semi-continuous may be indicative of reflector **IB2**, a structural discontinuity that passes through a strongly reflective zone near km 41 at a depth of 4.5 km along the line. The shallow-depth IB2 reflector may outline the roof of a subducted seamount, which shallowest point (Pk 28) lies immediately below the **A seafloor high**. Alternatively, reflector **IB1** located between 2.8 and 3.2 km in depth, which separates strongly reflective patch **Pa** from a semi-continuous set of underlying reflectors, could be interpreted either as an intra-basement reflector or as the top of a subducted seamount. A subducted peak (**Pk6**) was also interpreted mainly from crossing line SIS09 as part of the seamount. Based on crossing profile

SIS09 (Figure 6.11), we interpret reflector IB2 as the seamount top and therefore as the interplate fault De.

The upper slope segment of the outer wedge forms a slope basin ensconced between the shelf edge and seafloor high A. Layer **S2**, which is 0.8-1 km thick shows an internal unconformity separating a shallow, poorly reflective and stratified sediment infill (**S2c**) from underlying more reflective and disrupted strata (**S2a**), representing older and deformed sediment. Immediately trenchward from seafloor high A, layer S2 appears offset downward along listric normal fault **Fa**. Beneath the middle slope, layer S2a is twice thinner as beneath the upper slope, and tapers down prior to disappear at km 26. This structure suggests that layer S2a was peeled off during a submarine landslide. In this interpretation, the frontal prism beneath the lower slope would consist of a ~10km-wide megaslump. The prism comprises a reflective and stratified body (layer **S2b**) that shows landward tilted strata in its thickest section. This body might be interpreted as a slump or as a rafted block slid from the middle slope. The strata within the prism become wavy toward its apex. This body is overlain by well-stratified sub-horizontal deposits of layer S2c that likely sealed the landslide.

Beneath the upper slope, reflector **TB** lies sub-horizontal at a 1.3 to 1.8 km depth. Instead of dipping trenchward as in profiles SIS13, SIS05. TB does not show large fault offset, with the exception of listric fault Fa, which offsets both the seafloor and TB by ~300 m. Beneath the middle slope, reflector TB and the underlying strongly reflective strata outcrop at the seafloor (km 23-26) and show a wavy facies supporting gravity deformation during sliding along fault Fa.

In conclusion, the margin segment crossed by profile SIS66 is largely anomalous with respect to lines SIS05 and SIS62. A subducted seamount (SMt), which is 15-20 km wide and at least 1.5-2.0 km high is interpreted to have uplifted the upper slope by a minimum of ~400 m, thus trapping recent sediment in a perched slope basin. The seamount triggered a large collapse of the middle slope that generated a megaslump in the trench. In this scenario, the megaslump deposited over and trapped incoming trench sediment thus forming the subduction channel. With the exception of major listric fault Fa, this margin segment is not affected by normal faulting.

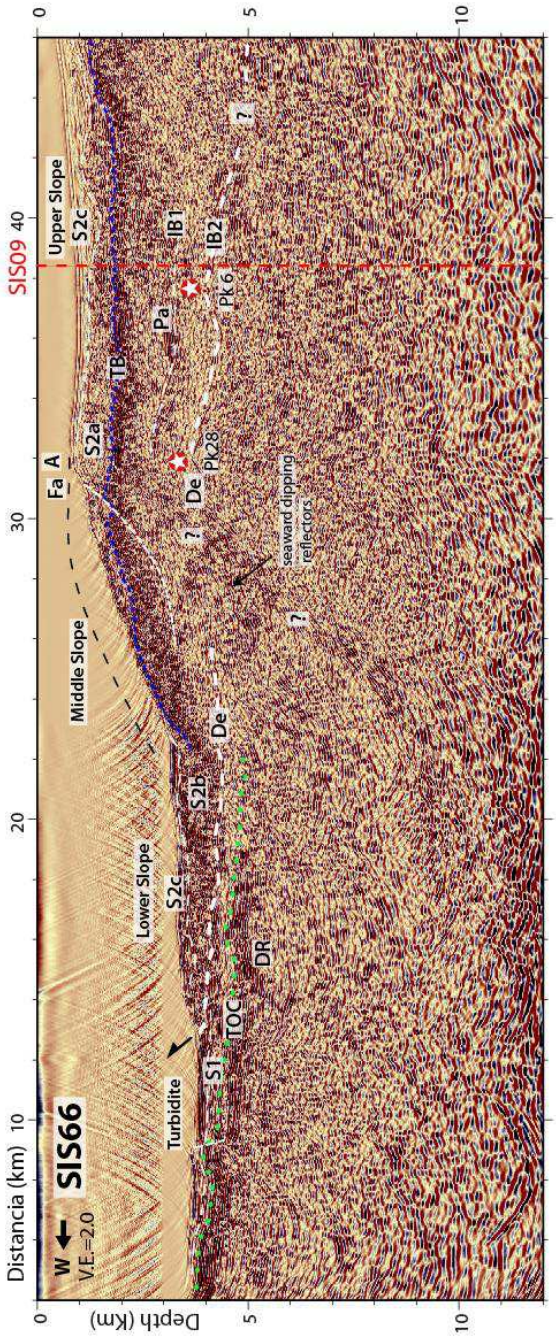

Figure 6. 6 Interpretation of the Pre-Stack-Depth Migration (PSDM) image of profile SIS66. Localization is shown in Figure 6.4. This profile cut the rough outer-wedge margin segment and it shows a very shallow upper slope dip angle of ~3°. TOC: top of the oceanic crust (green dashed line; Pk6 and 28: subducted seamounts; S1-S2: sedimentary layers, S2 is divided into S2a (upper slope layer), S2b (lower slope layer, a mass transport deposit), and S2c (middle slope layer); S1:Carnegie Ridge sediment); DR: deep reflector; thin white lines represent faults ; De: décollement (white thick dashed line); Fa: major listric fault; TB: top of the basement (blue dashed lines); IB1-IB2: intra-basement reflectors (in white); A: seafloor high; Pa: reflective patch; red vertical dashed line represents the intersection with strike MCS profile SIS09; V.E.: vertical exaggeration of 2.0 Line SIS14.

Although close to each other, Profile SIS14 (Figure 6.7) largely differs from profile SIS66 (Figure 6.6). Profile SIS14 crosses a seamount on the Carnegie Ridge, a chaotic trench seafloor at a depth of 3.7-km and an outer wedge that shows both upper and lower margin slopes, which are affected by numerous scarps. The upper slope rises with a 4 ° angle up a 0.4-km depth near the shelf edge, whereas the lower slope dips 7.5° trenchward.

On the down-going plate, Layer **S1** is ~0.3-0.8 km-thick and conformable with the underlying **TOC** reflector on both sides of the seamount. In the trench, the S1 layering is oblique to the seafloor, dipping landward together with the TOC beneath the margin wedge. There, they form the inlet of the Subduction Channel which extends landward up to km 51.

The TOC reflector dips with an angle of **4.5°** and can be followed beneath the lower slope as far as km 47-51, where the TOC is affected by a 4 km-wide graben. Deeper in the down-going crust, at a 6-7 km depth, a group of strong reflectors (**DR)** dips landward beneath the margin sub-parallel to the TOC. In this region, the SC shows a chaotic seismic facies suggesting either tectonic deformation or subduction of mass transport deposits. The SC thickness varies from < 200 m to 1 km, where it is associated with the graben. Landward of the graben, the seafloor multiple prevents from following the SC between km 52-58.

From km 58 to 70, the seismic profile reveals a 2.5-3 km-thick zone of very strong, landward dipping reflectors, which are parallel to each other. The sharp contact between the reflective zone and the overlying less reflective margin rocks may indicate the décollement (**De**) or inter-plate boundary. We tentatively interpret the TOC reflector by connecting the interpreted TOC beneath the graben with a prominent reflector 1-km deeper than the décollement within the reflective zone. Deep Reflectors DR are considered equivalent to those detected further seaward within the oceanic crust.

On profile SIS14, the margin outer wedge is deformed by a set of remarkable well-expressed trenchward-dipping, normal faults offsetting both the sedimentary cover (Layer **S2**) and the margin basement (TB). Along this profile, Layer S2 reaches 1.5 -2.0 km in thickness, being much thicker than along the profiles interpreted further north in this study. The normal faults have divided layer S2 into a series of 2-4 km–wide, rotational blocks as supported by fan-shaped layering in small slope basins (**S2c**) on the foot-wall side of the faults. The fault offsets are small (50 m) across the 4° angle upper slope. They increase up to 100 m along the 7.5° dipping lower slope. The rotational

block located at a 2-km water depth (km 50) is fronted by a 10 km-wide frontal prism. The wavy to chaotic seismic facies within the prism suggests that it resulted from gravitational collapse of over-hanging blocks.

Reflector **TB**, which outlines the basement top, is highly disrupted by the normal faults described above. The fault geometry, which changes from highly-dipping near the seafloor to shallow dipping at reflector TB supports listric normal fault. The basement wedge, which is defined between Reflector TB and the décollement (De), tapers down from 3.5 km at the landward end of the line to ~1 km beneath the toe of the lower margin slope supporting extensional thinning and basal tectonic erosion.

In conclusion, profile SIS14 differs largely from the previous profiles; it crosses a seamount on the oceanic plate, chaotic sediment in the trench, and an outer-wedge slope affected by numerous active normal faults that cut deeply through margin sediment and basement to form a series of rotational blocks. Although, the TOC has an average dipping angle of 4.5°, it is faulted showing at least one horst and graben- system. A 0.2-km-to-1-km-thick subduction channel is clearly visible, and presents a chaotic seismic facies that probably results from tectonic deformation or from subducting mass transport deposits. .

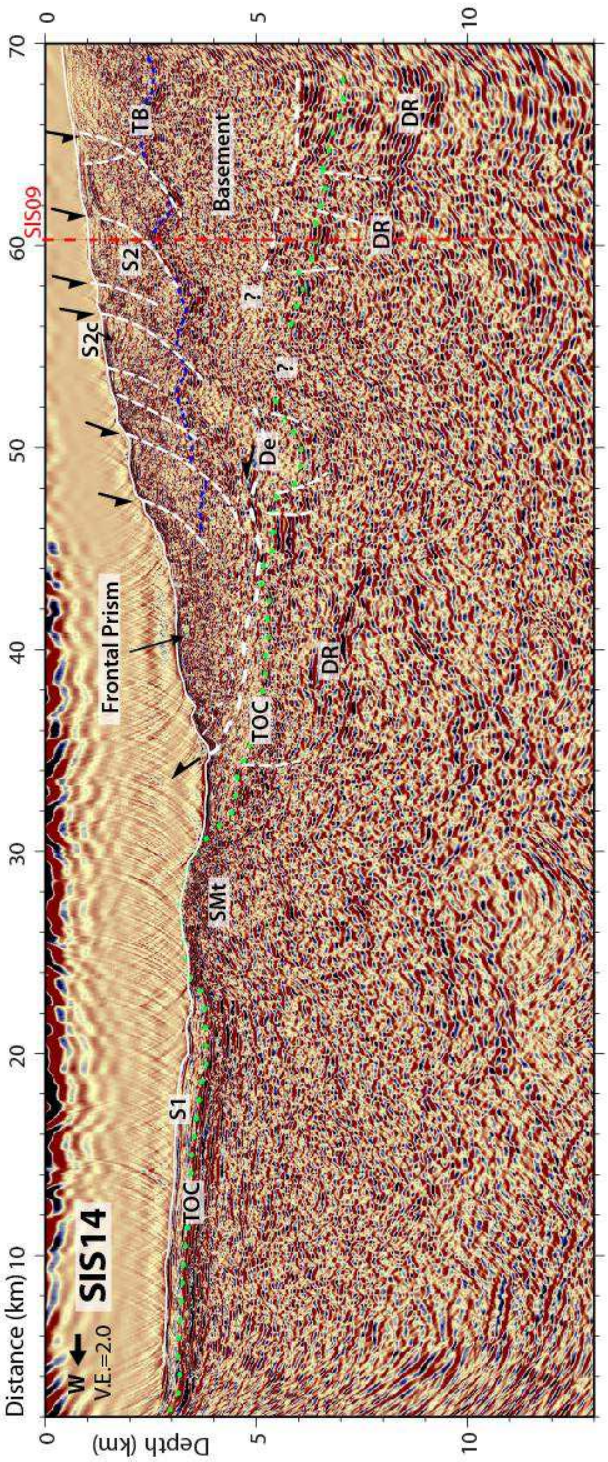

Figure 6. 7 Interpretation of the Pre-Stack-Depth Migration (PSDM) image of profile SIS14. Localization is shown in Figure 6.4. This profile cuts the rough outer-wedge margin segment and its décollement De (thick white dashed line) has a very shallow dipping angle of ~4.5°. TOC: top of the oceanic crust (green dashed line); S1-S2: sedimentary layers, S1: Carnegie Ridge sediment); SMt: seamount; DR: deep reflector; thin white dashed lines represent faults); TB: top of the basement (blue dashed lines); red vertical dashed line represents the intersection with strike MCS profile SIS09; V.E.: vertical exaggeration of 2.0.

6.2.3. Line SIS68

Profile SIS68 (Figure 6.8) shows a similar seafloor morphology and shallow structures than profile SIS14, regardless the seamount in the trench on line SIS14. Along profile SIS68, the seafloor reaches a maximum depth of ~4 km at the trench (the deepest in the study zone) and ~0.35 km at the shelf edge. The inner trench slope shows a ~2.5° trenchward-dipping upper slope segment, and a 7° dipping lower slope segment. This lower slope is abruptly interrupted, at km 42, by steep, 800 m-high scarp overhanging a ~8 km-wide frontal prism. The upper slope is affected by a set of < 100 m west-facing scarps.

On the Carnegie Ridge, the Top of the Oceanic Crust (**TOC**) is relatively smooth, and dips landward with an average **7º** angle up to km ~37 beneath the margin wedge. Further downdip in the subduction, the TOC presents a ~1-km-high and 17-km-wide peak (**Pk27**), which summit lies at a depth of 6.2 km, at km 28. Deep reflectors (**DR)** are interpreted along most of the profile as a series of patches forming all together a ~1 km-thick reflective layer dipping landward down to a ~10 km depth. This reflective layer appears to be thicker beneath the subducted peak (Pk27).

Beneath the trench, the TOC is overlain by layer **S1** that is ~0.4-0.6 km thick and finely stratified. Layer S1 underthrusts the frontal prism and lower margin segment, where the layer forms the Subduction Channel (SC). The SC thickness is 0.8-1 km beneath the frontal prism; the SC facies loses layer S1 fine stratification and turns discontinuous and locally wavy and disturbed as suggested by two possible oblique faults cutting the SC near km 46. Downdip, the SC reflectivity increases, and an internal fault (**F1**) dipping 8° landward with respect to the décollement may be interpreted. The SC pinches out against the trailing flank of the subducted seamount. Although it may exist, the SC cannot be interpreted landward of the subducted seamount (Pk27)

Beneath the outer wedge, layer **S2** shows a variable thickness from < 0.2 km to 1.5 km. The layer and the basement top (**TB** reflector) are deformed by two major normal faults in the shallower part (< 1 km near km 10) of the outer wedge, and by 3 other ones across the lower margin slope (km 30). The recent activity of these faults is testified by the development of small fan-shaped deposits (**S2c**) associated with the faults.

The frontal prism shows a rough topography with at least 3 highs. It is no thicker than 1 km and its seismic facies is discontinuous to chaotic, and locally wavy. These characteristics are those

of slump mass that may contain rafted blocks. We interpret the frontal prism as derived from the adjacent 800-high scarp.

In between the faulted areas (km 11-26), the seafloor remained undeformed, and the underlying reflector TB shows a geometry that is truly different from that along all other profiles from the study area. In this zone, TB reflector consists of two major segments up warped seaward. Three bands of reflectivity (**R1**, **R2**, and **R3**) appear to dip steeply landward as deep as ~7 km within the margin basement. The bands may be associated with ancient, large seaward-verging thrust faults. The upper band projects upward and separates the two up warped TB segments. Taken collectively, the 3 bands of reflectivity suggest that the margin basement results from the emplacement of an old thrust sheet complex.

In conclusion, profile SIS68 shows a margin basement that differs largely from that on the other profiles. It is characterized by three bands of reflectivity that are probably associated to an old thrust sheet complex. Reflector TB consists of two major segments up warped seaward. The TOC shows a 7° dipping angle and presents a small subducted seamount (Pk27) at km 28. The 0.8-km-to-1-km subduction channel shows a locally wavy and disturbed stratification possibly cut by two oblique faults. The frontal prism is made up of a tectonized chaotic slump mass.

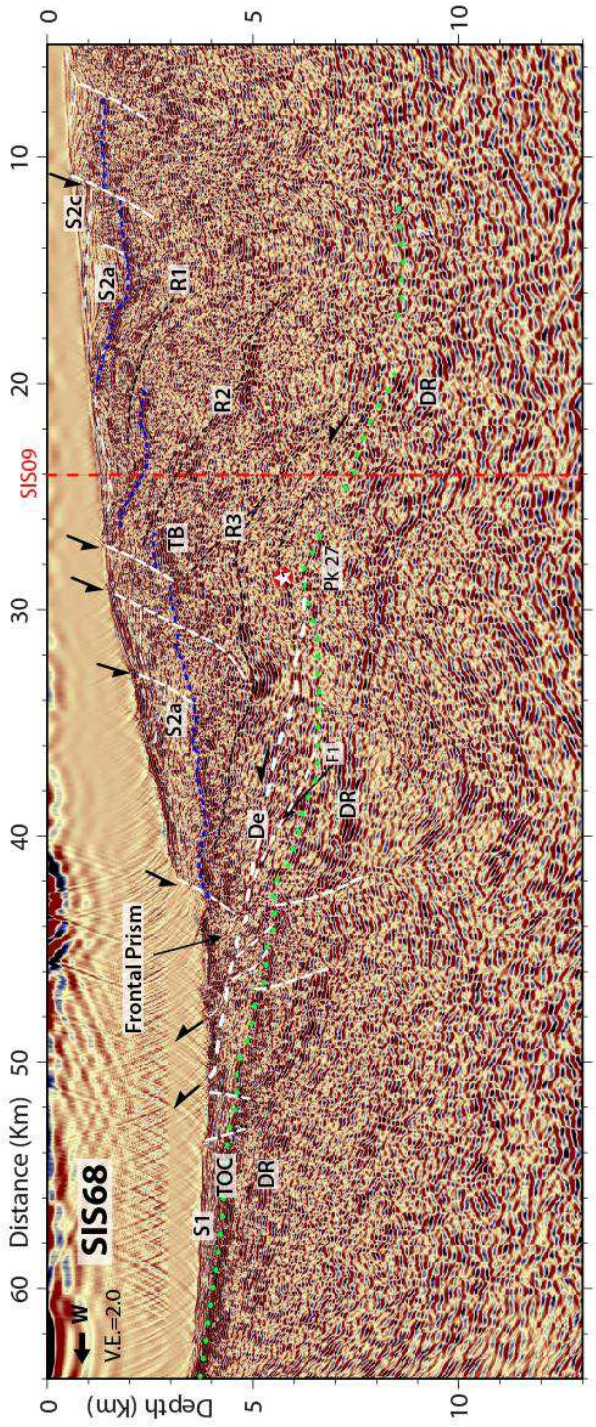

Figure 6. 8 Interpretation of the Pre-Stack-Depth Migration (PSDM) image of profile SIS68; Localization is shown in Figure 6.4. This profile cut the rough outer-wedge margin segment and its décollement shows a ~7° dip angle TOC: top of the oceanic crust (green dashed line); S1-S2: sedimentary layers, S2 is divided into S2a (upper slope layer), , and S2c (fan-shaped deposits associated with fault activity), S1: Carnegie Ridge sediment; Pk 27:subducted seamount; R1-R2-R3: reflective bands; DR: deep reflectors forming a sub-continuous layer; thin white dashed lines represent faults ; De: décollement (thick white dashed line); TB: top of the basement (blue dashed lines); red vertical dashed line represents the intersection with strike MCS profile SIS09; V.E.: vertical exaggeration of 2.0.

6.2.4. Main observations derived from the interpretation of profile SIS13, SIS66, SIS14, and SIS68

The outer-wedge seafloor imaged on these profiles is very rough, probably resulting of a series of seamount collision and margin collapses. On profiles SIS14 and SIS68, normal faults cut a relatively thick sedimentary covers and the basement, producing rotational blocks, whereas SIS13 is largely affected by thrust faults that deform both the margin basement and a mass transport deposit. Profiles SIS66 and SIS68 also show evidences for large mass transport deposits associated with steep morphological scars and listric faults. Although the Top of the Oceanic Crust (TOC) in these profiles is less undulated, it still presents differing-size subducted seamounts and horst-graben structures (SIS14). The average décollement dip angle is higher than that along the northern profiles, but do not exceed 7°. A Subduction Channel can be identified especially in the first 15-20 kilometers from the trench. The margin basement beneath the shelf edge is much thicker than along the northern segment, and in Profile SIS68 it shows an internal structure that may be associated with an old thrust sheet complex

6.3. Strike profiles crossing from smooth to rough section of the outer wedge slope: Profiles: SIS07 and SIS09

Profiles SIS07 and SIS09 extend along strike the margin sub-parallel to trench axis (Figure 6.9). These strike profiles cut the margin wedge from the smooth region north of latitude 01°35S to the rough region south of this latitude, and allow to linking the dip profiles between them.

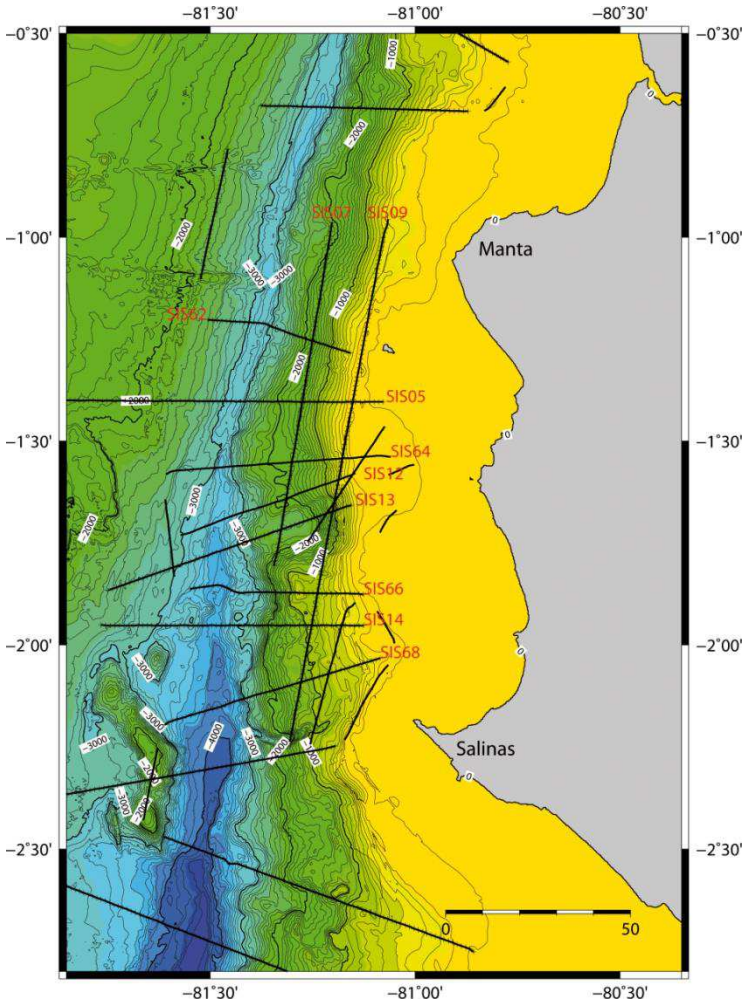

Figure 6. 9 Bathymetric map of the central Ecuador between Manta and Salinas (after Michaud et al., 2006), contour lines each 100m; black lines corresponds to the multichannel seismic reflection profiles from SISTEUR cruise (2000), in red their respective names; in yellow: shallower depths at continental shelf and in dark blue: deeper depths at the trench; the coast and La Plata Island are in grey.

6.3.1. Line SIS07

Strike Profile SIS07 (Figure 6.10) is ~90 km-long, lies only ~15 km inland from trench axis at an average 2-km water depth. The profile crosses the smooth, outer-wedge slope and terminates southward at the morphologic embayment E3 cut by Profile SIS13 (Figure 6.5).

Along Profile SIS07, we first interpreted the three major reflectors (**TB, De, and TOC**) from their reflectivity contrast and geometry. Then we plotted the intersections between Profile SIS07 and each dip profiles (SIS62 to SIS13) to verify the coherency of our interpretation and to adjust the location of the megathrust (De), the top of the oceanic crust (TOC) and the top of the margin

basement (TB).

Along Profile SIS07, the seafloor shows 2-low-amplitude, smooth bulges (Bulge 2 at km 44, and Bulge 1 at km 70) flanked by flat or depressed areas with undulated/rugged morphology. The TB reflector undulates at an average 3-km-depth with 10-15 km half-wavelength variations; its highest points A' and B' lay at a ~2 km depth (km 71 and 44). Across embayment E3, TB reflector is depressed down to 4 km and flanked by steep walls (13° and 21°). This overall geometry likely reflects tectonic deformation and possibly an eroded surface. At its northern termination TB deepens to 4 km with a 7° average dip. At a smaller scale, TB reflector is rippled indicating local tectonic deformation.

Along most of the profile, layer **S2** comprises two layers with differing seismic character. The deeper and older layer **S2o** is reflective, semi-continuous to chaotic and shows tectonic deformation associated with that of TB. Where Layer S2o underlies the flanks of the embayment, the layer is deformed by rotational slumps. Shallower layer **S2a** is poorly reflective, well-stratified and reaches a maximum thickness of 0.8 km south of bulge 2. The layer shows sedimentary structures, like levees associated with a gully at km 35, and its internal reflectors locally downlap onto layer S2o beneath bulge 1. Gentle deformation may affect layer S2a as indicated by a normal fault at km 82. In the embayment E3, the mass transport deposit (MTD, layer **S2b**) identified along profile SIS13 (Figure 6.5) reaches ~ 1 km in thickness and is unconformably overlain by well-stratified slope basin **S2c**.

The décollement (**De**) was interpreted from plotting its position from dip profiles at all crossing points. Then, we drew the De along Profile SIS07 by following segments of the strong reflectors associated with its position on the dip profiles. Between topographic bulges 1 and 2, "De" lies at an average 4.5 km-depth, and shows depths variations in the order of 0.5 to 1 km. In this region, "De" is sub-parallel to the basement top (reflector TB), with two remarkable décollement peaks (Pk8 and Pk9) corresponding to basement highs (**A'** and **B'**). Strong patches of reflectivity are associated to "De" all along the profile. In the region of the Pk8, the reflectivity lies below "De" and is interpreted as the acoustic response of lava flows in the subducting CR as suggested from dip profile SIS62 (Figure 6.3). Further South in the region of dip profile SIS05, "De" underlies the strong reflective patches, which according to our interpretation of profile SIS05 (Figure 6.2), characterizes the tip of margin basement unit **B2**.

South of bulge 2, the décollement lies at an average 5 km-depth, and shows large depths variations in the order of 0.5 to 1.8 km associated with 4 peaks. The overall shape of TB reflector mimics that of the underlying décollement, thus stressing the tectonic influence of the subducting CR structures on the margin basement. Based on the dip profiles SIS64, 12, 11, 13 and their detail velocity models (Sage *et al*., 2006; Sage, pers. Communication.), the 4 peaks (**Pk10, Pk11, Pk12**, and **Pk13**) are not associated with subducted seamount, but with low velocity sediment lenses (Le, in Figure 6.10) sandwiched between the TOC reflector and the décollement. According to Sage *et al.,* 2006, the strong patches of reflectivity overlying the décollement would represent the fluid-damaged base of the margin basement.

In conclusion, profile SIS07 shows 3 major undulated reflectors: the décollement, the top of the basement and the top of the oceanic crust, (De, TB, and TOC respectively); besides, it presents 2-low-amplitude, smooth bulges flanked by flat or depressed areas with undulated morphology. The overall geometry reflects tectonic deformation and probably eroded surface (TB). Rotational blocks and gentle deformation affect locally the sedimentary covers. The décollement highs **Pk7 to Pk9** are peaks of the subducted oceanic crust associated with margin basement elevations, whereas four of them (Pk 10-13) are related with sediment lenses (Le) corresponding to a discontinuous subduction channel.

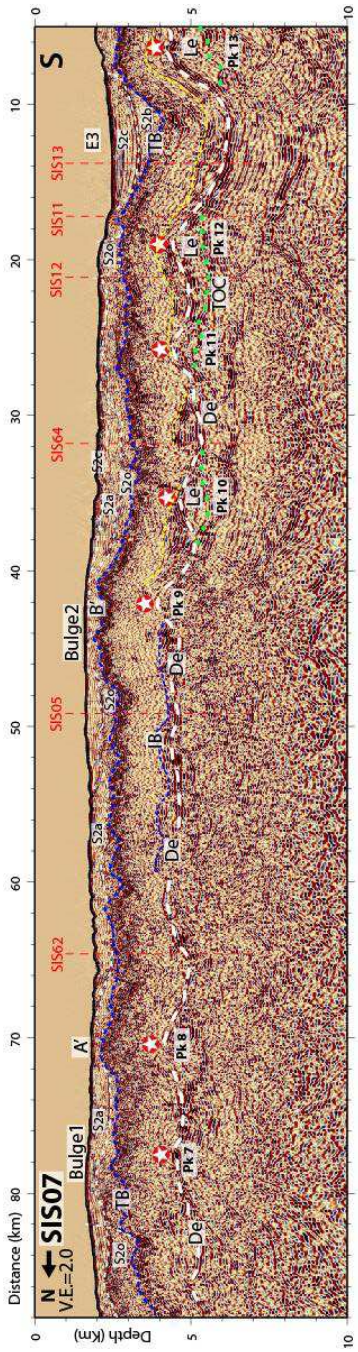

Figure 6. 10 Interpretation of the Pre-Stack-Depth Migration (PSDM) image of profile SIS07. Localization is shown in Figure 6.9. This profile is parallel to the trench and cuts both segments of our study zone. De: décollement (thick white dashed line); TOC: top of the oceanic crust (green dashed line); Décollement peaks, interpreted as Le: sedimentary lenses (star, Pk10, 11, 12, and 13), and subducted seamounts (Pk7, 8, and 9); S2: sedimentary layer, divided into S2o (oldest layer), S2a (youngest layer), S2b (mass transport deposit), and S2c (youngest layer in slope basin E3); thin white lines represent faults ; TB: top of the basement (blue dashed lines); A'-B': basement highs; ; red vertical dashed lines represent the intersection with perpendicular MCS profiles; V.E.: vertical exaggeration of 2.0 .

6.3.2. Line SIS09

Strike Profile SIS09 (Figure 6.11, and zooms: Figure 6.12 and 6.13) extends over a distance of ~140 km along the margin. It is localized ~20-30 km from trench axis along the upper slope of the outer wedge, and crosses the shelf (0.15 km) between km 30 and 62, only 5 km west of La Plata Island. The profile reaches 1.6 km in water depth in the embayment. The northern half of the profile shows a smooth seafloor, whereas its southern half shows evidence for topographic irregularities suggesting gullies and small canyons.

Along the northern half of the profile, the basement top (**TB**) forms a ~ 80 km-wide bulge, with its shallowest (0.5 km) point at km 42 close to the projection of La Plata Island. The bulge northern flank deepens northward until ~2 km. This flanks is highly disrupted by large inactive faults (1 km throw) associated with basement highs buried beneath recent sediment (**S2c**). The bulge southern flank reaches a ~2 km depth at km 75, and is generally flatter and less disrupted than the northern flank. Along the southern half of the profile, Reflector TB seems to outcrop at the seafloor at a depth of ~1.6 km, where the profile cuts across large embayment E3 (km 85-90). South of km 98, reflector TB loses its reflectivity, undulates and remains at an average depth of 2.5 km. A 10 km-wide, 1 km-high basement bump is interpreted at km 105, close to dip line SIS66.

The basement sediment cover, which is thin (300-m) along the shelf edge, becomes thicker (~1.5 -1.8 km) over both flanks of the bulge. **S2a/S2o** sediments have accumulated the most in the small slope basins (km 36, 25, 13) controlled by the large faults across the bulge northern flank. The faults were sealed by unconformity **C1** overlain by well-stratified and poorly deformed recent layer **S2c**. South of embayment E3, layer S2 reaches 1.8-2.0 km in thickness and is locally more reflective than along the northern half of the profile. Layer S2, overlying unconformity C1 and the seafloor are deformed by gentle folding suggesting active deformation. At km 133, a 0.8 km thick recent slope basin overlies unconformity C1.

The plate interface is mainly interpreted from dip MCS profiles and the reflectivity pattern of Profile SIS09. Along the profile, the averaged interface dips **1.5°** southward along a line that deepens from a ~4.8 km-depth at km 10 to ~7.8 km at km 138. The interpreted plate interface departs from this reference line by as much as 3.0 km, thus forming at least six peaks at km 17, 30, 46, 60, 72, 105 (Pk1 to Pk6). Among these peaks the 2.5-km high-and 14-km-wide **Pk3,** the 2-km-high, and 20 –km wide Pk6 stand out.

The margin basement thins northward from 5.5 km tick at the southern end of the profile to ~2.5 km near its northern termination. The thinnest margin segments (2.0-2.5 km) are associated with the subducted seamounts Pk3 and Pk6.

Patches of deep and strong reflectors (**DR**) are interpreted in the down-going crust as deep as 10 km. These reflectors, which are identified along all MCS lines in our study area, underlay in particular both flanks of Pk3 between 5 and 7 km in depth.

In conclusion, profile SIS09 was calibrated using the dip MCS profiles, and is characterized by patches of reflectivity. Profile SIS09 presents a ~80-km-wide-bulge at the northern margin segment and cuts through large embayment E3 crossed by profile SIS13 where the basement may outcrops. The décollement shows a slight southward dip of 1.5° along a referential line, along which several peaks or seamounts were interpreted. The northern segment shows a collection of five subducted peaks; whereas the southern segment reveals, a large isolated seamount (Pk6). The thickness of the margin basement increases southward. The Deep Reflector (DR) is observed along profile SIS09 as well as along all other interpreted MCS dip profiles.

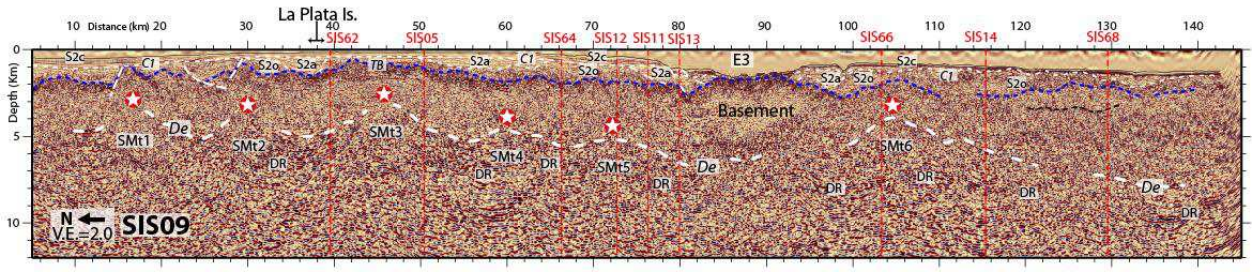

Figure 6. 11 Interpretation of the Pre-Stack-Depth Migration (PSDM) image of profile SIS09. Localization is shown in Figure 6.1. This profile is parallel to the trench and cuts both segments of our study zone. De: décollement (thick white dashed line); Pk: subducted peaks or seamounts; S2: sedimentary layer, divided into S2o, S2a, S2b , and S2c (from the oldest to the youngest sediment); E3: embayment (see Figure 3.4); thin white dashed lines represent the faults observed along the profile; DR: deep reflector; TB: top of the basement (blue dashed lines); C1: unconformity; red vertical dashed lines represent the intersection with perpendicular MCS profiles; V.E.: vertical exaggeration of 2.0.

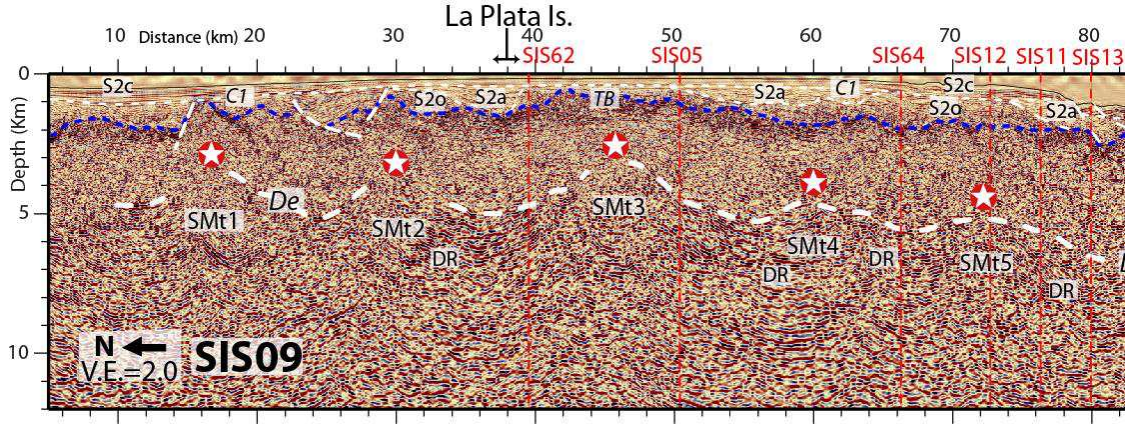

Figure 6. 12 Zoom of Profile SIS09, Figure 6.11 from km 7 to 82

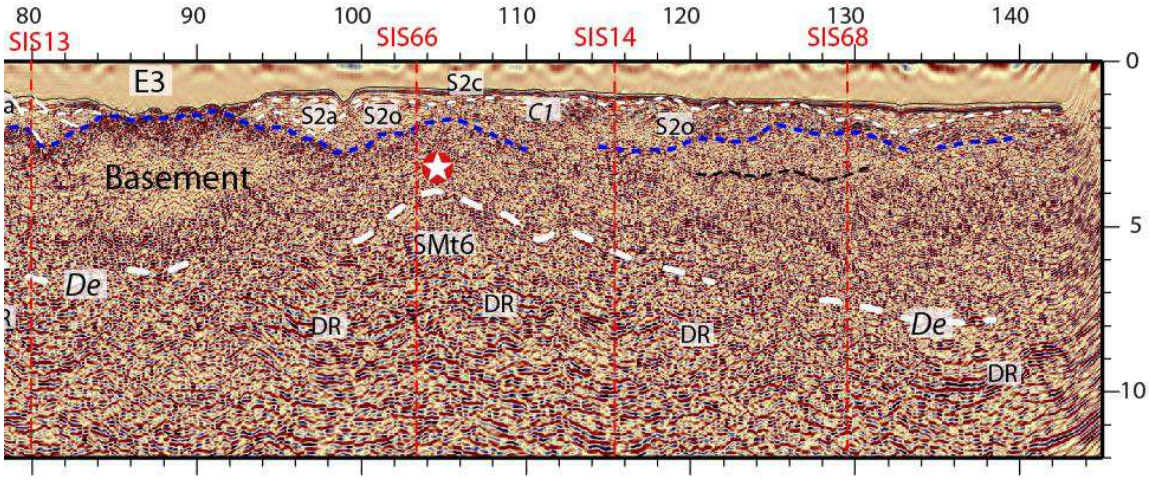

Figure 6. 13 Zoom of Profile SIS09, Figure 6.11 from km 78 to 145

6.4. The décollement is locally characterized by a seismic Reversed Polarity

According to Bang *et al*., (1996), the décollement is involved in discharging large volumes of fluids expelled from consolidating sediments and dehydration reactions of water-rich clay minerals in subduction zones. They modeled the seismic impedance associated with the décollement reflections, to constrain fluid pressure within the décollement in the northern Barbados Ridge. In

our study area, we selected several zones along profiles SIS62, SIS05, and SIS14 to analyze the polarity amplitude of the waveform and its variation along the décollement. This will help us to better characterize the structural interpretation of décollement.

As mentioned in section 1.2.2, reversed polarity results from changes in sediment porosity in the décollement zone rather than changes in the lithology (Bangs *et al.,* 1996). The water bottom, which generally shows a vertical positive velocity contrast, can be used as a reference to identify negative-amplitude reflections within the margin and in particular along the décollement (Figure 1.7). The seafloor along profiles (Figure 6.14.b, 6.15.a, and 6.16.a) is affected by diffractions and in some parts the mute module applied during the post-stack-time migration was too strong, thus complicating the identification of the large positive lobe that generally allows identifying the seafloor. After selecting the best segments of the seafloor with a positive Vp contrast, we proceed to select and analyze the amplitudes of segments that we interpreted as the décollement zone. Evidence for reverse Polarities along the décollement zone were found both at the north and south of the study area (Figure 6.14, 6.15, and 6.16). Several zooms along the interpreted décollement show that the reversed polarity is a signature of the décollement that slightly varies along strike and down-dip. These reverse polarity reflectors are not continuous along the décollement, probably due to processing artifacts or to 3D effects.

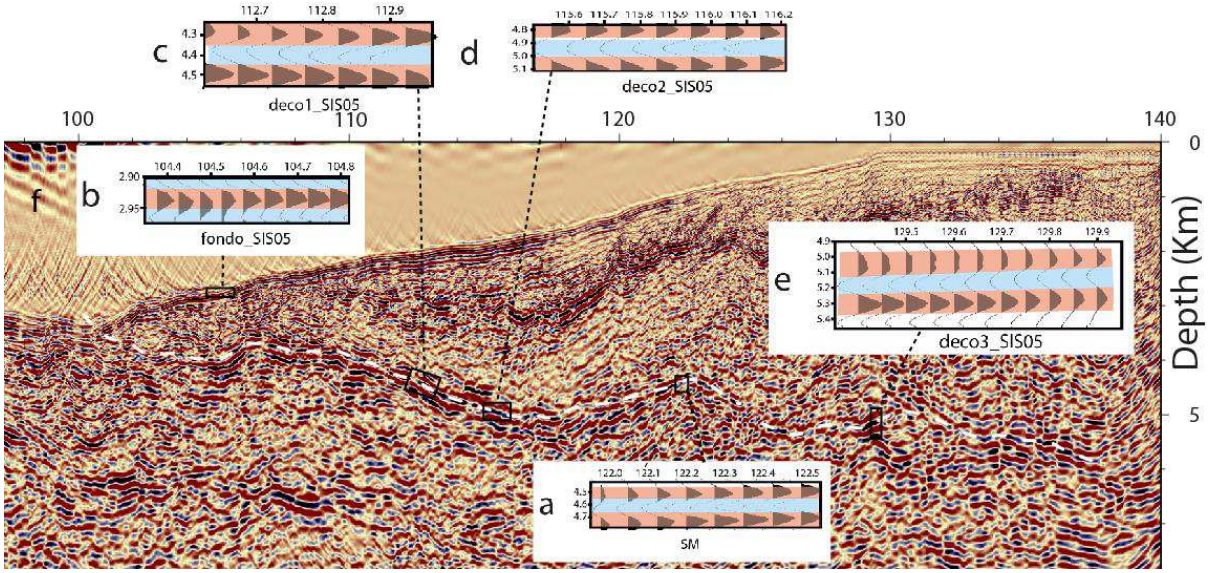

Figure 6. 14 Reverse polarities along the décollement of SIS05; location is shown in Figure 6.1;

décollement zooms: a, c, d, e; b: seafloor bottom zoom; and f: PSMD of profile SIS05, boxes indicating the zooms made on the image to better see the respective polarities. For the seafloor zoom, the large lobe is indicated in red; whereas for the décollement, the large negative amplitude is shown in blue; white dashed line corresponds to the décollement.

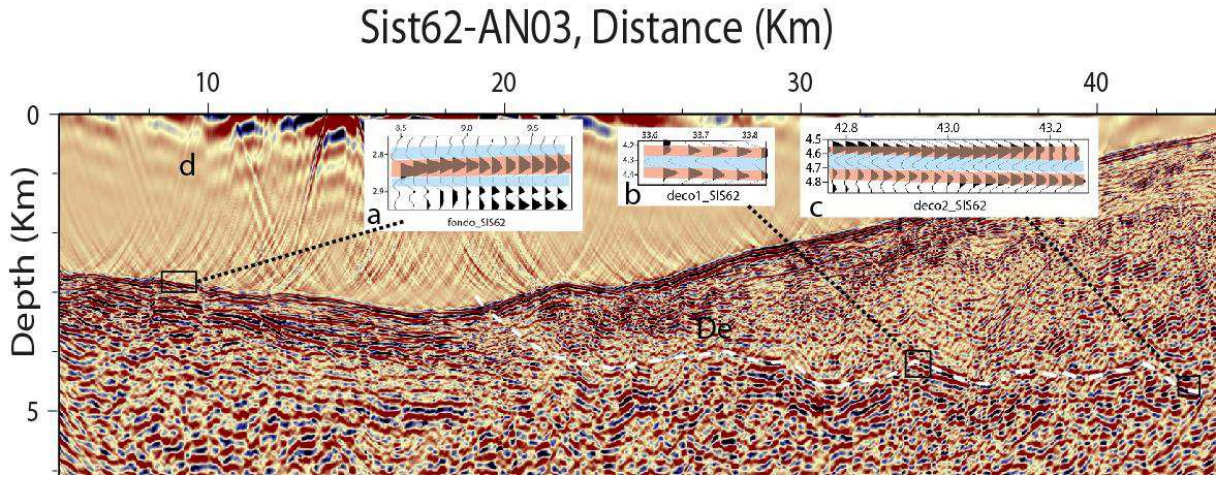

Figure 6. 15 Reverse polarities along the décollement of SIS62; location is shown in Figure 6.1; décollement zooms: b, and c; seafloor bottom zoom: a; and d: PSMD of profile SIS62, boxes indicating the zooms made on the image to better see the respective polarities; For the seafloor zoom, the large lobe is indicated in red; whereas for the décollement, the large negative amplitude is shown in blue; white dashed line corresponds to the décollement.

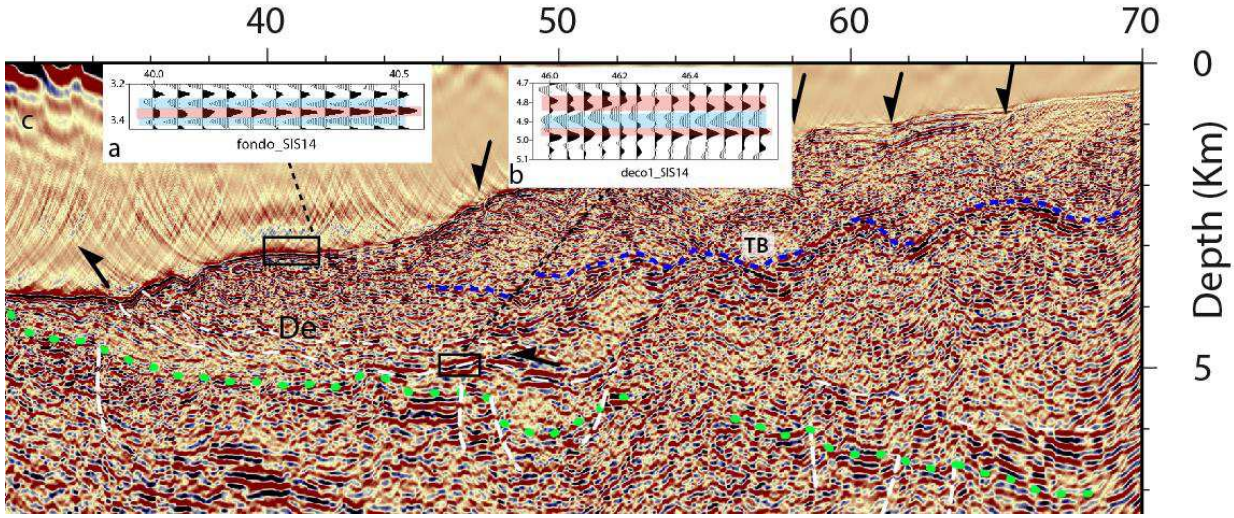

Figure 6. 16 Reverse polarities along the décollement of SIS14; location is shown in Figure 6.4; décollement zooms: b; seafloor bottom: a; and c: PSMD of profile SIS14, boxes indicating the zooms made on the image to better see the respective polarities; For the seafloor zoom, the large lobe is indicated in red; whereas for the décollement, the large negative amplitude is shown in blue; green dashed line corresponds to the top of the oceanic crust; De: décollement, dashed white line TB: top of the basement, dashed green line .

CHAPTER 7

DISCUSSION

7. Introduction

The new PSDM MCS data presented in Chapter 6, alone or combined with other data sets available in the study area, such as high-resolution bathymetry, velocity models derived from OBS data, interplate coupling obtained from GPS inversions, and seismicity allow us to discuss:

- The 2D-3D distribution of subducted seamounts.
- The relationship between subducted seamounts and margin seafloor morphology and shallow structures.
- La Plata Island Uplift as a result of a broad Oceanic Massif subduction.
- The tectonic interaction between subducted seamounts and the northern and southern margin wedge segments which show different geophysical characteristics and geologic natures.
- The Significance of reflectivity variation along the base of the margin tip (MCS Profile SIS07).
- The correlation between the spatial distribution of the inter-seismic coupling and micro-seismicity, and subducted seamounts, thickness and roughness of the SC and the variable nature of the margin wedge rocks.

7.1. The 2D-3D Distribution of the subducted seamounts within the central Ecuadorian margin

Our structural interpretations of the seismic sections in the study area (see Chap 6) suggest the existence of subducted seamounts, horst and graben structures, or other structural irregularities along the interplate contact that we call peaks. We recognized 28 peaks that were placed on the bathymetric map (Pk1-28 Figure 7.1). Each of them could represent a single seamount, although a group of them may reflect a multi-peak seamount. An example of this ambiguous interpretation is shown in the bathymetry of the down-going Nazca plate immediately west of the trench and facing Salinas, where a small conical seamount lies adjacent to an elongated multi-peak seamount (Figure 3.2.b). In some cases, the velocity model derived from MCS data suggest that some peaks along the interplate contact may not be subducted seamounts or structural irregularities, but sedimentary

lenses that deform the plate interface (Pk 10, 11, 12, 13, and 20, blue stars Figure 7.1) (Sage *et al.* 2006).

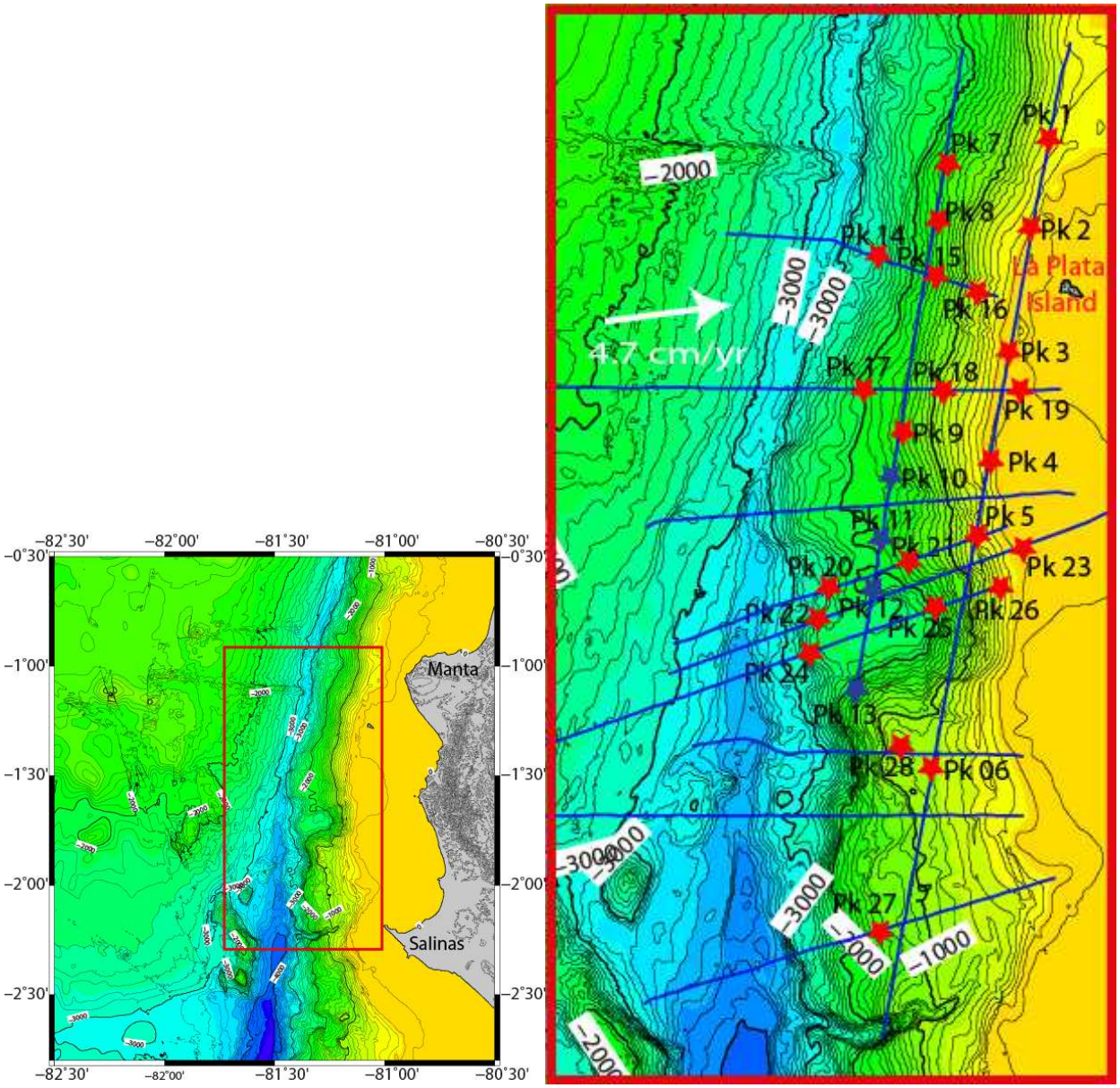

Figure 7. 1 Bathymetric map showing the subducted peaks and sedimentary lenses (after Michaud et al., 2006); left) the rectangle indicates our study zone between Manta and Salinas; right) the localization of the subducted peaks and sedimentary lenses observed in our PSDM seismic images; the location of the peaks (Pk) is indicated by the red stars (seamounts), and blue stars correspond to sediment lenses; contour lines indicate the seafloor depth each 100 meters; in yellow: shallower depths and in dark blue: deeper depths; blue lines indicate the position of Multichannel Seismic profiles from SISTEUR (2000); white arrow indicates the convergence rate is 4.7 cm/yr (Vallée et al., 2013).

The geographic distribution of the MCS profiles in the study area is considered roughly similar in the northern and southern margin segments so that the peak density between the two segments can be confidently compared. This density varies considerably, suggesting different interpretation in each segment.

In the northern segment, excluding the sediment lenses from our interpretation, the interplate contact is characterized by a high concentration of peaks that can be interpreted either as a collection of isolated subducted seamounts (Figure 7.2.a), several multi-peak seamounts (Figure 7.2.b) or as a large ~50 X ~50 km oceanic massif (OM) (Figure 7.2.c); the interpretation adopted will have important implications in terms of IS coupling, seismicity and seafloor deformation pattern. The join interpretation of SIS05 and SIS09 indicates that Pk3 and Pk19 may belong to a single multi-peak seamount, which may also include nearby Pk18 thus forming SMt3, (Figure 7.3). Depending of the average dip angle of the interplate contact, considered as a reference baseline (Figure 7.4), the peaks along line SIS05 can be either interpreted as isolated seamount (Figure 7.4) with respect to a low-dip base line (Baseline 1, Figure 7.4) or as parts of a broader subducting oceanic massif (Figure 7.4) (OM) in the case of a higher-dip base line (Baseline 2, in Figure 7.4). The average dip angle of the interplate contact across the outer wedge of the northern margin segment is very shallow, ranging between 2.5° (SIS62, Figure 6.3) and 4° (SIS05, Figure 6.2), and contrasting with a higher 6-7° dip angle of the inter-plate contact further south (SIS13 and SIS68, Figure 6.5 and 6.8, respectively) across the southern margin segment. The very shallow dip-angle of the inter-plate contact across the northern margin segment supports the presence of the trailing flank of a broad subducted oceanic massif (OM, Figure 7.3) that would include several peaks (Pk 7, 8, 9, 14, 15, 16, and 17, Figure 7.2) and seamounts (SMt 1 to SMt 4). This great number of peaks defines a high level of interplate roughness, an important parameter for the control of the Inter-Seismic Coupling.

On a regional scale, the interplate contact dip-angle derived from the regional depth contours of the subduction interface beneath the margin wedge is ~10° (Font *et al.,* 2013, Graindorge *et al*, 2004), an angle that is close to baseline 2 in Figure 7.4. Moreover, the interplate contact dip angle was calculated to be 10° beneath the La Plata Island, based on the micro-seismicity associated with the 2010 Slow Slip Event (Figure 10 in Vallée *et al.,* 2013). Therefore, the very shallow dip angle derived from the MCS data appears as a local dip-angle anomaly with respect to the regional dip-

angle. This observation reinforces our interpretation of the broad oceanic massif OM subducting beneath the northern margin segment. Due to its location, the OM massif collides with rocks of the inner margin wedge (SMt 2, 3, and 4), whereas its trailing flank deforms rocks of the outer margin wedge. In contrast, the southern margin segment that shows a steeper (6-7°) interplate contact dip-angle than across the northern segment, is characterized mainly by four isolated subducted seamounts of various sizes (SMt 5, 6, and 7), SMt6 being the highest with a 2-km height (~12 km) with respects to its base. All the four seamounts appear to impinge upon outer wedge margin rocks.

In conclusion, in the central Ecuadorian margin, the northern margin segment is characterized by broad and rough subducted oceanic massif OM, whereas fewer isolated smaller subducted seamounts like SMt6 characterize the southern margin segment.

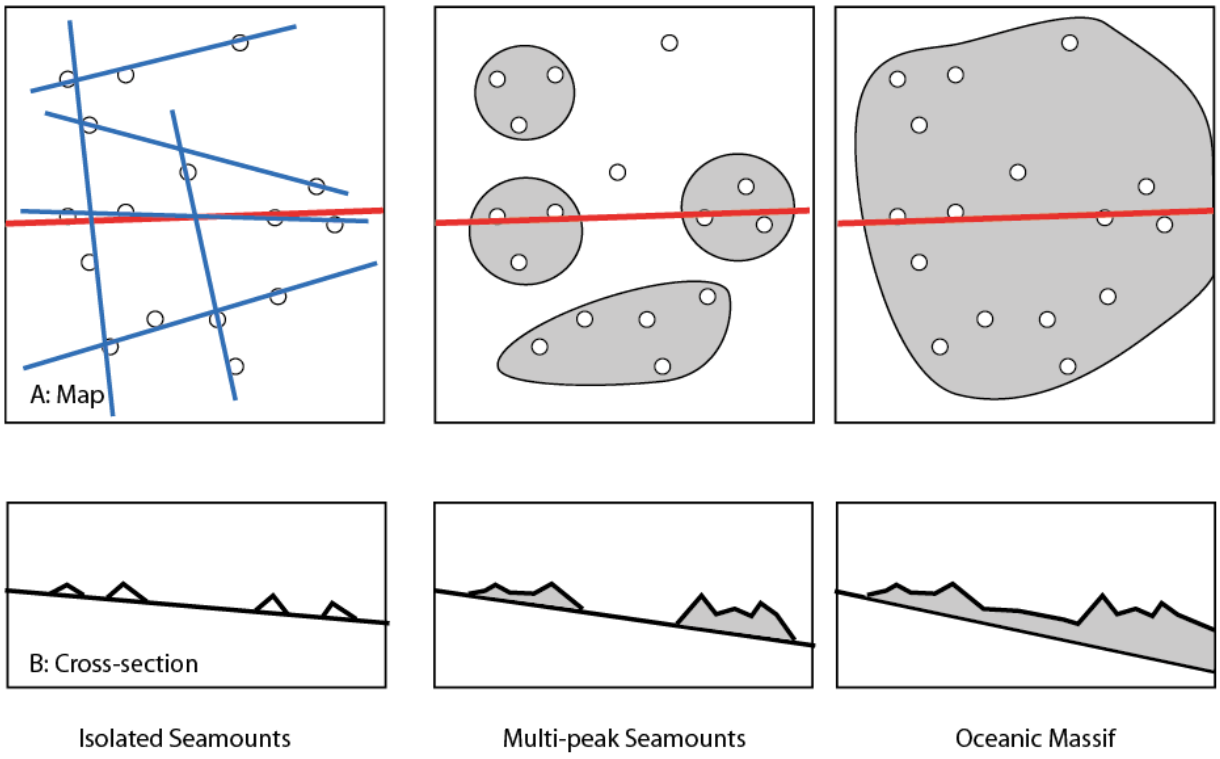

Figure 7. 2 Three Possible interpretations of inter-plate peaks identified from a grid of MSC profiles (blue lines) with respect to regional dip of the plate interface. When the dip angle increases the isolated seamounts (white circles) can be interpreted as multi-peak seamounts or a broad oceanic massif; red lines correspond to the cross-sections.

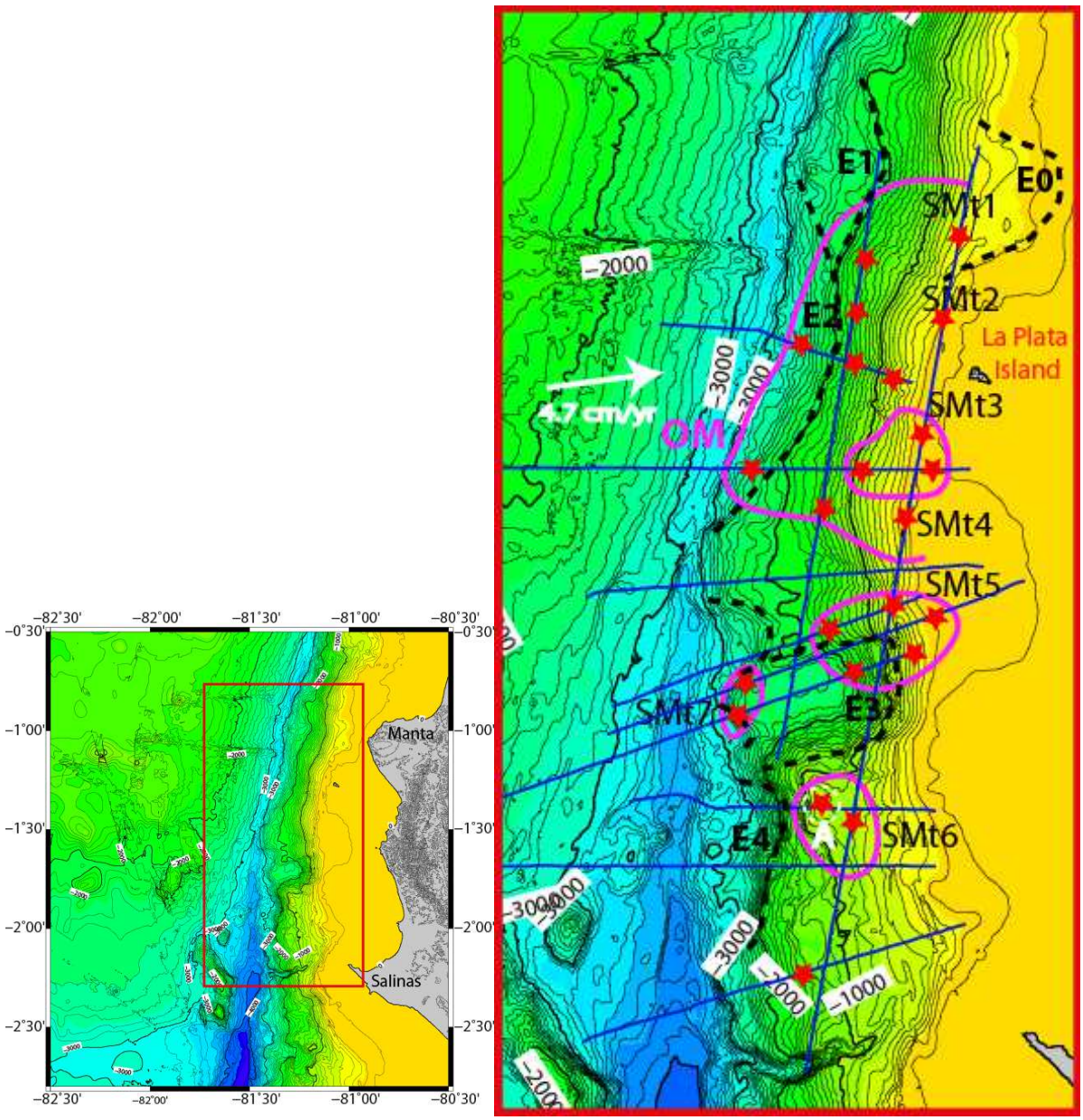

Figure 7. 3 Bathymetric map of our study zone between Manta ad Salinas (after Michaud et al., 2006) with the localization of the subducted seamounts; left) localization of the study area; right) the Oceanic massif (OM) and subducted seamounts (pink lines) interpreted from the PSDM seismic images. Subducted peaks are represented by red stars, and E1, E2, E3 and E4 (dashed black lines) correspond to embayments likely produced by subducted seamounts; A represents a seafloor high marked by a white small dashed circle. Contour lines indicate the seafloor depth each 100 meters; in yellow: shallower depths and in dark blue: deeper depths; black lines indicate the position of Multichannel Seismic profiles from SISTEUR (2000); white arrow indicates the convergence rate is 4.7 cm/yr (Vallée et al., 2013).

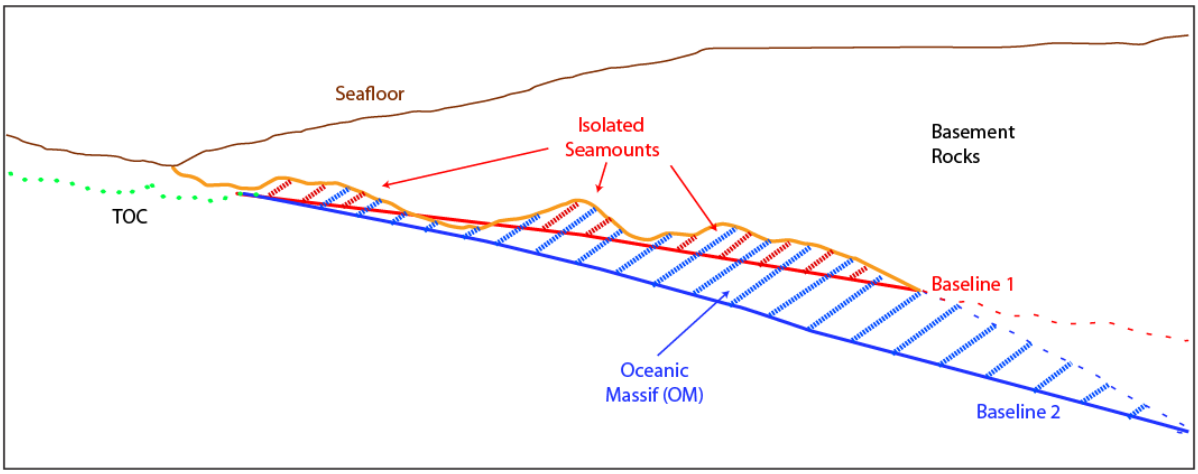

Figure 7. 4 Subducted isolated seamounts or a multi-peaks massif. The interplate contact based on MCS interpretation is indicated by an orange line (De); TOC: top of the oceanic crust in dashed green line. Depending of the regional dip angle of the interplate contact, the seamounts can be either interpreted as isolated seamount with respect to a low-dip interplate contact (baseline 1, in red) or as parts of a broader oceanic massif (OM) in the case of a higher dip interplate contact (baseline 2, in blue). The regional data available in central Ecuador support the higher dip interplate contact, and therefore the subduction of an oceanic massif.

7.2. Effects of the identified subducting seamounts on the margin wedge morphology and structures

The first indication of a subducting seamount often comes from an anomaly in the morphology of the overriding plate like a morphological re-entrant, a scarp, or an uplifted bulge (Dominguez *et al.,* 1998; Ranero *and* von Huene, 2000; Watts *et al.,* 2010).

7.2.1. Relationship between morphological re-entrants in the margin and subducted seamounts

A series of morphological re-entrants were identified along the Central Ecuador margin (see chapter 3). Among them, smooth re-entrant E2 incises the lower margin immediately west of the subducted oceanic massif suggesting that E2 resulted from its subduction (Figure 7.3).

According to the sandbox models proposed by Dominguez *et al.* (1998), this oceanic massif likely uplifted the thin frontal prism producing a seafloor bulge that likely extended for tens of kilometers. While the massif subducted, the seafloor was gently deformed (see SIS62 and SIS05, Figure 6.3 and 6.2) giving place to the smooth, gentle slope of reentrant E2. This gentle margin

seafloor deformation suggests that the OM massif, although it towers some 2 km above the surrounding Carnegie Ridge seafloor, has very low dip-angle flanks and a broad summit.

In contrast, morphologic re-entrant E4 severely breaches the front of the southern margin segment with a stronger and steeper morphologic impact than E2 (see chapter 3.2). Re-entrant E4 lies adjacent to interpreted large SMt6 (see SIS66, Figure 6.6) suggesting that they are related. Moreover, the remarkable topographic high H1 (Figure 7.3), which locally reverses the margin slope angle between re-entrant E4 and SMt6, is interpreted as a morphologic effect of the underlying subducting SMt6 (see chapter 6). This morphologic high is the only one detected along the outer slope in the study area. We suggest that the strong structural impact left by SMT6 in the outer-margin wedge might relate to a) the high and steep topography of the seamount and b) geological nature of the southern margin segment.

Re-entrant E3 is the deepest re-entrant in the dip direction (see Chapter 3.2). According to models by Dominguez *et al.,* (1998) this re-entrant was probably produced by a very large conical shape seamount with relatively steep slopes. E3 is underlain by smaller isolated multi-peak seamounts SMt 5 and 7 (Figure 7.4), which are not thought to be directly responsible for its creation, although SMt5 could be a seaward extent of a yet undetected broader seamount deeply-buried beneath the inner margin wedge (see SIS13, figure 6.5). The initial shape of re-entrant E3 was modified by the SMt10 that re-tunneled the re-entrant E3 creating a smaller re-entrant in the frontal prism.

According to Profile SIS13, recent sediment that deposited in the re-entrant E3 after its formation may reach ~1200 m in thickness (SIS13 between km 21 and km 26, Figure 6.5). Considering a mean sedimentation rate of ~0.83 mm/yr (core Kama01, Ratzov *et al*., 2010), the age of E3 could be in the order of ~ 1.45 Ma, indicating that re-entrant E3 is one of the oldest re-entrants in the study area. At the present-day convergence rate (4.7 cm/yr, Vallée *et al*., 2013), the large seamount responsible for the E3 formation would be located some 70 km landward from the trench beneath the coastline.

Morphologic re-entrants E0 and E1 (Figure 7.3) outline two stages of subsidence of the wedge immediately west of Manta Peninsula. They may have resulted from a similar process of seamount subduction, which could also be responsible for the Manta Peninsula Quaternary uplift.

7.2.2. Does the uplift of La Plata Island result from subduction of oceanic massif OM ?

According to Cantalamessa *and* Di Celma (2004) La Plata Island was produced by tectonic uplift in the order of 0.4 mm/yr, and glacioeustatic variations over at least the last 500 ka. Based on the chrono-stratigraphical interpretation of La Plata Island. Pedoja *et al*. (2006a) considered that the highest marine terrace of La Plata Island may correlate with terrace T4 of Manta Peninsula, whose age ranges from 643 and 710 kyr with a mean uplift rate of 0.30 mm/yr.

We have considered that the embayment E2 results mainly from the subduction of the broad oceanic massif OM that we identified from MCS data (Figure 7.3); and our hypothesis is that OM, which includes SMt3, may also have uplifted La Plata Island.

In order to calculate the time frame for Pk19 subduction to its present-day position, we made three considerations: 1) the Nazca/NAB plate convergence rate of 4.7 cm/yr (Vallée *et al*., 2013) remained constant over the last million year; 2) at our seismic resolution scale, the absence of large thrust faults within the margin and the undetectable subducting channel (SC) allow to assume very low shortening accommodation within the SC and margin rocks; and 3) diffuse deformation within the down-going plate is considered very low. Collot *et al*. (2011) consider a diffuse tectonic shortening within the SC and margin basement (a poorly known strain distribution), which values range from 10% (Adam *et al*., 2004) to a 50% upper bound. To quantify the error on the timing, we added a 10 % diffuse tectonic shortening. Based on these assumptions, Pk19 was about to enter subduction, some ~32 km seaward from its present position, ~ 680 ±68 kyr ago. Therefore, since the La Plata Island started to emerge between 643 and ~ 710 kyr, subducted Pk19, which was entering the trench at this time, may not be the direct cause of the island uplift, unless the main body of oceanic massif OM, which Pk19 is part of, extended at least some 30 km more eastward up to beneath the emerging island (Figure 7.5b). In conclusion, our hypothesis of the LP Island uplift caused by the OM subduction is fully supported by our structural interpretation. According to this hypothesis, the leading edge of OM may have started subduction ~1.3-1.4 Ma (Figure 7.5a).

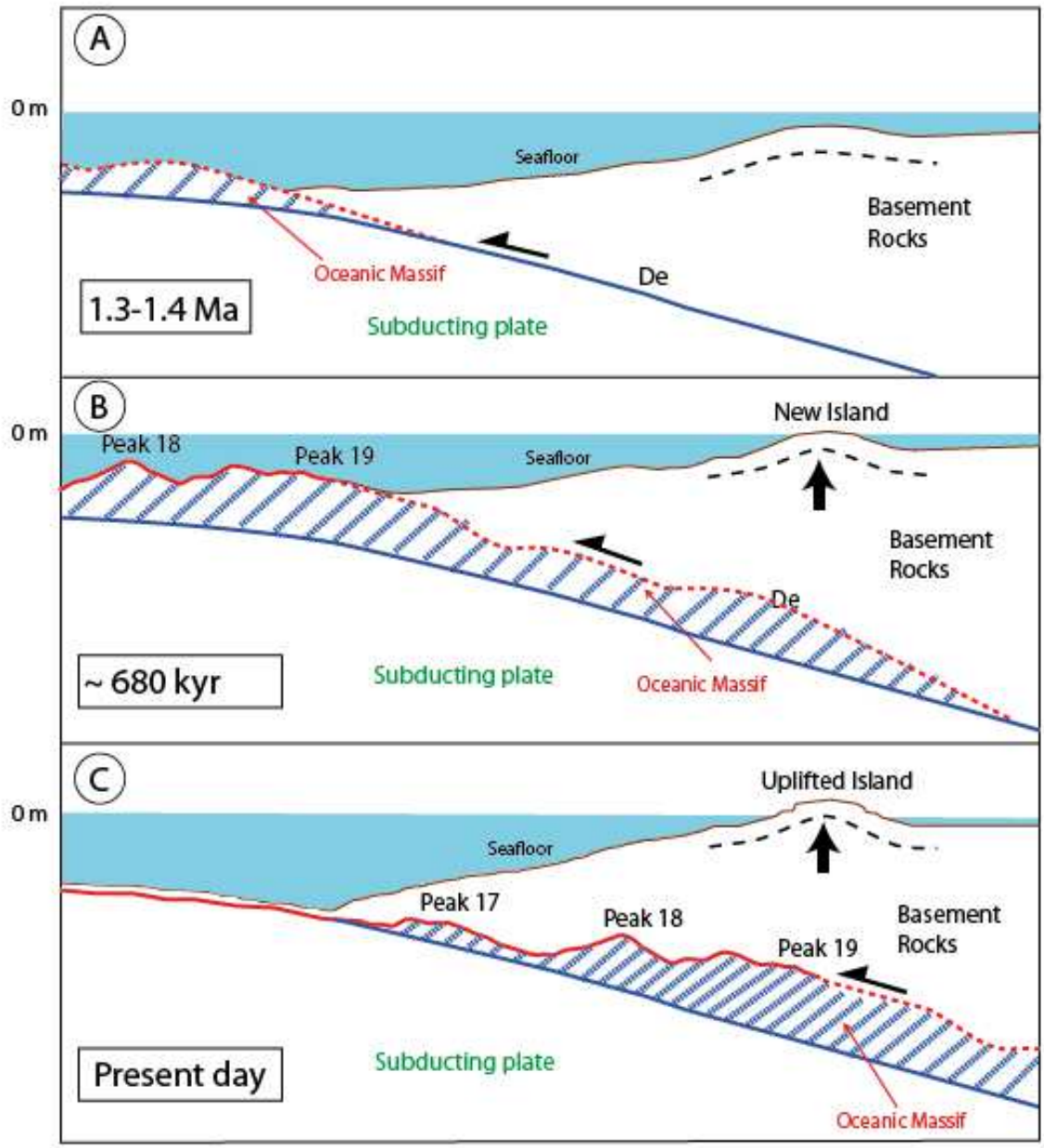

Figure 7. 5 Island uplift as result of the subduction of an oceanic massif; TOC: top of the oceanic crust (orange line); De: décollement; a) The oceanic massif starts to subduct, 1.3-1.4 Ma, the inner margin wedge is slightly deformed; b) the leading flank of oceanic massif is subducted and deforms the seafloor is deformed, creating the first marine terraces ~680 kyr; c) the oceanic massif is deeper than in B, and the seafloor uplifted giving place to a new island.

7.3. The nature and structure of the central Ecuadorian margin and subducted Carnegie Ridge based on wide-angle P-wave velocity models and MCS structural interpretations.

By superposing information from the MCS profiles SIS09 and SIS07 over the coincident WA seismic profiles SIS01 and SIS02, we pretend to relate P-wave velocity structures of the margin wedge with underlying Carnegie Ridge subducted seamounts interpreted along MCS profiles. This will help us to better understand the nature of the interplate coupling and seismicity in the study area. The Vp models from WA SIS01 and SIS02 profiles (Gailler, 2005; see chapter 3.7.2) are well constrained beneath the OBSs until 20 km of depth (uncertainties between 0.10-0.15 km/s) and less well constrained at their extremities (uncertainties between 0.15-0.20 km/s). However, taking into account the 10-km interspace between each OBS, Vp structures smaller than ~10 km cannot be detected and used for interpretation. Gailler (2005) identified a high velocity zone (HVZ) and a low velocity zone (LVZ) along both WA profiles SIS01 and SIS02 (Figure 7.6 and 7.7, see chapter 3.7.2.3). We propose new interpretations of the HVZ and LVZ based on both a new location of the interplate contact, and the presence of the subducted OM and isolated SMts.

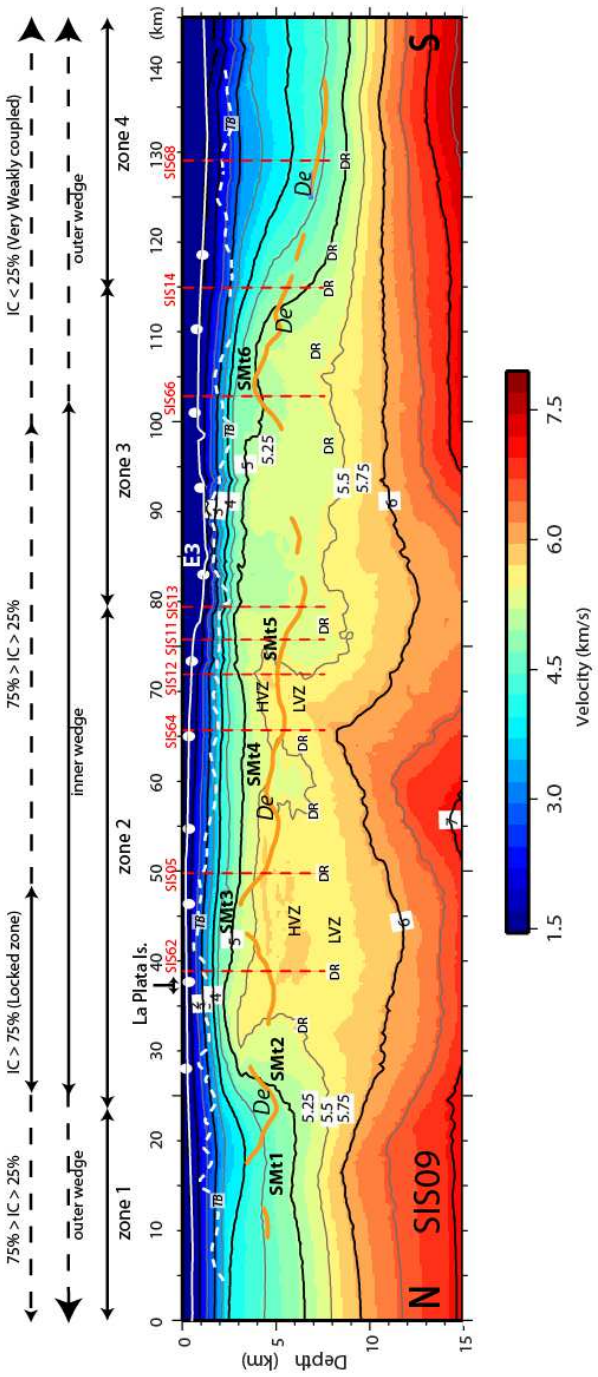

Figure7. 6 Interpretation of MCS profile SIS09 and P-wave velocity model of profile SIS01; location of profile SIS09/01 is shown in figure 3.10. Our interpretation superposed on the velocity model of Gailler (2005) showing a high velocity zone that coincides with the collection of seamounts. The profile is divided in four zones (1, 2, 3 and 4) using the velocity contour of 5 km/s; De: décollement, orange line; SMt: seamounts; TB: top of the basement, white dashed line; HVZ: high velocity zone; LVZ: low velocity zone; DR: deep reflector; red dashed lines: indicate the intersection with other profiles; E3corresponds to the embayment of Figure 3.4. Arrows indicate the zones, and the position of the profile within the wedge; colors correspond to the velocity scale, blue 1500 km/s, and red around 7 km/s; the inter-seismic coupling (ISC) come from Chlieh et al. (submitted).

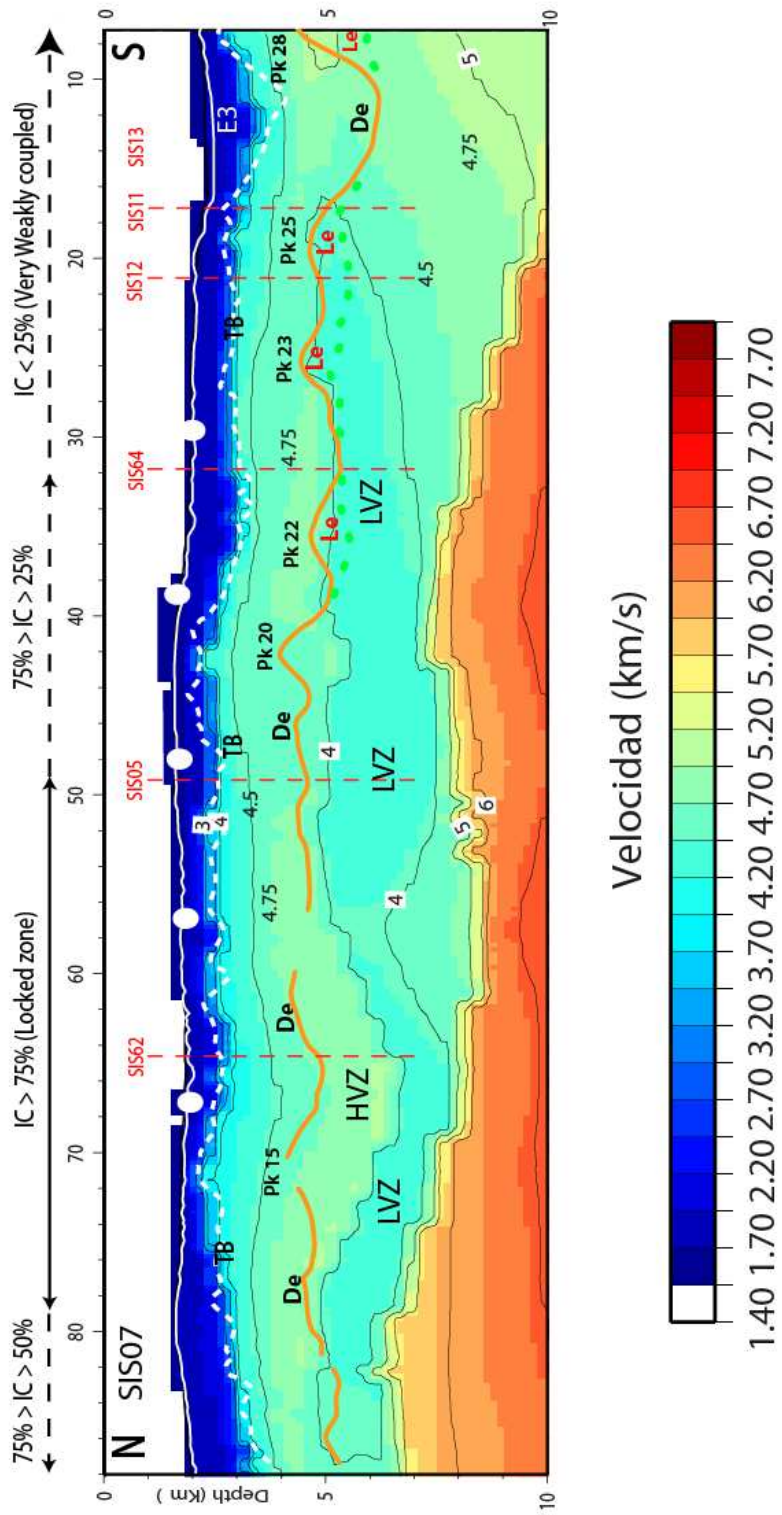

Figure 7. 7 Interpretation of the MCS profile SIS07 and P-wave velocity model of profile SIS02; location of profile SIS01 is shown on figure 3.10. Our interpretation superposed on the velocity model of Gailler (2005), showing a correlation between the high velocity zone and the peaks (Pk). Le: sedimentary lenses; De: décollement, orange line; SMt: seamounts; white circle: OBS position. E3: embayment from figure 3.4; the inter-seismic coupling (ISC) come from Chlieh et al. (submitted).

7.3.1. P-wave velocity model and subducted seamounts along profile SIS01/SIS09

The P-wave velocity structure shows significant variations along the WA velocity model of SIS01 (Figure 7.6). Based on Vp variations, we divided the model in 4 remarkable zones:

Zone 1 extends from km 0 to km 25. It shows an up to 5 km-thick wedge of rocks with velocities 3 km/s < Vp <5 km/s; the 5 km/s iso-velocity contour lies at a depth of ~6.5 km. These velocities characterize rocks the margin basement and part of the subducting plate like the poorly defined SMt1.

Zone 2 extends from km 25 to km 80 and explores the internal Vp structure of the margin inner-wedge and underlying OM and Carnegie Ridge. The thickness of the wedge of rocks with Vp velocities ranging from 3 to 5 km/s dramatically decreased to less than 2.2 km in comparison with zone 1, and the 5 km/s iso-velocity contour has risen to only ~3 km of depth (~3.5 km shallower than in zone 1). Modeling the OBS data (Gailler, 2005) in zone 2 provides evidence for a velocity inversion that is outlined by a High Velocity Zone (HVZ, 5.75 km/s between 4-6.5 km depths) underlain by a relative low velocity zone (LVZ 5.25-5.5 km/s between ~5 and ~9 km depths) that extends all along Zone 2. Superimposing our structural interpretation of the interplate contact "De" onto the WA model demonstrates that both the HVZ and the LVZ are embedded in the subducting plate beneath the subducting seamounts, so that the LVZ cannot be related to the subduction channel or main interplate contact as proposed by Gailler (2005). The HVZ is interpreted to form the core of the subducted OM. Interestingly, the LVZ coincides with the band of deep reflectors (DR) that lies at a ~6-8 km depth and reflects impedance contrasts within the down going Carnegie Ridge. This LVZ and DR might outline a weak zone of mechanical instability within the down-going plate.

Zone 3, which extends from km 80 to km 115, is similar to zone 2. However, rock velocities in both the inner margin wedge basement and down going CR are slightly lower than in zone 2 (5.0-5.25 km/s). Specifically beneath re-entrant E3 (80-87 km), a pocket of 5.0-5.25 km/s Vp velocity surrounded by higher Vp might be related to weaker margin rocks that were possibly fractured during the past subduction of the large seamount described in this chapter at section 2.1. In zone 3, the HVZ/LVZ is unclear although DRs are interpreted in this zone. Large subducted SMt6 appears to have slightly lower Vp (5.25 km/s) than the OM (up to 5. 75 km/s) possibly reflecting a difference in the seamount nature or structure.

Zone 4 extends from km 115 to km 145 and is very similar to Zone 1 in terms of velocity structure. Zone 4 shows however an up-to-7-km-thick wedge of rocks with velocities ranging from 3 to 5 km/s; the 5 km/s iso-velocity contour lies at a depth of ~8.5-9.0 km i.e. much deeper than in Zone 1. Consequently no clear subducted seamount is interpreted in zone 4. According to our interpretation of the plate interface, part of the 4.5-5.0 km/s Vp characterizes the shallow CR and no LVZ is identified in zone 4. Considering the slight obliquity of Line SIS-09 with respect to the shelf edge direction (Figure 7.3), Zone 4 Vp velocities characterize rocks of the margin outer wedge.

In conclusion, the main findings of section 3.1 show: **1)** the inner-margin wedge (Zones 2 and 3) is characterized by high velocity rocks (Vp 3.5-5.5 km/s) at depths less than 3 km, 2) the outer margin wedge (zones 1 and 4) shows lower Vp (2.5-4 km/s) down to 3 km depths, whereas rocks with 5 km/s Vp are found at much greater depths, down to 6-9 km in the underlying down-going plate. 3) The subducted OM (SMt 2 to 4) shows a HVZ core (Vp up to 5.75 km/s) underlain by a LVZ that is associated with deep reflectors DR in the subducting crust of the CR (Figure 7.3); **4)** SMt6 in zone 3 presents slightly lower velocities than the Vp of OM suggesting a different geological nature or structure; **5)** SMt1 might show low velocities compared to the other seamounts although zone 1, which hosts SMt1, lies outside of the well-controlled Vp zone; and **6)** between km 80 and 87, seafloor re-entrant E3 coincides locally with a gentle decrease of the margin basement velocity structure compared to the surrounding areas, suggesting locally damaged rocks that could result from the past subduction of a large SMt .

7.3.2. P-wave velocity model and subducted seamounts along profile SIS02/SIS07

The P-Wave velocity model constructed from OBS data along profile SIS02 coincident with MCS line SIS07 (Gailler, 2005) shows a well-constrained velocity inversion from a High Velocity Zone HVZ (Vp = 4. 75 km/s at 3.5-4.5 km depths) to a Low Velocity Zone LVZ (< 4. 0 km/s at 5-7 km depths) (Figure 7.7). Our interpretation of the plate interface (De) along profile SIS07 (Figure 7.3) was superposed on the P-wave velocity model of Gailler (2005). This figure (Figure 7.7) shows a correlation between the high velocity zone (HVZ) and a ~2 km-tick section of the tip of the margin basement as well as with some subducted peaks (Pk 15, 20) that belong to the Carnegie ridge. Down below, the low velocity zone (LVZ) is dominantly associated with the shallow oceanic crust (layer 2) of the downgoing CR at a 5-7 km depth as proposed by Graindorge *et al*., (2004), and therefore cannot be interpreted as the subduction channel such as proposed by Gailler (2005). This relatively low velocity layer that is embedded in the shallow downgoing crust may be

conducive to a mechanically weak zone in the CR, especially when subjected to higher stress from the plate convergence. Part of this LVZ may also correlate to the sedimentary lenses (Le) that we identified between km 18 to 38 along the plate boundary, although detailed velocity analysis conducted by Sage *et al*. (2006) on the lens interpreted along profile SIS12 reveals much lower velocities (2.2 to 2.8 km/s).

In conclusion, the well-controlled high velocity zone (HVZ) along Profile SIS02 reflect the nature of the rocks of the tip of the margin basement and subducted peaks interpreted as seamounts (Figure 7.3), whereas the LVZ corresponds to a weak zone within the subducting plate. The low-velocity sedimentary lenses (Le), which lay at the shallower part of the LVZ outside of the well-controlled area, are probably not linked to the CR mechanically weak zone but to fluid–rich sediments jammed into the plate boundary (Sage *et al*., 2006).

7.3.3. Significance of reflectivity variation along the base of the margin tip (MCS Profile SIS07)

Our cross interpretation of profile SIS07 using dip MCS profiles has revealed the complex nature of the rocks making up the base of the tip of the margin (Figure 6.10). As indicated in Chap 6 section1.1.1, irregular patches of strong reflectivity are associated with the topographically rough De megathrust along profile SIS07 (Figure 6.10). In places, such as near the crossing with profile SIS05, the megathrust "De" underlies a strongly reflective patch, which according to our interpretation of profile SIS05, characterizes the tip of the highly reflective, high Vp velocity margin basement unit B2. This unit, which is likely composed of the deep section of the Piñon Formation is here truncated by the megathrust and possibly altered by fluids. Further south, in the region of crossing profiles SIS64 to SIS13, where the megathrust is associated with sediment lenses, strong patches of reflectivity also overlay the décollement. However, according to crossing MCS lines these strongly reflective rocks belong to margin basement Unit B1, which is generally not that much reflective. The locally enhanced reflectivity at the base of Unit B1 (*e.g*., SIS13, Figure 6.5) has been attributed to fluid-damaging processes (Sage *et al.,* 2006).

7.3.4. P-wave velocity model and the subduction of Oceanic Massif OM along profile SIS05: nature of the interplate contact and interpretation of the velocity inversion

We superposed our structural interpretation of profile SIS05 (see chapter 6) on the velocity

model (Figure 5.13.d) that resulted from mixing the velocity models of MCS profile SIS05 and WA profile SIS04 (see chapter 5).

As mentioned in Chapter 3, Graindorge *et al*. (2004) consider that the velocity inversion modeled along profile SIS04 results from a thin layer of underthrust sediments and the 3-km-thick Carnegie Ridge (CR) oceanic layer 2, whose velocity (5.1 km/s) is lower than that of the overlying margin wedge (their layer C, 6.1 km/s to 6.4 km/s) (see section 3.7). However, based on our interpretation of the PSDM profile SIS05, we found that the thin layer of underthrust sediments along the interplate contact cannot be detected with the MCS data and that the interplate contact (De) interpreted from MCS lines SIS05, SIS07 and SIS09 does not coincide with the velocity inversion zone modeled by Graindorge *et al*. (2004), and Gailler (2005) along cross profiles SIS01 and SIS02. Rather, our interplate contact appears highly irregular and dips with a ~2.5-4° angle that is shallower than the regional subduction dip angle (Figure 6.2). Thus, the velocity inversion zone lies within the subducting Carnegie Ridge and coincides with deep reflectors DR, a result that is corroborated by our interpretation of the WA Vp models obtained by Gailler (2005) along profiles SIS01 and SIS02 (Figure 7.6 and 7.7). Besides, as proposed for profiles SIS07 and SIS09, this intra-plate velocity inversion zone may correspond to a mechanically weak zone that is likely to concentrate part of the seismicity when transported further down dip in a higher stress field environment.

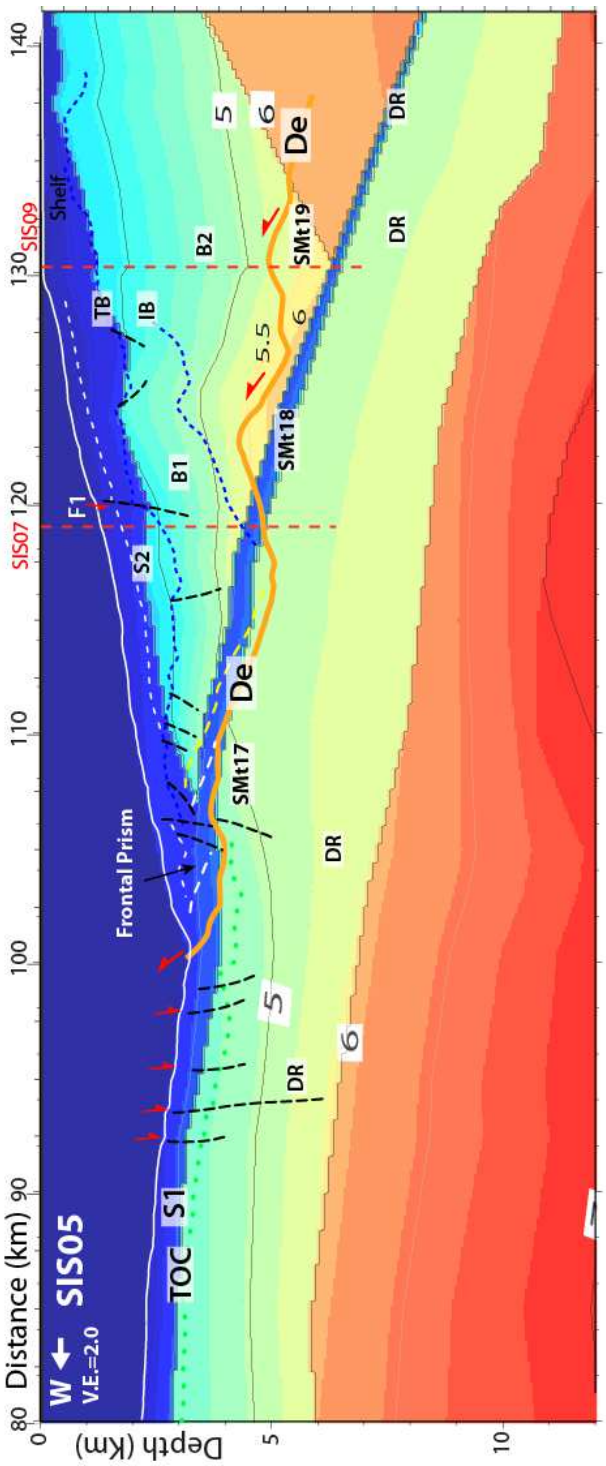

Figure 7. 8 Interpretation and P-wave velocity model of profile SIS05. Location map of profile SIS05 is shown on figure 3.10. Our interpretation superposed on the velocity model shows that the interplate contact is shallower than that expected in previous studies; De: décollement, in orange line; Pk: peaks of Oceanic Massif (OM); TB: top of the basement, blue dashed line; TOC: top of the oceanic crust, light green dashed line; DR: deep reflector; dashed red lines indicate the intersection with profiles SIS07 and SIS09; S1 and S2are sedimentary layers; IB: intra-basement reflector, blue dashed line within the basement; black lines are normal faults; Vp contours in km/s.

7.3.5. Geophysical evidence for a change in rock nature and structure between the northern and southern margin segments of Central Ecuador.

We selected MCS profiles SIS05 and SIS68 (Figure 7.1) as end-members representative of the structure and nature of the northern and southern margin segments, respectively. These two profiles reveal contrasting basement Vp velocities and structures that support different rock nature and tectonic history, and will help define two differing mechanical domains in relation with inter-seismic plate coupling and seismicity.

Along profile SIS-05, basement units B1 and B2, which show contrasting reflectivity and internal structures dipping dominantly trenchward, make up the basement of the margin wedge (Figure 6.2). According to Figure 7.8, Vp basement velocities range between 4.5-5.5 km/s with an average 5.0 km/s Vp velocity. The Vp tomography model along NS-trending Profile SIS09 (SIS01) (Gailler, 2005, Figure 7.6), which cuts profile SIS05 along the shelf edge, provides 4.0-5.5 km/s Vp velocities for Unit B2 in agreement with Vp velocity obtained along profile SIS05. The B2 basement high "H" (Figure 6.2) that underlies the shelf immediately south of La Plata Island suggests that this basement consists of rocks similar to the Cretaceous basalts of the Piñon formation that outcrops on the island (Cantalamessa and Di Celma, 2004) (Figure 7.9.a). Therefore, although possibly fractured, mafic basement rocks in the northern segment of Central Ecuador might be strongly resistant and prone to accumulate elastic strain before breaking.

In contrast, Profile SIS-68 does not show basement Units B1 and B2 but a complex internal structure that is characterized by bands of reflectivity dipping landward within the basement (Figure 6.8). Similar bands were observed in profile SIS16 (Figure 7.10a, Calahorrano (2005, page 117), a profile that is located in front of Salinas, south of our study zone. The basement velocity structure along Profile SIS68 can be approximated from the Vp tomography model along Profile SIS09 (SIS-01) (Gailler, 2005, Figure 7.6), which cuts profile SIS68 midway across the outer margin wedge. The velocities range between 2.5 km/s near the basement top to ~4.5 km/s near the plate interface, thus providing an average Vp of 3.5 km/s. This average velocity is consistent with the Vp model obtained by Calahorrano (2005) along profile SIS-16 (Figure 7.10b). We interpret the basement nature as an ancient thrust sheet complex that may involve dominantly sedimentary rocks (Figure 7.9b). These rocks possibly tend to deform easier than mafic basement rocks of the northern margin segment, thus accumulating less elastic strain during the deformation process.

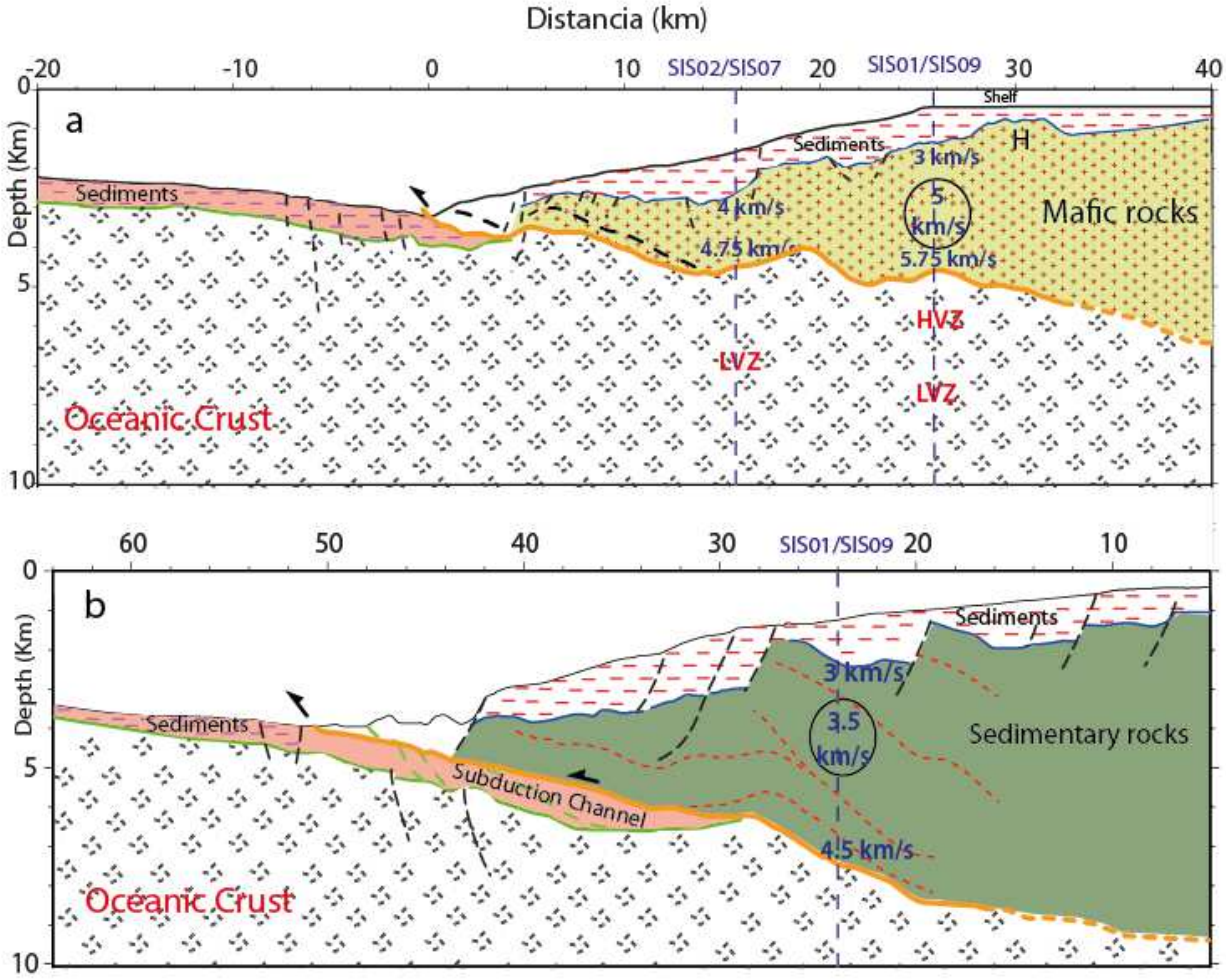

Figure 7. 9 Representation of basement rocks of the northern and southern segment of our study zone using profiles SIS05 (a) and SIS68 (b), respectively; on both sections the top of the oceanic crust (TOC, green lines) is undulated as results of subducted seamounts; across the northern segment, a subduction channel cannot be identified, whereas across the southern segment an up to ~ 1 km-thick subduction channel is recognized down to a 7 km depth; Normal faulting is more developed across the southern segment showing rotation blocks. In (a) the basement is ~5 km-thick, 40 km from the trench, and its average 5 km/s P-wave velocity correlates with mafic rocks of the Piñon Formation (Graindorge et al., 2004; Gailler, 2005); In (b), the basement is ~8 km-thick, 45 km from the trench and its average 3.5 km/s P-wave velocity and internal imbricate structure (red dash lines) suggest sedimentary rocks.

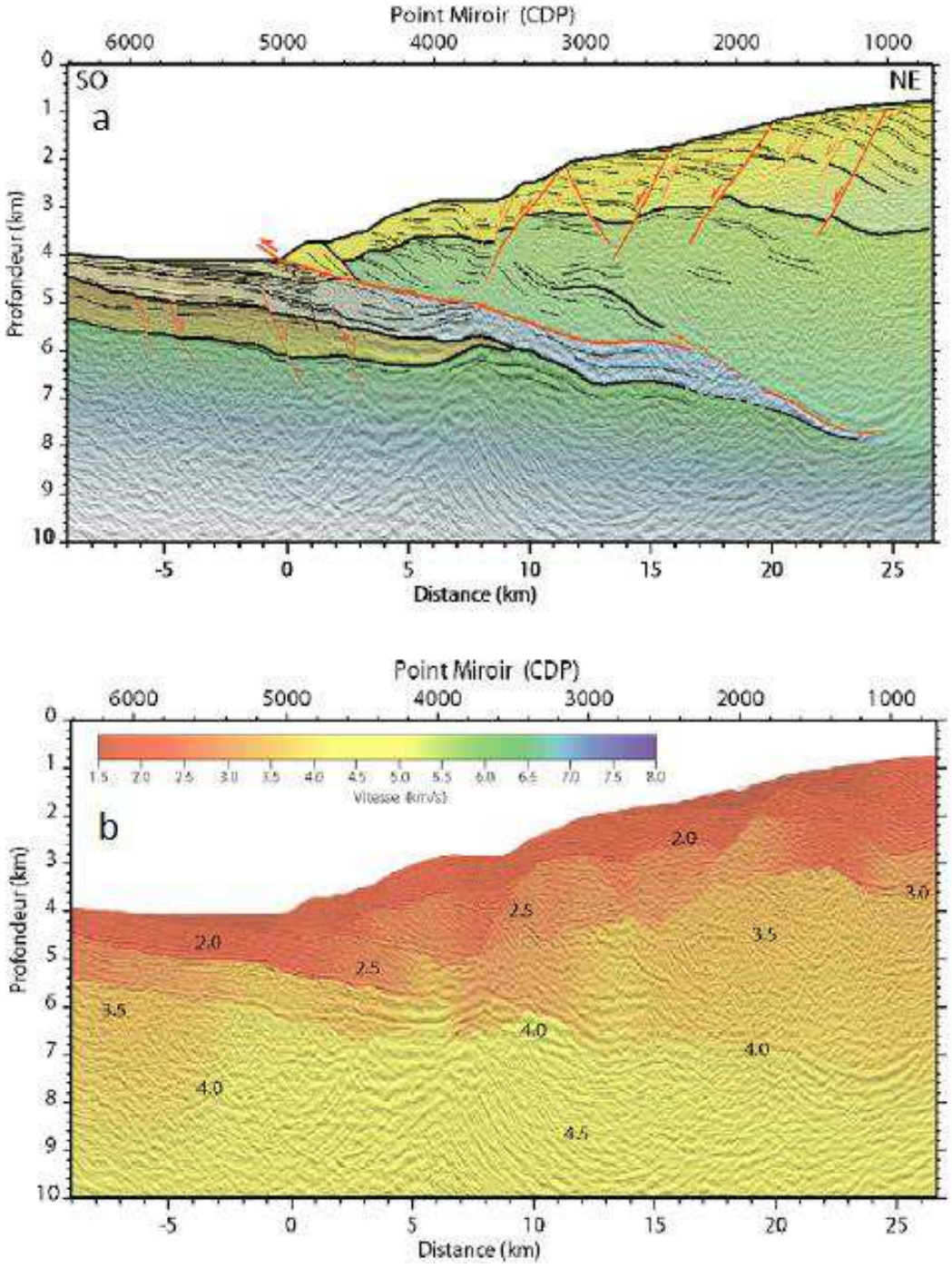

Figure 7. 10 Profile SIS16 located south of the study area in front of Salinas; a) profile SIS16 with line drawing showing normal faults; b) velocity model of profile SIS66 (Calahorrano, 2005).

The boundary zone between these two major mechanical domains remains uncertain. The Vp Velocity structure of the margin basement between profiles SIS13 and SIS66 is on the average ~5.0 km/s (Figure 7.6) indicating that the nature of this basement is likely to be similar to the interpreted mafic basement along Profile SIS05. Moreover, the Vp structure of the margin basement along Profile SIS14 (Figure 7.6) is similar (average ~3.7 km/s) to that of Profile SIS68, and the landward dipping band of reflectivity Pa/IB1 in profile SIS66 (Figure 6.6) might figure out an ancient thrust sheet. Therefore we tentatively place the boundary between the two mechanical domains slightly north of profile SIS66.

In conclusion, comparing MCS profiles from the northern and the southern segments of the study area, we found that 1) the structures within the margin basement at the north are characterized by the presence of the high Vp velocity associated to mafic rocks of the Piñon Formation, whereas the southern segment is rather characterized by an interpreted thrust sheet complex with lower Vp velocities; 2) this result suggests that the rock nature changes from more resistant in the north capable of accumulating more elastic strain before breaking, to possibly less resistant sedimentary rocks that tend to deform more easily without accumulating so much stress

7.4. Correlations between Inter-seismic coupling, seismicity, and margin outer-wedge and inter-plate structures along the Central Ecuador margin

As presented in Chap 3, the work by Nocquet *et al*., (2014), Chlieh *et al*., (submitted), Font *et al*., (2013) show that the inter-seismic coupling (Figure 3.6) and seismicity (Figure 3.7) of the Central Ecuador margin vary strongly from the northern margin segment and its fully locked patch off La Plata Island and low magnitude seismicity within the adjacent inner margin wedge, to the southern margin segment that is characterized by a very weak coupling and an absence of seismicity (Figure 7.11); these variations that reflect a complex stress and strain distribution may be caused by different factors such as the presence or absence of subducted seamounts (Scholz *and* Small, 1997), thickness variations and physical properties of the subduction channel (Contreras *et al*., 2011), and the geological nature and fracturing degree of the margin rocks. In the study area, as indicated in Figure 7.3, subducted seamounts are omnipresent and distributed over both the highly and weakly coupled zones (Figure 7.12) differing only in their distribution and shape along and across the Ecuadorian central margin. Moreover, as discussed in section 3.4, the geological nature and structure of the margin change drastically between the northern and southern margin segments.

7.4.1. Inter-seismic coupling and seismicity variations and their relation to subducted seamounts

7.4.1.1. The strong inter-seismic coupling and high micro-seismicity associated with the La Plata Island patch is related to the subducted broad oceanic massif OM.

The highly coupled La Plata Island patch in the northern margin segment coincides nicely with subducted oceanic massif OM (Figure 7.12). The area of strongest inter-seismic coupling (ISC > 70% and up to 90%) is located west of the La Plata Island and correlate with the highest (~1-2 km) peaks like SMt 2 and 3 that spot the **trailing flank** of the OM. These peaks are evidence for a strong interplate roughness. Moreover in this region, a classical **subduction channel** consisting of thick soft, water-rich sediment blanketing the subducting crust of the OM **is absent** or thin enough (< 150m) not to be detected in the PSDM MCS data (Figure 6.2, and 6.3). Therefore the much greater than 1 ratio of the peaks height over the SC thickness supports a strong ISC. Additionally as discussed in section 7.3.4, the **basement of the margin outer-wedge is believed to be mechanically resistant** as it is inferred to consist of high Vp, mafic rocks of the Piñon Formation. Consequently, the strong roughness of the OM trailing flank, together with the resistant nature of the basement of the outer-margin wedge, and the absence of a subduction channel likely account for the locking the plate interface beneath the shelf edge and outer-margin wedge upper slope.

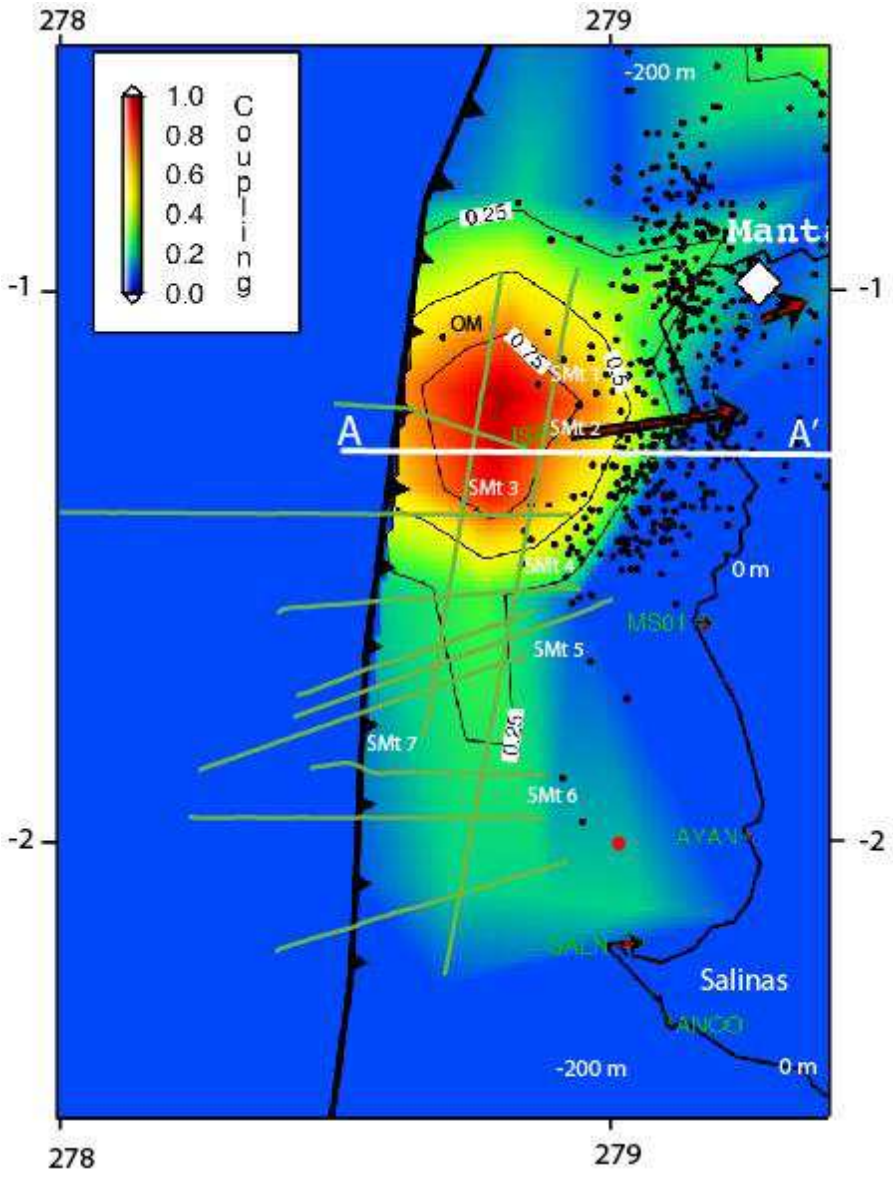

Figure 7. 11 Distribution of the inter-seismic coupling around La Plata Island derived from the inversion of the inter-seismic GPS velocities, it varies from blue (0% of coupling) to red (100% of coupling) (personal communication from Chieh et al.); seismicity is indicated by black dots from the RENSIG catalog (1994-2007); red dot indicates the 1981, Mw 6.4 earthquake occurred in the southern margin segment (CMT catalog). Green lines indicate the position of SISTEUR MCS profiles; white line corresponds to the cross-section A-A'.

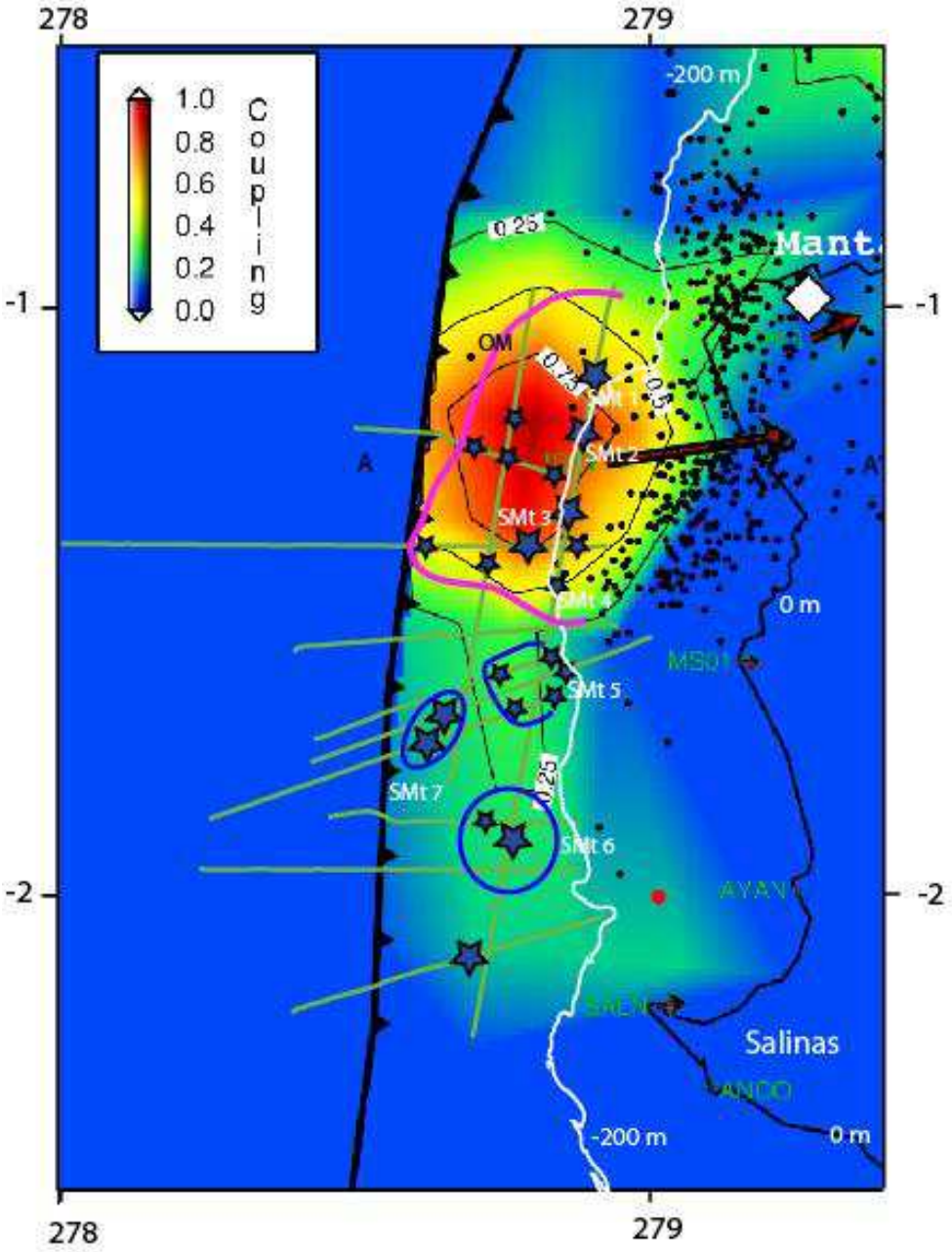

Figure 7. 12 Map showing the Oceanic Massif and Seamounts within the inter-seismic coupled zone. Inter-seismic coupling derived from the inversion of the inter-seismic GPS velocities varies from blue (0% of coupling) to red (100% of coupling) (personal communication from Chieh et al.); OM :oceanic massif outlined by a pink line; stars: subducted peaks; Blue contours and SMt : seamounts or multi-peaks seamounts; the -200 m contour shown in white shows the shelf edge, and coastline is in black; green lines corresponds to the MCS profiles; red dot indicates the 1981, Mw 6.4 earthquake (CMT catalog). Green lines indicate the position of SISTEUR MCS profiles.

It is remarkable to note the quasi-absence of seismicity in the outer-wedge locked zone (Figure 7.12, and 7.13). In other subduction zones, this region is generally inferred mechanically weak, frictionally stable and aseismic (Byrne *et al.,* 1988; Scholtz, 1998) so that during the inter-seismic period, the shear stress on the updip fault segment may be low (Wang *and* Dixon, 2004; Wang *and* Hu, 2006). In the La Plata Island region, the outer-wedge is aseismic although it is highly coupled suggesting that stress is high and strain is accumulating possibly preparing for a larger earthquake than those that occurred during the clustering events (Vallée *et al*., 2013). In contrast with the outer-margin wedge, the micro-seismicity has been quite dense over the last ~15 years within the inner-margin wedge East of La Plata Island (Font *et al.,* 2013). This micro-seismicity extends sub-parallel to the trench from the interplate contact to the surface within an 80-km-long-and-30-km-wide area that underlies well the circular shape of the locked patch (Chlieh *et al*., submitted) and the landward part of the broad subducted OM as inferred from the uplift history of the La Plata Island. The micro-seismicity (Figure 7.11) is surprisingly associated with an inter-seismic coupling (ISC) < 50%, which is in turn characteristic of the Central Ecuador margin.

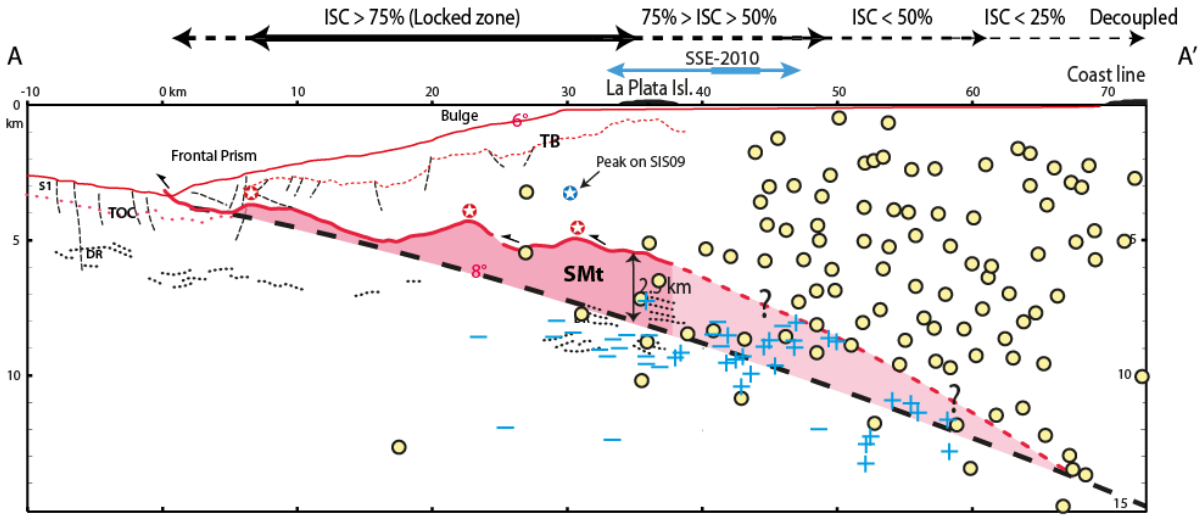

Figure 7. 13 Cross-section A-A' in the vicinity of the interplate seismogenic zone. The localization of cross-section A-A' is shown in figure 7.11. Yellow circles indicate the 1994-2007 earthquake hypocenters relocated in a 3D model by Font et al., (2013); black dashed line corresponds to the expected interplate contact of Graindorge et al., (2004); red line indicates the décollement interpreted from the MCS profile SIS05, whereas the dashed red line represents the inferred décollement beneath the inner margin wedge; light-blue "+ and -" indicate motion polarities of earthquakes during the 2010 slow slip event (SSE, Vallée et al., 2013); SMt: oceanic massif (OM); TB: top of the basement; TOC: top of the oceanic crust; DR; deep reflectors within the subducting plate.

Wang *and* Bilek (2011) consider that seamounts subduct largely aseismically generating

numerous small earthquakes; this is opposite to the held expectation about seamounts producing large earthquakes (Das *and* Watts, 2009). In our study area, the GPS data, the seismicity (clusters and SSE), and structural interpretation indicate that the mode of subduction of the OM differs from the above proposed models (aseismic subduction or stick-slip subduction). The analysis of the temporal sequences of earthquake swarms and potential slow slip events (Figure 3.8), together with their relationship with the distribution of the inter-seismic coupling across the region of the subducted OM, allow to proposing a refined model of seamount subduction:

a) Between two periods of earthquake swarms and SSEs, the leading flank of the OM partially creeps aseismically and stress increases within the inner margin wedge because this flank is not locked (at this location the ISC < 50%). In the meantime, the trailing flank of the OM remains fully locked so that the elastic strain accumulates within the outer margin wedge. This first stage is considered as a time period during which the OM front slightly creeps, while the stress/strain gradually builds up across the margin wedge (Figure 7.14.a).

b) When a SSE occurs with a mean 10-40 cm slip (Vallée *et al.,* 2013), the ISC decreases along a short segment of the subduction fault and an earthquake swarm is triggered either within the inner margin wedge (e.g., 2002, and 2005; Vaca *et al*., 2009; Vallée *et al*., 2013) or within the subducted OM as suggested in this work for the 2010 SSE. This implies that part of the strain accumulated within inner margin wedge is released. In contrast, since most of the OM trailing flank remains locked, elastic strain keeps building up within the outer margin wedge. This second stage corresponds to a small aseismic advance of the OM leading flank while its trailing flank remains stuck to the outer-wedge igneous basement (Figure 7.14.b).

c) Although the equivalent magnitude of the SSE and its associated swarm is ~6.1 Mw (Vallée *et al.,* 2013), the full rupture of the 50 km by 50 km highly coupled La Plata Island patch could generate a larger 6.9-7.1 Mw subduction earthquake with a possible 1-2 m co-seismic slip (Figure 7.14.c). Although there is no evidence for such an earthquake in the last century catalogs (CMT, EHB, and SISRA), it could occur with a time interval that is even larger than the number of SSE between large earthquakes is high. This large earthquake may be triggered by a swarm/SSE, whose rupture might propagate towards the outer wedge. This third stage corresponds to a larger and infrequent seismic advance of the OM.

d) If the stress was to concentrate along the weakened layer that we interpreted from the

reflectors DR and the low P-wave velocity zone (LVZ in section 3.1, Figure 7.6) within the under-riding crust, then a series of small fault ruptures could occur within this layer (Figure 7.14.b), and connect to each other to form a possible detachment or new décollement fault. For example, during the 2005 swarm, the 6.1 Mw thrust earthquake (0501211345) that occurred beneath La Plata Island at 11.56 km depth, slipped by 0.46 m (Vaca *et al.,* 2009). The location of this earthquake roughly coincides with our interpreted DR reflectors within the LVZ, supporting thrusting within the OM, along a possible detachment fault under creation. When dragged downdip in a higher stress environment, this fault may further develop and separate a fragment of the OM from the underlying subducting plate. Such an OM fragment could be later under-plated beneath the margin.

In conclusion, our refined model supports that the OM subduction is accommodated by creeping phases along the OM leading flank, alternating with slip phases that may occur as SSEs along the OM leading flank, and as larger subduction earthquakes rupturing the locked OM trailing flank. , Some slip localizes within the under-riding crust likely as a result of local high-stress interplate locking, thus anticipating the development of an intra-down going plate detachment or décollement fault. The above-described stages of OM subduction can be viewed as the margin over-riding the OM according to a process that may be compared with the advance of a caterpillar. In essence the mode of OM subduction that includes locking the updip fault segment and the triggering of a possible large earthquake agrees with the model by Scholtz and Small, (1997) in a decoupled subduction zone.

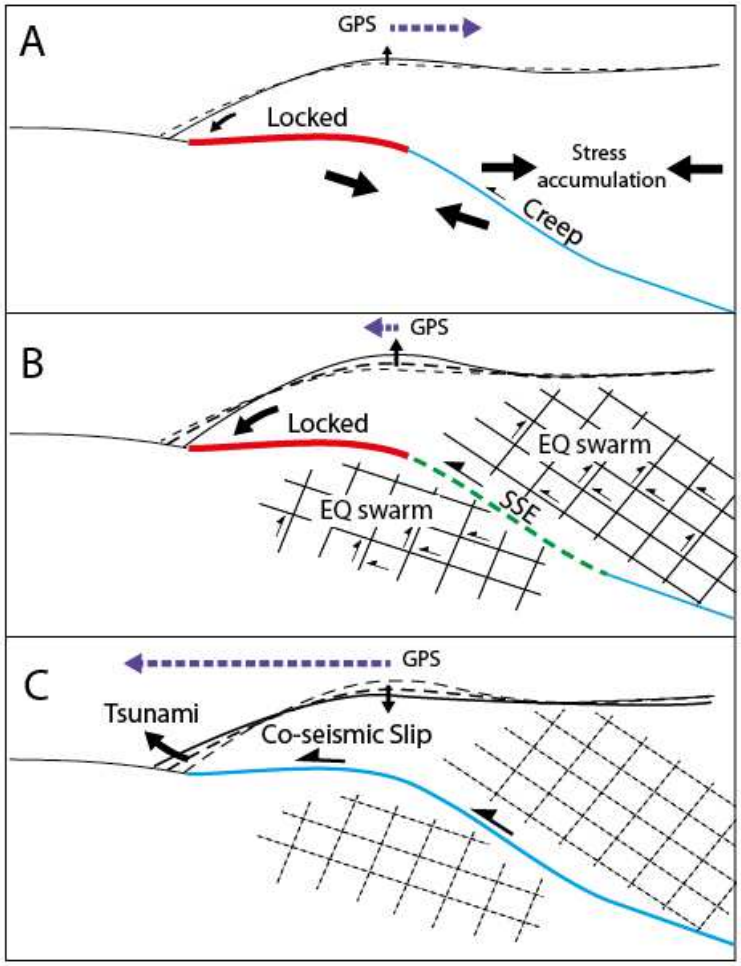

Figure 7. 14 Model of seamount's subduction. The three stages of subduction: a) the oceanic massif (OM) is locked along its trailing flank, and creeping along its leading flank; stress accumulates across the margin wedge, the GPS data indicates an uplift of the seafloor and a continuous landward displacement; b) the trailing flank of the OM remains locked while a slow slip event (SSE) and an earthquake swarm occur, the GPS data indicates a slight uplift of the seafloor and a slight reverse displacement seaward; c) the strain is released during a large coseismic slip that may trigger a tsunami .

7.4.1.2. **The weak inter-seismic coupling and the lack of seismicity within the southern margin segment are also related to the seamount subduction: why?**

In contrast to the highly coupled La Plata Island patch, the southern margin segment of the study area lies within a low ISC region (ISC < 40%), although it coincides with the subduction of several isolated seamounts (SMt5, SMt6, and SMt7, Figure 7.12). SMt6 is the largest seamount reaching 2 km in height from its base. However, a relatively stronger inter-plate coupling associated with the SMt5 and SMt6 (Figure 7.12) may not be discriminated by the GPS measurements as they

are distributed along the coast, as far as 40 to 50 km from the SMt6.

In between the seamounts, the under-riding plate is covered by a smoothed ~1 km thick sediment layer that forms locally a well-defined subduction channel (SC) interpreted from the PSDM MCS data (Figure 6.5-6.8).

Another contrast with the northern margin segment deals with a different nature of the margin rocks that have been interpreted as sedimentary (Figure 7.9). Therefore, these rocks are considered mechanically less resistant than rocks of the Piñon Formation (see section 7.3.5).

Consequently, the SC may work as lubricant facilitating the weak ISC, and the sedimentary nature of the margin basement, which is characterized by a lower yield stress than mafic rocks, accommodates the tectonic deformation related to the seamount subduction more easily than Piñon Formation. Therefore, the outer wedge of the southern margin segment is neither prone to accumulate large elastic strain nor generate very large earthquakes. The southern margin segment is characterized by a remarkable absence of micro-seismicity over the 1996 - 2010 time period (Figure 7.12). This absence of seismicity may indicate that SMt5 and SMt6 have not yet reached the most resistant part of the inner margin wedge basement. However, the inner margin wedge experienced some thrust earthquakes with Mw > 6 such as the 1981 thrust earthquake (6.4 Mw, CMT catalog). These earthquakes cannot be however ascribed to seamount subduction as they could result from normal subduction processes.

In conclusion, the mode of seamount subduction in the southern segment is rather controlled by aseismic creep and gravity tectonics, and in that sense conforms to the model of Wang *and* Bilek (2011).

Conclusion

The structural interpretation of the 2D Pre-stack Depth Migrated images obtained from the Multichannel Seismic data (SISTEUR, 2000) was combined with other data sets available (high-resolution bathymetry, OBS wide-angle velocity models, GPS inversion model, and seismicity) to better characterize the Ecuadorian convergent margin between Manta and Salinas. The main findings of our study suggest that:

1) the Roughness of the Interplate Contact varies across the study area

The density of the subducted peaks, observed along the PSDM images of dip/strike profiles, varies considerably in the study area suggesting different interpretations for each margin segment. The northern segment is characterized by the subduction of a broad Oceanic Massif (OM). The presence of the OM is corroborated by the shallow dip angle between 2.5° and 4° within a zone where the regional scale dip angle is ~10°. The interplate contact in the northern segment is rough, and the sedimentary layer (<150m) covering the OM is not thick enough to reduce the roughness of interplate contact. In contrast, the interplate contact of the southern segment is relative less rough than that of the northern segment. It has a relative higher dip angle of 6-7°, and is spotted by isolated seamounts surrounded by a ~1 km average thick sedimentary layer.

2) The nature of the basement rocks differs at both margin segments

The P-wave velocity models together with the structural interpretations show that the basement at the northern segment is more resistant and correlates with the basaltic rock from Piñon Formation; whereas the southern segment is constituted mainly of sedimentary rocks. The dipping landward reflectivity bands interpreted within the southern basement margin suggest the basement is rather characterized by thrust sheet complex, which has lower Vp velocities than those of Piñón Formation.

In previous study, high and low velocity zone (HVZ, and LVZ, respectively) were observed along the OBS wide-angle velocity models. We found that the HVZ correlate with the core of the Oceanic Massif (OM), and the LVZ does not correspond to the Subduction Channel (SC) proposed by others authors, but to a weak velocity layer within the subducting plate.

We further found that this LVZ coincide with the interpreted deep reflectors DR, which appear along all the profiles.

3) the Subduction Channel Thickness increases southward

The thickness of the Subduction Channel in the study area varies, being relative thin (<150 m) in the northern segment and thick (~1 km) in the southern segment. Between the northern and southern margin segments, there is a transitional zone characterized by the presence of rich-fluid sedimentary lenses and dry sections of the subduction channel.

4) The Inter-seismic Coupling along the trench is mainly controlled by the roughness of the Interplate Contact.

The high Inter-Seismic Coupling (ISC) in the northern segment results from the subduction of the broad Oceanic Massif beneath the basaltic rocks of Piñon Formation. This massif corresponds to a rough surface, which lacks of a relative thick sedimentary cover that acts as lubricant reducing the locking. In contrast, the southern segment coincides with a weak locked zone. This weak locked correlates with an interplate contact that is less rough and is covered by a ~1 km thick sedimentary layer than smooth the interplate contact.

5) The classic subduction model may not be applied for the La Plata Island Patch

The seismicity and variations of the inter-seismic coupling indicate that the accumulation and release of elastic strain vary remarkable across the study area. Based on the available data, we found that the Oceanic Massif (OM) is accommodated during four stages that do not correspond to the classic subduction models (stick-slip, and aseismic subduction). Our refined model compared with the advance of a caterpillar proposes that: 1) the OM subduction is accommodated by creeping phases along the OM leading flank, whereas the OM trailing flank remains locked accumulating elastic strain; 2) part of the strain accumulated within inner margin wedge is released by earthquake swarms and slow slip events (SSEs), whereas the elastic strain keeps building up within the outer margin wedge; 3) a large earthquake in the locked zone is probably triggered by a swarm/SSE, resulting in an infrequent advance of the OM and probably a tsunami; and 4) apparition of a new décollement along a weakened surface, and under-plating of OM fragments to the basement rocks. These stages apply only for the strongly locked northern margin segment of our study area. The data sets suggest that the southern segment is accommodated by aseismic creeping.

6) **The uplift of La Plata Island results from the subduction of the Oceanic Massif**

Previous studies show than La Plata Island is formed by marine terraces and rock of Piñón Formation. We found that La Plata Island started to emerge between 643 and ~ 710 kyr as results of the subduction of the Oceanic Massif (OM). The OM leading flank subducted ~1.3-1.4 Ma, and now lies probably beneath the coastline. This hypothesis is supported by our structural interpretations and coincides with the dates of marine terraces suggested by other authors.

7) Morphological re-entrants resulted from the subduction of seamounts

The re-entrants along the study area coincide with the position of area affected during the seamount subduction; besides, the size and shape of the scars are coherent with the seamount expected shape interpreted from the seismic profiles. Another morphologic change linked to the seamount tunneling is indicated by the seafloor high "A" that lies above a seamount peak.

In conclusion, we consider that the central Ecuadorian margin is mainly characterized by the subduction of the broad Oceanic massif that increases considerable the inter-seismic coupling, and lifts up La Plata Island. The classic model of stick-slip may not be used for La Plata Island Patch. The increase of the subduction channel thickness and smoothing of the interplate contact reduces the inter-seismic coupling, and facilitates the aseismic subduction in the southern margin segment.

Perspectives

Our work presents several factors that probably control the variations of the inter-seismic coupling and seismicity along the central Ecuadorian margin. However, a higher density of MCS and WA profiles would permit to better understand the effects of the subducted structures. Other MCS profiles from SISTEUR (2000) obtained both at the north and south of our study area may be processed to see if our results are similar in other segment of the Ecuadorian margin.

The link between the micro-seismicity and the subducted Oceanic Massif (OM) must be analyzed with more detail using profiles between La Plata Island and the coastline that permit to image the prolongation of the OM and to corroborate the hypothesis about the uplift of Manta Peninsula linked to the subduction of the OM.

The perspectives of my work also concern the processing of the data.

First, during the processing of the dataset, the external mute needs to be redesign in order to improve the seafloor reconstruction. This task would facilitate the detection of the polarity of the reflectors on the migrated image (i.e., the reversed polarity at the décollement).

Only some MCS profiles have their equivalent in OBS wide-angle data. The existing OBS velocity models may be incorporated (i.e., mixed), as "a priori" information to the MCS velocity models which are relative closed. In this way, we hope to better image the deep structures and define more precisely the position of the interplate contact.

Finally, the post-processing of the migrated images (Ribodetti *et al*., 2011; Collot *et al*., 2011) should be applied in zones where the interplate contact and the bottom of the margin basement may be linked to rich-fluid sediments in order to obtain a refined P-wave velocity model .

Annex A

(Paper to be submitted)

Subducted Seamount locks the outer-wedge megathrust in Central Ecuador.

E. Sanclemente, J-Y Collot, A. Ribodetti, M. Chlieh

Subducted Seamount locks the outer-wedge megathrust in Central Ecuador.

E. Sanclemente, J-Y Collot, A. Ribodetti, M. Chlieh

Abstract: The influence of subducted seamounts on inter-plate coupling has remained controversial. Using seismic reflection imaging offshore Central Ecuador, we detected a broad, shallow multi-peak seamount spatially associated with an aseismic locked patch along the up-dip segment of the megathrust in the La Plata Island region. This patch was modeled from New Global Positioning System (GPS) measurements as close as 35 km from the trench axis above the seamount apex. The correlation between the seamount and the strongly coupled zone suggests that the absence of subduction channel, the highly jagged seamount-trailing flank and the mafic nature of the margin basement are the main cause of the megathrust locking. In contrast, the leading front of the seamount is less coupled and associated with severe faulting within the margin basement as illustrated by repeated earthquake swarms. An earthquake swarm related to the 2010 Slow Slip Event supports thrusting beneath the seamount, along a 7-10 km-deep highly reflective, low velocity layer.

One Sentence Summary: New MCS and GPS data provide evidence for a subducted seamount locking the outer-wedge megathrust, while the inter-plate coupling is weaker at the leading flank of the seamount, and earthquake swarms and SSE episodically deform both the margin wedge and the seamount.

Introduction

Conceptual and mechanical models support that seamount subduction enhance inter-plate frictional resistance, thus acting as an asperity or a barrier to rupture during an earthquake [Cloos, 1992; Scholz and Small, 1997; Yang, 2012]. Conversely, seamount subduction was equally associated to weak inter-plate coupling [*Mochizuki et al.*, 2008], highly fractured media around the seamount [*Dominguez et al.*, 1998; *von Huene and Lallemand*, 1990; *Wang and Bilek*, 2011] and subduction erosion [Bangs, 2006; von Huene et al., 2004], a situation that favors aseismic creep and small earthquakes [*Cummins et al.*, 2002; *Wang and Bilek*, 2011]. Various examples of correlations between subducting seamounts and large earthquakes or tsunami earthquakes have been proposed [*Bell et al.*, 2010; *Duan*, 2012; *Hicks*, 2012; *Husen et al.*, 2002; *Kodaira et al.*, 2000; *McIntosh et al.*, 2007; *Mochizuki et al.*, 2008; *Singh et al.*, 2011]. Nevertheless, correlating a

subducted seamount with a specific state of inter seismic plate coupling has remained a major challenge because in near-coastal regions where inter seismic coupling is well resolved, the coupling effect of a deeply buried seamount is not easily discriminated. Besides, where shallow subducting seamounts (< 10 km) are detected [*Bangs*, 2006; *McIntosh et al.*, 2007], interseismic coupling is poorly determined in absence of seafloor geodetic data.

The Ecuador margin: a locked patch near La Plata Island.

At the Ecuador convergent margin, seamounts carried by the Carnegie Ridge are subducting eastward at 47 mm/yr [*Vallée et al.*, 2013] beneath a very narrow margin wedge, which allowed GPS measurements to less than 70 km, and up to 35 km from the trench axis at La Plata Island (LPI) (Fig. 1) [*Chlieh et al.*, submitted; *Nocquet et al.*, 2014]. The framework of this erosive margin [*Sage et al.*, 2006] consists of a high-Vp velocity (3.5-6 km/s) [Graindorge et al., 2004] Cretaceous oceanic basaltic complex that outcrops on the LPI [Baldock, 1983]. Megathrust earthquakes (7.7<Mw<8.8) have repeatedly occurred in 1906, 1942, 1958, and 1979 along the northern Ecuador subduction interface, north of Manta Peninsula (Fig. 1A) [Kanamori and McNally, 1982; Kelleher, 1972]. In contrast, Central Ecuador, from Manta to Puerto Lopez (Fig. 1), recorded recurring, 1-3 months-lasting, Mw 4.0 to 6.2, intense earthquake swarms in 1998, 2002 and 2005 [*Font et al.*, 2013] (Fig. 1B), and a slow slip event (SSE) in August 2010 (Fig. 1C) [*Vallée et al.*, 2013].

GPS data inversion revealed the megathrust earthquakes region to be characterized by a series of patches locked to depths of ~35 km beneath the coastal region [*Chlieh et al.*, submitted]. In the earthquake swarms region, i.e. close to LPI and further south, the plate interface is weakly coupled with the conspicuous exception of the well-resolved, 50 X 50 km, strongly coupled LPI patch (Fig. 1B) [*Chlieh et al.*, submitted; *Vallée et al.*, 2013]. At this location, the subduction interface is currently locked from near the trench to a depth of ~10 km, where the August 2010, SSE occurred (Fig. 1C). The shallow locked zone, which peaks up ~15 km trenchward from the LPI, contradicts the widely accepted concept that the updip segment of the plate boundary is a poorly coupled area characterized by stable sliding and a rate-strenghtening behavior [Byrne et al., 1988; Scholz, 1998]. While at shallow depth the inter-seismic coupling is generally poorly resolved, few examples such as central Peru [Gagnon, 2005] and the Ecuador example report strong coupling near the trench, although their cause has remained unclear.

Multichannel Seismic Reflection Data

We conducted a Multichannel Seismic Reflection (MCS) survey in the proposed La Plata Island locked zone (Fig. 1B) to investigate the potential causes of the high inter-seismic coupling and its relation to seismicity and 2010 SSE. We shot coincident MCS and wide-angle data along lines SIS05, SIS07 and SIS09, and MCS data only along the other lines. Tomographic Vp models based on a join refraction-reflection travel-time inversion were first conducted along lines SIS05 and SIS09 (Gailler, 2005, 2007). Then, mixed velocity models were constructed [Agudelo, 2009] from WA and MCS data, prior to depth migrate the MCS data (see Supplementary Material).

A broad multi-peak subducted seamount

From the PSDM seismic reflection lines, we infer the absence of a subduction channel and the presence of anomalous plate boundary topography beneath the margin wedge, west of LPI. A strong and highly uneven, negative-polarity reflector interpreted as the plate interface dips landward with a shallow, 3°- 4° average angle (Fig. 2a), so that, beneath the shelf edge, the inter-plate fault departs by ~2.5 km above the, otherwise smoothly curved, ~8°-dipping, regional subduction interface that was constructed from wide-angle seismic data [Graindorge et al., 2004] and the earthquake hypocenters distribution [*Font et al.*, 2013]; *Vallée et al.* [2013] (Fig. 2b). From the plate-interface reflector on all MCS sections, we constructed a 3D geometry of the plate-interface. It outlines a collection of closely spaced peaks that belong to a broad (55 X ~50 km) multi-peak subducted seamount (Fig. 1b), one of them climax 3.2 km beneath the seafloor ~10 km SW of LPI (Pk1 in Fig. 3). As the peaks are subducted, the outer-wedge conforms to their shape (Fig. 2a) but no large active fault is identified in the margin. This overall interpretation is supported by: (1) the 50-km-wide and 10-km-deep E2 re-entrant (Fig. 1b) that gently scallops the lower margin slope and is evidence for the seamount passage, (2) subduction erosion of this margin segment [*Sage et al.*, 2006] and its steep taper angle, (3) a seaward protrusion of the upper margin slope and shelf edge adjacent to LPI, reflecting uplift with respect to its depressed northern (off Manta) and southern (Lat 1°45S) extremities, which echo local subsidence (Fig. 1b), (4) - uplift of LPI attested by Pleistocene marine terraces [*Pedoja et al.*, 2006].

Subducted seamount and inter-seismic coupling

In map view, the subducted seamount coincides with the geodetically determined locked zone (Fig. 1b). This concurrence implies that the buried seamount increases strongly the interseismic

coupling in an otherwise weakly coupled margin segment, a finding that confirms the model proposed by [*Scholz and Small*, 1997]. However, the coupling is found to be the highest along the trailing flank of the seamount, and lower at its leading flank. We suggest that the strong roughness caused by resistant peaks arising from the subducted seamount, the absence of a noticeable subduction channel, and the strength of the margin mafic basement are the primary causes for holding the megathrust locked along the seamount trailing flank. An explanation for the lower coupling at the seamount front may rely on the stratified nature of a seamount that encompasses a stiff igneous core plastered by weaker extrusive and volcaniclastic sequences underlying a pelagic cap [*Contreras-Reyes et al.*, 2010; *Expedition 330 Scientists*, 2012]. During subduction, this sediment imbricates with outer-wedge tectonic slivers to form a weak sediment shield that wedges beneath the margin ahead of the seamount. The shield might behave as a strain buffer that cannot be described using friction laws on a single fault plane [*Wang and Bilek*, 2011]. Such a highly-tectonized wedge was identified from a deep-sea submersible traverse across the collision zone between the Bougainville seamount and the New–Hebrides arc [*Collot et al.*, 1992]. This wedge tends to smooth the relative high-drag shape of a seamount and facilitates its subduction by streamlining and reducing normal stress. High-amplitude seismic reflectivity attributed to entrained sediment ahead of the subducted seamount [*Bangs*, 2006; *Bell et al.*, 2010] support fluid-rich media and high fluid pressure, thus reducing inter-plate friction and stick-slip behavior. As a result, large strain may not accumulate at the plate interface ahead of the seamount and aseismic slip may dominate.

Subducted seamount and seismicity

On a broader scale, a massive subducting seamount likely concentrates significant stress in it and in the adjacent margin basement [Wang and Bilek, 2011]. Relocated earthquakes recorded by the IG-EPN local network (1994-2007) [Font et al., 2013] attest that most of the margin crust inboard from the subducted seamount is being pervasively fractured and faulted (Fig.1b), essentially during repeated swarms, which largest events exhibit thrust motion. This result supports strain distribution in the margin ahead of the seamount, and agrees with sandbox experiments [Dominguez et al., 1998], which predict that, when tunneling, a seamount fractures surrounding margin rocks [von Huene and Lallemand, 1990]. Some relocated earthquakes (Font et al., 2013) happen within the inferred shield or beneath the leading flank of the seamount (Fig. 2b). Interestingly, the August 2010 SSE occurred near the interpreted leading flank of the seamount (Fig. 1c and 2b) as also suggested for the Tokai SSE in Japan [*Kodaira et al.*, 2004]. The SEE-

related sharp increase in seismicity [Vallée et al., 2013] focused at 7-10 km depths and delineated a circular shape possibly outlining seamount structures beneath the continental shelf. Despite an estimated ± 2 km depth uncertainty, most 2010-SSE earthquakes occurred in or beneath the seamount within a highly reflective (DR reflectors, Fig. 2 and 3), low Vp velocity zone that results from underthrusting the 5.1 km/s Carnegie Ridge oceanic layer 2 beneath the > 6.0 km/s margin wedge basement [*Graindorge et al.*, 2004], and features a layer of mechanical instability. The earthquakes thrust motions-consistent polarities and waveforms [*Vallée et al.*, 2013] support contractional shearing within the stressed seamount. This implies that the seamount is bound to shear along a detachment thrust or fragment further down-dip, and contribute to feed a subduction mélange or possibly underplate. Conversely, in the locked zone, both the seamount and outer margin wedge remain largely unaffected by earthquakes, attesting that although fractured, the outer wedge stores substantial elastic strain.

A model for seamount subduction

Although an equivalent moment magnitude of 6.0-6.3 [*Vallée et al.*, 2013] was released during the SEE and the largest repeaters, they do not preclude from generating a larger, shallow thrust Mw ~6.9-7.1 earthquake if the entire LPI locked patch was broken. We thus propose that, at shallow depths (< 12 km), rather than moving down dip steadily either aseismically or fully by stick-slip, the seamount progresses episodically by frontal creeping and SSE events alternating with less frequent larger seismic slips along its trailing flank (Fig; 4). SSE events accompanied by repeated thrust swarms would accommodate small-steps of this progress as well as internal seamount deformation, while between swarms and SSEs, i.e. during periods of ~3 to 5 years, the weakly-coupled front of the seamount would creep, until the seamount faces a strong enough frictional resistance allowing renewing stress for the next SSE and earthquake swarm. During this slow advance, the stiff part of the outer-wedge basement is believed to remain stuck to the seamount-trailing flank, thus down-flexing and accumulating elastic strain. Strain is eventually released on occasional bigger events causing larger increments in the seamount progress, and tsunamis during the elastic rebound. This displacement mode reflects the margin wedge crawling over the seamount in an undulating wave motion, as would a caterpillar.

On the long term, the subducted seamount likely caused the uplift of the LPI margin segment. The LPI highest marine terrace started uplifting 643 to 710 kyr ago (Pedoja et al. 2006). At this time, based on a constant 4.7 cm/yr convergence rate, the interpreted top of the subducted seamount

lied ~30-35-km seaward of its present position (Fig. 5). To be accountable for the initial island uplift, the seamount or an extension of it should extend down-dip by another ~30 km beyond our MCS observations.

Is the locked outer-wedge megathrust favorable to a tsunami earthquake?

The setting of a potential bigger event is comparable to that of the 1947 and 1992 shallow tsunami earthquakes [*Kanamori*, 1972], which occurred in a region of seamount subduction of the Hikurangi and Nicaragua convergent margins [*Bell et al.*, 2010; *McIntosh et al.*, 2007]. Such events were responsible for larger tsunamis than expected from the surface wave magnitude, due to a large amount of slip [*Sakatake*, 1994] with a long duration and a slow rupture propagation on a shallow dipping fault [*Kanamori and Kikuchi*, 1993; *Velasco et al.*, 1994].

A weak interplate rupture partially caused by subducted sediment is believed to cause tsunami earthquakes [*Kanamori and Kikuchi*, 1993]. In our study area, the trench is devoid of significant turbidites and no subduction channel is resolved (Fig. 2 and 3), substantiating very few sediment in the interplate zone, with the exception of some low velocity (2.2-2.8 km/s) sediment lenses [*Sage et al.*, 2006]. In addition, robust seaward thinning of the margin basaltic basement accompanied by fluid-damaged rocks interpreted from a 500m-thick, 3.7-4.3 km/s Vp reflective zone at the base of the margin [*Sage et al.*, 2006] may reduce the rigidity near the plate interface, along the first ~10-15 km landward from the trench. Considering that the basalt is water-saturated, its critical porosity is ~15% [*Nur et al.*, 1998]. According to the Vp-porosity relation for igneous rocks, the basement rocks with Vp lower than 4.3 km/s (i.e. porosity higher than 15%) [*Sallares and Ranero*, 2005], would consist of fully shattered material. Such highly disaggregated material at the base of the margin basement, together with the fluid-rich sediment lenses at the plate interface may promote the slow rupture process and long duration required to excite a large tsunami [*Fukao*, 1979].

Figure and Captions

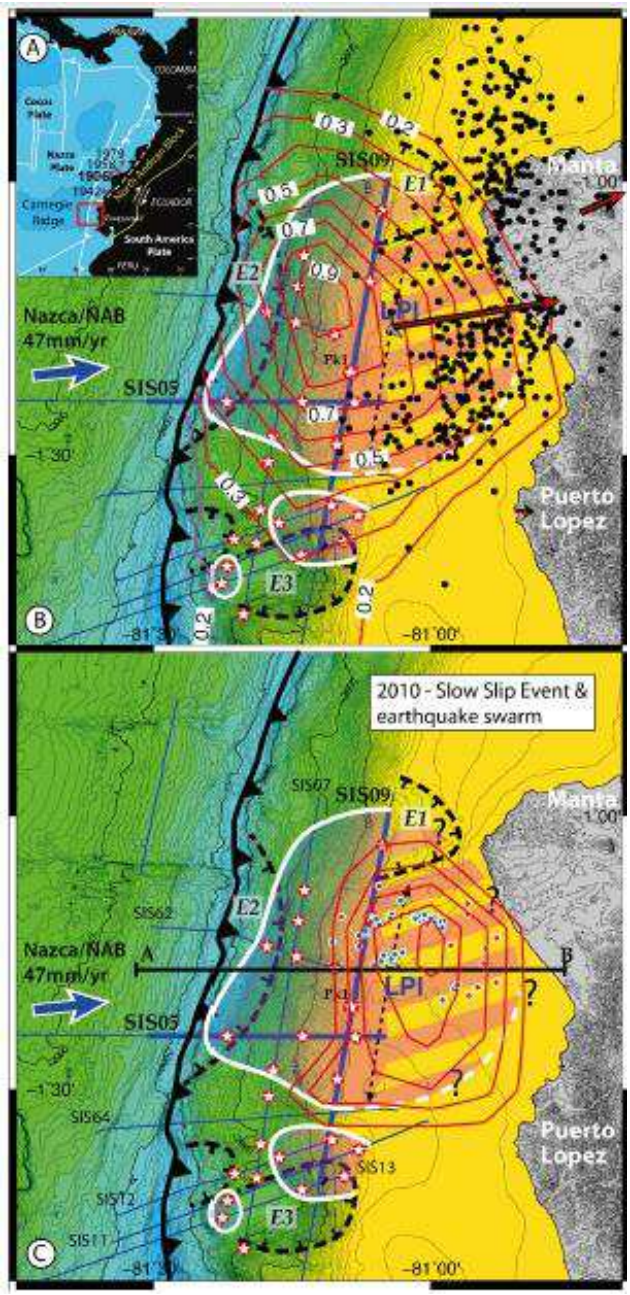

Fig. 1: A- Inset: location of study area in Central Ecuador, and major XXth century subduction earthquakes.

B-Bathymetry of the study area, contour interval is 50 m. Barbed-line is the trench axis and ticked black dashed lines with ticks are morphologic re-entrants (E1, E2, E3); Thin black dashed-line with arrows shows N-S axis of La Plata Island (LPI) basement high; Blue lines are SISTEUR MCS seismic reflection lines. Transparent orange body bounded by thick white contour is the interpreted broad subducted seamount with peaks (red/white stars along MCS lines). Striped orange/yellow area is inferred leading flank of the subducted seamount. Black arrows are observed GPS velocities expressed with respect to the NAB; red arrows are modeled velocities corresponding to the optimal spatial distribution of inter-seismic coupling (ISC) shown by the red contours with values each 0.1 (Vallée et al., 2013; Chlieh et al., sub.). Note that the locked patch (ISC>0.7) is located west of LPI and coincides with the subducted seamount. Seismicity (Black dots) from the RENSIG catalog (IG-EPN 1994-2007) relocated in a 3D model (Font et al., 2013) underlies well the sub-circular shape of the locked patch.

C-The August 2010 Slow Slip Event and its microseismicity associated with the leading flank of the subducted seamount and the coupled-uncoupled down dip transition; red contours are slip distribution each-5 mm (Chlieh et al., sub.); microseismicity (blue dots = depth <10 km; red dots =depth >10 km (Vallée et al., 2013).

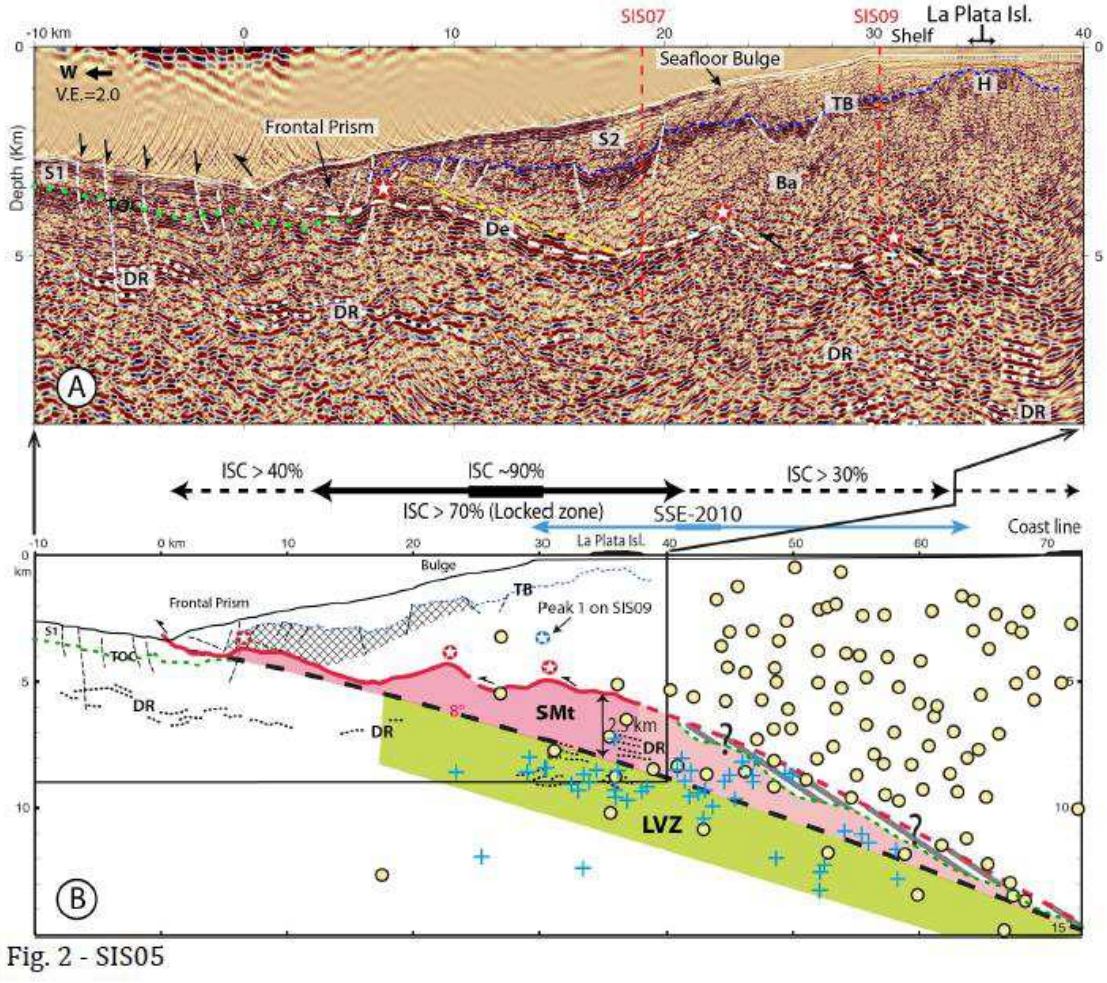

Fig. 2 - SIS05

Fig. 2: Section across the Central Ecuador margin and La Plata Island.

A- Prestack depth-migrated (PSDM) MCS line SIS05. S1, S2 = sediment, TB = Top of Basement Ba, H = Basement High; De = inter-plate megathrust; Stars = main peaks along De; DR = Deep Reflectors;

B- Synthetic cross section AB located in Fig. 1c; SMt= multipeak seamount; curved black dashed-line = regional subduction interface from Graindorge et al, (2004) and Font et al., (2013); inter-sesimic coupling (ISC) variation (Chlieh et al., sub); cross stitch pattern = mafic basement with Vp < 4.3 km/s (Graindorge et al., 2004) interpreted as shattered material (Sallares and Ranero, 2005); LVZ (green) = Low Velocity Zone (Graindorge et al., 2004); Grey hatch pattern = proposed weak sediment shield plastered over seamount leading flank; Note the correlation between rough SMt trailing flank and locked zone; dense earthquake distribution within the inner-margin wedge (yellow circles = relocated 1994-2007 earthquakes from Font et al., 2013), and 2010-SSE thrust events (blue crosses) (Vallée et al. 2013) laying dominantly within the LVZ subducting plate.

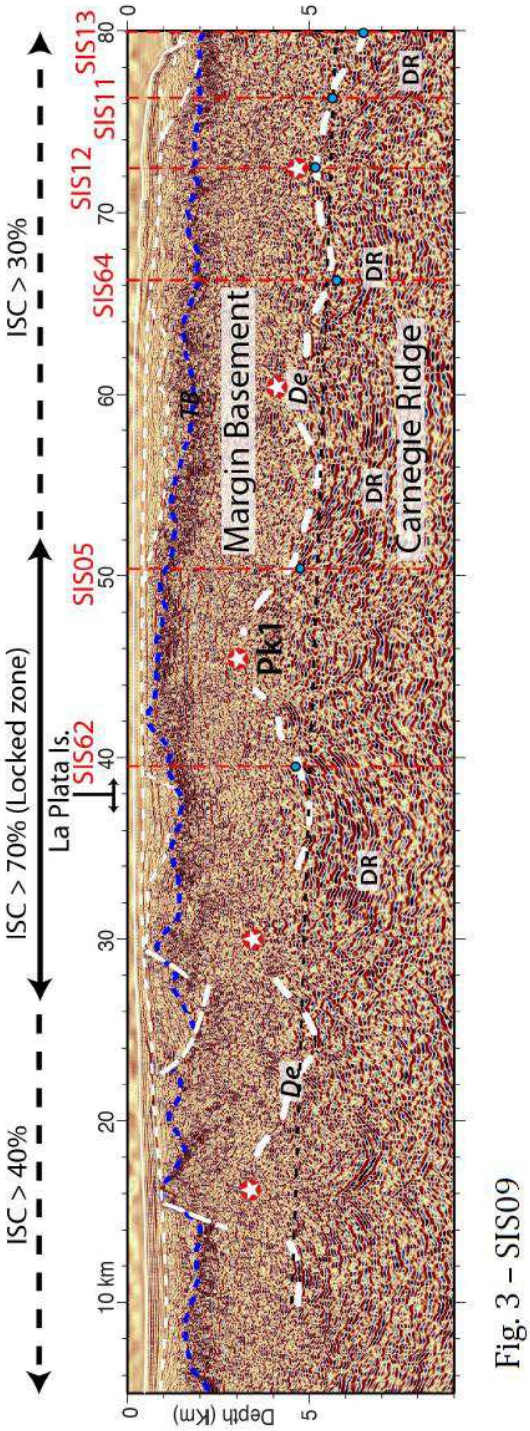

Fig. 3 – SIS09

Fig. 3: Prestack depth-migrated (PSDM) MCS line SIS09. Location is show in Fig. 1b. Blue dots = location of the inter-plate megathrust from crossing PSDM MCS lines; Heavy white dashed-line De = Megathrust; TB = top of basement; Inter-sesimic coupling (ISC) variation (Chlieh et al., sub); Note the high peak density (stars like Pk1) along De and the correlation between highest peaks and the locked zone; DR = Deep Reflectors.

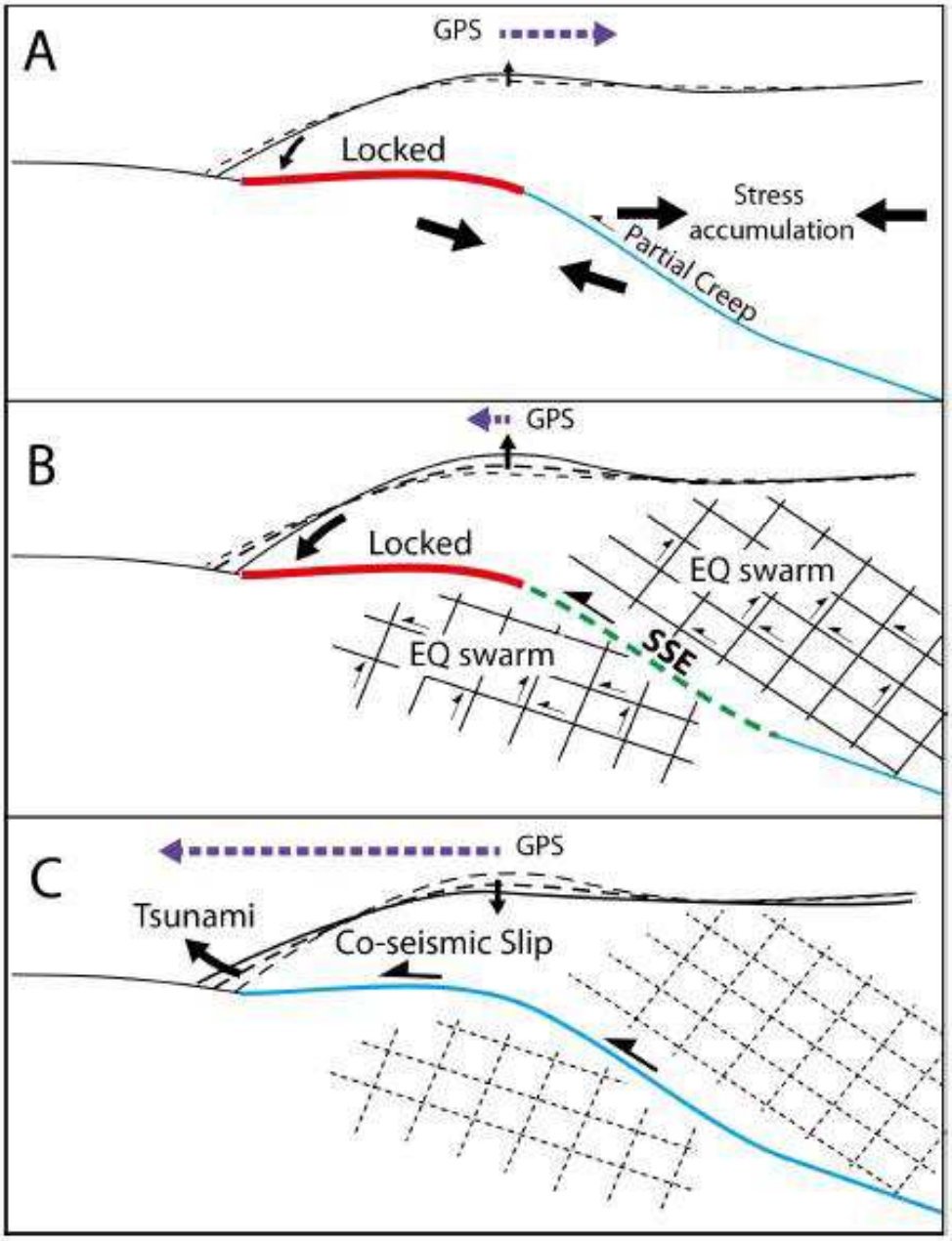

Fig. 4

Fig. 4: Scenario for multi-stage seamount subduction.

(A) – Stress accumulates in the margin wedge as Seamount creeps forward while its trailing flank remains locked;

(B)- Stress is partially liberated during Earthquake Swarms and Slow Slip Events, while trailing flank remains locked and outer-margin wedge keeps accumulating elastic strain. Stages A and B may repeat up to the yield stress is reached and the upper megathrust unlocks generating a subduction earthquake (C).

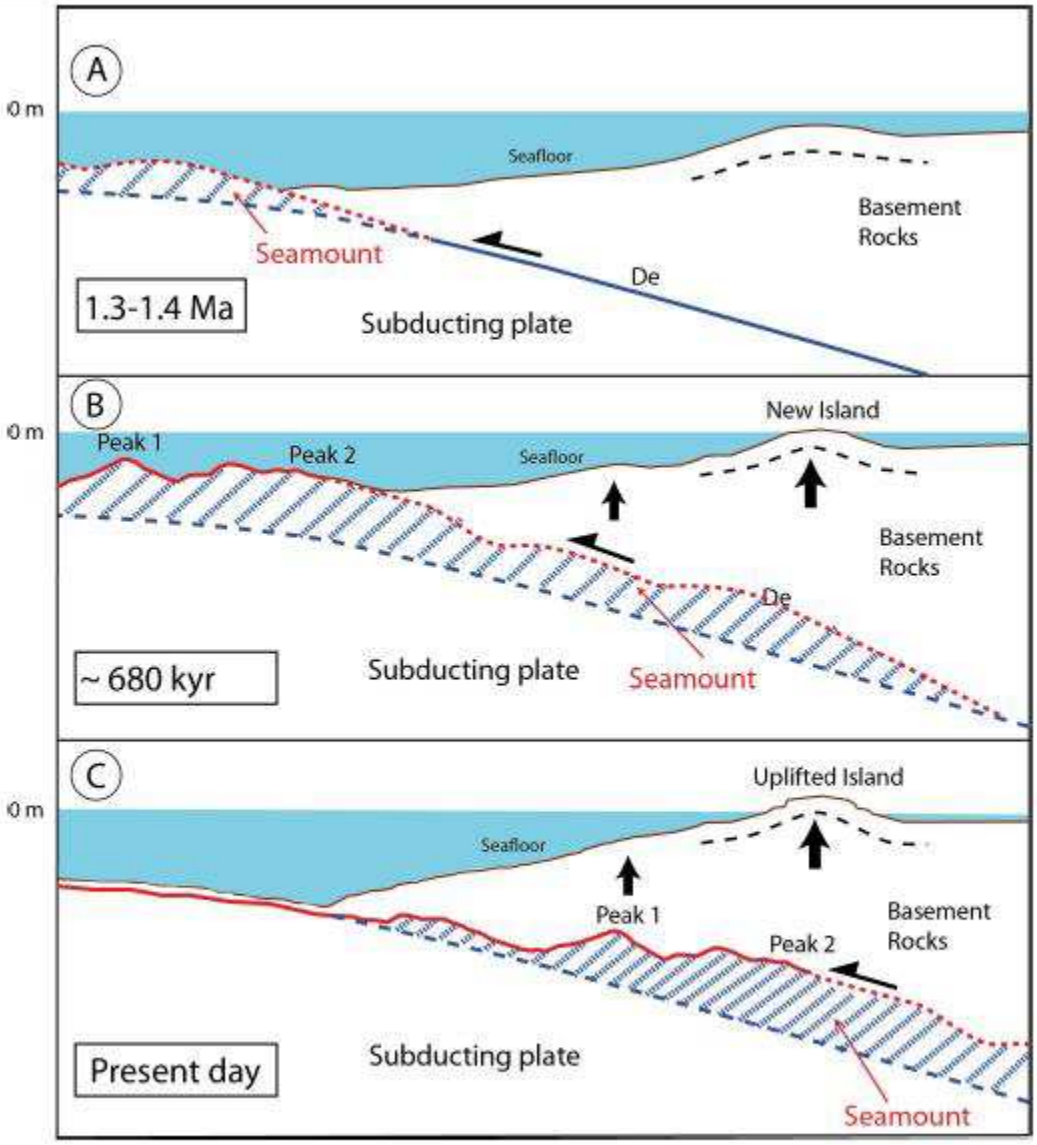

Fig. 5

Fig. 5: Sketch of seamount subduction driving the LPI uplift over the past 1.4-1.5 Ma.

References:

Agudelo, W., A. Ribodetti, J.-Y. Collot, S. Operto, (2009), Joint inversion of multichannel seismic reflection and wide-angle seismic data: Improved imaging and refined velocity model of the crustal structure of the north Ecuador–south Colombia convergent margin, Journal of Geophysical Reasearch, 114(B02306), doi:10.1029/2008JB005690.

Baldock, J. W. (1983), The Northern Andes: A Review of the Ecuadorian Pacific Margin, in The Ocean Basins and Margins - The Pacific Ocean, edited by A. E. Nairn, F. G. Stehli and S. Uyeda, pp. 181-217, Plenum Press, New York and London.

Bangs, N. L. B., Gulick, S. P.S., Shipley, T. H. (2006), Seamount subduction erosion in the Nankai Trough and its potential impact on the seismogenic zone, Geology, 34(8), 701–704, doi: 10.1130/G22451.1.

Bell, R., R. Sutherland, D. H. N. Barker, S. Henrys, S. Bannister, L. Wallace, and J. Beavan (2010), Seismic reflection character of the Hikurangi subduction interface, New Zealand, in the region of repeated Gisborne slow slip events, Geophys. J. Int., 180, 34-48,

Byrne, D. E., D. M. Davis, and L. R. Sykes (1988), Loci and maximum size of thrust earthquakes and the mechanics of the shallow region of subduction zones, Tectonics, 7(4), 833-857,

Chlieh, M., P. A. Mothes, J.-M. Nocquet, P. Jarrin, P. Charvis, D. Cisneros, Y. Font, J.-Y. Collot, J.-C. Villegas-Lanza, F. Rolandone, M. Vallée, M. Regnier, M. Segovia, X. Martin, and H. Yepes (submitted), Distribution of discrete seismic asperities and aseismic slip along the Ecuadorian Megathrust, Earth Planet. Sci. Lett.,

Cloos, M. (1992), Thrust-type subduction-zone earthquakes and seamount asperities: A physical model for seismic rupture, Geology, 20, 601-604,

Collot, J.-Y., S. Lallemand, B. Pelletier, J.-P. Eissen, G. Glaçon, M. A. Fisher, H. G. Greene, J. Boulin, J. Daniel, and M. Monzier (1992), Geology of the d'Entrecasteaux-New Hebrides Arc collision zone: results from a deep submersible survey, Tectonophysics, 212, 213-241,

Contreras-Reyes, E., I. Grevemeyer, A. B. Watts, L. Planert, E. R. Flueh, and C. Peirce (2010), Crustal intrusion beneath the Louisville hotspot track, Earth Planet. Sci. Lett., 289, 323-333,

Cummins, P. R., T. Baba, S. Kodaira, and Y. Kaneda (2002), The 1946 Nankai earthquake and segmentation of the Nankai Trough, Phys. Earth. Panet. Inter., 132, 75-87,

Dominguez, S., S. Lallemand, J. Malavieille, and R. von Huene (1998), Upper plate deformation associated with seamount subudction, Tectonophysics, 293, 207-224,

Duan, B. (2012), Dynamic rupture of the 2011 Mw 9.0 Tohoku-Oki earthquake: Roles of a possible subducting seamount, Journal of Geophysical Reasearch, 117(B05311), doi:10.1029/2011JB009124.

Expedition 330 Scientists (2012), Expedition 330 summary, in Proc. IODP, 330: Tokyo (Integrated Ocean Drilling Program Management International, Inc.). edited by A. A. P. Koppers, Yamazaki, T., Geldmacher, J., and the Expedition 330 Scientists,.

Font, Y., M. Segovia, S. Vaca, and T. Theunissen (2013), Seismicity patterns along the Ecuadorian subduction zone: new constraints from earthquake location in a 3-D a priori velocity model, Geophys. J. Int., 193, 263–286, doi: 10.1093/gji/ggs083.

Fukao, Y. (1979), Tsunami earthquake and subduction processes near deep-sea trenches, J. Geophys. Res., 84, 2301-2314,

Gagnon, K., C. D. Chadwell, E. Norabuena (2005), Measuring the onset of locking in the Peru–Chile trench with GPS and acoustic measurements, Nature, 434, 205-207, doi:10.1038/nature03412.

Graindorge, D., A. Calahorrano, P. Charvis, J.-Y. Collot, and N. Bethoux (2004), Deep structures of the Ecuador convergent margin and the Carnegie Ridge, possible consequence on great earthquakes recurrence interval, Geophysical Research Letter, 31, 4, L04603, doi :10.1029/2003GL018803,,

Hicks, S. P., Rietbrock, A., Haberland, C. A., Ryder, I. M. A., Simons, M., Tassara, A. (2012), The 2010 Mw 8.8 Maule, Chile earthquake: Nucleation and rupture propagation controlled by a subducted topographic high, Geophys. Res. Lett., 39,(L19308), doi:10.1029/2012GL053184.

Husen, S., E. Kissling, and R. Quintero (2002), Tomographic evidence for a subducted seamount beneath the Gulf of Nicoya, Costa Rica : the cause of the 1990 Mw = 7.0 Gulf of Nicoya earthquake, Geophys. Res. Lett., 29, 8, 10.1029/2001GL014045,

Kanamori, H. (1972), Mechanism of tsunami earthquakes Phys. Earth Planet. Interiors, 6, 346-359,

Kanamori, H., and K. C. McNally (1982), Variable rupture mode of the subduction zone along the Ecuador-Colombia coast, Bull. Seismol. Soc. Am., 72(4), 1241-1253,

Kanamori, H., and M. Kikuchi (1993), The 1992 Nicaragua earthquake : a slow tsunami earthquake associated with subducted sediments, Nature, 361, 714-716,

Kelleher, J. (1972), Rupture zones of large South American earthquakes and some predictions, J. Geophys. Res., 77, 2087-2103,

Kodaira, S., N. Takahashi, A. Nakanishi, S. Miura, and Y. Kaneda (2000), Subducted seamount imaged in the rupture zone of the 1946 Nankaido earthquake, Sciences, 289, 104-106,

Kodaira, S., T. Likada, A. Kato, J.-O. Park, T. Iwasaki, and Y. Kaneda (2004), High pore fluid pressure may cuase silent slip in the Nankai Trough, Science, 304, 1295-1298,

McIntosh, K. D., E. A. Silver, I. Ahmed, A. Berhorst, C. R. Ranero, K. Kelly, and E. R. Flueh

(2007), The Nicaragua Convergent Margin, Seismic Reflection Imaging of the Source of a Tsunami Earthquake, in The Seismogenic Zone of Subduction Thrust Faults, edited by T. H. Dixon and J. C. Moore, pp. 257-287, Colombia University Press, New York.

Mochizuki, K., T. Yamada, M. Shinohara, Y. Yamanaka, and T. Kanazawa (2008), Weak interplate coupling by seamounts and repeating M∼7 earthquakes, Science, 321, 1194-1197, 10.1126/science.1160250.

Nocquet, J.-M., J. C. Villegas-Lanza, M. Chlieh, P. A. Mothes, F. Rolandone, P. Jarrin, D. Cisneros, A. Alvarado, L. Audin, F. Bondoux, X. Martin, Y. Font, M. Régnier, M. Vallée, T. Tran, C. Beauval, J. M. Maguiña Mendoza, W. Martinez, H. Tavera, and H. Yepes (2014), Motion of continental slivers and creeping subduction in the northern Andes, Nature Geoscience, DOI: 10.1038/NGEO2099.

Nur, A., G. Mavko, J. Dvorkin, and D. Galmudi (1998), Critical porosity: A key relating physical properties to porosity in rocks, Leading Edge, 17, 357-362,

Pedoja, K., L. Ortlieb, J. F. Dumont, M. Lamothe, B. Ghaleb, M. Auclair, and B. Labrousse (2006), Quaternary coastal uplift along the Talara Arc (Ecuador, Northern Peru) from new marine terrace data, Marine Geoology, 228, 73-91,

Sage, F., J.-Y. Collot, and C. R. Ranero (2006), Interplate patchiness and subduction-erosion mechanisms : Evidence from Depth Migrated Seismic Images at the Central Ecuador convergent margin, Geology, 34(12), 10.1130/G22790A.22791, 22997-21000,

Sakatake, K. (1994), Mechanism of the 1992 Nicaragua tsunami earthquake, Geophysical Research Letter 21(23), 2519-2522,

Sallares, V., and C. Ranero (2005), Structure and tectonics of the erosional convergent margin off Antofagasta, north Chile (23° 30'S), Journal of Geophysical Reasearch, 110(B06101), doi:10.1029/2004JB003418.

Scholz, C. H., and C. Small (1997), The effect of seamount subduction on seismic coupling, Geology, 25, 487 - 490,

Scholz, C. H. (1998), Earthquakes and friction laws, Nature, 391(1), 37-42,

Singh, S. C., N. Hananto, M. Mukti, D. P. Robinson, S. Das, A. Chauhan, H. Carton, B. Gratacos, S. Midnet, Y. Djajadihardja, and H. Harjono (2011), Aseismic zone and earthquake segmentation associated with a deep subducted seamount in Sumatra, Nature Geoscience, 4, 308-311, 10.1038/NGEO1119.

Vallée, M., J-M Nocquet, J. Battaglia, Y. Font, M. Segovia, M. Régnier, P. Mothes, P. Jarrin, D. Cisneros, S. Vaca, H. Yepes, X. Martin, N. Béthoux, and M. Chlieh (2013), Intense interface seismicity triggered by a shallow slow slip event in the Central Ecuador subduction zone, Journal of Geophysical Reasearch, 118, 1–17, doi:10.1002/jgrb.50216.

Velasco, A., C. J. Ammon, T. Lay, and J. Zhang (1994), Imaging a slow bilateral rupture with broadband seismic waves: The September 2, 1992 Nicaragua tsunami earthquake,

Geophysical Research Letter, 21(24), 2629-2632,

von Huene, R., and S. Lallemand (1990), Tectonic erosion along the Japan and Peru convergent margins, Geol. Soc. Am. Bull., 102, 704-720,

von Huene, R., C. R. Ranero, and P. Vannucchi (2004), Generic model of subduction erosion, Geology, 32(10), 913-916,

Wang, K., and S. L. Bilek (2011), Do subducting seamounts generate or stop large earthquakes ?, Geology, 39(9), 819-822, doi:10.1130/G31856.1.

Yang, H., Liu Y., Lin, J. (2012), Effects of subducted seamounts on megathrust earthquake nucleation and rupture propagation, Geophys. Res. Lett., 39, L24302, doi:10.1029/2012GL053892.

Supplementary material

Accuracy of depth migrated images

Accurate seismic velocity modeling plays a central role in PSDM of seismic data and in their geological interpretation since it controls the accuracy of the positioning in depth of the reflectors and the quality of the stacking of the redundant information provided by multifold data set, to improve the PSDM images of the reflectors located at larger depths (z > 4.5 km, i.e. greater than the maximum offset of the streamer, for MCS data is 4.5 km, *[Lines, 1993; Ross, 1994]*. To obtain an accurate depth-migrated image we build a composite velocity model by mixing the velocity model inferred from PSDM plus MVA and that inferred from first-arrival traveltime tomography. This velocity model integrates the information provided by the two data sets (MCS and WA) *[Agudelo et al. 2009]*. The resultant mixed model is composed of three zones: (1) the shallow part corresponds to that of the MCS model, and the thickness of this zone is estimated from the maximum acquisition offset and reaches a value of 5 km. (2) The deep part corresponds to that of the WA model. (3) A transition part corresponds to a weighted average between the MCS and the WA models and allows avoidance of a sharp discontinuity between the shallow and deep parts of the mixed model. The mixed velocity model provides a quantitative structural model parameterized by P wave velocities, which integrates all the information coming from the MCS data and the traveltimes from the WA data. The mixed velocity model was used as velocity macromodel for PSDM of MCS data.

Quality control and the accuracy of the migrated images *(Figures 2A and 3)*are analyzed by common image gathers (CIG) analysis. CIGs (or IsoX) panels, and represent the traces sorted by angle and extracted from each partial seismic image at a given x coordinate *(Figure A1)*. A partial image is a collection of diffracting points, which are illuminated under different angles. A continuous reflector is treated as a line of diffracting points, and the stack of all diffracting points over all angles forms the reflector image *[Thierry et al., 1999]*. Inaccuracies of the velocity macromodel used for PSDM migration curve the reflector on CIGs. The velocity macromodel is iteratively corrected during migration until CIG are flattened. When this condition is satisfied, CIG are stacked to get the final migrated image. The final CIGs are presented in FigureA1 for the lines SIS05 and SIS09.

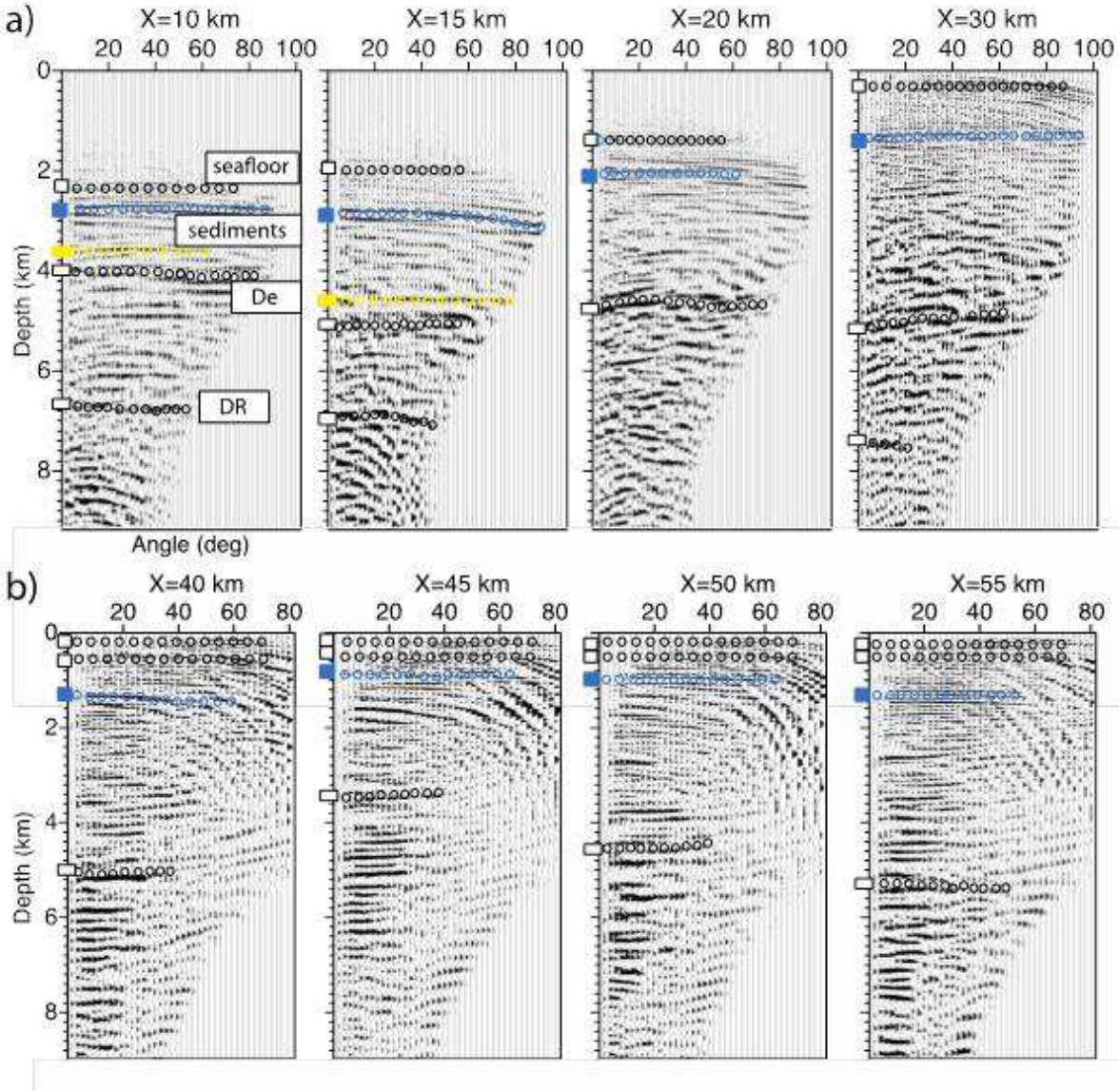

Figure A1 (a) IsoX panels (CIGs) obtained with the mixed velocity model along line SIS-05 and b) SIS09. IsoX are exacted at X=10, 15, 20, 30 km along the profile SIS05 and at X=40, 45, 50, 55 Km along the line SIS09. White, yellow, and blue circle plotted on the panels indicate the main reflectors according to Figures 2A and 3. Note that the décollement presents a reverse polarity. Note also that IsoX are quite flat and coherent, indicating that the seismic reflectors are confidently imaged.

References (Supplementary material)

Agudelo, W. (2005), Imagerie sismique quantitative de la marge convergente d'Equateur-Colombie, Ph.D. thesis, Univ. Pierre et Marie Curie, Paris.

W. Agudelo, A. Ribodetti,J.-Y. Collot,and S. Operto, (2009), Joint inversion of multichannel seismic reflection and wide-angle seismic data: Improved imaging and refined velocity model of the crustal structure of the north Ecuador–south Colombia convergent margin, Journal of Geophysical Research, vol. 114, B02306, doi:10.1029/2008JB005690

Al-Yahya, K. (1989), Velocity analysis by iterative profile migration, Geophysics,54, 718– 729.

Lines, L. (1993), Ambiguity in analysis of velocity and depth, Geophysics,58, 596–597.

Ross, W. S. (1994), The velocity depth ambiguity in seismic travel-time data, Geophysics, 59, 830–843.

Thierry, P., S. Operto, and G. Lambaré, (1999), Fast 2-D ray + born migration/inversion in complex media, Geophysics, 64, 162–181.

Annex B

Profiles SIS12, SIS11, and SIS64
(Sage, perso communication)

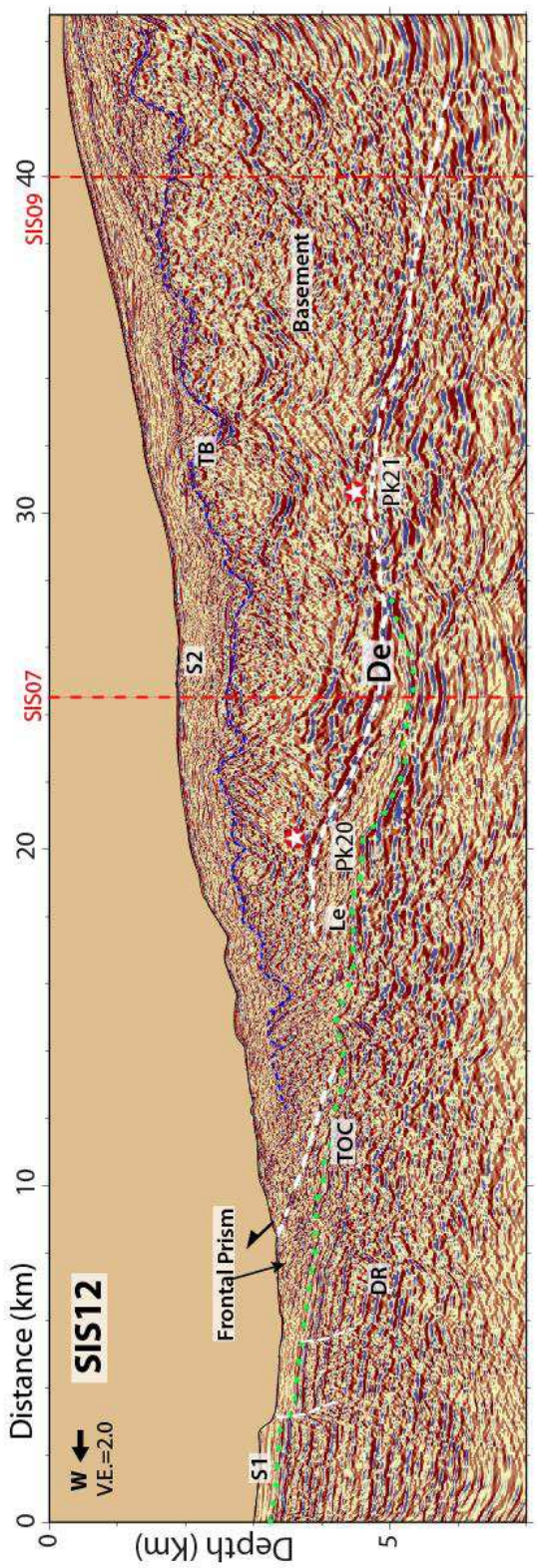

Figure B.1, PSDM of profiles SIS12 (Sage, perso. Communication); Location of profiles is in Figure 6.9; S1 and S2: TOC: top of the oceanic crust, in green dashed line; De: décollement, in white dashed line; Pk: subducted peaks, indicated by the stars; TB: top of the basement, in blue dashed line; Le: sediment lens; sedimentary layers; DR: deep reflectors; red dashed line indicate the intersection with the strike profiles.

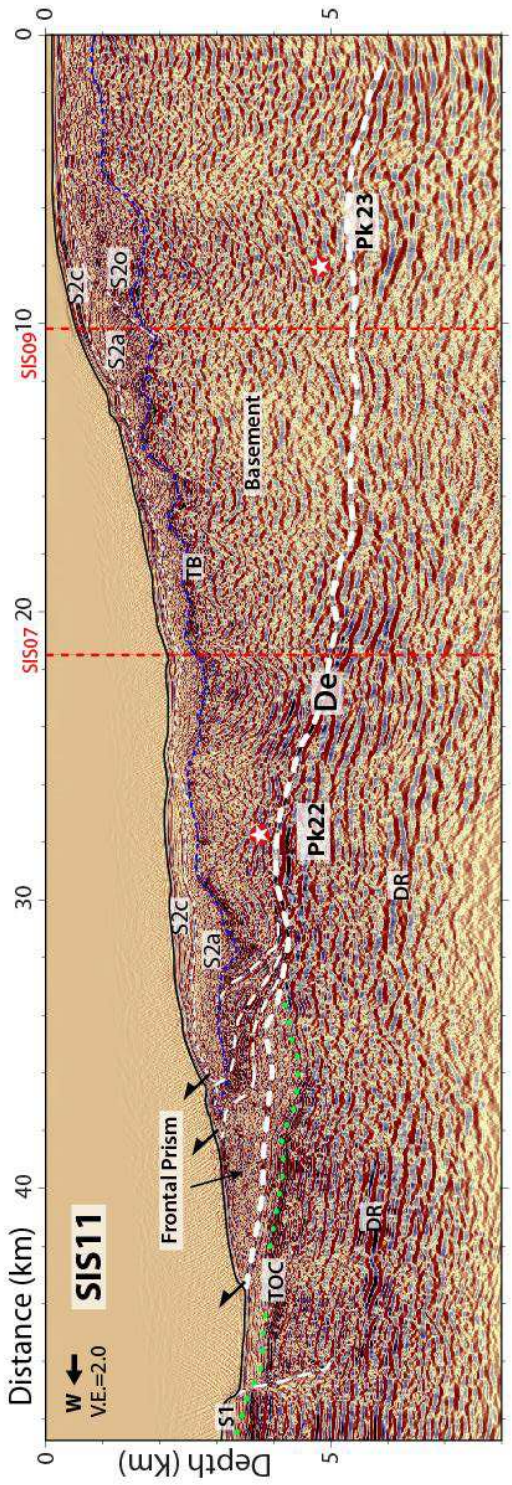

Figure B.2, PSDM of profile SIS11 (Sage, perso. Communication); Location on Figure 6.9, between profiles SIS12 and SIS13; TOC: top of the oceanic crust, in green dashed line; De: décollement, white dashed line; TB: top of the basement, blue dashed line; DR: deep reflectors; Pk: subducted peaks, indicated by the stars; S1: sediments on Carnegie; S2o, S2a, and S2c: sediment layers of the slope; red dashed line corresponds to the intersection with strike profiles.

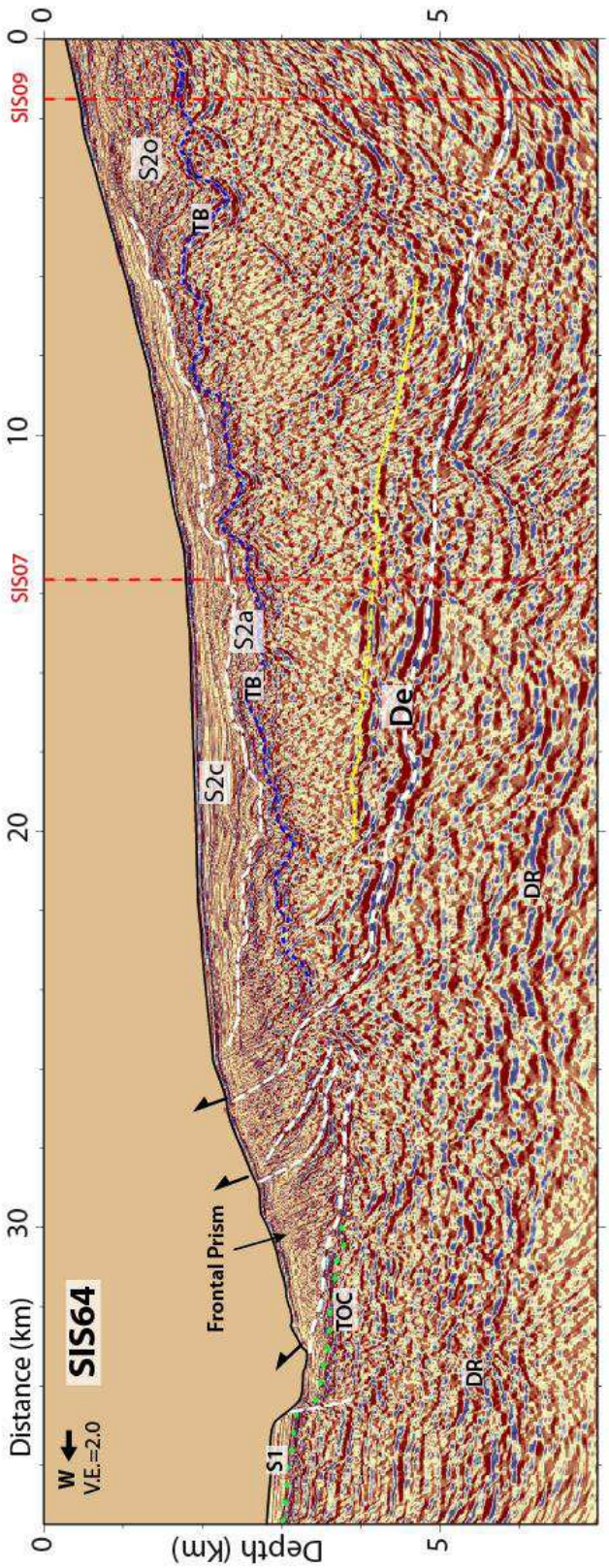

Figure B.3, PSDM of profile SIS64 (Sage, perso. Communication); Location on Figure 6.9; TOC: top of the oceanic crust, in green dashed line; De: décollement, white dashed line; TB: top of the basement, blue dashed line; DR: deep reflectors; S1: sediments on Carnegie; S2o, S2a, and S2c: sediment layers of the slope; red dashed line corresponds to the intersection with strike profiles.

References

- Abercrombie, R. E., Antolik, M., Felzer, K., and Ekström, G. (2001). The 1994 Java tsunami earthquake: Slip over a subducting seamount. Journal of Geophysical Research: Solid Earth (1978–2012), 106(B4), 6595-6607.

- Adam, J., D. Klaeschen, N. Kukowski, and E. R. Flueh (2004), Upward delamination of Cascadia Basin sediment infill with landward frontal accretion thrusting caused by rapid glacial age material flux, Tectonics, 23, TC3009, doi: 10.1029/2002TC001475.

- Agudelo, W., 2005. Imagerie sismique quantitative de la marge convergente d'Equateur-Colombie: application des méthodes tomographiques aux données de sismique réflexion multitrace et réfraction-réflexion grand-angle des campagnes SISTEUR et SALIERI. Univerité Pierre et Marie Curie

- Agudelo, W., Ribodetti, A., Collot, J.Y. and Operto, S., 2009. Joint inversion of multichannel seismic reflection and wide-angle seismic data; improved imaging and refined velocity model of the crustal structure of the north Ecuador-south Colombia convergent margin, J. geophys. Res., 114(B2), doi:10.1029/2008JB005690.v

- Al-Yahya, K. (1989). Velocity analysis by iterative profile migration. Geophysics, 54 :718–729

- Ammon, C. J., Ji, C., Thio, H. K., Robinson, D., Ni, S., Hjorleifsdottir, V., and Wald, D. (2005). Rupture process of the 2004 Sumatra-Andaman earthquake.Science, 308(5725), 1133-1139.

- Askew, B.L. and Algermissen, S.T., 1985. Catalog of Earthquakes for South America: Hypocenter and Intensity Data, Volumes 4, 6, 7a, 7b, and 7c, Centro Regional de Sismologia para America del Sur (CERESIS), Lima, Peru.

- Baldock, J.W., 1982. Geology of Ecuador, Explanatory Bulletin of the National Geological Map of Republic of Ecuador, 1:1.000.000 Scale, Division de Investigacion Geologico-Minera, Quito, 55pp.

- Baldock, J. W. (1983), The Northern Andes: A Review of the Ecuadorian Pacific Margin, in The Ocean Basins and Margins - The Pacific Ocean, edited by A. E. Nairn, F. G. Stehli and S. Uyeda, pp. 181-217, Plenum Press, New York and London.

- Bangs, N. L., Shipley, T. H., and Moore, G. F. (1996). Elevated fluid pressure and fault zone dilation inferred from seismic models of the northern Barbados Ridge decollement. Journal of Geophysical Research: Solid Earth (1978–2012),101(B1), 627-642.

- Bangs, N. L. B., Gulick, S. P.S., Shipley, T. H. (2006), Seamount subduction erosion in the Nankai Trough and its potential impact on the seismogenic zone, Geology, 34(8), 701–704, doi: 10.1130/G22451.1.

- Bangs, N. L. B., Moore, G. F., Gulick, S. P. S., Pangborn, E. M., Tobin, H. J., Kuramoto, S., and Taira, A. (2009). Broad, weak regions of the Nankai Megathrust and implications for shallow coseismic slip. Earth and Planetary Science Letters, 284(1), 44-49.

- Barckhausen, U., Ranero, C. R., Huene, R. V., Cande, S. C., and Roeser, H. A. (2001). Revised tectonic boundaries in the Cocos Plate off Costa Rica: Implications for the segmentation of the convergent margin and for plate tectonic models. Journal of Geophysical Research: Solid Earth (1978–2012), 106(B9), 19207-19220.

- Beck, S. L., and Ruff L.. (1984) "The rupture process of the great 1979 Colombia earthquake: Evidence for the asperity model." Journal of Geophysical Research: Solid Earth (1978–2012) 89.B11: 9281-9291.

- Bell, R., Sutherland, R., Barker, D., Henrys, S., Bannister, S., Wallace, L., and Beavan, J. Seismic reflection character of the Hikurangi subduction interface, New Zealand, in the region of repeated Gisborne slow slip events. Geophys. J. Int. (2010) 180, 34–48 doi: 10.1111/j.1365-246X.2009.04401.

- Beaumont, C., Ellis, S., and Pfiffner, A. (1999). Dynamics of sediment subduction-accretion at convergent margins: Short-term modes, long-term deformation, and tectonic implications. Journal of Geophysical Research: Solid Earth (1978–2012), 104(B8), 17573-17601.

- Beylkin, G. (1985). Imaging of discontinuities in the inverse scattering problem by inversion of a causal generalized Radon transform. Journal of Mathematical Physics, 26, 99.

- Bilek, S. L., and Lay, T. (1999). Rigidity variations with depth along interplate megathrust faults in subduction zones. Nature, 400(6743), 443-446.

- Bilek, S.L. and Lay, T., 2002. Tsunami earthquakes possibly widespread manifestations of frictional conditional stability, Geophys. Res. Lett., 29(14), doi: 10.1029/ 2002GL015215.

- Bilek, Susan L. "Influence of subducting topography on earthquake rupture."The Seismogenic Zone of Subduction Thrust Faults (2007): 123-146.

- Bird, Peter, and Yan Y. Kagan. "Plate-tectonic analysis of shallow seismicity: Apparent boundary width, beta, corner magnitude, coupled lithosphere thickness, and coupling in seven tectonic settings." Bulletin of the Seismological Society of America 94.6 (2004): 2380-2399.

- Bourdon, E., Eissen, J. P., Gutscher, M. A., Monzier, M., Hall, M. L., and Cotten, J. (2003). Magmatic response to early aseismic ridge subduction: the Ecuadorian margin case (South America). Earth and Planetary Science Letters,205(3), 123-138.

- Bristow, C.R., Hoffstetter, R., 1977. Léxique Stratigrapgique, Amérique Latine. Ed CNRS, Paris, Fas. 5 à 2, Ecuador: 410.

- Byerlee, J. D. (1967). Frictional characteristics of granite under high confining pressure. Journal of Geophysical Research, 72(14), 3639-3648.

- Byrne, D. E., Davis, D. M., and Sykes, L. R. (1988). Loci and maximum size of thrust earthquakes and the mechanics of the shallow region of subduction zones. Tectonics, 7(4), 833-857.

- Calahorrano A. (2005). Structure de la Marge du Golfe de Guayaquil (Équateur) et propietés physiques du chenal de subduction, a partir de données de sismique marine reflexion et refraction. PhD's thesis from University Pierre et Marie Curie Paris VI

- Calahorrano B, A., Sallarès, V., Collot, J. Y., Sage, F., and Ranero, C. R. (2008). Nonlinear variations of the physical properties along the southern Ecuador subduction channel: Results from depth-migrated seismic data. Earth and Planetary Science Letters, 267(3), 453-467.

- Cantalamessa, G. and Di Celma, C., 2004. Origin and chronology of Pleistocene marine terraces of Isla de la Plata and of flat, gently dipping surfaces of the southern coast of Cabo San Lorenzo (Manabi, Ecuador), J. South Am. Earth Sci., 16, 633–648.

- Carena, S., (2011). Subducting-plate topography and nucleation of great and giant earthquakes along the South American trench. Seismological Research Letters, 82(5), 629-637.

- Cembrano, J., González, G., Arancibia, G., Ahumada, I., Olivares, V., and Herrera, V. (2005). Fault zone development and strain partitioning in an extensional strike-slip duplex: A case study from the Mesozoic Atacama fault system, Northern Chile. Tectonophysics, 400(1), 105-125.

- Chapel, D., and C. Small. "The distribution of large seamounts in the Pacific."Eos 77.46 (1996): F770.

- Chemenda, A., Lallemand, S., and Bokun, A. (2000). Strain partitioning and interplate friction in oblique subduction zones: Constraints provided by experimental modeling. Journal of Geophysical Research: Solid Earth (1978–2012), 105(B3), 5567-5581.

- Chlieh, M., J. P. Avouac, K. Sieh, D. H. Natawidjaja, and J. Galetzka (2008), Heterogeneous coupling of the Sumatran megathrust constrained by geodetic and paleogeodetic measurements, J. Geophys. Res., 113(B05305), doi:10.1029/2007JB004981.

- Chlieh, M., H. Perfettini, H. Tavera, J.-P. Avouac, D. Remy, J.-M. Nocquet, F. Rolandone, F. Bondoux, G. Gabalda, and S. Bonvalot (2011), Interseismic coupling and seismic potential along the Central Andes subduction zone, J. Geophys. Res., 116(B1245), doi: 10.1029/2010JB008166.

- Chlieh, M., P. A. Mothes, J.-M. Nocquet, P. Jarrin, P. Charvis, D. Cisneros, Y. Font, J.-Y. Collot, J.-C. Villegas-Lanza, F. Rolandone, M. Vallée, M. Regnier, M. Segovia, X. Martin, and H. Yepes (submitted), Distribution of discrete seismic asperities and aseismic slip along the Ecuadorian Megathrust, Earth Planet. Sci. Lett.

- Christensen, Douglas H., and Larry J. Ruff. "Seismic coupling and outer rise earthquakes." Journal of Geophysical Research: Solid Earth (1978–2012)93.B11 (1988): 13421-13444.

- Christeson, G. L., Bangs, N. L., and Shipley, T. H. (2003). Deep structure of an island arc backstop, Lesser Antilles subduction zone. Journal of Geophysical Research: Solid Earth (1978–2012), 108(B7).

- Clift, P., and Vannucchi, P. (2004). Controls on tectonic accretion versus erosion in subduction zones: Implications for the origin and recycling of the continental crust. Reviews of Geophysics, 42(2).

- Clift, P. D., Schouten, H., and Vannucchi, P. (2009). Arc-continent collisions, sediment recycling and the maintenance of the continental crust. Geological Society, London, Special Publications, 318(1), 75-103.

- Cloos, M., and Shreve, R. L. (1988). Subduction-channel model of prism accretion, melange formation, sediment subduction, and subduction erosion at convergent plate margins: 1. Background and description. Pure and Applied Geophysics, 128(3-4), 455-500.

- Cloos, M. (1992), Thrust-type subduction-zone earthquakes and seamount asperities: A physical model for seismic rupture, Geology, 20, 601-604,

- Cloos, Mark, and Ronald L. Shreve. "Shear-zone thickness and the seismicity of Chilean- and Marianas-type subduction zones." Geology 24.2 (1996): 107-110.

- Collot, J.-Y., S. Lallemand, B. Pelletier, J.-P. Eissen, G. Glaçon, M. A. Fisher, H. G. Greene, J. Boulin, J. Daniel, and M. Monzier (1992), Geology of the d'Entrecasteaux-New Hebrides Arc collision zone: results from a deep submersible survey, Tectonophysics, 212, 213-241,

- Collot, J.-Y., Lewis, K., Lamarche, G., and Lallemand, S.E., 2001. The giant Rutoria debris avalanche on the northern Hikurangi margin, New Zealand: Result of oblique seamount subduction: Journal of Geophysical Research, v. 106, p. 19,271–19,297.

- Collot, J.-Y., Charvis, P., Gutscher, M.A., and Operto, S., 2002, Exploring theEcuador-Colombia active margin and interplate seismogenic zone: Eos (Transactions, American Geophysical Union), v. 83, p. 189–190.

- Collot, J. Y., Marcaillou, B., Sage, F., Michaud, F., Agudelo, W., Charvis, P., .and Spence, G. (2004). Are rupture zone limits of great subduction earthquakes controlled by upper plate structures? Evidence from multichannel seismic reflection data acquired across the northern Ecuador–southwest Colombia margin. Journal of Geophysical Research: Solid Earth (1978–2012),109 (B11).

- Collot, J. Y., Agudelo, W., Ribodetti, A., and Marcaillou, B. (2008). Origin of a crustal splay fault and its relation to the seismogenic zone and underplating at the erosional north Ecuador–south Colombia oceanic margin. Journal of Geophysical Research: Solid Earth (1978–2012), 113(B12).

- Collot Jean-Yves Collot, Michaud F., Alvarado A., Marcaillou B., Sosson M., Ratzov G., Migeon S, Calahorrano A., Pazmino A., (2009) Geología y Geofísica Marina y Terrestre del 1025 Ecuador, Spec. Pub. INOCAR-IRD, 151-166 (in spanish with english abstract).

- Collot, J. Y., A. Ribodetti, W. Agudelo, and F. Sage (2011), The South Ecuador subduction channel: Evidence for a dynamic mega-shear zone from 2D fine-scale seismic reflection imaging and implications for material transfer, J. Geophys. Res., 116, B11102, doi:10.1029/2011JB008429.

- Contreras, E., Flueh, E., Grevemeyer, I., 2010. Tectonic control on sediment accretion and subduction off south-central Chile: Implications for coseismic rupture processes of the 1960 and 2010 megathrust earthquakes. Tectonics 29, TC6018, doi: 10.1029/2010TC002734.

- Contreras, E., Carrizoa, D., 2011. Control of high oceanic features and subduction channel on earthquake ruptures along the Chile–Peru subduction zone. Physics of the Earth and Planetary Interiors 186 (2011) 49–58 doi:10.1016/j.pepi.2011.03.002

- Cummins, P. R., T. Baba, S. Kodaira, and Y. Kaneda (2002), The 1946 Nankai earthquake and segmentation of the Nankai Trough, Phys. Earth. Panet. Inter., 132, 75-87,

- Dahlen, F. A. (1990). Critical taper model of fold-and-thrust belts and accretionary wedges. Annual Review of Earth and Planetary Sciences, 18, 55.

- Davis, D., Suppe, J., and Dahlen, F. A. (1983). Mechanics of fold-and-thrust belts and accretionary wedges. Journal of Geophysical Research: Solid Earth (1978–2012), 88(B2), 1153-1172.

- Das, S., and A. B. Watts. "Effect of subducting seafloor topography on the rupture characteristics of great subduction zone earthquakes." Subduction Zone Geodynamics. Springer Berlin Heidelberg, 2009. 103-118.

- DeMets, C., Gordon, R. G., Argus, D. F., and Stein, S. (1994). Effect of recent revisions to the geomagnetic reversal time scale on estimates of current plate motions. Geophysical research letters, 21(20), 2191-2194.

- Deniaud Y. (2000). Enregistrements sedimentaire et structural de l'evolution Geodynamique des Andes Equatoriennes au cours du Neogene: Etude des Bassin d'avant-arc et Bilans de Masse. PhD's from University Joseph Fourier - Grenoble I Sciences and Géographie

- Dragert, H., Wang, K., and James, T. S. (2001). A silent slip event on the deeper Cascadia subduction interface. Science, 292(5521), 1525-1528.

- Di Celma, C., 2001. I livelli a molluschi come mezzo di distinzione delle sequenze deposizionali e della loro architettura interna in successioni sedimentarie plio-pleistoceniche dell'Ecuador. Unpublished PhD thesis, University of Pisa, Italy.

- Di Celma, C., Ragaini, L., Cantalamessa, G., Curzio, P., 2002. Shell concentrations as tools in characterizing sedimentary dynamics at sequence-bounding unconformities: examples from the lower unit of the Canoa Formation (Late Pliocene, Ecuador). Geobios Mémoire Spécial 24(35), 72–85.

- Dixon, T. H., and Moore, J. C. (Eds.). (2013). The seismogenic zone of subduction thrust faults. Columbia University Press.

- Dominguez, S., S. Lallemand, J. Malavieille, and R. von Huene (1998), Upper plate deformation associated with seamount subudction, Tectonophysics, 293, 207-224,

- Doser, D. I., and Lomas, R. (2000). The transition from strike–slip to oblique subduction in southeastern Alaska from seismological studies. Tectonophysics,316(1), 45-65.
- Douglas, A., et al. "Slow slip on the northern Hikurangi subduction interface, New Zealand." Geophysical Research Letters 32.16 (2005).

- Duan, B. (2012), Dynamic rupture of the 2011 Mw 9.0 Tohoku-Oki earthquake: Roles of a possible subducting seamount, Journal of Geophysical Reasearch, 117(B05311), doi: 10.1029/2011JB009124.

- Dumont, J.F., Santana, E.,Wilema,W., Pedoja, K., Ordoñez, M., Cruz, M., Jimenez, N., Zambrano, I., 2005. Morphological and microtectonic analysis of Quaternary deformation from Puna and Santa Clara Islands, Gulf of Guayaquil, Ecuador (South America). Tectonophysics 399 (1–4), 331–350.

- Ehinger, A., and Lailly, P. (1991). SEG Technical Program Expanded Abstracts 1991.

- Ego, F., M. Sébrier, A. Lavenu, H. Yepes, and A. Egues (1996), Quaternary state of stress in the Northern Andes and the restraining bend model for the Ecuadorian Andes, Tectonophysics, 259, 101–116, doi:10.1016/0040-1951(95)00075-5.

- Ekström G., M. Nettles, and A. M. Dziewonski (2012), The global CMT project 2004–2010: Centroid-870 moment tensors for 13,017 earthquakes, Phys. Earth Planet. Inter., 200–201, 1-9.

- Ellis, S., Beaumont, C., and Pfiffner, O. A. (1999). Geodynamic models of crustal‐scale episodic tectonic accretion and underplating in subduction zones. Journal of Geophysical Research: Solid Earth (1978–2012), 104(B7), 15169-15190.

- Engdahl, E.R., Van Der Hilst, R.D. and Buland, R., 1998. Global teleseismic earthquake relocationwith improved travel times and procedures for depth relocation, Bull. seism. Soc. Am., 88, 722–743.

- Engdahl, E.R., and Villaseñor, A., (2002). Global Seismicity: 1900-1999. International handbook of Earthquake and Engineering Seismology, volume 81A. ISBN: 0-12-440685-1

- Feininger, T., and Bristow, C. R. (1980). Cretaceous and Paleogene geologic history of coastal Ecuador. Geologische Rundschau, 69(3), 849-874.

- Feininger, T., and Seguin, M. K. (1983). Simple Bouguer gravity anomaly field and the inferred crustal structure of continental Ecuador. Geology, 11(1), 40-44

- Fitch, T. J. (1972). Plate convergence, transcurrent faults, and internal deformation adjacent to southeast Asia and the western Pacific. Journal of Geophysical Research, 77(23), 4432-4460.

- Font, Y., M. Segovia, S. Vaca, and T. Theunissen (2013), Seismicity patterns along the Ecuadorian subduction zone: new constraints from earthquake location in a 3-D a priori velocity model, Geophys. J. Int., doi: 10.1093/gji/ ggs1083

- Forgues, E. (1996). Inversion linéalisée multiparamètres via la théorie des rais (application aux données de sismique réflexion de surface). Thèse de Doctorat de l'Université de Paris VII., Paris.

- Fruehn, J., Huene, R., and Fisher, M. A. (1999). Accretion in the wake of terrane collision: The Neogene accretionary wedge off Kenai Peninsula, Alaska.Tectonics, 18(2), 263-277.

- Fukao, Y. (1979), Tsunami earthquake and subduction processes near deep-sea trenches, J. Geophys. Res., 84, 2301-2314,

- Gadallah, M. R., and Fisher, R. (2009). Seismic Interpretation. In Exploration Geophysics (pp. 149-221). Springer Berlin Heidelberg.

- Gailler, A. 2005. Structure de la marge d'Equateur-Colombie par modélisation des données de sismique grand-angle marines. Université de Nice-Sophia Antipolis, Nice, France, 257 p, PhD.

- Gailler, A., Charvis, P., and Flueh, E. R. (2007). Segmentation of the Nazca and South American plates along the Ecuador subduction zone from wide angle seismic profiles. Earth and Planetary Science Letters, 260(3), 444-464.

- Gagnon, K., Chadwell, C. D., and Norabuena, E. (2005). Measuring the onset of locking in the Peru–Chile trench with GPS and acoustic measurements. Nature,434(7030), 205-208.

- Geist, Eric L., et al. "Implications of the 26 December 2004 Sumatra–Andaman earthquake on tsunami forecast and assessment models for great subduction-zone earthquakes." Bulletin of the Seismological Society of America 97.1A (2007): S249-S270.

- Gerya, T. V., Stöckhert, B., and Perchuk, A. L. (2002). Exhumation of high‐pressure metamorphic rocks in a subduction channel: A numerical simulation.Tectonics, 21(6), 6-1.

- Gerya, T. V., Fossati, D., Cantieni, C., and Seward, D. (2009). Dynamic effects of aseismic ridge subduction: numerical modelling. European Journal of Mineralogy, 21(3), 649-661.

- Ghosh, A., Vidale, J. E., Sweet, J. R., Creager, K. C., Wech, A. G., Houston, H., and Brodsky, E. E. (2010). Rapid, continuous streaking of tremor in Cascadia.Geochemistry, Geophysics, Geosystems, 11(12).

- Graindorge, D., Calahorrano, A., Charvis, P., Collot, J.-Y., and Béthoux, N., 2004, Deep structures of the Ecuador convergent margin and the Carnegie Ridge, possible consequence on great earthquakes recurrence interval: Geophysical Research Letters, v. 31, p. L044603, doi: 10.1029/2003GL018803.

- Gray, W. C. (1979). Variable norm deconvolution (Doctoral dissertation, Stanford University).

- Guillier, Bertrand, et al. "Seismological evidence on the geometry of the Orogenic System in central-northern Ecuador (South America)." Geophysical Research Letters 28.19 (2001): 3749-3752.

- Gulick, S. P., Bangs, N. L., Moore, G. F., Ashi, J., Martin, K. M., Sawyer, D. S., and Taira, A. (2010). Rapid forearc basin uplift and megasplay fault development from 3D seismic images of Nankai Margin off Kii Peninsula, Japan.Earth and Planetary Science Letters, 300(1), 55-62.

- Gutscher, M. A., Kukowski, N., Malavieille, J., and Lallemand, S. (1998). Material transfer in accretionary wedges from analysis of a systematic series of analog experiments. Journal of Structural Geology, 20(4), 407-416.

- Gutscher, M.-A., Malavieille, J., Lallemand, S., and Collot, J.-Y. (1999). Tectonic segmentation of the north andean margin : impact of the Carnegie ridge collision. Earth and Planet. Sci. Let., 168 : 255–270.

- Gutscher, M.-A.; Sparkman, W.; Bijwaard, H.; Engdahl, E.-R., 2000. Geodynamics of flat subduction: Seismicity and tomographic constraints from the Andean margin. Tectonics, v19, No. 5, p. 814-833.

- Gutscher, M. Andean subduction styles and their effect on thermal structure and interplate coupling. J. S. Am. Earth Sci. 15, 3–10 (2002).

- Hackney, R. I., Echtler, H. P., Franz, G., Götze, H. J., Lucassen, F., Marchenko, D., and Wienecke, S. (2006). The segmented overriding plate and coupling at the south-central Chilean margin (36–42 S). In The Andes (pp. 355-374). Springer Berlin Heidelberg

- Handschumacher, D. W. (1976). Post-Eocene plate tectonics of the eastern Pacific (Vol. 19, pp. 177-202). American Geophysical Union.

- Hampel, Andrea, Juergen Adam, and Nina Kukowski. "Response of the tectonically erosive south Peruvian forearc to subduction of the Nazca Ridge: Analysis of three-dimensional analogue experiments." Tectonics 23.5 (2004).

- Heki, K., and Tamura, Y. (1997). Short term afterslip in the 1994 Sanrik-Haruka-Oki Earthquake. Geophysical research letters, 24(24), 3285-3288.

- Hey, P. (1977). Tectonic evolution of the cocos-nazca spreading center. Geological Society of America Bulletin, 88 :1404–1420.

- Hicks, S. P., Rietbrock, A., Haberland, C. A., Ryder, I. M. A., Simons, M., Tassara, A. (2012), The 2010 Mw 8.8 Maule, Chile earthquake: Nucleation and rupture propagation controlled by a subducted topographic high, Geophys. Res. Lett., 39,(L19308), doi:10.1029/2012GL053184

- Hoffmann-Rothe, A., Kukowski, N., Dresen, G., Echtler, H., Oncken, O., Klotz, J. and Kellner, A. (2006). Oblique convergence along the Chilean margin: partitioning, margin-parallel faulting and force interaction at the plate interface. InThe Andes (pp. 125-146). Springer Berlin Heidelberg.

- Hoffstetter, R., 1948. Notas sobre el cuaternario de la Peninsula de Santa Elena (Ecuador). Boletin de Informaciones Cientificas Nacionales II(11 et 12), pp. 19–44.

- Hyndman, R. D., Yamano, M., and Oleskevich, D. A. (1997). The seismogenic zone of subduction thrust faults. Island Arc, 6(3), 244-260.

- Ide, S., Baltay, A., and Beroza, G. C. (2011). Shallow dynamic overshoot and energetic deep rupture in the 2011 Mw 9.0 Tohoku-Oki earthquake. Science,332 (6036), 1426-1429.

- Igarashi, T., Matsuzawa, T., and Hasegawa, A. (2003). Repeating earthquakes and interplate aseismic slip in the northeastern Japan subduction zone. Journal of geophysical research, 108(B5), 2249.

- Isozaki, Y., Sh Maruyama, and F. Furuoka. "Accreted oceanic materials in Japan." Tectonophysics 181.1 (1990): 179-205.

- Ito, Y., Tsuji, T., Osada, Y., Kido, M., Inazu, D., Hayashi, Y., and Fujimoto, H. (2011). Frontal wedge deformation near the source region of the 2011 Tohoku-Oki earthquake. Geophysical Research Letters, 38(7).

- Jackson, D. D., and Kagan, Y. Y. (2011). Characteristic earthquakes and seismic gaps. In Encyclopedia of Solid Earth Geophysics (pp. 37-40). Springer Netherlands.

- Jaillard, E., Ordoñez, M., Benitez, S., Berrones, G., Jiménez, N., Montenegro, G., and Zambrano, I. (1995). Basin development in an accretionary, oceanic-floored fore-arc setting: southern coastal Ecuador during late Cretaceous-late Eocene time.

- Jaillard, E., Benitez, S., Mascle, G.H., 1997. Les déformations paléogènes de la zone d'avant-arc sud-équatorienne en relation avec l'évolution géodynamique, vol. 168. Bull. Soc. Géol, France (4): pp. 403e412

- Jaillard, E., Lapierre, H., Ordoñez, M., Álava, J. T., Amórtegui, A., and Vanmelle, J. (2009). Accreted oceanic terranes in Ecuador: southern edge of the Caribbean Plate? Geological Society, London, Special Publications, 328(1), 469-485.

- Jackson, David D., and Yan Y. Kagan. "Testable earthquake forecasts for 1999." Seismological Research Letters 70.4 (1999): 393-403.

- Jin, S., Madariaga, R., Virieux, J., and Lambaré, G. (1992). Two dimensional asymptotic iterative elastic inversion. Geophys. J. Internat., 108 :1–14.

- Kagan Y. Characteristic Earthquake Model, 1884–2011, R.I.P. doi: 10.1785/ 0220120107 Seismological Research Letters Volume 83, Number 6 November/ December 2012

- Kanamori, H. (1972), Mechanism of tsunami earthquakes Phys. Earth Planet. Interiors, 6, 346-359,

- Kanamori, H., and Given, J.W., (1981). Use of long-period surface waves for rapid determination of earthquake-source parameters. Phys. Earth Planet. Inter., 27, 8–31, doi: 10.1016/0031-9201(81)90083-2.

- Kanamori, H., and K. C. McNally (1982), Variable rupture mode of the subduction zone along the Ecuador-Colombia coast, Bull. Seismol. Soc. Am., 72(4), 1241-1253,

- Kanamori, H., and M. Kikuchi (1993), The 1992 Nicaragua earthquake : a slow tsunami earthquake associated with subducted sediments, Nature, 361, 714-716,

- Kay, R. W. (1978). Aleutian magnesian andesites: melts from subducted Pacific Ocean crust. Journal of Volcanology and Geothermal Research, 4(1), 117-132.

- Kay, S. M., Godoy, E., and Kurtz, A. (2005). Episodic arc migration, crustal thickening, subduction erosion, and magmatism in the south-central Andes.Geological Society of America Bulletin, 117(1-2), 67-88.

- Kelleher, J. (1972), Rupture zones of large South American earthquakes and some predictions, J. Geophys. Res., 77, 2087-2103,

- Kelleher, John, Lynn Sykes, and Jack Oliver. Possible criteria for predicting earthquake locations and their application to major plate boundaries of the Pacific and the Caribbean. (1973) Journal of Geophysical Research 78.14: 2547-2585.

- Kelleher, John, and William McCann. "Buoyant zones, great earthquakes, and unstable boundaries of subduction." Journal of Geophysical Research 81.26 (1976): 4885-4896.

- Kendrick, E., Bevis, M., Smalley Jr, R., Brooks, B., Vargas, R. B., Laurıa, E., and Fortes, L. P. S. (2003). The Nazca–South America Euler vector and its rate of change. Journal of South American Earth Sciences, 16(2), 125-131.

- Krabbenhöft, A., Bialas, J., Kopp, H., Kukowski, N., and Hübscher, C. (2004). Crustal structure of the Peruvian continental margin from wide-angle seismic studies. Geophysical Journal International, 159(2), 749-764.

- Kimura, G., E. A. Silver, and P. Blum, and the ODP Leg 170 Shipboard Scientific Party (1997), Proceedings of the Ocean

- Kodaira, S., Takahashi, N., Nakanishi, A., Miura, S. and Kaneda, Y., 2000. Subducted seamount imaged in the rupture zone of the 1946 Nankaido earthquake, Science, 289, 104–106.

- Kodaira, S., T. Likada, A. Kato, J.-O. Park, T. Iwasaki, and Y. Kaneda (2004), High pore fluid pressure may cuase silent slip in the Nankai Trough, Science, 304, 1295-1298,

- Korenaga, J., Holbrook, W., Kent, G., Kelemen, P., Detrick, R., Larsen, H.-C., Hooper, J., and Dahl-Jensen, T. (2000). Crustal structure of the southeast greenland margin from joint refraction and reflection seismic tomography. J.Geophys. Res., 105 :21591–21614.

- Lallemand, S. E., Schnürle, P., and Malavieille, J. (1994). Coulomb theory applied to accretionary and nonaccretionary wedges: Possible causes for tectonic erosion and/or frontal accretion. Journal of Geophysical Research: Solid Earth (1978–2012), 99(B6), 12033-12055.

- Lambaré, G., J. Virieux, R. Madariaga, and S. Jin (1992), Iterative asymptotic inversionof seismic profiles in the acoustic approximation, Geophysics, 57, 1138–1154.

- Lambaré, G., Operto, S., Podvin, P., and Thierry, P. (2003). 3dray+born migration/inversion - part1: Theory. Geophysics, 68 :1348–1356.

- Lavenu, A., Noblet, C., and Winter, T. (1995). Neogene ongoing tectonics in the Southern Ecuadorian Andes: analysis of the evolution of the stress field. Journal of Structural Geology, 17(1), 47-58.

- Lay, T., and Schwartz, S. Y. (2004). Comment on "Coupling semantics and science in earthquake research". Eos, Transactions American Geophysical Union, 85(36), 339.

- Lay, T., Yamazaki, Y., Ammon, J. C. Cheung K. F., Kanamori, H. (2011a) The 2011 Mw 9.0 off the Pacific coast of Tohoku Earthquake: Comparison of deep-water tsunami signals with finite-fault rupture model predictions. Earth Planets Space, 63, 797–801, 2011

- Lay, T., Ammon, C. J., Kanamori, H., Xue, L., and Kim, M. J. (2011b). Possible large near-trench slip during the 2011 M (w) 9. 0 off the Pacific coast of Tohoku Earthquake. Earth, planets and space, 63(7), 687-692.

- Lebras, M., Mégard F., Dupuy, C., and Dostal, J., (1987). Geochemistry and tectonic setting of pre-collision Cretaceous and Paleogene volcanic rocks of Ecuador. Geol. Soc. Am. Bull., 99, 569–578.

- Lines, L. (1993), Ambiguity in analysis of velocity and depth, Geophysics, 58, 596–597.

- Lonsdale, P. and Klitgord, K. (1978). Structure and tectonic history of the eastern Panama Basin. Geological Society of America Bulletin, 89 :981–999.

- Loveless, J.P., and Meade, B. 2010. Geodetic imaging of plate motions, slip rates, and partitioning of deformation in Japan. Journal of Geophysical Research: Solid Earth, Vol 115 Issue B2 DOI: 10.1029/2008JB006248

- Loveless, J. P., and Meade, B. J. (2011). Spatial correlation of interseismic coupling and coseismic rupture extent of the 2011 MW= 9.0 Tohoku-oki earthquake. Geophysical Research Letters, 38(17).

- Lowry, A. R., Larson, K. M., Kostoglodov, V., and Bilham, R. (2001). Transient fault slip in Guerrero, southern Mexico. Geophysical Research Letters, 28(19), 3753-3756. Macharé, J., and Ortlieb, L. (1992). Plio-Quaternary vertical motions and the subduction of the Nazca Ridge, central coast of Peru. Tectonophysics, 205(1), 97-108.

- Malavieille, J. (2010). Impact of erosion, sedimentation, and structural heritage on the structure and kinematics of orogenic wedges: Analog models and case studies. GSA Today, 20(1), 4-10.

- Marcaillou, B., Spence, G., Collot, J. Y., and Wang, K. (2006). Thermal regime from bottom simulating reflectors along the north Ecuador–south Colombia margin: Relation to margin segmentation and great subduction earthquakes.Journal of Geophysical Research: Solid Earth (1978–2012), 111(B12).

- Marcaillou, B., Henry, P., Kinoshita, M., Kanamatsu, T., Screaton, E., Daigle, H., and Yamano, M. (2012). Seismogenic zone temperatures and heat-flow anomalies in the To-nankai margin segment based on temperature data from IODP expedition 333 and thermal model. Earth and Planetary Science Letters, 349, 171-185.

- Marchant, S., 1961. A photogeological analysis of the structure of the western Guayas Province, Ecuador with discussion of thestratigraphy and tablazo formation derived from surface mapping. Quat. Geol. Soc. Lond. 114, 215–233.

- Martinod, J., Husson, L., Roperch, P., Guillaume, B., and Espurt, N. (2010). Horizontal subduction zones, convergence velocity and the building of the Andes. Earth and Planetary Science Letters, 299(3), 299-309.

- McGarr, A. (1976). Seismic moments and volume changes. Journal of Geophysical Research, 81(8), 1487-1494.

- McIntosh, K. D., E. A. Silver, I. Ahmed, A. Berhorst, C. R. Ranero, K. Kelly, and E. R. Flueh (2007), The Nicaragua Convergent Margin, Seismic Reflection Imaging of the Source of a Tsunami Earthquake, in The Seismogenic Zone of Subduction Thrust Faults, edited by T. H. Dixon and J. C. Moore, pp. 257-287, Colombia University Press, New York.

- Melnick, Daniel, et al. "Segmentation of megathrust rupture zones from fore-arc deformation patterns over hundreds to millions of years, Arauco peninsula, Chile." Journal of Geophysical Research: Solid Earth (1978–2012) 114.B1 (2009).

- Mendoza, C. and Dewey, J., 1984. Seismicity associated with the great Colombia-Ecuador earthquakes of 1942, 1958 and 1979: Implicationsfor barrier models of earthquake rupture, Bull. Seismol. Soc. Am., 74, 577–593.

- Michaud, F., Chabert, A., Collot, J. Y., Sallarès, V., Flueh, E. R., Charvis, P., and Bialas, J. (2005). Fields of multi-kilometer scale sub-circular depressions in the Carnegie Ridge sedimentary blanket: Effect of underwater carbonate dissolution? Marine Geology, 216(4), 205-219.

- Michaud, F., J-Y Collot, A. Alvarado, E. López, and y el personal científico y técnico del INOCAR (2006), República del Ecuador, Batimetría y Relieve Continental, IOA-CVM-02-Post, Inst. Oceanogr. de la Armada del Ecuador, Guayaquil.

- Michaud, F., Witt, C., and Royer, J. Y. (2009). Influence of the subduction of the Carnegie volcanic ridge on Ecuadorian geology: Reality and fiction. Backbone of the Americas: Shallow Subduction, Plateau Uplift, and Ridge and Terrane Collision, 204, 217.

- Mitsui, N., and Hirahara, K. (2004). Simple spring-mass model simulation of earthquake cycle along the Nankai trough in southwest Japan. In Computational Earthquake Science Part II (pp. 2433-2450). Birkhäuser Basel.

- Mix, A. C., R. Tiedemann, and P. Blum (2003), Proceedings of the Ocean Drilling Program, Initial Reports [CD-ROM], vol. 202, Ocean Drill. Program, College Station, Tex.

- Minelli, L., and Faccenna, C. (2010). Evolution of the Calabrian accretionary wedge (central Mediterranean). Tectonics, 29(4)

- Moore, G. F., Karig, D. E., Shipley, T. H., (1991). CHARACTER OF THE DECOLLEMENT IN THE LEG 131 AREA, NANKAI TROUGH. Proceedings of the Ocean Drilling Program, Scientific Results, Vol. 131

- Mora, P. (1989). Inversion= migration+ tomography. Geophysics, 54(12), 1575-1586.

- Moreno, M., Melnick, D., Rosenau, M., Baez, J., Klotz, J., Oncken, O., and Hase, H. (2012). Toward understanding tectonic control on the< i> M</i>< sub> w</sub> 8.8 2010 Maule Chile earthquake. Earth and Planetary Science Letters, 321, 152-165.

- Moore, J. C., and Vrolijk, P. (1992). Fluids in accretionary prisms. Reviews of Geophysics, 30(2), 113-135.

- Moore, G. F., Bangs, N. L., Taira, A., Kuramoto, S., Pangborn, E., and Tobin, H. J. (2007). Three-dimensional splay fault geometry and implications for tsunami generation. Science, 318(5853), 1128-1131.

- Nakanishi, A., Kodaira, S., Miura, S., Ito, A., Sato, T., Park, J. O., and Kaneda, Y. (2008). Detailed structural image around splay-fault branching in the Nankai subduction seismogenic zone: Results from a high-density ocean bottom seismic survey. Journal of Geophysical Research: Solid Earth (1978–2012), 113(B3).

- Nishizawa, A., Kaneda, K., Watanabe, N., and Oikawa, M. (2009). Seismic structure of the subducting seamounts on the trench axis: Erimo Seamount and Daiichi-Kashima Seamount, northern and southern ends of the Japan Trench.Earth Planets Space, 61(3), e5-e8.

- Nocquet, J.-M., J. C. Villegas-Lanza, M. Chlieh, P. A. Mothes, F. Rolandone, P. Jarrin, D. Cisneros, A. Alvarado, L. Audin, F. Bondoux, X. Martin, Y. Font, M. Régnier, M. Vallée, T. Tran, C. Beauval, J. M. Maguiña Mendoza, W. Martinez, H. Tavera, and H. Yepes (2014), Motion of continental slivers and creeping subduction in the northern Andes, Nature Geoscience, DOI: 10.1038/NGEO2099.

- Norabuena, E., Dixon, T. H., Schwartz, S., DeShon, H., Newman, A., Protti, M., and Sampson, D. (2004). Geodetic and seismic constraints on some seismogenic zone processes in Costa Rica. Journal of Geophysical Research: Solid Earth (1978–2012), 109(B11).

- Obana, K., Kodaira, S., Kaneda, Y., Mochizuki, K., Shinohara, M., and Suyehiro, K. (2003). Microseismicity at the seaward updip limit of the western Nankai Trough seismogenic zone. Journal of Geophysical Research: Solid Earth (1978–2012), 108(B10).

- Obara, K., Hirose, H., Yamamizu, F., and Kasahara, K. (2004). Episodic slow slip events accompanied by non-volcanic tremors in southwest Japan subduction zone. Geophysical Research Letters, 31(23).

- Operto, S., Lambare, G., Podvin, P., and Thierry, P. (2003). 3D ray+ Born migration/inversion-Part 2: Application to the SEG/EAGE overthrust experiment.Geophysics, 68(4), 1357-1370.

- Ota, Y. (1986). Marine terraces as reference surfaces in late Quaternary tectonics studies: examples from the Pacific Rim. In Royal Society of New Zealand (Vol. 24, pp. 357-375).

- Outerbridge, K. C., Dixon, T. H., Schwartz, S. Y., Walter, J. I., Protti, M., Gonzalez, V., and Rabbel, W. (2010). A tremor and slip event on the Cocos-Caribbean subduction zone as measured by a global positioning system (GPS) and seismic network on the Nicoya Peninsula, Costa Rica. Journal of Geophysical Research: Solid Earth (1978–2012), 115(B10).

- Ozawa, S., Nishimura, T., Suito, H., Kobayashi, T., Tobita, M., and Imakiire, T. (2011). Coseismic and postseismic slip of the 2011 magnitude-9 Tohoku-Oki earthquake. Nature, 475(7356), 373-376.

- Pacheco, J. F., L. R. Sykes, and C. H. Scholz (1993), Nature of seismic coupling along simple plate boundaries of the subduction type, J. Geophys. Res., 98, 14,133–14,159, doi: 10.1029/93JB00349.

- Park, J. O., Tsuru, T., Kodaira, S., Cummins, P. R., and Kaneda, Y. (2002). Splay fault branching along the Nankai subduction zone. Science, 297(5584), 1157-1160.

- Peacock, S. M., and Hyndman, R. D. (1999). Hydrous minerals in the mantle wedge and the maximum depth of subduction thrust earthquakes. Geophysical Research Letters, 26(16), 2517-2520.

- Pedoja, K., 2003. Les terrasses marines de la marge Nord Andine (Equateur et Nord P´erou): relations avec le contexte g´eodynamique, PhD thesis, Université de Pierre et Marie Curie, Villefranche-sur-Mer, France.

- Pedoja, K., Dumont, J.F, Lamlthe, M., Ortlieb, L., Collot, J.-Y., Ghaleb, B., Auclair, M., Alvarez, V., Labrousse, B. Plio-Quaternary uplift of the Manta Peninsula and La Plata Island and

the subduction of the Carnegie Ridge, central coast of Ecuador. Journal of South American Earth Sciences 22 (2006a) 1–21

- Pedoja, K., L. Ortlieb, J. F. Dumont, M. Lamothe, B. Ghaleb, M. Auclair, and B. Labrousse (2006b), Quaternary coastal uplift along the Talara Arc (Ecuador, Northern Peru) from new marine terrace data, Marine Geoology, 228, 73-91,

- Pennington, W. (1981). Subduction of the eastern panama basin and seismotectonics of nothwestern South America. J. Geophys. Res., 86 : 10753–10770.

- Perfettini, H., Avouac, J. P., Tavera, H., Kositsky, A., Nocquet, J. M., Bondoux, F., and Soler, P. (2010). Seismic and aseismic slip on the central Peru megathrust. Nature, 465(7294), 78-81.

- Pennington, W. D. (1981). Subduction of the eastern Panama Basin and seismotectonics of northwestern South America. Journal of Geophysical Research: Solid Earth (1978–2012), 86(B11), 10753-10770.

- Pritchard, M. E., Norabuena, E. O., Ji, C., Boroschek, R., Comte, D., Simons, M., and Rosen, P. A. (2007). Geodetic, teleseismic, and strong motion constraints on slip from recent southern Peru subduction zone earthquakes.Journal of Geophysical Research: Solid Earth (1978–2012), 112(B3).

- Raimbourg, H., Ujiie, K., Kopf, A., Hisamitsu, T., Hamano, Y., Saito, S., and Kinoshita, M. (2011). The role of compaction contrasts in sediments in decollement initiation in an accretionary prism. Marine Geology, 282(3), 188-200.

- Ranero, C. R., and R. von Huene (2000), Subduction erosion along the Middle America convergent margin, Nature, 404, 748–752, doi:10.1038/35008046

- Ranero, C. R., Grevemeyer, I., Sahling, H., Barckhausen, U., Hensen, C., Wallmann, K., and McIntosh, K. (2008). Hydrogeological system of erosional convergent margins and its influence on tectonics and interplate seismogenesis. Geochemistry, Geophysics, Geosystems, 9(3).

- Ratzov, G., Sosson, M., Collot, J. Y., Migeon, S., Michaud, F., Lopez, E., and Le Gonidec, Y. (2007). Submarine landslides along the North Ecuador–South Colombia convergent margin: possible tectonic control. In Submarine Mass Movements and Their Consequences (pp. 47-55). Springer Netherlands.

- Ratzov, Gueorgui, et al. "Mass-transport deposits in the northern Ecuador subduction trench: Result of frontal erosion over multiple seismic cycles." Earth and Planetary Science Letters 296.1 (2010): 89-102.

- Rawlinson, N., Houseman, G. A., Collins, C. D. N., and Drummond, B. J. (2001). New evidence of Tasmania's tectonic history from a novel seismic experiment. Geophysical research letters, 28(17), 3337-3340.

- Ross, W. S. (1994). The velocity depth ambiguity in seismic travel-time data. Geophysics, 59 :830–843.

- Ribodetti, A., Valero, H., Operto, S., Virieux, J., and Gibert, D. (1998). Geophysical and medical tomography by viscoacoustic asymptotic waveform inversion of ultrasonic laboratory data. IEEE Transactions Instrumentation and Thecnology.

- Ribodetti, A., Operto, S., Virieux, J., Lambare, G., Valero H.P., and Gibert, D. Asymptotic viscoacoustic difraction tomography of ultrasonic laboratory data: a tool for rock properties analysis. Geophys. J. Int. (2000) 140, 324-340

- Rosenbaum, G., Mo, W. 2011. Tectonic and magmatic responses to the subduction of high bathymetric relief. Gondwana Research, 19, 571-582.

- Rudolph, E., and Szirtes, S., (1991). El terremoto Colombiano del 31 de Enero de 1906. Traducción al español de la Universidad del Valle, Cali-Colombia. Publicaciones Ocasionales del OSSO #1. 1991 5–10.

- Ruff, Larry, and Hiroo Kanamori. "Seismicity and the subduction process."Physics of the Earth and Planetary Interiors 23.3 (1980): 240-252.

- Ruff, L., and Kanamori, H. (1983). Seismic coupling and uncoupling at subduction zones. Tectonophysics, 99(2), 99-117

- Ruff, L., 1989. Do trench sediments affect great earthquake occurrence in subduction zones. Pure Appl. Geophys. 129, 263–282, doi: 10.1007/ BF00874629

- Sage, F., J.-Y. Collot, and C. R. Ranero (2006), Interplate patchiness and subduction-erosion mechanisms: Evidence from depth migrated seismic images at the central Ecuador convergent margin, Geology, 34, 997–1000, doi:10.1130/G22790A

- Sallares, V. and Charvis, P., 2003. Crustal thickness constraints on the geodynamic evolution of the Galapagos volcanic province, Earth planet. Sci.Lett., 214 (3–4), 545–559.

- Sallares, V., and C. Ranero (2005), Structure and tectonics of the erosional convergent margin off Antofagasta, north Chile (23° 30'S), Journal of Geophysical Reasearch, 110(B06101), doi: 10.1029/2004JB003418.

- Satake, K., and Kanamori, H. (1991). Use of tsunami waveforms for earthquake source study. In Tsunami Hazard (pp. 193-208). Springer Netherlands.

- Satake, K. (1993). Depth distribution of coseismic slip along the Nankai Trough, Japan, from joint inversion of geodetic and tsunami data. Journal of Geophysical Research: Solid Earth (1978–2012), 98(B3), 4553-4565.

- Sample, J. C., and Fisher, D. M. (1986). Duplex accretion and underplating in an ancient accretionary complex, Kodiak Islands, Alaska. Geology, 14(2), 160-163.

- Scherwath, M., Contreras-Reyes, E., Flueh, E. R., Grevemeyer, I., Krabbenhöft, A., Papenberg, C., ... and Weinrebe, R. W. (2009). Deep lithospheric structures along the southern central Chile margin from wide-angle P-wave modelling. Geophysical Journal International, 179(1), 579-600.
- Schwartz, S. Y., and Rokosky, J. M. (2007). Slow slip events and seismic tremor at circum‐Pacific subduction zones. Reviews of Geophysics, 45(3).
- Schofield, J. C. (1960). Sea level fluctuations during the last 4,000 years as recorded by a chenier plain, Firth of Thames, New Zealand. New Zealand journal of geology and geophysics, 3(3), 467-485.
- Scholz, C. H., and J. T. Engelder. "The role of asperity indentation and ploughing in rock friction—I: Asperity creep and stick-slip." International Journal of Rock Mechanics and Mining Sciences and Geomechanics Abstracts. Vol. 13. No. 5. Pergamon, 1976.
- Scholz, C. H., and C. Small (1997), The effect of seamount subduction on seismic coupling, Geology, 25, 487 - 490,
- Scholz, C. H. (1998), Earthquakes and friction laws, Nature, 391, 37–42,doi:10.1038/34097
- Segovia, M., 2009. "Análisis espacio-temporal del enjambre de Puerto López entre enero y febrero de 2005 con observaciones de la estación de banda ancha de OTAVALO", Master 2 thesis, Universite de Nice.
- Segovia M., Alvarado A., (2009). Breve Análisis de la Sismicidad y del Campo de Esfuerzos en el Ecuador. Geología y Geofísica Marina y Terrestre del 1025 Ecuador, Spec. Pub. INOCAR-IRD, 151-166 (in spanish with english abstract).
- Selzer, C., Buiter, S. J., and Pfiffner, O. A. (2008). Numerical modeling of frontal and basal accretion at collisional margins. Tectonics, 27(3).
- Shearer, Peter, and Roland Bürgmann. "Lessons learned from the 2004 Sumatra-Andaman megathrust rupture." Annual Review of Earth and Planetary Sciences 38.1 (2010): 103.
- Simons, M., Minson, S. E., Sladen, A., Ortega, F., Jiang, J., Owen, S. E., and Webb, F. H. (2011). The 2011 magnitude 9.0 Tohoku-Oki earthquake: Mosaicking the megathrust from seconds to centuries. Science, 332(6036), 1421-1425.
- Sikder, A. M., and Alam, M. M. (2003). 2-D modelling of the anticlinal structures and structural development of the eastern fold belt of the Bengal Basin, Bangladesh. Sedimentary Geology, 155(3), 209-226.
- Soloviev, S.L., and Go, C., (1975). Catalogue of Tsunamis on the Eastern Shore of the Pacific Ocean. Academy of Science of the USSR, Nauka Publishing House, Moscow, Translated from Russian to English by Canadian Institute for Science and Technical Information, No. 5078, National Research Council, Ottawa, Canada, 1984, 293 pp.

- Soofi, M. A., and King, S. D. (2002). Oblique convergence between India and Eurasia. Journal of Geophysical Research: Solid Earth (1978–2012), 107(B5), ETG-3.

- Sparkes, R., Tilmann, F., Hovius, N., and Hillier, J. (2010). Subducted seafloor relief stops rupture in South American great earthquakes: Implications for rupture behaviour in the 2010 Maule, Chile earthquake. Earth and Planetary Science Letters, 298(1), 89-94.

- Stern, C. R. (2011). Subduction erosion: rates, mechanisms, and its role in arc magmatism and the evolution of the continental crust and mantle. Gondwana Research, 20(2), 284-308.

- Subarya, C., Chlieh, M., Prawirodirdjo, L., Avouac, J. P., Bock, Y., Sieh, K., ... & McCaffrey, R. (2006). Plate-boundary deformation associated with the great Sumatra–Andaman earthquake. Nature, 440(7080), 46-51.

- Swenson, J.L. and Beck, S.L., 1996. Historical 1942 Ecuador and 1942 Peru subduction earthquakes, and Earthquake Cycle along Colombia-Ecuador and Peru subduction segments, PAGEOPH, 146(1), 67–101.

- Sykes, Lynn R. "Aftershock zones of great earthquakes, seismicity gaps, and earthquake prediction for Alaska and the Aleutians." Journal of Geophysical Research 76.32 (1971): 8021-8041.

- Taboada, A., Rivera, L. A., Fuenzalida, A., Cisternas, A., Philip, H., Bijwaard, H., & Rivera, C. (2000). Geodynamics of the northern Andes: Subductions and intracontinental deformation (Colombia). Tectonics, 19(5), 787-813.

- Taira, A., Hill, I., Firth, J., Berner, U., Brückmann, W., Byrne, T., and Zhang, J. (1992). Sediment deformation and hydrogeology of the Nankai Trough accretionary prism: Synthesis of shipboard results of ODP Leg 131. Earth and Planetary Science Letters, 109(3), 431-450.

- Theunissen, T., Font, Y., Lallemand, S., and S. Gautier (2012), Improvements of the Maximum 1014 Intersection Method for 3D absolute earthquake location, Bull. Seismol. Soc. Am., 102, 1764-1785.

- Thierry, P., Lambaré, G., Podvin, P., and Noble, M. (1999a). 3-d preserved amplitude prestack depth migration on a workstation. Geophysics, 64 :222–229.

- Thierry, P., S. Operto, and G. Lambare´ (1999), Fast 2-D ray + born migration/ inversion in complex media, Geophysics, 64, 162–181.

- Trenkamp, R., Kellogg, J. N., Freymueller, J. T., and Mora, H. P. (2002). Wide plate margin deformation, southern Central America and northwestern South America, CASA GPS observations. Journal of South American Earth Sciences,15(2), 157-171.

- Tsuji, T., Ito, Y., Kido, M., Osada, Y., Fujimoto, H., Ashi, J., and Matsuoka, T. (2011). Potential tsunamigenic faults of the 2011 off the Pacific coast of Tohoku Earthquake. Earth Planets and Space, 63(7), 831-834.

- Tichelaar, B. W., & Ruff, L. J. (1991). Seismic coupling along the Chilean subduction zone. Journal of Geophysical Research: Solid Earth (1978–2012),96(B7), 11997-12022.

- Vaca, S., M. Regnier, N. Béthoux, V. Alvarez, and B. Pontoise (2009), Sismicidad de la región de 1024 Manta (Ecuador): enjambre sísmico de Manta-2005, Geología y Geofísica Marina y Terrestre del 1025 Ecuador, Spec. Pub. INOCAR-IRD, 151-166 (in spanish with english abstract).

- Vallée, M., Nocquet, J. M., Battaglia, J., Font, Y., Segovia, M., Régnier, M., and and Chlieh, M. (2013). Intense interface seismicity triggered by a shallow slow slip event in the Central Ecuador subduction zone. Journal of Geophysical Research: Solid Earth, 118(6), 2965-2981.

- Vannucchi, P., and Tobin, H. (2000). Deformation structures and implications for fluid flow at the Costa Rica convergent margin, ODP Sites 1040 and 1043, Leg 170. Journal of Structural Geology, 22(8), 1087-1103.

- Vannucchi, P., Remitti, F., and Bettelli, G. (2008). Geological record of fluid flow and seismogenesis along an erosive subducting plate boundary. Nature,451 (7179), 699-703.

- Vogt, Peter R. "Plumes, subaxial pipe flow, and topography along the mid-oceanic ridge." Earth and Planetary Science Letters 29.2 (1976): 309-325.

- Wallace, L.M., Beavan, J., McCaffrey, R. and Darby, D., 2004. Subduction zone coupling and tectonic block roatations in the North Island, New Zealand, J. geophys. Res., 109, B12406.

- Watts, Anthony B., Anthony AP Koppers, and David P. Robinson. "Seamount subduction and earthquakes." (2010).

- Yilmaz, Ö. (2001). Seismic data analysis (Vol. 1, pp. 74170-2740). Tulsa: Society of Exploration Geophy

- Wei, S., Graves, R., Helmberger, D., Avouac, J. P., and Jiang, J. (2012). Sources of shaking and flooding during the Tohoku-Oki earthquake: A mixture of rupture styles. Earth and Planetary Science Letters, 333, 91-100.

- Vallée, M. et al., 2013. Intense interface seismicity triggered by a shallow slow-slip event in the Central-Ecuador subduction zone. J. geophys. Res.,doi:2012JB009899.

- Van Andel, T. H. (1973). Texture and dispersal of sediments in the Panama Basin. The Journal of Geology, 434-457

- Vigny, C., Socquet, A., Peyrat, S., Ruegg, J. C., Métois, M., Madariaga, R., and Kendrick, E. (2011). The 2010 Mw 8.8 Maule megathrust earthquake of Central Chile, monitored by GPS. Science, 332(6036), 1417-1421.

- van ANDEL, T. H., Rea, D. K., von Herzen, R. P., and Hoskins, H. (1973). Ascension fracture zone, Ascension Island, and the mid-Atlantic ridge.Geological Society of America Bulletin, 84(5), 1527-1546.

- von Huene, R., and Miller, J. (1988). Migrated multichannel seismic-reflection records across the Peru continental margin. Proc. Ocean Drill. Prog. Initial Rep, 112, 109-124.

- von Huene, R., and Scholl, D. W. (1991). Observations at convergent margins concerning sediment subduction, subduction erosion, and the growth of continental crust. Reviews of Geophysics, 29(3), 279-316.

- Von Huene, R., Ranero, C. R., and Vannucchi, P. (2004). Generic model of subduction erosion. Geology, 32(10), 913-916.

- Von Huene, Roland, Cesar R. Ranero, and Dave W. Scholl. "Convergent margin structure in high-quality geophysical images and current kinematic and dynamic models." Subduction Zone Geodynamics. Springer Berlin Heidelberg, 2009. 137-157.

- Vrolijk, P. (1990). On the mechanical role of smectite in subduction zones.Geology, 18(8), 703-707.

- Waldhauser, F., Schaff, D. P., Diehl, T., and Engdahl, E. R. (2012). Splay faults imaged by fluid-driven aftershocks of the 2004 Mw 9.2 Sumatra-Andaman earthquake. Geology, 40(3), 243-246.

- Wang, K. and Dixon, T. “Coupling” semantics and science in earthquake research. Eos 85, 180 (2004).

- Wang, K., and Hu, Y. (2006). Accretionary prisms in subduction earthquake cycles: The theory of dynamic Coulomb wedge. Journal of Geophysical Research: Solid Earth (1978–2012), 111(B6).

- Wang, P., Zhang, W., and Hu, T. (2007). An approximation to the P-wave reflection coefficient for amplitude variation with long-offset seismic data.Applied Geophysics, 4(1), 29-36.

- Wang, K., Hu, Y., Von Huene, R., and Kukowski, N. (2010). Interplate earthquakes as a driver of shallow subduction erosion. Geology, 38(5), 431-434.

- Wang, K., and S. L. Bilek (2011), Do subducting seamounts generate or stop large earthquakes?, Geology, 39, 819–822, doi:10.1130/G31856.1.

- Westbrook, G. K., Ladd, J. W., Buhl, P., Bangs, N., and Tiley, G. J. (1988). Cross section of an accretionary wedge: Barbados Ridge complex. Geology,16(7), 631-635.

- White, R. S. (1992). Magmatism during and after continental break-up.Geological Society, London, Special Publications, 68(1), 1-16.

- Winter, T., Avouac, J. P., and Lavenu, A. (1993). Late Quaternary kinematics of the Pallatanga strike-slip fault (Central Ecuador) from topographic measurements of displaced morphological features. Geophysical Journal International, 115(3), 905-920.

- Xu, S. (2001). Migration/inversion en milieu complexe par des méthodes asymptotiques haute fréquence. PhD thesis, Ecole de Mines de Paris.

- Yagi, Y., and Fukahata, Y. (2011). Rupture process of the 2011 Tohoku-oki earthquake and absolute elastic strain release. Geophysical Research Letters, 38(19).

- Yang, H., Y. Liu, and J. Lin (2012), Effects of subducted seamounts on megathrust earthquake nucleation and rupture propagation, Geophys. Res. Lett., 39, L24302, doi: 10.1029/2012GL053892.

- Yang, Hongfeng, Yajing Liu, and Jian Lin. "Geometrical effects of a subducted seamount on stopping megathrust ruptures." Geophysical Research Letters40.10 (2013): 2011-2016.

- Zelt, C. A., and Smith, R. B. (1992). Seismic traveltime inversion for 2-D crustal velocity structure. Geophysical journal international, 108(1), 16-34.